

# Applications of Space-Time Duality

Brent W. Plansinis

Submitted in Partial Fulfillment of the  
Requirements for the Degree  
Doctor of Philosophy

Supervised by Professor Govind P. Agrawal  
and Dr. William R. Donaldson

The Institute of Optics  
Arts, Sciences and Engineering  
Edmund A. Hajim School of Engineering and Applied Sciences  
University of Rochester  
Rochester, New York

2017

---

# Table of Contents

<b>Biographical Sketch</b>	<b>v</b>
<b>Acknowledgments</b>	<b>vii</b>
<b>Abstract</b>	<b>viii</b>
<b>Contributors and Funding Sources</b>	<b>ix</b>
<b>1 Introduction</b>	<b>1</b>
1.1 Historical Overview . . . . .	1
1.2 Problems studied . . . . .	2
1.3 Thesis outline . . . . .	3
<b>2 Background on space-time duality</b>	<b>5</b>
2.1 The space-time analogy . . . . .	5
2.1.1 Dispersive Fourier Transformation . . . . .	6
2.2 Time lenses . . . . .	8
2.2.1 Phase-modulator based time lens . . . . .	9
2.2.2 Cross-phase modulation based time lens . . . . .	10
2.2.3 Four-wave mixing based time lens . . . . .	11
2.3 Applications of time lenses . . . . .	12
2.3.1 Temporal imaging . . . . .	12
2.3.2 Time-to-frequency and Frequency-to-Time Conversion . . . . .	13
<b>3 A Temporal Imaging System for OMEGA EP</b>	<b>16</b>
3.1 Motivation and Background on Short Pulse Measurement . . . . .	16
3.2 System Design . . . . .	18
3.3 Experimental Results . . . . .	20
3.4 Future Work . . . . .	22
<b>4 Spectral changes induced by a phase modulator acting as a time lens</b>	<b>25</b>
4.1 Theory and Numerical Simulations . . . . .	25
4.2 Experimental Results . . . . .	30
4.3 Conclusions . . . . .	34

<b>5</b>	<b>Background on time reflection and refraction</b>	<b>35</b>
5.1	Spatial Boundary Reflection and Refraction . . . . .	35
5.1.1	Laws of Spatial Reflection and Refraction . . . . .	35
5.1.2	The laws of reflection and refraction . . . . .	36
5.1.3	The Fresnel Equations . . . . .	37
5.2	Time Boundary Reflection and Refraction . . . . .	38
5.2.1	Frequency Shifts at a Temporal Boundary . . . . .	39
5.2.2	Temporal Fresnel Equations . . . . .	40
5.3	Moving Boundary Reflection and Refraction . . . . .	41
5.3.1	Subluminal boundary . . . . .	42
5.3.2	Superluminal boundary . . . . .	43
5.3.3	Co-propagating moving boundary . . . . .	44
<b>6</b>	<b>Space-time Reflection and Refraction</b>	<b>46</b>
6.1	Numerical Study . . . . .	46
6.2	Space-time laws of reflection and refraction . . . . .	52
6.3	Conclusions . . . . .	57
<b>7</b>	<b>Temporal Waveguides for Optical Pulses</b>	<b>59</b>
7.1	Example of a Temporal Waveguide . . . . .	59
7.2	Modes of a Temporal Waveguide . . . . .	61
7.3	Single-Mode Temporal Waveguide . . . . .	66
7.4	Conclusions . . . . .	71
<b>8</b>	<b>Single-pulse interference caused by temporal reflection at moving refractive-index boundaries</b>	<b>72</b>
8.1	Two-pulse interference . . . . .	72
8.2	Self-interference caused by Time Reflection . . . . .	75
8.3	Self-imaging in a Temporal Waveguide . . . . .	80
8.4	Conclusions . . . . .	83
<b>9</b>	<b>Higher-Order Dispersion Effects</b>	<b>84</b>
9.1	Temporal Reflection and Refraction . . . . .	84
9.2	Third-order Dispersion Effects . . . . .	86
9.3	Higher-order Dispersion Effects . . . . .	91
9.4	Temporal Waveguides . . . . .	92
9.5	Conclusions . . . . .	97
<b>10</b>	<b>XPM-Induced Time Reflection</b>	<b>98</b>
10.1	Time Reflection and Refraction . . . . .	98
10.1.1	Super-Gaussian pump pulses . . . . .	99
10.1.2	Soliton pump . . . . .	103
10.2	Time Waveguide . . . . .	105
10.2.1	Super-Gaussian boundaries . . . . .	107
10.2.2	Soliton boundaries . . . . .	109

---

10.3 Pulse jitter compensation . . . . .	113
10.4 Conclusions . . . . .	115
<b>Bibliography</b>	<b>116</b>
<b>A Sample Code for Time Reflection</b>	<b>128</b>
<b>B Spectral reflection and refraction</b>	<b>133</b>

## Biographical Sketch

The author was born in Kittanning, PA in 1989. He enrolled in the Physics program at Penn State Erie, The Behrend College in 2007, and obtained his Bachelor of Science degree in Physics in 2011. In the fall of 2011, he enrolled in the PhD program at The Institute of Optics at the University of Rochester, and joined Professor Govind Agrawal's nonlinear photonics group in the summer of 2012. Since then he has worked to model the propagation of optical pulses in the presence of time-dependent refractive index boundaries, and collaborated with the Laboratory for Laser Energetics to develop a temporal imaging system to measure the shape in time of picosecond optical pulses.

**The following publications were a result of work conducted during doctoral study:**

**B. W. Plansinis**, W. R. Donaldson, and G. P. Agrawal, "Spectral changes induced by a phase modulator acting as a time lens," *J. Opt. Soc. Am. B* **35**, p. 1550–1554, Aug. 2015.

**B. W. Plansinis**, W. R. Donaldson, and G. P. Agrawal, "What is the temporal analog of reflection and refraction of optical beams?," *Phys. Rev. Lett.* **115**, pp. 183901, Oct. 2015.

**B. W. Plansinis**, W. R. Donaldson, and G. P. Agrawal, "Temporal waveguides for optical pulses," *J. Opt. Soc. Am. B* **33**, pp. 1112–1119, June 2016.

**B. W. Plansinis**, W. R. Donaldson, and G. P. Agrawal, "Spectral Splitting of Optical Pulses Inside a Dispersive Medium at a Temporal Boundary," *IEEE J. Quantum Electron.* **52**, pp. 6100708:1–8, Nov. 2016.

**Conference presentations**

**B. W. Plansinis**, W. R. Donaldson, and G. P. Agrawal, "Removing pulse jitter with temporal waveguides," *Frontiers in Optics Conference*, Rochester, NY, Optical Society of America, Oct. 2016.

**B. W. Plansinis**, W.R. Donaldson, and G.P. Agrawal, "Temporal analog of reflection and refraction at a temporal boundary," *Frontiers in Optics Conference*, San Jose, CA, Optical Society of America, Oct. 2015.

**B. W. Plansinis**, W.R. Donaldson, and G.P. Agrawal, "Spectral changes induced by a phase modulator acting as a time lens," *Frontiers in Optics Conference*, Tuscon, AZ, Optical Society of America, Oct. 2014.

# Acknowledgments

I would like to acknowledge the numerous individuals who made this thesis possible, and express my sincere gratitude to each of them.

I am thankful for the support and guidance from my thesis advisor Professor Govind Agrawal over the past five years. His expertise was instrumental to every aspect of my research, both theoretical and experimental, and he helped me to refine my writings for each of my publications.

Dr. William Donaldson, my supervisor at the Laboratory for Laser Energetics, has been an excellent source of both experimental and theoretical knowledge. His advice helped me to overcome the numerous hurdles encountered for the experimental work in this thesis.

I also wish to thank the final member of my thesis committee, Professor Wayne Knox, for providing useful discussions.

I would also like to thank Shaival Buch for assisting with aligning the autocorrelator, as well as the other members of the Agrawal research group, Aku Antikainen, Paco Arteaga-Sierra and Simranjit Singh for insightful discussions.

I owe a great deal of thanks to several scientists at the Laboratory for Laser Energetics for assisting with the experimental work in this thesis. I am grateful to Dr. Christophe Dorrer for providing the components used to create my time lens and for useful discussions on short pulse measurement. I am thoroughly indebted to Dr. Ildar Begishev for keeping my laser up and running, despite the persistent alignment issues that have cropped up in this decade-old laser. The streak camera measurements would not have been possible without the work of Andrew Sorce, who aligned, calibrated and operated the IR3 ROSS for all of my measurements. Joseph Katz was also helpful in synchronizing the streak camera to the laser pulse train. Thank you to Dr. Bob Boni for helping me to understand the results of these streak camera traces and the limitations of the ROSS.

Finally, I would like to thank all of my family for their endless love and support. Thank you to my mother and father for showing me how to work hard and pushing me to pursue my love of science. To my brothers Mark, Doug, Justin, Kyle and Kevin for striving to keep me humble by never letting me forget that I am sometimes the dumbest smart guy around. Most of all, I would like to thank my brilliant wife, Ashley Cannaday, for giving me love, inspiration, and a life of happiness.

# Abstract

The concept of space-time duality is based on a mathematical analogy between paraxial diffraction and narrowband dispersion, and has led to the development of temporal imaging systems.

The first part of this thesis focuses on the development of a temporal imaging system for the Laboratory for Laser Energetics. Using an electro-optic phase modulator as a time lens, a time-to-frequency converter is constructed capable of imaging pulses between 3 and 12 ps. Numerical simulations show how this system can be improved to image the 1-30 ps range used in OMEGA-EP.

By adjusting the timing between the pulse and the sinusoidal clock of the phase modulator, the pulse spectrum can be selectively narrowed, broadened, or shifted. An experimental demonstration of this effect achieved spectral narrowing and broadening by a factor of 2. Numerical simulations show narrowing by a factor of 8 is possible with modern phase modulators.

The second part of this thesis explores the space-time analog of reflection and refraction from a moving refractive index boundary. From a physics perspective, a temporal boundary breaks translational symmetry in time, requiring the momentum of the photon to remain unchanged while its energy may change. This leads to a shifting and splitting of the pulse spectrum as the boundary is crossed. Equations for the reflected and transmitted frequencies and a condition for total internal reflection are found. Two of these boundaries form a temporal waveguide, which confines the pulse to a narrow temporal window. These waveguides have a finite number of modes, which do not change during propagation. A single-mode waveguide can be created, allowing only a single pulse shape to form within the waveguide.

Temporal reflection and refraction produce a frequency dependent phase shift on the incident pulse, leading to interference fringes between the incident light and the reflected light. In a waveguide, this leads to self-imaging, where the pulse shape reforms periodically at finite propagation lengths.

Numerical simulations are performed for the specific case where the moving boundary is produced through cross-phase modulation. In this case, the Kerr nonlinearity causes the boundary to change during propagation, leading to unique temporal and spectral behavior.

## Contributors and Funding Sources

This work was supervised by a thesis committee including Professors. Govind Agrawal and Wayne Knox of The Institute of Optics and Dr. William Donaldson of the Laboratory for Laser Energetics. Portions of this dissertation have been presented and published elsewhere; co-authorship with Dr. William Donaldson and Professor Govind Agrawal, who both assisted with editing.

The streak camera measurements were performed in collaboration with Andrew Sorce from the Laboratory for Laser Energetics. The autocorrelation measurements were done in collaboration with Shaival Buch of Professor Agrawal's Nonlinear Photonics Group. Various components of the time lens system were provided by Drs. Christophe Dorrer and Robert Cuffney of the Laboratory for Laser Energetics.

This material is based upon work supported by the Department of Energy National Nuclear Security Administration under Award Number DE-NA0001944, the University of Rochester, the New York State Energy Research and Development Authority, and the National Science Foundation under award ECCS-1505636.

This report was prepared as an account of work sponsored by an agency of the U.S. Government. Neither the U.S. Government nor any agency thereof, nor any of their employees, makes any warranty, express or implied, or assumes any legal liability or responsibility for the accuracy, completeness, or usefulness of any information, apparatus, product, or process disclosed, or represents that its use would not infringe privately owned rights. Reference herein to any specific commercial product, process, or service by trade name, trademark, manufacturer, or otherwise does not necessarily constitute or imply its endorsement, recommendation, or favoring by the U.S. Government or any agency thereof. The views and opinions of authors expressed herein do not necessarily state or reflect those of the U.S. Government or any agency thereof.

# Chapter 1

## Introduction

### 1.1 Historical Overview

The development of the scalar theory of diffraction in the nineteenth century has played an important role in advancing optical imaging and signal processing systems [1]. The theory has provided a theoretical basis for developing numerous diffraction-based optical elements, such as diffraction gratings, spatial filters, spatial light modulators, and holograms. One particularly interesting property is Fraunhofer diffraction, or far-field diffraction, where the optical beam is allowed to diffract over a long distance. In this regime, the observed intensity pattern will have the same shape as the initial angular spectrum. In other words, the output intensity distribution is a scaled replica of the Fourier transform of the input distribution [1].

Perhaps equally important to scalar diffraction theory, lenses have been an essential tool for realizing optics as we know it today. They have been used for their imaging properties alone in countless applications such as telescopes, cameras, lithography, angular scattering, and lasers to name only a few. In addition to image formation, lenses bring far-field diffraction to short distances, allowing the angular spectrum to be measured or even manipulated with spatial filters.

A mathematical symmetry between paraxial diffraction and narrowband dispersion was first noted in 1964 by Tournois [2,3] and later by Akhmanov [4]. Put simply, these papers noted that the equations governing diffraction and dispersion share the same solution. In other words, dispersion causes optical pulses to broaden in time in the same way that optical beams spread out in space due to diffraction.

This so-called space-time analogy allows us to apply the techniques from Fourier optics to the time domain [5]. For example, a temporal analog of Fraunhofer diffraction occurs when an optical pulse is sent through a large amount of dispersion, e.g., by traveling through a long optical fiber or by reflecting from a chirped Bragg grating. As with the far-field diffraction pattern, the high-dispersion optical pulse shape will be a Fourier transform of the input pulse shape. The pulse shape at the output will mimic the shape of the input pulse spectrum, effectively transferring the frequency spectrum to the time domain. This process is sometimes called frequency-to-time conversion or a dispersion Fourier transformation.

Several applications have already arisen based on frequency-to-time conversion. The simplest of these applications involve spectroscopy of ultrafast, single-shot, or rare events by converting the spectrum to the time-domain and recording it with a fast photodiode and a digitizer. The technique has also been used for ultrafast imaging and fast raster-scanning by first encoding the spatial information onto the pulse spectrum by spreading the spectrum in space with a diffraction grating. A frequency-to-time conversion is then used to transfer the spatial information from the pulse spectrum to the time domain, effectively creating a space-to-time converter. [6–11].

Given this symmetry between dispersion and diffraction, it follows that there could be a temporal analog to a lens, a so-called time lens. The mathematical function of an ideal lens is to apply a quadratic phase along the transverse direction of the spatial intensity pattern. Likewise, a device that applies a quadratic phase along the temporal pulse could be devised, creating a time lens. Early time lenses used electro-optic phase modulators driven by a synchronized sinusoidal signal to create a quadratic phase modulation near the extrema of the sinusoid [5, 12–18]. Such time lenses are limited by the modulation frequency and modulation amplitudes that are possible with electro-optic phase modulators. More recently, nonlinear processes such as four-wave mixing (FWM) have been used to provide high peak phase modulations over long temporal apertures [5, 19–25]. In the FWM method a pump pulse is linearly chirped, giving a quadratic phase in time, then mixed with the signal in a nonlinear medium, transferring the quadratic phase of the pump to the signal pulse.

Regardless of how the time lens is created, these time lenses can be used as the building blocks for temporal analogs of spatial lens systems [13, 14, 16, 26–30]. The most fundamental of these is temporal imaging, where an optical pulse can be magnified or compressed in time. Such a system has many applications in measuring the shape of short pulses, as well as for pulse compression. However, just like their spatial counterparts, time lenses allow the spectrum to be transferred to the pulse shape, and the pulse shape to the spectrum, while requiring far less dispersion. This potentially allows for unique pulse shapes to be generated by creating a spectral filter with the desired profile, then using a time lens to transfer the spectrum shape to the pulse shape. These are only a few examples of the applications of time lenses. As with their spatial counterparts, time lenses are a tool with which to build numerous new systems.

## 1.2 Problems studied

When thinking of the similarity between spatial lenses and time lenses, we can also begin to examine how these lenses operate. In a traditional glass lens, the quadratic phase is produced through refraction, where a changing refractive index in space causes the beam to change angle according to Snell’s law. In the case of the time lens, all of the methods used to implement the time lens also produce a change in the refractive index, but now the refractive index varies in time and causes the pulse frequency to change. This observation, together with the space-time analogy, leads to the conclusion that there may be a temporal analog to Snell’s laws of refraction. Not only that, but because the equations governing diffraction allow for reflection at a refractive index boundary, we

would also expect to see a temporal analog of reflection at a moving refractive index boundary. The development of the temporal analogs of reflection and refraction at a moving refractive index boundary will be the primary focus of this thesis. We will also explore how we can push this theory past the space-time analogy to observe new, interesting phenomena that arise due to higher order dispersion.

Once we have established the temporal analog of reflection and refraction at a single refractive index boundary, we can use the space-time analogy to lead us toward new temporal systems based on classic spatial systems. Of particular interest is using two temporal boundaries to create a temporal analog of the waveguide. This allows an optical pulse to be confined in time in precisely the same way a planar waveguide confines light in the transverse spatial direction during propagation [31]. These waveguides exhibit the same properties as their spatial counterparts. Most notably, we will see that a temporal waveguide can support a finite number of modes, allowing for single-mode waveguides that allow a single pulse shape to propagate.

### 1.3 Thesis outline

In Chapter 2, we will review the theory behind the space-time analogy, starting from the equations governing diffraction and dispersion. We will then examine in detail how each of the methods for creating a time-lens produce the required quadratic phase modulation, as well as the advantages and limitations of each method. We will then examine how time lenses can be used for temporal imaging, as well as for converting between the time and frequency domains.

Chapter 3 will discuss the particular case of developing a time lens system for measuring picosecond pulses used in the OMEGA EP laser system at the Laboratory for Laser Energetics. We will review the motivation behind developing this system before comparing the experimental results to both numerical simulations and measurements made using a streak camera.

Chapter 4 shows numerically and experimentally how the same system developed for the LLE can be used to produce different spectral changes by adjusting the timing between the optical pulse and the phase modulation. In particular we focus on how the spectrum can be selectively narrowed, broadened or shifted simply by changing the delay of a sinusoidal phase modulation.

In Chapter 5, we first examine traditional reflection and refraction from a spatial refractive index boundary. We then cover the case of a temporal boundary where the refractive index for a uniform medium suddenly changes in time. Finally, we discuss previous works on a moving refractive index boundary.

In chapter 6, we develop the theory for space-time analog reflection and refraction. We first perform a numerical study demonstrating time reflection and refraction from a moving refractive index boundary. Based on the conservation of momentum at the moving boundary, we derive the temporal analogs of Snell's laws, and use them to find the temporal Fresnel equations as well as the condition for temporal total internal reflection (TIR)

Using two boundaries that meet the conditions for time TIR, we can create a temporal

waveguide, which confines the optical pulse between the two boundaries. Chapter 7 shows how such a time waveguide functions and develops the equations for the waveguide modes. We also discuss the unique properties of a single-mode temporal waveguide.

In Chapter 8, we investigate how light reflected from a space-time boundary interferes with the initial pulse in a configuration reminiscent of the Lloyd's mirror. We derive temporal analogs of the reflection and transmission coefficient to show how this interference pattern is affected by the phase shift that occurs during reflection. Then we show how the interference inside of a multi-mode temporal waveguide leads to a reformation of the original pulse shape, and relate this process to the Talbot effect.

Chapter 9 examines the effects of higher-order dispersion and how it allows for multiple temporal reflections and refractions at a single moving refractive index boundary. We will also examine how this affects a temporal waveguide formed in a medium where third-order dispersion is non-negligible.

Finally, in chapter 10 we will look at the specific case of a temporal boundary formed by a pump pulse through cross-phase modulation (XPM). We will compare the behavior when the pump wavelength is in the normal dispersion region and when the pump pulse is a soliton with a wavelength in the anomalous dispersion region. We will also demonstrate how such a system could be used to compensate jitter between two short pulses.

# Chapter 2

## Background on space-time duality

The mathematical symmetry between diffraction and dispersion was first noted in the late 1960's [2–4]. Despite this observation being well known, the space-time analogy remained largely un-utilized for nearly two decades until a temporal imaging system was proposed by Kolner and Nazarathy in the late 1980's [27]. Since then the analogy has seen use in a broad range of applications including pulse compression and magnification, ultrafast spectroscopy, pulse shaping, and image processing. In this chapter I review the theory behind space-time duality and temporal imaging. Section 2.1 describes the mathematical duality between diffraction and dispersion that drives the space-time analogy and some of the experimental methods that arise from its application. The function of a time lens and several practical ways to implement one are discussed in Sect. 2.2. Finally, Sect. 2.3 explores the systems that have been created with time lenses and some of their applications.

### 2.1 The space-time analogy

The space-time analogy is most simply demonstrated by examining the equations that govern paraxial diffraction and narrowband dispersion. The equation for diffraction in one transverse direction,  $x$ , for propagation in the  $z$  direction, and for dispersion of an optical pulse in the  $z$  direction can be expressed as

$$\frac{\partial U(z, x)}{\partial z} - \frac{i}{2k} \frac{\partial^2 U(z, x)}{\partial x^2} = 0, \quad (2.1)$$

$$\frac{\partial A(z, t)}{\partial z} + \frac{i\beta_2}{2} \frac{\partial^2 A(z, t)}{\partial t^2} = 0, \quad (2.2)$$

where  $U(z, x)$  is the spatial beam distribution (in one dimension),  $k$  is the amplitude of the wave vector,  $A(z, t)$  is the temporal pulse envelope, and  $\beta_2$  is the group-velocity dispersion (GVD) coefficient [1, 5, 14, 32, 33]. By inspection, we can see that the two equations are functionally the same aside from a minus sign, and therefore share the same solution. However, unlike the wave number in diffraction which is always positive for passive systems, the GVD can be either negative (anomalous dispersion) or positive (normal dispersion) allowing for setups unique to temporal imaging. We emphasize that

the case of anomalous dispersion most closely resembles paraxial diffraction, as the sign of the second term will be the same in each equation. Note that we are using anomalous and normal dispersion to refer to anomalous and normal *group velocity* dispersion, as is common in telecommunications. There is another definition of anomalous dispersion in physics which refers to the case where the *phase velocity* is higher for shorter wavelengths than longer wavelengths.

Solving Eq. (2.2) using the Fourier transform method [33], we can model the output from a dispersive path according to the equation:

$$\tilde{A}(z, \omega - \omega_0) = \tilde{A}(0, \omega - \omega_0) \exp\left(\frac{i\beta_2 z}{2} (\omega - \omega_0)^2\right), \quad (2.3)$$

where

$$\tilde{A}(z, \omega - \omega_0) = \int_{-\infty}^{\infty} A(z, t) \exp[i(\omega - \omega_0)t] dt, \quad (2.4)$$

is the temporal Fourier transform of the output pulse,  $\tilde{A}(0, \omega)$  is the temporal Fourier transform of the input pulse at  $z = 0$ , and  $\omega = \omega_0$  corresponds to the central angular frequency of the pulse. Note that neither the GVD ( $\beta_2$ ) nor the distance ( $z$ ) alone can define how the pulse spreads over a given distance. Instead, it is the group delay dispersion (GDD) defined as  $D = \beta_2 z$  that determines the temporal extent of the pulse at the output.

The above formulation does not include any distortions caused by higher-order dispersion terms. If the higher-order dispersion terms are included, the differential equation governing dispersion is modified to become

$$\frac{\partial A}{\partial z} = -\frac{i\beta_2}{2} \frac{\partial^2 A}{\partial t^2} + \frac{\beta_3}{3!} \frac{\partial^3 A}{\partial t^3} + \frac{i\beta_4}{4!} \frac{\partial^4 A}{\partial t^4} + \dots, \quad (2.5)$$

where  $\beta_n$  is the  $n$ th derivative of  $\beta(\omega)$  at the central frequency  $\omega_0$ . The propagation equation then becomes

$$\tilde{A}(z, \omega) = \tilde{A}(0, \omega) \exp\left[\frac{i\beta_2 z}{2} (\omega - \omega_0)^2 + \frac{i\beta_3 z}{3!} (\omega - \omega_0)^3 + \frac{i\beta_4 z}{4!} (\omega - \omega_0)^4 + \dots\right]. \quad (2.6)$$

We can see that the GVD term provides diffraction-like propagation, and the higher-order dispersion terms cause deviations from this ideal, which leads to aberrations [34] or time-warp [35]. Due to the mathematical duality between Eq. (2.1) and Eq. (2.2), the equation for  $U(z, x)$  can be derived using the same technique.

### 2.1.1 Dispersive Fourier Transformation

The simplest application of the space-time analogy is the dispersive Fourier transformation, which is also called frequency-to-time conversion [6, 8, 10, 11, 36–38]. This process uses only the duality between diffraction and dispersion to look at the temporal analog of the far-field diffraction, also called Fraunhofer diffraction. In far-field diffraction, the spatial profile at the output will be the Fourier transform of the input field, which is the

angular spectrum. Similarly, we can create a highly dispersive path either through a long length of dispersive material such as optical fibers or a short length of highly dispersive material such as a Bragg grating. In this case, we expect that the output pulse shape will be the Fourier transform of the input field, which is simply the spectrum of the pulse.

We can easily show the dispersive Fourier transform for highly dispersive paths using Eq. (2.3). If we take the inverse Fourier transform of Eq. (2.3), we find the output pulse shape is given by

$$A(z, t) = \int_{-\infty}^{\infty} \tilde{A}(0, \omega - \omega_0) \exp \left[ \frac{i\beta_2 z}{2} (\omega - \omega_0)^2 - i(\omega - \omega_0)t \right] d\omega. \quad (2.7)$$

Equation (2.7) can be simplified by completing the square in the exponential function to give

$$A(z, t) = \exp \left( -\frac{it^2}{2\beta_2 z} \right) \int_{-\infty}^{\infty} \tilde{A}(0, \omega - \omega_0) \exp \left[ \frac{i\beta_2 z}{2} \left( \omega - \omega_0 - \frac{t}{\beta_2 z} \right)^2 \right] d\omega. \quad (2.8)$$

For large dispersion or long distances ( $\beta_2 z \gg 0$ ), the exponential term in the integrand of Eq. (2.7) will oscillate quickly and average out to zero everywhere except at the frequency  $(\omega - \omega_0) = t/\beta_2 z$  where the phase vanishes. This exponential term behaves precisely like a delta-function,  $\delta(\omega - \omega_0 - t/\beta_2 z)$ . Therefore, the output pulse shape in time will have the form

$$A(z, t) = \exp \left( -\frac{it^2}{2\beta_2 z} \right) \tilde{A}(0, t/\beta_2 z). \quad (2.9)$$

Outside of the leading phase term, the output pulse shape will be a scaled replica of the input spectrum with the conversion factor  $(\omega - \omega_0) = t/(\beta_2 z)$ .

This simple technique is already seeing use for making spectroscopic measurements of ultrafast processes [9, 39–46]. This is typically done by using a broad spectrum laser pulse to probe a given sample. The pulse spectrum, which is now encoded with the absorption information from the sample, is then transferred to the time domain using a dispersive Fourier transformation and then read out with a fast photodiode and digitizer. This allows the spectrum to be measured at the repetition rate of the pulse train, giving a high temporal resolution for how the absorption spectrum changes in time. The technique has also been used to examine the nonlinear spectrum on a shot-by-shot basis [47, 48], which helped lead to the discovery of optical rogue waves [41].

In addition to fast spectroscopic analysis, the dispersive Fourier transform can be used for ultrafast imaging [7, 49–58]. In this method, the pulse spectrum is laid out in space with diffraction gratings, allowing the spatial information to be encoded onto the spectrum. This can be done in one dimension for line scanning [51, 53, 54, 56, 57], or in two dimensions for full image formation [50, 52, 55]. The light is then re-collected and a dispersive Fourier transform is performed to read out the spectrum on a shot-by-shot basis. This allows individual images to be recorded at the repetition rate of the laser pulses, which can be in the MHz to GHz range.

## 2.2 Time lenses

The second building block for systems using the space-time analogy is the time lens. While most traditional lenses are created by grinding and polishing glass, the ideal end result is to create a parabolic phase shift in the transverse directions  $x$  and  $y$ . On its own, an ideal lens does not change the shape of the beam, but instead stretches or compresses the angular spectrum. We can express the effect of a lens on the spatial intensity pattern in the  $x$  direction as

$$U_{out}(x) = U_{in}(x) \exp\left(i\frac{k}{2f}x^2\right), \quad (2.10)$$

where  $f$  is the focal length of the lens. This focal length is the distance over which the lens brings a collimated beam to the smallest beam diameter.

To create a time lens, we wish to find methods that create a time-dependent phase shift that is parabolic. This will cause the pulse frequency spectrum to broaden or narrow, while the temporal profile is unchanged. We can model propagation through a time lens device as

$$A_{out}(t) = A_{in}(t) \exp[i\Phi(t)], \quad (2.11)$$

where  $\Phi(t)$  is the phase change produced by the time lens. This can be approximated for any modulation by expanding  $\Phi(t)$  in a Taylor series around the center of the time lens at  $t=0$  as

$$\Phi(t) = \Phi_0 + \Phi_1 t + \frac{\Phi_2}{2} t^2 + \frac{\Phi_3}{3!} t^3 + \frac{\Phi_4}{4!} t^4 + \dots, \quad (2.12)$$

where  $\Phi_n$  is the  $n$ th derivative of  $\Phi$  at  $t = 0$ . The first term in the expansion is a constant phase shift which can be ignored. The second term is a linear phase shift which only causes a translation in the spectrum, and therefore it can also be ignored for this discussion. The quadratic term provides the ideal parabolic phase required for a time lens, and all higher order terms in this expansion are aberrations that cause distortions in the output spectrum [34]. If we use only the second order term in Eq. (2.12) and plug it into Eq. (2.11) we get

$$A_{out}(t) = A_{in}(t) \exp\left(i\frac{\Phi_2}{2}t^2\right) = A_{in}(t) \exp\left(i\frac{1}{2D_f}t^2\right), \quad (2.13)$$

where we have defined a focal GDD  $D_f = 1/\Phi_2$  that is analogous to the focal length of a traditional lens. The focal GDD is the amount of dispersion required to compress a quasi-monochromatic pulse to its smallest duration.

One important figure of merit for a time lens is the ratio of the duration of the time aperture,  $\Delta T$ , to the temporal resolution,  $\delta t$ . The time aperture is defined as the FWHM of the longest Gaussian pulse that can be captured by the lens, and varies based on the implementation of the time lens. Unlike a spatial lens, a time lens will usually still transmit light that is outside of the time aperture. Therefore, the aperture is simply the time range over which the higher order terms in Eq. (2.12) are negligible.

Similar to the spatial resolution of a lens, we can write the temporal resolution in

terms of the time aperture and the focal GDD as [5]

$$\delta t = 4 \ln(2) \frac{|D_f|}{\Delta T}. \quad (2.14)$$

This resolution is the shortest pulse that could be produced by passing a narrow-band pulse through the time lens followed by a dispersive path. The figure of merit for the time lens is then given simply as

$$N = \frac{\Delta T}{\delta t} = \frac{\Delta T^2}{4 \ln(2) |D_f|}. \quad (2.15)$$

with a higher value of  $N$  being more desirable [5]. The maximum achievable  $N$  depends on the implementation of the time lens. Modern electro-optic phase modulator-based lenses have maximum values of  $N \approx 11$ , but cascading multiple phase modulators has led to FOMs of  $N \approx 56$  [5, 17, 18]. Cross-phase modulation (XPM) based lenses, where the intensity profile of a second pulse provides the parabolic phase change through the Kerr nonlinearity, have also been explored using parabolic pump pulses, and have demonstrated performance on the order  $N \approx 20$  [5, 59–61]. Four-wave mixing based lenses provide by far the best performance with FOMs exceeding  $N = 400$  [5, 24]. We next consider each of these time lens mechanisms in greater detail and discuss their advantages and disadvantages.

### 2.2.1 Phase-modulator based time lens

An electro-optic phase modulator is perhaps the most straight-forward method for creating a time lens. In this arrangement the phase modulator is driven by a sinusoidal voltage that travels with the pulse along a lithium niobate waveguide. The sinusoidal signal creates a time-dependent refractive index change through the Pockels effect, producing a sinusoidal phase shift that matches the applied voltage as

$$\phi(t) = \phi_0 \cos(2\pi\nu_m t), \quad (2.16)$$

where  $\phi_0$  is the amplitude of the phase modulation and  $\nu_m$  is the frequency of the sinusoidal signal. If we Taylor expand around  $t = 0$  such that we are near an extremum, Eq. (2.16) becomes

$$\phi(t) = \phi_0 \left[ 1 - \frac{(2\pi\nu_m)^2}{2} t^2 + \frac{(2\pi\nu_m)^4}{4!} t^4 + \dots \right]. \quad (2.17)$$

We see that for times close to the extrema, the phase modulation is approximately parabolic, which is the desired phase profile for a time lens. Therefore, the peak of the pulse should be aligned with the maximum or minimum of the phase modulation. Comparing Eq. (2.17) to Eq. (2.12) we see that  $\Phi_2 = -(2\pi\nu_m)^2 \phi_0$  for a phase modulator based time lens, giving a focal dispersion of

$$D_f = - \left[ (2\pi\nu_m)^2 \phi_0 \right]^{-1}. \quad (2.18)$$

As the time  $t$  moves further from  $t = 0$ , the higher order terms in Eq. (2.17) cause to aberrations from the ideal lens behavior. These aberrations distort the spectrum of the pulse, which will change the image formed by the time lens. We define the time aperture as the temporal region over which these aberrations are small and can be largely ignored. Previous works have established the time aperture for the phase-modulator based time lenses as [5, 27]

$$\Delta T = 1/(2\pi\nu_m). \quad (2.19)$$

A typical driving frequency of 10 GHz will give a time aperture of a 15.9 ps. Note that the time aperture is determined only by the frequency of the sinusoidal driving voltage,  $\nu_m$ . It is often desirable to have the largest aperture possible, which corresponds to the lowest frequency that will still allow you to reach the desired time resolution. The temporal resolution is found using Eq. (2.14) to be

$$\delta t = 4 \ln(2)/(2\pi\nu_m\phi_0). \quad (2.20)$$

Using these values for the time aperture and resolution, we find the figure of merit for a phase modulator based time lens is given by

$$N = \frac{\phi_0}{4 \ln(2)}. \quad (2.21)$$

As can be seen from Eq. (2.21), the major limitation for the phase modulator time lens is the amplitude  $\phi_0$  of the phase modulation that can be created. The amplitude of the phase modulation is determined by the voltage we can drive the phase modulator with, such that  $\phi_0 = \pi V_m/V_\pi$ , where  $V_m$  is the drive voltage and  $V_\pi$  is the voltage required to produce a phase shift of  $\pi$ . Although commercially available phase modulators can have values of  $V_\pi$  as low as 1 V, using too high of a driving voltage damages the modulator. For this reason, phase modulators are currently limited to  $\phi_0 \approx 30$ . Therefore the ratio of the aperture to the resolution is at most  $N \approx 11$ . However, as mentioned previously, this can be improved by chaining multiple phase modulators in series.

### 2.2.2 Cross-phase modulation based time lens

For an XPM based time lens, a parabolic pump pulse produces the time-dependent phase shift through the nonlinear refractive index shift. These parabolic pulses can be produced with fiber Bragg gratings or inside a fiber amplifier. For a low-dispersion material, the probe pulse experiences a phase shift given by

$$\phi(t) = 2\gamma LP(t) = 2\gamma LP_0 \left(1 - \frac{t^2}{T_0^2}\right), \quad (2.22)$$

where  $P_0$  is the peak power of the pump, and  $T_0$  is the half-width of the pump pulse. The term  $\gamma$  is the nonlinear coefficient defined as [33]

$$\gamma = \frac{2\omega_0 n_2}{\epsilon_0 n c^2 A_{eff}}, \quad (2.23)$$

where  $n_2$  is the nonlinear-index coefficient.  $A_{eff}$  is the effective mode area given by

$$A_{eff} = \frac{\left( \int \int_{-\infty}^{\infty} |F(x, y)|^2 dx dy \right)^2}{\int \int_{-\infty}^{\infty} |F(x, y)|^4 dx dy}, \quad (2.24)$$

where  $F(x, y)$  is the spatial profile of the mode. It is easy to see that the time aperture is just the full width of the pump pulse such that  $\Delta T = 2T_0$ . If we take the second derivative of  $\phi(t)$ , we find that  $\Phi_2 = 4\gamma LP_0/T_0^2$ , which gives a focal GDD of  $D_f = T_0^2/(4\gamma LP_0)$ . Using Eq. (2.14), the temporal resolution is  $\delta t = \ln(2)T_0/2\gamma LP_0$ . Therefore, the figure of merit for this type of time lens is given by

$$N = \frac{4\gamma LP_0}{\ln(2)}. \quad (2.25)$$

The main limitation of the XPM based time lens is the requirement for high pump powers to achieve better resolution. This high peak power will lead to self-phase modulation within the pump itself, which distorts the temporal profile of the pump in the presence of dispersion, introducing aberrations in the time lens phase. Walkoff between the pump and probe pulses can also lead to further distortions. Despite these difficulties, experimental demonstrations of the XPM approach have demonstrated  $N \approx 20$  [60, 61]

### 2.2.3 Four-wave mixing based time lens

The four-wave mixing (FWM) based time lens is created by mixing the signal pulse with a linearly chirped pump pulse. The linear frequency chirp of the pump manifests as a quadratic phase profile across the pump pulse. The four-wave mixing process then transfers the field of the signal and the phase profile of the pump to the idler pulse, fulfilling the requirement of the time lens. The linear chirp of the pump pulse can be generated simply by passing a short pulse through a highly dispersive path as can be seen in Eq. (2.9).

The field of the idler pulse from degenerate FWM can be written as [33, 62]

$$A_i(t) = \eta A_p^2(t) A_s^*(t), \quad (2.26)$$

where  $\eta$  is the conversion efficiency,  $A_p$  is the pump field, and  $A_s^*$  is the complex conjugate of the signal field. For a sufficiently large initial chirp, the pump pulse will have the form of Eq. (2.9). Substituting Eq. (2.9) for  $A_p$  in Eq. (2.26), we see that the phase profile induced by FWM has the form

$$\phi(t) = -\frac{t^2}{D_P}, \quad (2.27)$$

where  $D_P$  is the GDD of the dispersive path that the pump was sent through. This phase profile gives a focal GDD of  $D_f = -D_P/2$ . As Eq. (2.9) indicates, the width of the time aperture will depend on the spectral width of the initial pump pulse. Assuming a flat-top spectral profile with width  $\Delta\omega_P$ , the time aperture will be approximately  $\Delta T = |D_P|\Delta\omega_P$ . The temporal resolution is then given by  $\delta t = 2\ln(2)/\Delta\omega_P$ . Interestingly, the resolution

only depends on the spectral bandwidth of the pump, and not on the GDD  $D_P$ .

Based on the above time aperture and resolution, we find the figure of merit for a FWM time lens is

$$N = \frac{|D_P|\Delta\omega_P^2}{2\ln(2)}. \quad (2.28)$$

Note that the figure of merit is not dependent on the pump power. The pump power is only important for the conversion efficiency of the FWM process. For this reason, the main limitation on the FWM time lens is higher order dispersion in the pump dispersion path. The higher order dispersion terms will change the phase profile that is transferred from the pump to the idler, which results in distortions of the idler pulse. In order to avoid this problem, shorter lengths of dispersive material must be used, which reduces the time aperture. Therefore, even though the resolution can be arbitrarily small, the time aperture will be limited by  $D_P$ . Recent works have attempted to combat this limitation using integrated photonics platforms, which allow great control over the device dispersion. Using a silicon-based platform, a temporal resolution of 220-fs with a time aperture of 100 ps has been achieved, giving a figure of merit of  $N = 450$  [5, 63].

An important property of the FWM time lens is the complex conjugate  $A_s^*$  in Eq. (2.26), which causes a sign change between the phase of the signal and the phase of the idler. In the temporal systems that follow, this sign change is equivalent to inverting the sign of the GDD of the input path.

## 2.3 Applications of time lenses

Regardless of how they are implemented, all time lenses perform the same function on an optical pulse as a traditional lens performs on an optical beam. Together with the dispersion equations, this provides the fundamental framework for all of the time lens systems. We can now begin combining lengths of dispersion with time lenses to create temporal versions of classic lens systems that can perform tasks such as imaging, Fourier transformation, and spectral magnification.

### 2.3.1 Temporal imaging

A temporal imaging system can be created by properly balancing input and output dispersions and the focal dispersion of a time lens [5, 21, 23, 64–66]. This system is directly analogous to imaging with a normal lens and can be used to magnify or compress a temporal pulse. Figure 2.1 shows schematics for these analogous imaging systems. In Fig 2.1(a), the dispersion is shown as a coil of fiber, but any dispersive medium can be used including diffraction grating pairs, fiber Bragg gratings, and prism pairs.

The condition for temporal imaging with a single time lens is found to be:

$$\frac{1}{D_1} + \frac{1}{D_2} = \frac{1}{D_f}, \quad (2.29)$$

where  $D_1$  and  $D_2$  are the input and output GDD given by  $D_n = \beta_{2,n}z_n$ . As expected, this temporal imaging condition has the same form as the traditional paraxial imaging

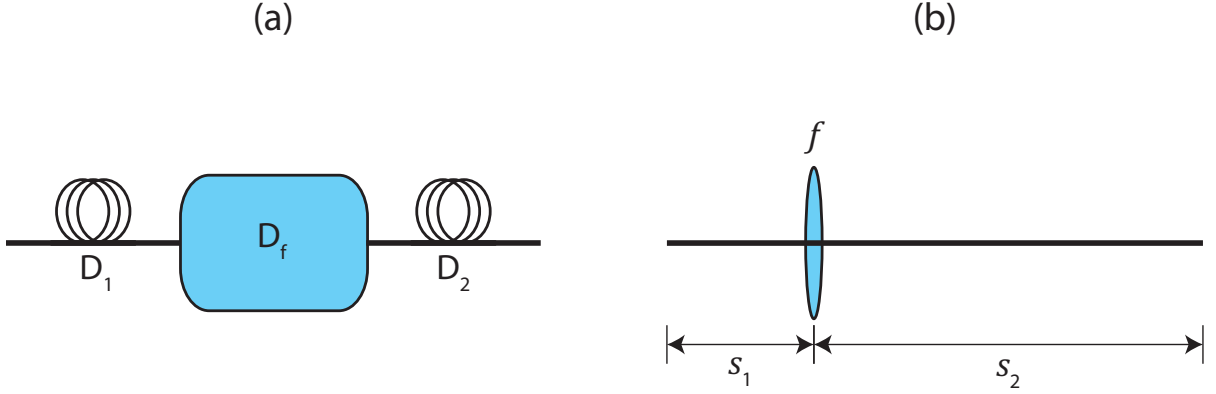


Figure 2.1: Schematic of (a) a temporal imaging system and (b) its spatial counterpart.

condition. Likewise, the magnification of such a time lens system is also analogous to the spatial magnification and is given by:

$$M = -\frac{D_2}{D_1}. \quad (2.30)$$

Using this imaging condition with the propagation equation for dispersion in Eq. (2.6) and for the time lens in Eq. (2.13), the output field has the form [5]

$$A_{out}(t) = M^{\frac{1}{2}} \exp\left(\frac{it^2}{2MD_f}\right) A_{in}\left(\frac{t}{M}\right). \quad (2.31)$$

Note the additional parabolic phase term that prevents the output pulse from being transform limited. For magnifications  $|M| \ll 1$ , this phase term becomes significant when input pulse duration is long or the focal GDD is small. Therefore, while the pulse shape at the output will be a magnified copy of the input, the output spectrum will not necessarily be a scaled replica of the input spectrum.

These temporal imaging systems are beginning to see many applications. Many early studies were looking at this effect for pulse compression in order to create shorter optical pulses [13, 19, 67]. Pulse magnification allows for real-time measurement of sub-picosecond pulses, and is even being used to examine the formation of rogue waves and their role in supercontinuum formation [25, 64, 65]. Most of these imaging systems use only a single time lens, leaving room for multiple lens systems that could be designed to compensate the aberrations from both higher order dispersion and higher order phase terms [34, 68].

### 2.3.2 Time-to-frequency and Frequency-to-Time Conversion

We can also apply the Fourier transform properties of lenses to the case of the time lens. As we will see, this will allow us to convert back and forth between the time and frequency domains. We will first examine the case of time-to-frequency conversion. In this configuration, the input GDD is equal to the focal GDD  $D_1 = D_f$  as shown in Fig. 2.2(a). This is analogous to having the object located at a distance equal to the

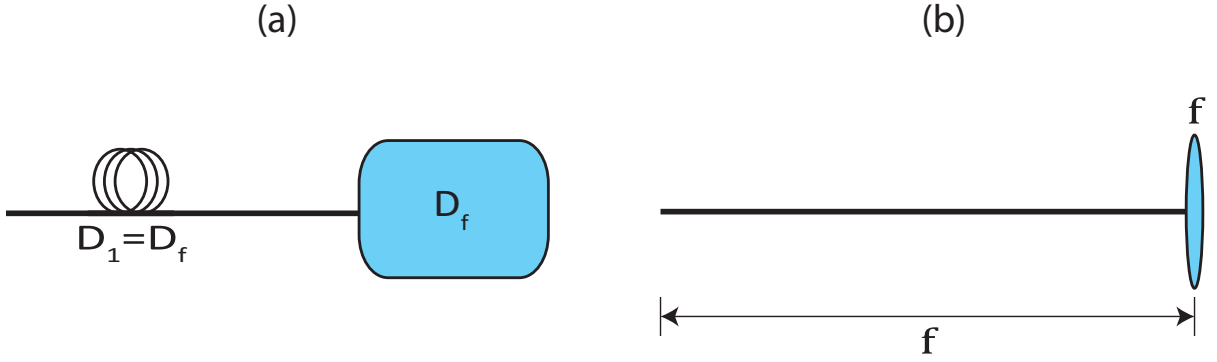


Figure 2.2: Schematic of (a) a time-to-frequency system and (b) its spatial counterpart.

focal length of the lens as shown in Fig. 2.2(b).

Using a dispersion operation from Eq. (2.3) followed by a time lens operation from Eq. (2.13), we find that when  $D_1 = D_f$  the output spectrum is given by [15, 28]

$$\tilde{A}_{out}(\omega) = A_{in}(t = D_f\omega) \exp\left(-i\frac{D_f}{2}\omega^2\right). \quad (2.32)$$

As we can see, in this configuration the output spectrum mimics the input pulse shape in time, with an additional quadratic phase factor. The conversion factor between frequency and time is simply the focal GDD,  $D_f$ . This allows the pulse shape in time to be read out using an optical spectrum analyzer, or a diffraction grating with a CCD array for single-shot detection. This is an appealing alternative to temporal imaging for measuring picosecond pulses, as it removes the need for the large output GDDs needed for large temporal magnifications.

If an additional dispersive element with GDD  $D_2 = D_f$  is added after the time lens as shown in Fig. 2.3 (a), the quadratic phase factor in Eq. (2.32) will be compensated and the output spectrum will mimic the input pulse shape without any additional phase factors. Therefore, the output pulse shape should be the Fourier transform of this, which is simply the input pulse spectrum. This temporal Fourier processor is the analog of a 2-f system, swapping the time and frequency profiles, such that the shape of the output spectrum mimics that of the input pulse shape and the output pulse shape mimics the shape of input pulse spectrum. The conversion factor between the input time and output frequency is once again the focal GDD,  $D_f$ , and the same factor converts between the output time and input frequency. Thus, the temporal Fourier processor simultaneously performs time-to-frequency conversion and a frequency-to-time conversion processes. This allows the frequency-to-time operation to be performed without the large GDD values required for a dispersive Fourier transform. One of the earliest applications of time lenses used this configuration to compress optical pulses by using a temporally long, but narrowband pulse as the input, which produces a temporally short, but broadband pulse when passed through the Fourier processor [5, 69, 70]. While this process is passive in a spatial lens,

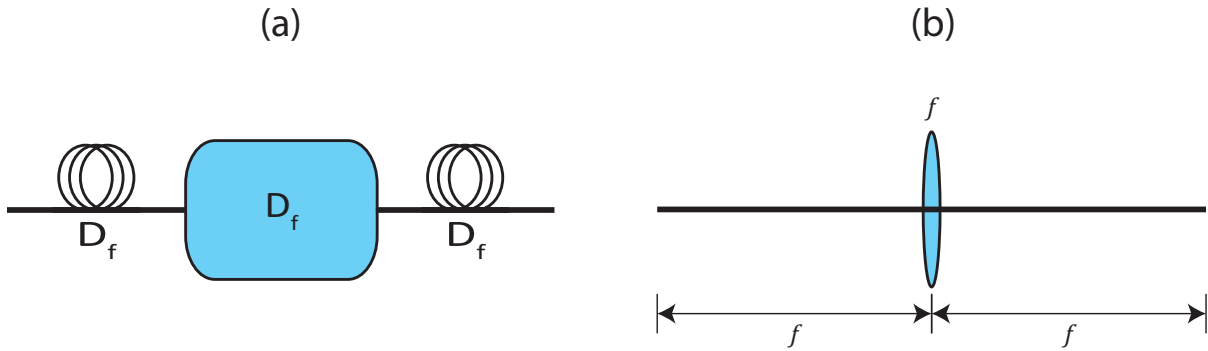


Figure 2.3: Schematic of (a) a temporal Fourier processor and (b) its spatial counterpart, the 2-f system. In each case, the input, output, and focal lengths are all equal.

for a time lens these extra spectral components are generated by the active process used to produce the time-dependent phase shift, such as Pockel's effect, XPM, or FWM. The Fourier processor has also been proposed as a method for compensating higher order dispersion and timing jitter by transferring the temporal fluctuations to the spectrum, and the relatively unchanged spectral shape becomes the detected pulse shape [71–73]

Finally, we can string two Fourier processors together one right after the other to create a temporal analog of a telescope. If the focal lengths of each time lens are different, the pulse shape and spectrum to be either magnified or compressed without the additional phase factors that arise from single-lens imaging [22, 68]. Similar arrangements have been used for spectral phase conjugation [74], and temporal cloaking [75].

---

## Chapter 3

# A Temporal Imaging System for OMEGA EP

A proof-of-concept system based on the time-to-frequency conversion configuration has been developed for the Laboratory for Laser Energetics (LLE) to transfer the pulse shape in time to the optical spectrum. The spectrum is then recorded using an optical spectrum analyzer (OSA), allowing the pulse shape to be retrieved using the conversion factor from Chapter 2. While our simulations show that this system can accurately measure pulses between 3 ps and 13 ps, using multiple state-of-the-art phase modulators should allow the entire temporal range of interest to the LLE (1–30 ps) to be imaged accurately. Single-shot performance can be achieved using a diffraction grating to spread out the spectrum in space and reading it out with a CCD array..

In Sect. 3.1 I review the motivation for developing a pulse imaging system at the LLE, and discuss the difficulties faced by the streak cameras that are currently used for this purpose. The design of the time-to-frequency converter and the limitations of the system are covered in Sect. 3.2. The experimental results are then discussed in Sect. 3.3, and the future work needed to improve the system is addressed in Sect. 3.4.

### 3.1 Motivation and Background on Short Pulse Measurement

One of the diagnostic needs at the LLE is to measure the shape of infrared ( $\lambda = 1053$  nm) pulses with durations in the range of 1 ps to 30 ps. This temporal range is important because it corresponds to the width of the OMEGA-EP short-pulse beams. Pre-shot characterization of the short-pulse beams is important to prevent damage to the system and on-shot diagnostics are needed to properly interpret the experimental results.

Optical streak cameras are traditionally used at LLE for measuring pulses of the OMEGA-EP beams [76–78]. However, there are several challenges to streak cameras that limit their use. First, time-of-flight broadening occurs due to variations in the kinetic energy of the generated photo-electrons. These variations in kinetic energy lead to different electron velocities, and therefore different amounts of time to reach the other end of the streak tube. For the infrared sensitive Ag-O-Cs photocathode (designated

S1 photocathode) used in a streak camera, this leads to impulse responses several picoseconds wide. Second, space-charge effects cause the electrons generated from short, intense pulses to repel each other. This leads to a broadening of the electron pulse in the drift region of the streak tube, which causes the measured pulse to be longer [78–81]. The space-charge effects can be reduced by using lower power pulses, but the lower powers lead to issues with the signal-to-noise ratio. The combination of these two factors means that streak cameras are not particularly well suited to measuring pulses with durations  $< 10$  ps. Finally, and perhaps most importantly, recent experience at LLE has shown that Photonis, the prime manufacturer of optical streak tubes, has lost the ability to fabricate long lasting ( $> 1$  year) S-1 photocathodes, which has significantly increased the long-term costs of operating the streak cameras. Therefore, it would be beneficial to develop new diagnostic techniques as alternatives to the streak cameras.

While autocorrelators are capable of determining the duration of pulses in the 1–30 ps range, the autocorrelation traces provide no information on asymmetries in the pulse shape. The technique also requires knowledge of the approximate shape of the input pulse to accurately determine the pulse duration. The measured pulses must also have a fairly high peak power for efficient nonlinear conversion. Furthermore, most commercial autocorrelators cannot operate in a single-shot mode, and only provide information on the average pulse shape from a train of pulses. While single-shot autocorrelators can be created, they require cylindrical lenses and have a much more limited scanning range than their multi-shot counterparts.

Frequency resolved optical gating (FROG) [82] is another common method for measuring the shape of short pulses. The method of FROG is similar to autocorrelation except the photodetector is replaced by a high resolution spectrometer. The FROG technique is particularly useful because it can provide full-field information even for single-shot pulses. While a FROG trace that averages multiple pulses can be scaled up for any pulse duration, this typically requires extremely high resolution spectrometers and long delay lines. Single-shot FROG systems have also been demonstrated, but they face the same issues of traditional FROG as well as the same limitations as single-shot autocorrelators and are therefore limited to measuring femtosecond pulses. However, a cross-correlation FROG system has recently demonstrated a range of 28 ps in the single-shot mode [83].

Temporal imaging systems are of particular interest because they can be run in both single-shot and averaging modes without changing the aperture and resolution of the time lens [66]. They are also well suited to imaging picosecond to tens-of-picosecond pulses [5]. In particular, electro-optic phase modulators driven by GHz RF signals can have apertures in the tens of picoseconds. As a proof-of-concept, we have developed a pulse imaging system that uses an electro-optic phase modulator as a time lens in a time-to-frequency converter. This system maps the pulse shape onto the spectrum, allowing the pulse shape to be recorded with an optical spectrum analyzer. In the sections that follow, we will address the design of this system, compare its performance to streak camera and autocorrelator traces, and discuss how the system can be scaled up to meet the demands of the LLE.



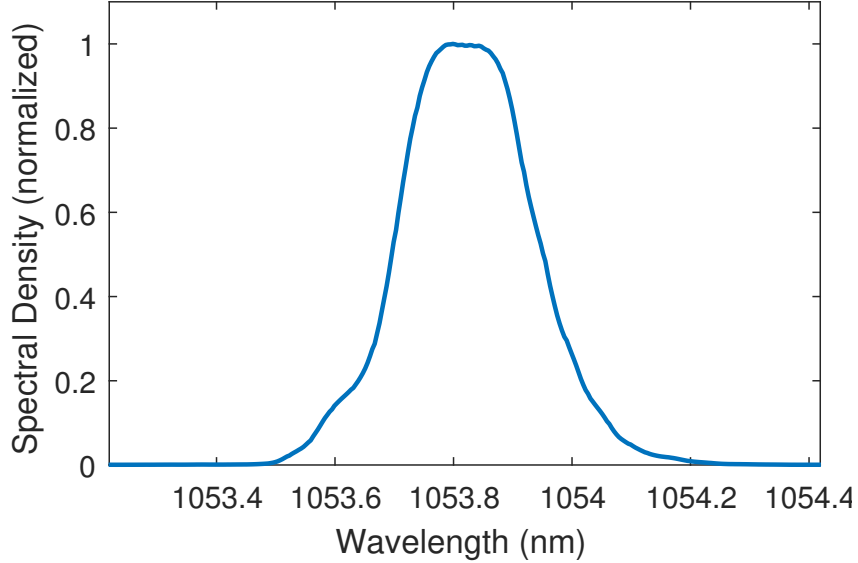


Figure 3.2: Optical spectrum analyzer trace of pulse spectrum after filtering by the volume Bragg grating.

modulator and the spectrum was recorded using an optical spectrum analyzer.

Because the laser source produces pulses shorter than the resolution of the time lens, a spectral filter needs to be applied to the laser signal to broaden the pulse in time. A volume Bragg grating (VBG) with a bandwidth of 0.5 nm was used filter the spectrum. This grating was used in a double-pass configuration to better attenuate the wings of the spectrum, resulting in a final spectral bandwidth of 0.254 nm as shown in Fig. 3.2.

The second arm of the RF line was filtered to 38 MHz and was used as a clock for a a Stanford Instruments DG645 digital delay generator, which triggered an acousto-optic modulator (AOM) and a Rochester Optical Streak System (ROSS) [76]. The AOM was used to gate the pulse train to achieve a 0.1 Hz repetition rate in order to prevent damage to the photocathode of the ROSS, and to allow only a single pulse to be captured in the streak camera image thus eliminating jitter. The ROSS was then used to capture images of the pulse shape, which are used as a comparison for the time lens measurements.

Although the time lens has a theoretical aperture of 15.9 ps, this value was found based on the FWHM of the measured pulse being largely the same as the FWHM of the actual pulse. However, even if we work with pulses shorter than the time aperture, the wings of the pulse can still see significant distortions. To explore this effect we performed numerical simulations of the pulse shape measured by a time-to-frequency converter with the same parameters as our experimental time lens. The input GDD was modeled in the frequency domain by solving Eq. (2.3) such that

$$\tilde{A}_1 = \tilde{A}_0 \exp\left(\frac{i\beta_2 z}{2}(\omega - \omega_0)^2\right), \quad (3.1)$$

where  $\tilde{A}_0$  and  $\tilde{A}_1$  are the temporal Fourier transforms of the input pulse and the pulse after dispersion respectively. The output of the time lens is then modeled using Eq. (2.11

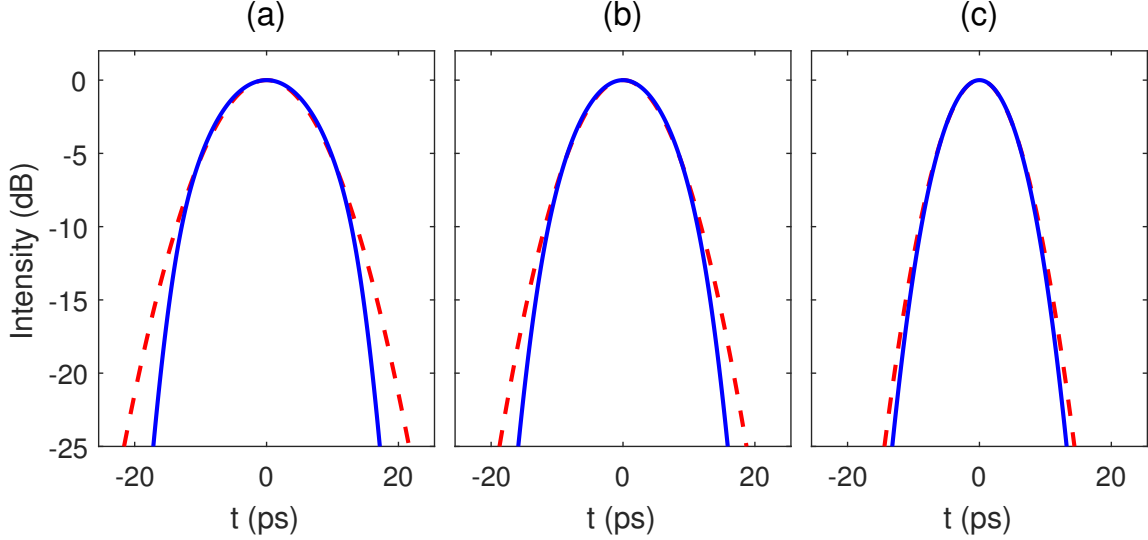


Figure 3.3: Numerical simulations showing the pulse shape at the input (dashed red) and the pulse shape measured using the time-to-frequency-converter. Initial pulse widths are (a)  $T_{FWHM} = 15$  ps, (b)  $T_{FWHM} = 12$  ps, and (c)  $T_{FWHM} = 10$  ps.

with  $\Phi(t) = \phi_0 \cos(2\pi\nu_m t)$  such that

$$A_{out}(t) = A_1(t) \exp[\phi_0 \cos(2\pi\nu_m t)], \quad (3.2)$$

Figure 3.3 shows the results for pulses with (a)  $T_{FWHM} = 15$  ps, (b)  $T_{FWHM} = 12$  ps, and (c)  $T_{FWHM} = 10$  ps. The pulse shape is plotted on a logarithmic scale to better show the behavior of the pulse wings. Comparing the three plots, we see that the 12 ps and 10 ps pulses in Fig. 3.3(b) and (c) are well imaged in the wings, while the 15 ps pulse has significant errors. We can see that the wings are beginning to be distorted for the 12 ps pulse in Fig. 3.3(b), so our effective aperture is close to 12 ps. Note that the FWHM of the 15 ps pulse is largely unchanged, with the errors arising from a suppression of the wings. A similar problem occurs for the time resolution, with our simulations showing that the resolution is closer to  $\delta t = 3$  ps.

### 3.3 Experimental Results

Three experimentally recorded spectra are shown in Fig. 3.4 in dashed red. The wavelength axis has been converted to a time axis by first converting wavelength to frequency and then using the focal GDD,  $D_f = 15.8$  ps<sup>2</sup> as a conversion factor to time. A Gaussian fit for each pulse is shown in solid blue, providing a measure of the FWHM duration of the pulse. Our measurements show a typical pulse width of around 7.2 ps, with a few traces showing FWHM pulse durations near 7.32 ps as in Fig. 3.4(a).

We first compare these measurements to an autocorrelation trace of the pulse as shown in Fig. 3.5(a). Because the autocorrelation signal was very weak due to the low peak intensity of our filtered pulses, the oscilloscope trace was averaged over 512 traces.

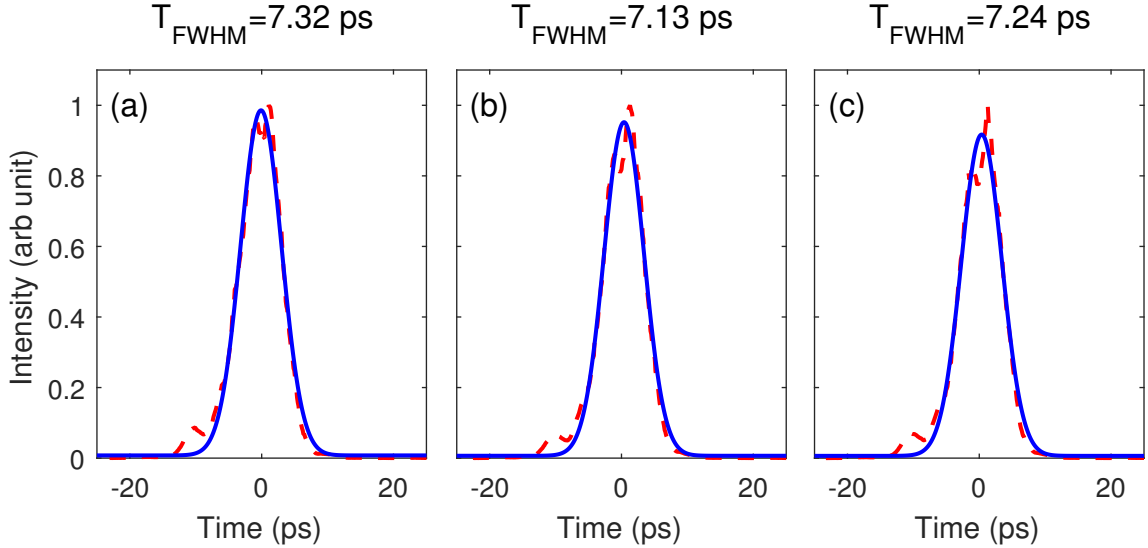


Figure 3.4: Measurement of the pulse shape produced by the volume Bragg grating using a time lens (dashed red). A Gaussian fit to the data is shown in solid blue.

The autocorrelation was then fit with a Gaussian profile and found to have FWHM duration of 10.31 ps, and using the decorrelation factor of 0.707 gives a pulse width of  $T_{FWHM} = 7.29$  ps. This agrees very well with the FWHM calculated from the time lens measurements in Fig. 3.4 of  $7.20 \pm 0.08$  ps. To obtain this value, we had to assume the input pulse shape was approximately Gaussian. While this was a good assumption in our case, the decorrelation factor can change drastically for different pulse shapes, taking a value of 0.65 for sech-shaped pulses. For the time lens, this is not a problem because no assumptions need to be made for the pulse shape. Finally, the pulses measured by the time lens have a small asymmetric peak located near  $t = -9$  ps. This peak is likely caused by a secondary reflection in the volume Bragg grating. This is not present in the autocorrelation because autocorrelations measure the overlap of two copies of the same pulse, which is a symmetric process. This ability of the time lens to measure asymmetries in the pulse shape is a major benefit of time lenses over autocorrelation.

We now compare our results to measurements from the ROSS. Figure 3.5(b) shows an example streak trace from the streak camera using the fastest sweep of 1.75 ns, with the signal pulse marked on the trace. Each image is averaged along the displacement axis to produce a temporal profile for a single pulse. Figure 3.6 shows the resulting temporal profiles from three streak camera image traces, using 0.85 ps per pixel for the 1.75 ns sweep. After multiple shots, the pulse width measured on the streak camera was found to be  $9.29 \pm 0.76$  ps. We first notice that the signal is inherently noisier than the other traces due to the single-shot nature of the streak camera. We have also reduced the power in our pulses to prevent space-charge effects, which has decreased the signal-to-noise ratio. The primary reason the streak camera measurements are consistently over a picosecond longer than those found with either the time lens or autocorrelator is due to the time-of-flight broadening. For an impulse response  $\tau$ , the measured pulse width will be  $T_m = \sqrt{T_0^2 + \tau^2}$ . The measured impulse response of  $5.78 \pm 0.63$  ps accounts for

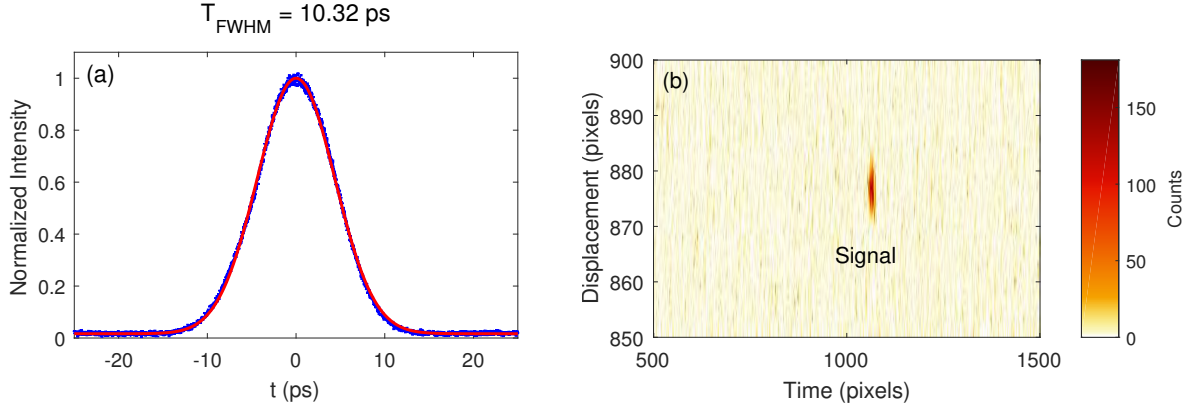


Figure 3.5: (a) Autocorrelation of the pulse produced by the volume Bragg grating. (b) Streak image for the pulse produced by the volume Bragg grating. The signal is labeled in the image.

this discrepancy between the streak camera and the other two methods of measuring the pulse duration. Furthermore, even though the streak camera can potentially see the asymmetries in the pulse shape, the impulse response of the camera is longer than the asymmetry, which can no longer be resolved. Therefore, we do not see the same consistent bump in the pulse shape that could be clearly seen in the time lens measurements.

### 3.4 Future Work

Although this proof-of-concept system has successfully demonstrated the time-to-frequency conversion process, there are several improvements that must be made to meet the requirements of OMEGA EP. The most challenging task is to expand the range of pulse durations that can be successfully imaged to cover the required 1–30 ps range. As we saw earlier, the current time lens can image only up to 12 ps pulses accurately, so we must expand the time aperture by lowering the drive frequency,  $\nu_m$ . To reliably image the wings of 30-ps pulses, the drive frequency must be less than  $\nu_m = 4$  GHz, with a time aperture of  $\Delta T = 39.8$  ps.

By lowering the RF frequency, the time resolution will be expanded by the same factor according to Eq. (2.20). Therefore, the peak phase modulation must also increase by the same factor to maintain the same time resolution. However, we also wish to lower the resolution from 3 ps to 1 ps, and we must increase the amplitude of the phase modulation to  $\phi_0 = 120$  rad. The first step to accomplishing this is to use a phase modulator designed for our wavelength. Such modulators can produce phase amplitudes up to  $\phi_0 = 30$  rad. If we then connect four of these modulators in series, we will achieve the required phase amplitude. With the new frequency and amplitude for the time lens, the focal dispersion becomes  $D_f = 13.2$  ps<sup>2</sup>, requiring only 554 m of single-mode fiber.

Figure 3.7 shows simulations for a time lens with the above parameters for input pulses with widths of (a)  $T_{FWHM} = 30$  ps, (b)  $T_{FWHM} = 15$  ps, and (c)  $T_{FWHM} = 1$  ps. While the pulses in (a) and (b) are well imaged, we see that the 1 ps pulse is no longer

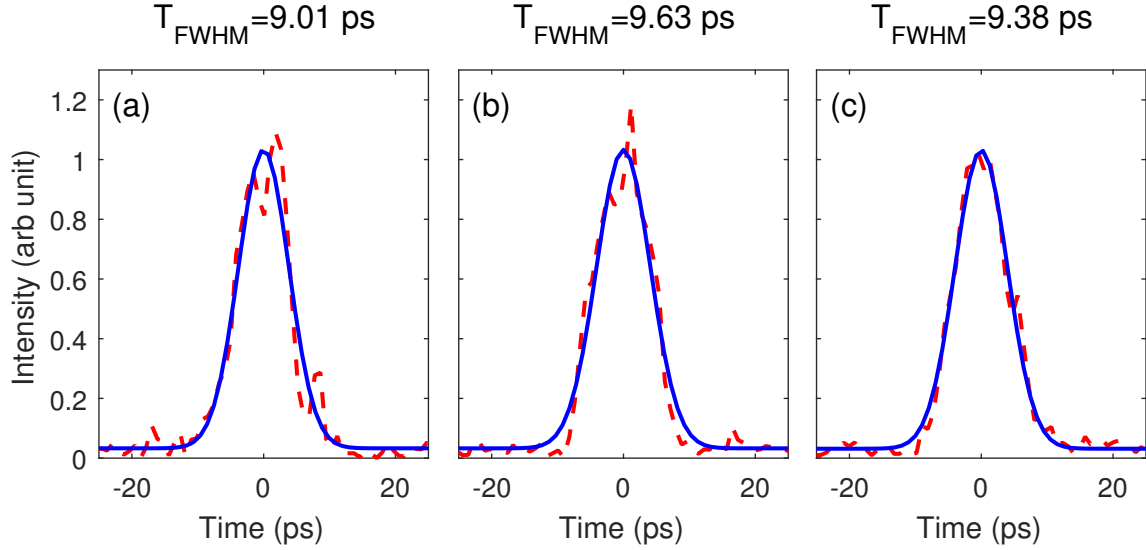


Figure 3.6: ROSS measurements of the pulse shape produced by the volume Bragg grating (dashed red) and a Gaussian fit to data (solid blue) for three different shots. The FWHM of the calculated fit is shown above each plot.

well imaged even though it is above the resolution of the time lens. This is likely caused by the aperture of the time lens being smaller than predicted in Eq. (2.19). Therefore, the resolution will actually be larger than the predicted value according to Eq. (2.14). Indeed, a 2 ps pulse should be well imaged by this time lens. In order to image pulses with durations down to 1 ps, the total phase amplitude would have to be doubled. This would require eight phase modulators to be connected in series, which would lead to even more insertion loss.

For the OMEGA-EP system in particular, we can work around this limitation because the longer pulses are formed by chirping a shorter pulse with diffraction gratings. Because optical fiber has the opposite GVD of the diffraction gratings, the 30-ps pulse will actually re-compress during propagation through the input fiber, allowing it to fit within the aperture of the time lens. Figure 3.8 shows simulated measured pulse shapes from a time-to-frequency converter where the drive frequency is increased to  $\nu_m = 7$  GHz and the phase amplitude is  $\phi_0 = 120$  rad. The input pulses were formed by dispersing a Gaussian pulse with  $T_{FWHM} = 1$  ps to a final pulse duration of (a)  $T_{FWHM} = 1$  ps, (b)  $T_{FWHM} = 15$  ps, and (c)  $T_{FWHM} = 30$  ps. As we can easily see, each of the pulses are well imaged with only slight errors in the 1 ps pulse. Therefore, we can image much longer pulses with a considerably weaker time lens if the long pulses are properly chirped.

Once the time-to-frequency converter can image the proper range of pulses, the system can be converted to a single-shot mode. This can be accomplished by feeding the output of the time lens into a single-shot spectrometer. For the system used in Fig. 3.8, the spectrometer needs to be able to resolve spectral widths as small as 160 pm. Using a diffraction grating with a line density of 1200 g/mm and a CCD with  $13.5 \mu\text{m}$  pixels, this resolution can be achieved with a spectrometer that is less than 300 mm long.

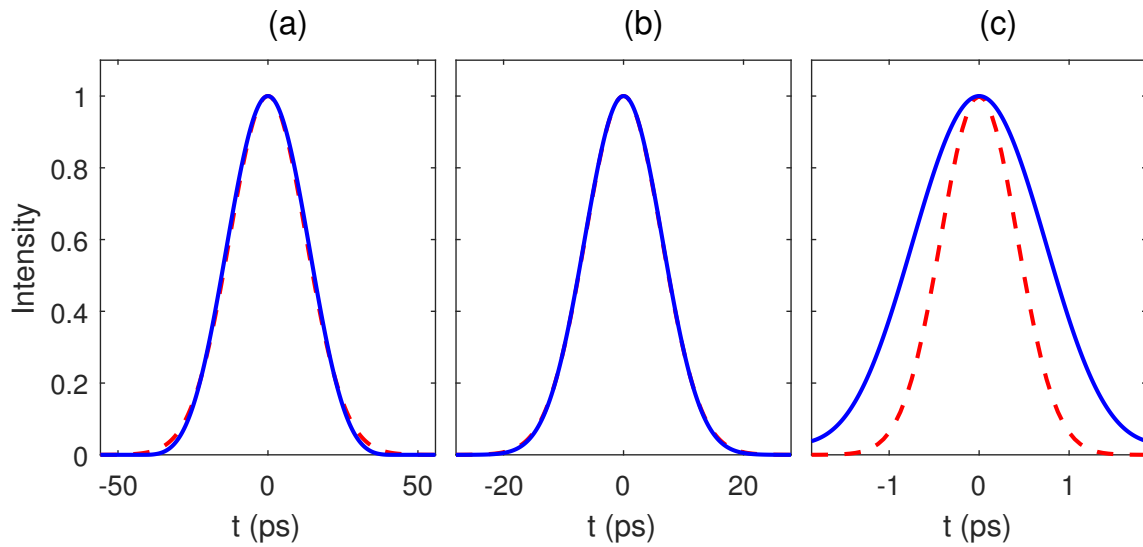


Figure 3.7: Numerical simulations showing the pulse shape at the input (dashed red) and the pulse shape measured using a time-to-frequency converter with  $\nu_m = 4$  GHz and  $\phi_0 = 120$  rad. Initial pulse widths are (a)  $T_{FWHM} = 30$  ps, (b)  $T_{FWHM} = 15$  ps, and (c)  $T_{FWHM} = 1$  ps.

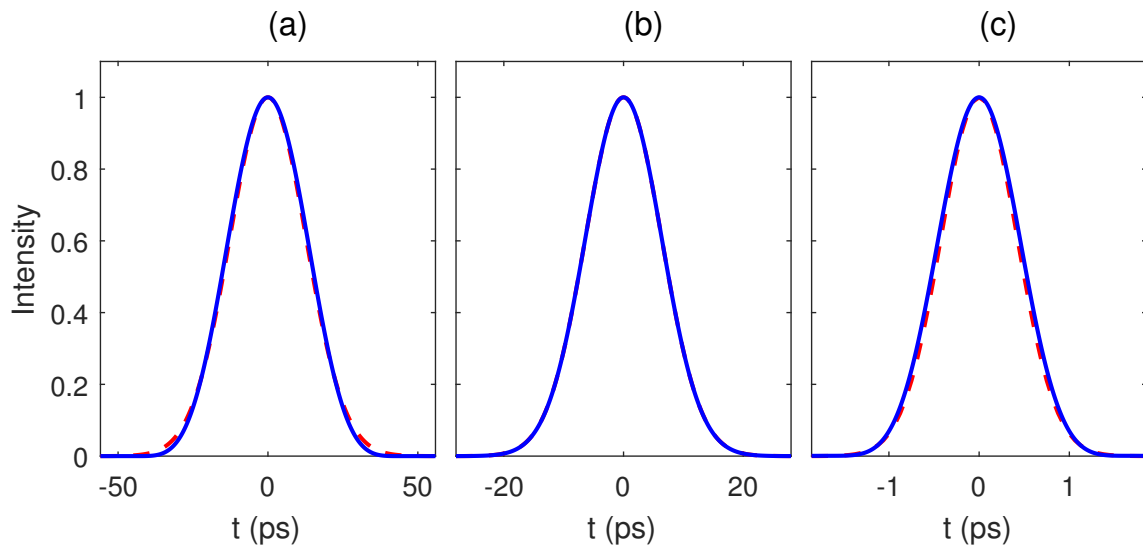


Figure 3.8: Numerical simulations showing the pulse shape at the input (dashed red) and the pulse shape measured using a time-to-frequency converter with  $\nu_m = 4$  GHz and  $\phi_0 = 120$  rad. Initial pulse widths are (a)  $T_{FWHM} = 30$  ps, (b)  $T_{FWHM} = 15$  ps, and (c)  $T_{FWHM} = 1$  ps.

## Chapter 4

# Spectral changes induced by a phase modulator acting as a time lens

An electro-optic phase modulator driven by a sinusoidal signal approximates the parabolic phase of a time lens. This approximation holds for optical pulses aligned with a local maximum or minimum of the modulation cycle. Time lenses made with this arrangement have been well explored as discussed in Chapter 2 [5,12,13]. The behavior for nonstandard configurations, however, where a temporal offset exists between the modulator voltage and optical pulse, has attracted much-less attention [85]. In this chapter, I show that by changing this temporal offset, the spectrum of an optical pulse can be selectively broadened, narrowed, or frequency shifted without requiring the Kerr nonlinearities. In Sect. 4.1 I present the relevant theory and show the results of numerical simulations. In Sect. 4.2 I verify theoretical predictions with an experiment performed using 4-ps pulses at 1053 nm and a lithium niobate phase modulator capable of providing a maximum phase shift of 16 rad at a 10-GHz modulation frequency. The main results are summarized in Sect. 4.3.

### 4.1 Theory and Numerical Simulations

We consider the Fourier-lens configuration in which an input pulse first propagates inside a dispersive medium before passing through a time lens, as discussed in Sect. 2.3. The GDD of the dispersive path of length  $L$  ( $D_1 = \beta_2 L$ ) in this configuration is chosen to be equal to the focal dispersion ( $D_f$ ) of the time lens. For a linear system, the electric field at the output of the dispersive medium can be related to the input electric field as

$$E_{out}(t) = \int_{-\infty}^{\infty} E_{in}(t')h(t-t')dt' \quad (4.1)$$

where  $h(t)$  is the impulse response of the linear dispersive medium with the Fourier transform  $\exp[i\beta(\omega)L]$  and  $\beta(\omega)$  is the propagation constant inside the dispersive medium. If  $\phi_m(t)$  is the phase shift imposed by the modulator, the pulse spectrum is obtained by

taking the Fourier transform as

$$\tilde{E}_{out}(\omega) = \int_{-\infty}^{\infty} E_{out}(t) \exp[i\phi_m(t)] e^{i\omega t} dt. \quad (4.2)$$

Using the convolution theorem in Eq. (4.1),  $E_{out}(t)$  is related to the Fourier transform of  $E_{in}(t)$  as

$$E_{out}(t) = \frac{1}{2\pi} \int_{-\infty}^{\infty} \tilde{E}_{in}(\omega) \exp[i\beta(\omega)L] \exp(-i\omega t) d\omega. \quad (4.3)$$

In practice, the propagation constant  $\beta(\omega)$  is Taylor expanded around the central frequency  $\omega_0$  of the pulse spectrum as [33]

$$\beta(\omega) = \beta_0 + \beta_1(\omega - \omega_0) + \frac{\beta_2}{2}(\omega - \omega_0)^2 + \dots \quad (4.4)$$

Here,  $\beta_0$  leads to a constant phase shift and  $\beta_1$  causes a constant temporal delay with no impact on the pulse shape or spectrum. In contrast,  $\beta_2$  affects not only the width but also the chirp of the pulse.

When an electro-optic phase modulator driven by a sinusoidal clock signal is used as the time lens, the phase shift imposed by it has the form

$$\phi_m(t) = \phi_0 \cos(\omega_m t - \theta) \quad (4.5)$$

where  $\phi_0$  is the peak amplitude,  $\omega_m = 2\pi\nu_m$  is the angular modulation frequency, and  $\theta = \omega_m t_0$  is the phase offset resulting from the time offset  $t_0$  between the peak of the sinusoidal voltage and the peak of the optical pulse. For  $\theta = 0$ , the peak of the sinusoid coincides with the peak of the optical pulse at  $t = 0$ .

Recall that the focal GDD is used to describe a time lens [14] and is given by  $D_f = -1/(\phi_0\omega_m^2)$  for a phase-modulator based time lens. In the Fourier-lens configuration, the length of the dispersive medium is chosen such that  $D_f = D_1$ .

To study the impact of finite values of  $\theta$ , we calculated the integral in Eq. (4.3) numerically and then obtained the spectrum of the output pulse as indicated in Eq. (4.2). The results are presented in Fig. 4.1, which shows the pulse spectra as a function of  $\theta$  over one modulation cycle as a color-coded surface plot. The parameter values for numerical simulations were chosen to match the capabilities of a modern, commercially available LiNbO<sub>3</sub> phase modulator operating at  $\lambda_0 = 1053$  nm. More specifically,  $\omega_m/2\pi = 10$  GHz and  $\phi_0 = 30$  rad. These values result in a time aperture of  $\Delta T = 1/\omega_m = 15.9$  ps and a temporal resolution of  $\delta t = 2.77/(\phi_0\omega_m) = 1.47$  ps [5]. The focal GDD for the time lens is  $D_f = -8.44$  ps<sup>2</sup>. The temporal phase imparted by the time lens was included exactly using Eq. (4.5). The dispersion for these simulations is assumed to be ideal, and all coefficients beyond  $\beta_2$  in Eq. (4.4) are ignored.

Figure 4.1 shows the results for Gaussian input pulses of widths (a) 1.5 ps, (b) 7 ps, and (c) 20 ps, with spectral bandwidths of 1.08 nm, 233 pm, and 81.4 pm, respectively (all full widths at half maximum). The spectral behavior is quite different for the three pulse widths. We stress that even though the pulse spectrum varies considerably with the relative phase  $\theta$ , the temporal shape of output pulses remains the same for all values

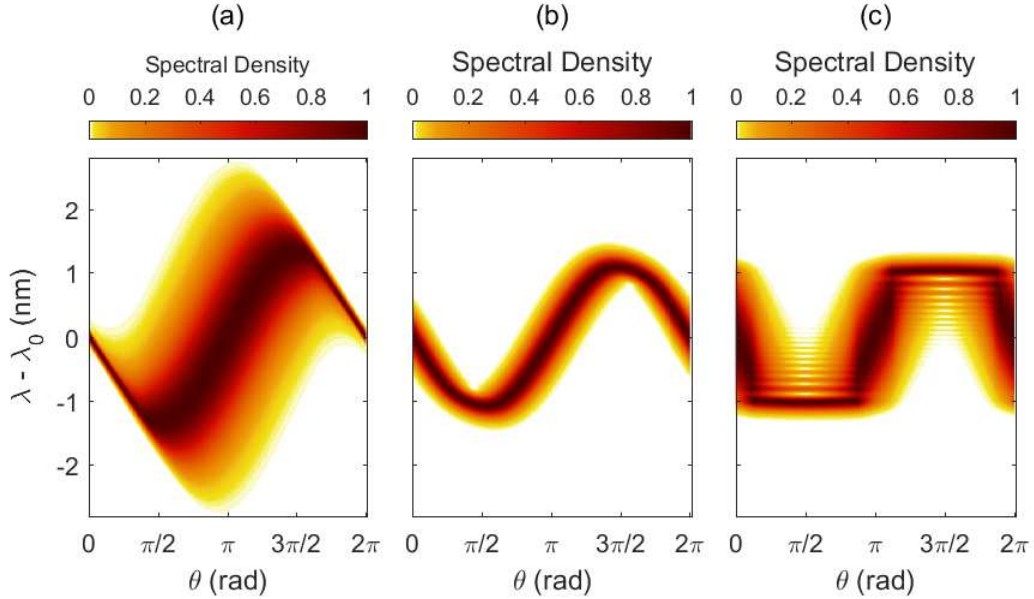


Figure 4.1: Surface plots showing simulated output spectra for different values of  $\theta$  when (a) 1.5-ps, (b) 7-ps, and (c) 20-ps Gaussian pulses are sent through a phase modulator acting as a time lens. The color bars show the range of spectral density, normalized to 1 at its peak for each value of  $\theta$ .

of  $\theta$ .

Figure 4.1(a) obtained for 1.5-ps input pulses shows that the pulse spectrum is narrowest near  $\theta = 0$ . It begins to broaden and shift toward shorter wavelengths as  $\theta$  increases, and the maximum shift of about 1.32 nm occurs for  $\theta = \pi/2$ . After this value, the spectrum shifts toward longer wavelengths, and the spectral width continues to increase until  $\theta = \pi$ , where it reaches its maximum value of 2.23 nm. The spectrum continues to shift toward longer wavelengths until  $\theta$  reaches the value  $3\pi/2$ . Beyond this, the spectrum begins to narrow and recovers its original size at  $\theta = 2\pi$ . Note that the spectral evolution is antisymmetric with respect to  $\theta - \pi$ .

To understand the physical origin of these spectral changes, it is useful to expand  $\phi_m(t)$  in Eq. (4.5) as a Taylor series around  $t = 0$  as

$$\phi_m(t) = \phi_0 \left[ \cos \theta - (\omega_m \sin \theta)t - \left( \frac{\omega_m^2}{2} \cos \theta \right) t^2 + \dots \right] \quad (4.6)$$

When there is no phase offset ( $\theta = 0$ ), all odd-order terms vanish in the Taylor expansion. If we further retain the terms only up to second order,

$$\phi_m(t) = \phi_0 \left( 1 - \frac{\omega_m^2 t^2}{2} \right) \quad (4.7)$$

The quadratic term provides a time-dependent parabolic phase shift and fulfills the function of an ideal time lens. The higher-order phase terms in Eq. (4.6) lead to the tem-

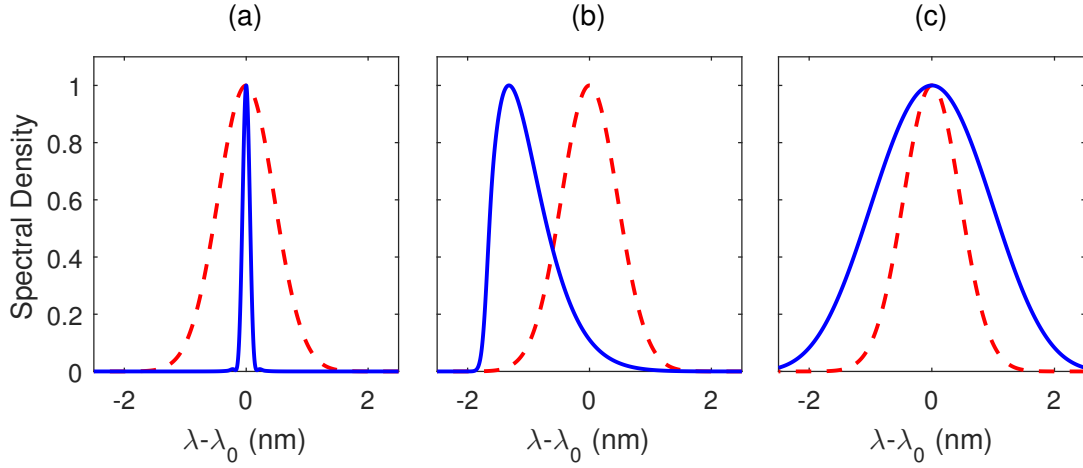


Figure 4.2: Comparison of input (dashed) and output (solid) spectra for a 1.5-ps input pulse at clock phases (a)  $\theta = 0$ , (b)  $\theta = \pi/2$ , and (c)  $\theta = \pi$ .

poral equivalent of spatial aberrations and cause distortions in the output pulse shape and spectrum [34]. The time aperture, as defined earlier, is the temporal range over which these higher-order phase terms are small and do not noticeably distort the output of the time lens [19].

The features seen in Fig. 4.1(a) can be understood from Eqs. (4.2) and (4.6). It is easy to see that the linear term in the Taylor expansion in Eq. (4.6) corresponds to a frequency shift in the pulse spectrum by an amount

$$\Delta\omega = \phi_0(\omega_m \sin \theta). \quad (4.8)$$

This shift is maximum when  $\theta = \pi/2$  and has the value  $\Delta\nu = \phi_0\omega_m/2\pi$ . For values of  $\phi_0 = 30$  rad and  $\omega_m/2\phi = 10$  GHz, this gives a maximum shift of 300 GHz or 1.11 nm at  $\lambda = 1053$  nm—a value that is close but not identical to the numerical value of 1.32 nm in Fig. 4.1(a). The source of this difference will be discussed later. It is important to note that the frequency shift is the same regardless of the central wavelength of the input pulse. Therefore, a phase modulator with the same parameters operating at a longer wavelength would produce a larger wavelength shift. For example, a phase modulator at 1550 nm with the same parameters would produce a wavelength shift of about 2.4 nm.

In addition to the linear phase term, the parabolic phase term changes with  $\theta$  as  $\phi_2 = -\phi_0\omega_m^2 \cos \theta$ . This dependence changes the focal GDD of the time lens as  $D_f(\theta) = -(\phi_0\omega_m^2 \cos \theta)^{-1}$ . The minimum focal GDD occurs at  $\theta = 0$  and increases in magnitude for other phase offsets. Additionally, the sign of the focal GDD is inverted between  $\theta = \pi/2$  and  $\theta = 3\pi/2$ . In our situation this is analogous to changing from a convex to a concave lens. Changes in the bandwidth of the output spectrum seen in Fig. 4.1(a) result from this  $\theta$  dependence of the focal GDD.

Figure 4.2 compares the output and input spectra of 1.5-ps pulses for three specific values of  $\theta$ . In Fig. 4.2(a), the width of the output spectrum is only 0.136 nm, i.e., the output spectrum is narrowed by a factor of nearly 8 when compared to the input spectrum. This spectral compression is the temporal analog of the collimation of an

optical beam realized with a lens and may be useful for applications requiring a narrow-bandwidth source. Just as in the spatial case, where angular divergence is reduced by expanding the size of the optical beam, spectral compression is accomplished at the expense of a broader pulse. The dispersive medium broadens the pulse while chirping it simultaneously, and the modulator is used to cancel the chirp and produce a transform-limited pulse. For this reason, the spectrum is compressed by the same factor by which the pulse broadens in the time domain.

Figure 4.2(b) drawn for  $\theta = \pi/2$  shows that the spectrum is shifted toward shorter wavelengths by 1.32 nm without a significant change in the spectral width. Such wavelength shifts do not require the Fourier-lens configuration and has been previously demonstrated for pulses passed directly through a modulator [86–88]. In our case, the spectral shift reaches a maximum at  $\theta = \pi/2$  and  $\theta = 3\pi/2$  as predicted by the theory, where the peak of the pulse coincides with the maximum slope of the time-dependent phase. Deformation of the spectral shape in Fig. 4.2(b) is caused by the cubic term in Eq. (4.6). This term is also responsible for the larger 1.32-nm shift compared to that predicted by the linear term. Indeed, if we repeat our simulations and only keep up to the quadratic terms of Eq. (4.6), the input and output spectra become identical except for a spectral shift whose magnitude of 1.11 nm coincides with the theoretical estimate presented earlier.

Figure 4.2(c) shows that the spectral shift disappears for  $\theta = \pi$ . This feature is easily understood from Eq. (4.6), showing that both the linear and cubic terms vanish for this value of  $\theta$ . Finally, the spectral broadening seen in Fig. 4.2(c) originates from the sign change of the quadratic term in Eq. (4.6) for  $\theta = \pi$ . In effect, the modulator is now acting analogous to a concave lens that increases the angular spread of a beam incident on it.

The 2.23-nm spectral bandwidth, occurring at  $\theta = \pi$ , indicates broadening by a factor of about 2. Unlike spectral broadening from effects like self-phase modulation, the spectrum broadened by a time lens maintains its initial shape, as is apparent in Fig. 4.2(c). Slight distortions in the spectral wings have their origin in the fourth-order term in Eq. (4.6).

Here we briefly discuss the results shown in Fig. 4.1(b) and Fig. 4.1(c). The 7-ps input pulse does not experience spectral narrowing at  $\theta = 0$ , instead broadening to a bandwidth of 0.49 nm. This is due to the time-to-frequency conversion process mapping longer pulses, which have narrower bandwidths to begin with, to a wider spectrum. Meanwhile, the broadening factor at  $\theta = \pi$  increases to a factor of 3, which is a result of the narrower initial bandwidth and longer duration of the initial pulse. We will discuss this in more detail shortly. Other than these effects, the behavior of the 7-ps pulse is nearly the same as the 1.5-ps pulse. The behavior for the 20-ps input pulse in Fig. 4.1(c) is markedly different from the other two. The pulse experiences negligible broadening when passing through the dispersive medium. However, the pulse is already longer than the aperture of the time lens. The spectrum is wider at  $\theta = 0$  and becomes narrowest at  $\theta = \pi/2$ , reaching a minimum bandwidth of 0.158 nm. The spectrum then broadens again near  $\theta = \pi$ , where the time lens once again acts like a concave lens and reaches a bandwidth of 1.58 nm. The behavior at  $\theta = 0$  and  $\theta = \pi$  is analogous to a highly collimated optical beam incident on either a convex lens or a concave lens, respectively.

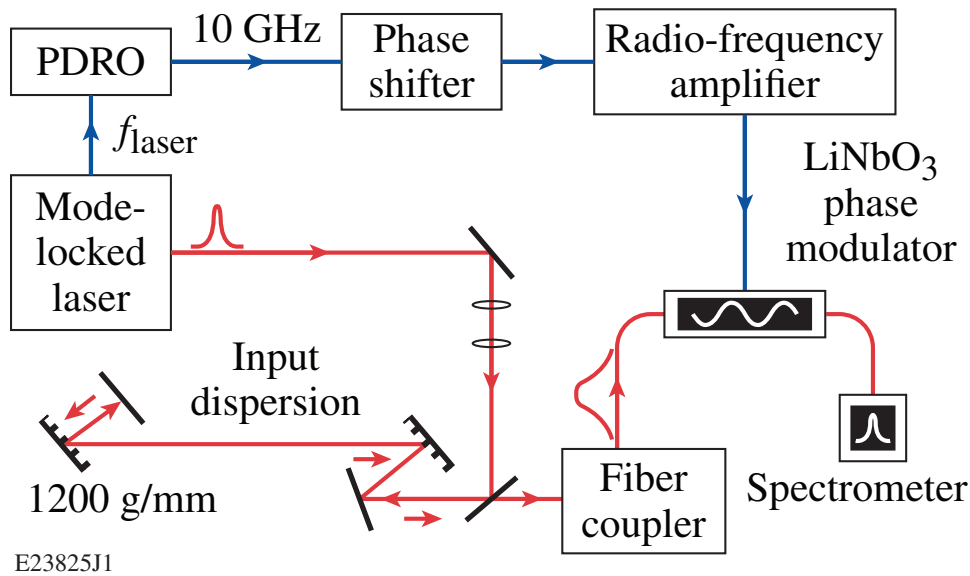


Figure 4.3: Experimental setup for a time-to-frequency converter using a phase modulator as a time lens. PDRO: Phase-locked dielectric resonator oscillator..

For a highly collimated beam, the beam shape does not change with propagation. The angular spread of the beam is affected, however, by the lens where both convex and concave lenses expand it. Near  $\theta = \pi/2$ , the 20-ps pulse experiences smaller spectral shifts than the 4-ps pulse and the spectrum appears "flattened" in Fig. 4.1(b). Because the 20-ps pulse is much longer than the time aperture, the effects of the cubic term are larger, leading to additional shifting of the spectral shape toward the central frequency, which causes the flattening of the spectrum observed in Fig. 4.1(b).

Clearly the spectral magnification and shape preserving property of the time lens when  $\theta = \pi$  changes as the input pulse duration increases. This is because when  $D_f = -D_1$ , the system acts in a similar manner to a temporal imaging system with magnification factor  $M = 1/2$ . This means that if an output dispersion  $D_2 = -D_1/2$  were placed after the time lens, the output pulse would be half as long in time as the input pulse. If this imaging system were a perfect magnifier that did not impose an additional phase term, the spectrum would be broadened by a factor of 2 for all input pulses. However, as we saw in Sect. 2.3, this imaging system would have an extra parabolic phase factor of  $\exp(it^2/D_f)$ . When the input pulse duration is short or when  $D_f$  is large, this term is nearly constant across the pulse duration, and therefore causes no additional broadening of the pulse spectrum. However, as the input pulse duration increases, this phase factor begins to dominate, leading to additional broadening of the pulse spectrum.

## 4.2 Experimental Results

A schematic of the experimental setup is shown in Fig. 4.3, which is nearly identical to the experimental setup from the previous chapter except for a few important differences. First, the streak camera arm was not used for this experiment. Second, the "trombone"

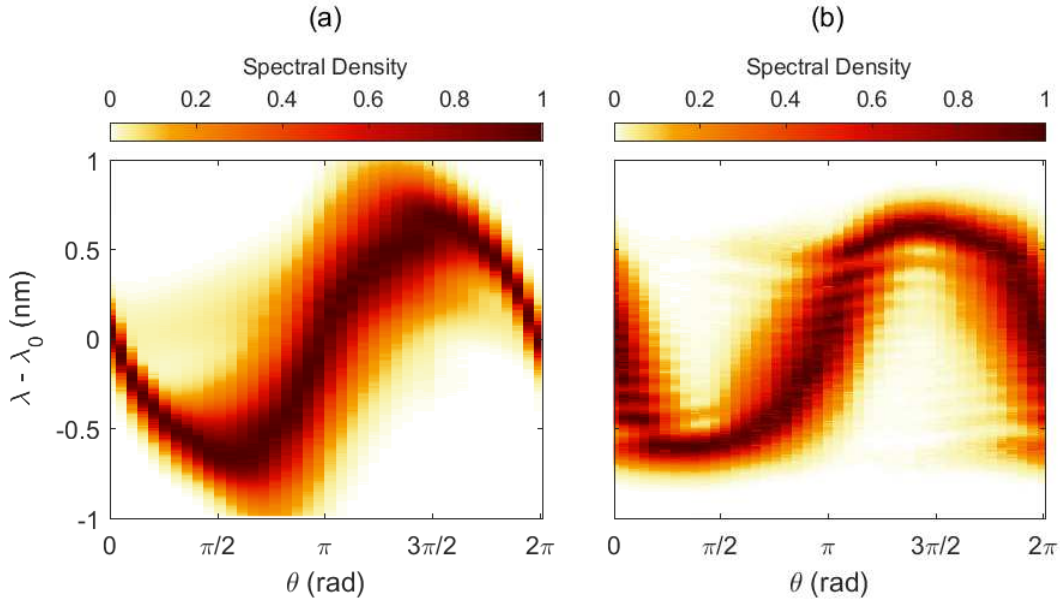


Figure 4.4: Surface plots showing experimental output spectra for different values of  $\theta$  when input pulses were filtered to produce (a) 0.407- and (b) 0.107-nm-wide input spectra. The color bars show the range of spectral density, normalized to 1 at its peak for each value of  $\theta$ .

phase shifter was controlled with a translation stage driven by a stepper motor. Using an oscilloscope, each step of the motor was found to produce a 42-fs delay in the 10-GHz clock signal, corresponding to 2.63 mrad of clock phase shift. The input dispersion is now provided by a parallel grating pair used as a dispersive delay line. The delay line was created using two 1200-lines/mm reflective diffraction gratings separated by 80 cm with an incident angle of  $25.3^\circ$  to produce a GDD that matched  $Df = 15.8 \text{ ps}^2$  of our time lens. The chirped and broadened pulse was then sent through the phase modulator. For different clock phases, the pulse spectrum was recorded using an optical spectrum analyzer.

Finally, two different filters were applied to the laser signal to broaden the 150-fs pulses. A slit filter was used between the parallel gratings to create a spectral width of 0.407 nm, corresponding to Gaussian pulses of 4-ps duration. In addition, a volume Bragg grating with a spectral width of 0.108 nm produced longer pulses of  $\sim 19$  ps duration, assuming transform-limited pulses.

Note that this setup produced a peak phase shift of  $\phi_0 = 16$  rad, a value lower than the 30 rad used in numerical simulations. For this reason, the range of spectral bandwidths and spectral shifts is reduced compared to the simulations. Our time lens has a time aperture of 15.9 ps, a resolution time of  $\delta t = 2.8$  ps, and a focal GDD of  $D_f = -15.8 \text{ ps}^2$ .

The experimentally recorded spectra are shown in Fig. 4.4. Comparing the short-pulse cases of Fig. 4.4(a) with Fig. 4.1(a), we see that the two cases agree qualitatively. In particular, the experimental spectra follow an identical progression as  $\theta$  advances through the phase-modulation cycle. As predicted by theory in Sect. 4.1, the experimental spectrum

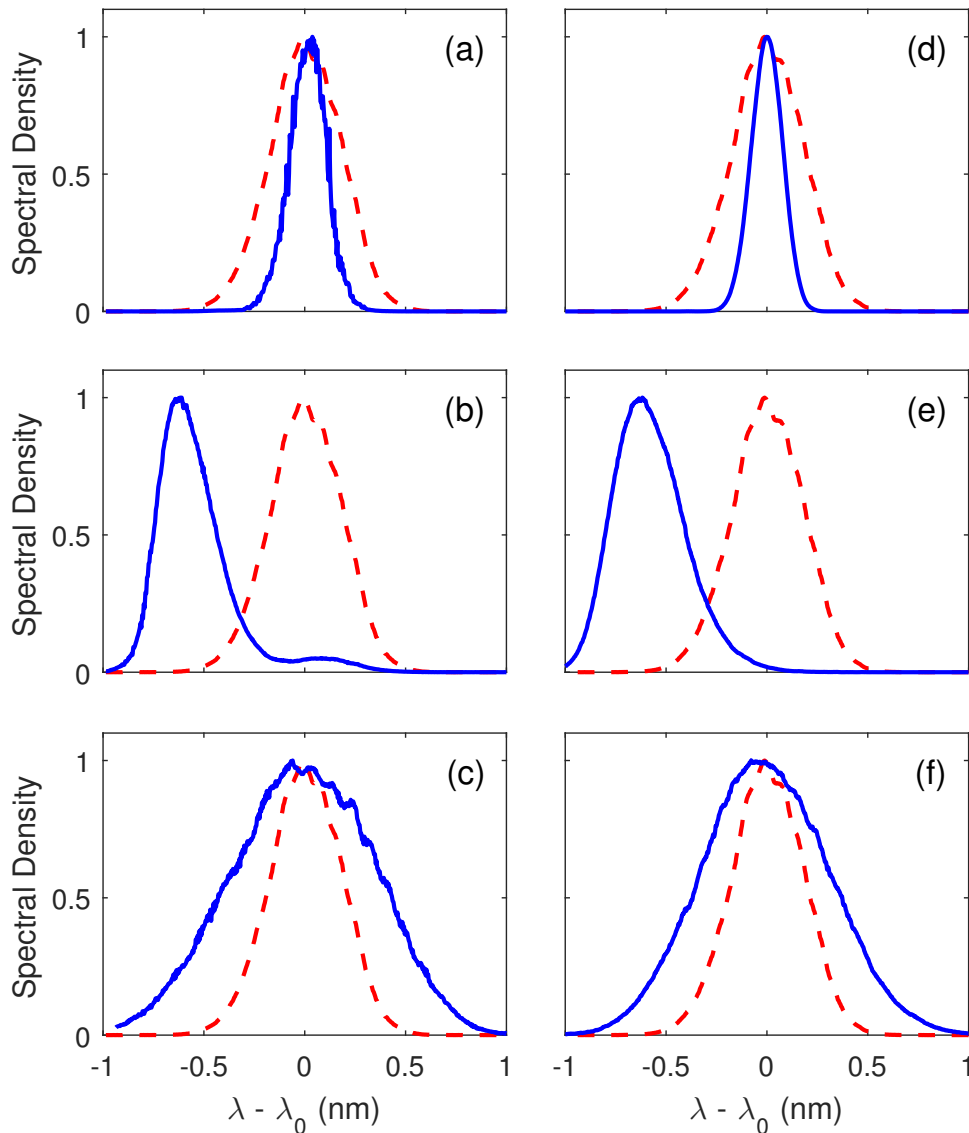


Figure 4.5: Comparison of [(a)-(c)] experimental and [(d)-(f)] simulated output spectra (solid blue line) for [(a),(d)]  $\theta = 0$ , [(b),(e)]  $\theta = \pi/2$ , and [(c),(f)]  $\theta = \pi$ . The input spectrum is shown by the dashed red line.

is narrowest at  $\theta = 0$ , reaches maximum spectral shift at  $\theta = \pi/2$  and  $\theta = 3\pi/2$ , and exhibits the largest spectral broadening at  $\theta = \pi$ .

Figure 4.5 compares [(a)-(c)] the experimentally recorded and [(d)-(f)] theoretically predicted output spectra for the same three values of  $\theta$  in the case of 4.8-ps input pulses. The numerical simulations used the experimentally recorded input spectrum (shown by a red dashed line for comparison) to obtain the temporal profile. This temporal profile was found by adding a dispersive chirp to the simulated input pulse until the time-to-frequency conversion (spectral narrowing) agreed with the experimental value. This was found to occur when the initial pulse chirp corresponded to a dispersion of  $D_i = -D_f/8$ . We can quantify the agreement of the experimental and simulated spectral shapes by

looking at the normalized convolution of the two spectra as

$$\psi = 1 - \frac{\max \left( |\tilde{A}_{sim}|^2 \otimes |\tilde{A}_{exp}|^2 \right)}{\sqrt{\max \left( |\tilde{A}_{sim}|^2 \otimes |\tilde{A}_{sim}|^2 \right) \max \left( |\tilde{A}_{exp}|^2 \otimes |\tilde{A}_{exp}|^2 \right)}}, \quad (4.9)$$

where  $|\tilde{A}_{exp}|^2$  is the experimentally recorded spectrum, and  $|\tilde{A}_{sim}|^2$  is the simulated spectrum. A value of  $\psi = 0$  corresponds to perfect agreement of the spectral shapes, and a value of  $\psi = 1$  corresponds to completely different spectral shapes.

In agreement with our numerical simulations in Sect. 4.1, we observe spectral compression at  $\theta = 0$  in Figs. 4.5(a) and 4.5(d), with an error metric of  $\psi = 0.006$ . The width of the output spectrum is 0.18 nm, indicating that the pulse spectrum is compressed by a factor of about 2, which is considerably smaller than the factor of 8 observed in Fig. 4.2(a). The reduced compression factor is caused by the smaller spectral width of 4.8-ps input pulses and 16-rad maximum phase shift of the modulator used in our experiment. For the same reason, the spectral shift of 0.68 nm seen in Fig. 4.5(b) for  $\theta = \pi/2$  is also smaller compared to that seen in Fig. 4.2(b). The spectrum in Fig. 4.5(b) also has a small bump near  $\lambda = \lambda_0$  that is not present in Fig. 4.5(e), which leads to a higher error metric of  $\psi = 0.011$ . This bump arises from the polarization dependence of our phase modulator. More specifically, the modulator produces a significantly smaller value of  $\lambda_0$  along the slow axis compared to the fast axis. A small mismatch between the pulse's polarization direction and the slow axis of the phase modulator produces the bump in the spectrum seen in Fig. 4.5(b). Because our theory does not include polarization effects, this bump is not reproduced in Fig. 4.5(e).

As seen in Figs. 4.5(c) and 4.5(f), the pulse spectrum has a bandwidth of 0.86 nm when  $\theta = \pi$ , i.e., it has been broadened by a factor of 2.1, while the shape of the input spectrum is nearly preserved. This is supported by the low error metric between the simulated and experimental spectra of  $\psi = 0.004$ . Some distortion of the spectral shape is observed because the pulse is chirped in time during the input dispersion, causing wavelengths farther away from the central wavelength to move toward the wings of the pulse. Because our input pulse is close to the resolution of the time lens, the output spectrum should nearly be a magnified copy of the input spectrum instead of just a broadened spectrum. To demonstrate this, a thin wire was moved within the razor-blade filter to create different spectral shapes. Figure 4.6 shows the input (dashed) and output (solid) spectral shapes for two different positions of the wire. As can easily be seen, the asymmetric pulse shape is nearly preserved and magnified by a factor of two. However, since the pulse wings experience aberrations from higher-order phase terms in the time lens, small distortions appear in the shape of the spectrum. We emphasize, however, that a suitably designed time lens can broaden the spectrum of a pulse without significantly distorting its shape. In this respect, a time lens is superior to the use of self-phase modulation, which invariably distorts the spectrum while broadening it (and also requires high pulse energies).

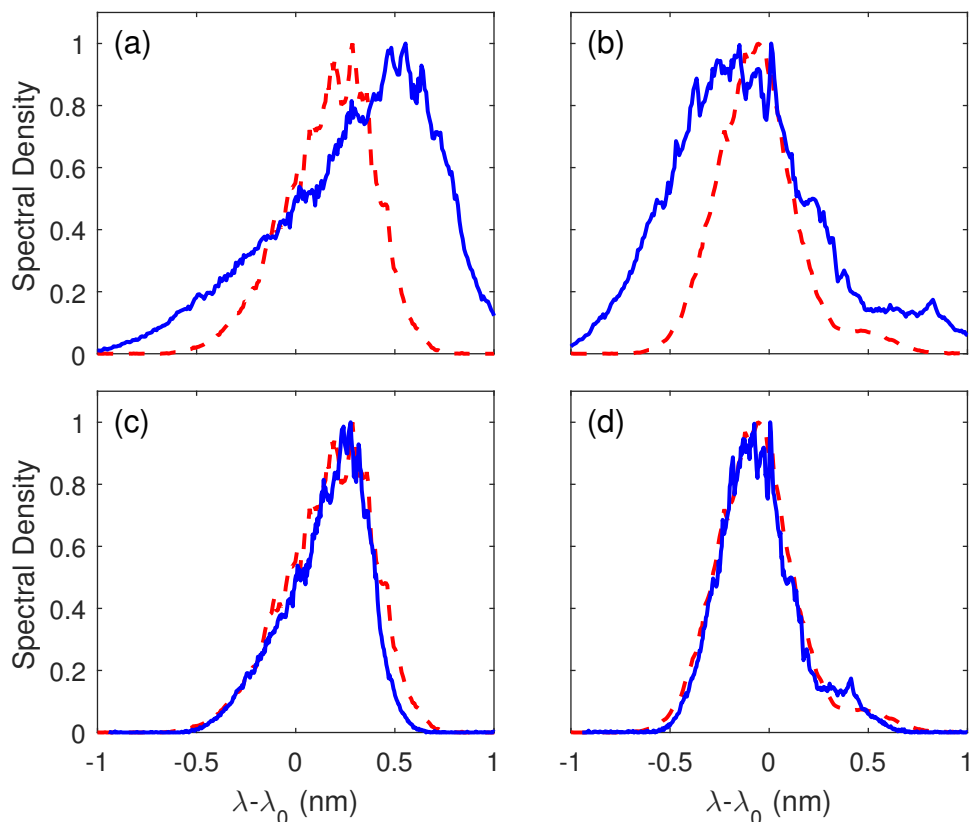


Figure 4.6: [(a),(b)] Comparison of experimental input spectra (dashed red) and output spectra (solid blue) for  $\theta = \pi$ , for an input spectrum with a tail on one side (left) and one with a bump on one side (right). [(c),(d)] Same as [(a),(b)] but scales the output wavelength by  $1/2$  to show that the pulse is indeed a magnified copy of the input.

### 4.3 Conclusions

Spectral narrowing, broadening, and shifts have been demonstrated for picosecond pulses using a lithium niobate electro-optic phase modulator acting as a time lens. These spectral effects depend on the maximum phase shift that can be imposed by the modulator. In our numerical simulations, the pulse spectrum could be compressed by a factor of 8 for a 30-rad phase shift. Experimentally, spectral shifts over a 1.35-nm range and spectral narrowing and broadening by a factor of 2 were demonstrated using a lithium niobate phase modulator with a maximum phase shift of 16 rad at a 10-GHz modulation frequency. More-dramatic narrowing, broadening, and shifts could be achieved by cascading multiple phase modulators to produce higher phase amplitudes and shorter focal GDD's. Our work shows that a phase modulator can be used to tune the central frequency and the spectral bandwidth of picosecond pulses emitted by mode-locked lasers.

## Chapter 5

# Background on time reflection and refraction

In this chapter we review previous works and relevant theory related to reflection and refraction from refractive index boundaries. In section 5.1 we consider reflection and refraction from a refractive index boundary that is stationary in space and derive the laws of reflection and refraction. Section 5.2 covers time reflection and refraction from a temporal boundary, where the refractive index changes for the entire medium at a single instant in time. Using the temporal boundary conditions, we derive time versions of the laws of reflection and refraction. In section 5.3 we examine the more general case of moving refractive index boundaries. These boundaries can be broken down into subluminal boundaries that propagate slower than the speed of light in the material, and superluminal boundaries that propagate faster than the speed of light. We conclude by reviewing studies that have observed the effects of reflection and refraction at a moving boundary while exploring specific processes such as plasma waves, XPM, and analog gravity.

### 5.1 Spatial Boundary Reflection and Refraction

Traditional reflection and refraction of light and Snell's law describing them have been known for centuries and are topics discussed at length in physics textbooks [32, 89, 90]. These processes occur when a beam of light encounters a region of space where the refractive index changes suddenly. From a fundamental physics perspective, this change in refractive index breaks translational symmetry in space. As a result, the energy of the photon is conserved across the boundary while its momentum is free to change. In this process, the transmitted wave continues to propagate forward in space, while the reflected wave travels backward.

#### 5.1.1 Laws of Spatial Reflection and Refraction

We briefly review the derivation of Snell's laws to provide a basis for understanding their temporal counterparts later on. In the absence of sources, Maxwell's equations take the

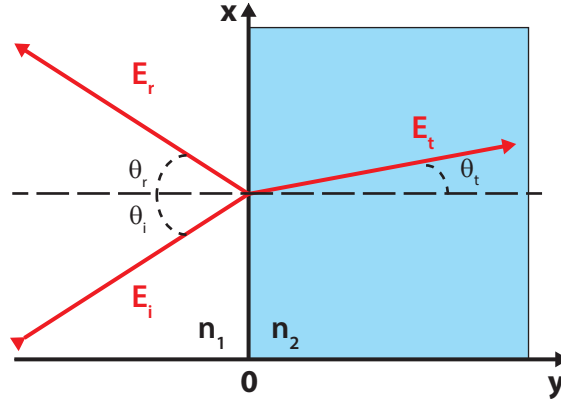


Figure 5.1: Diagram of the reflection and refraction process. The dashed black line is normal to the surface.

form

$$\begin{aligned} \nabla \times \mathbf{E} &= -\frac{\partial \mathbf{B}}{\partial t}, & \nabla \times \mathbf{H} &= \frac{\partial \mathbf{D}}{\partial t}, \\ \nabla \cdot \mathbf{D} &= 0, & \nabla \cdot \mathbf{B} &= 0, \end{aligned} \quad (5.1)$$

where  $\mathbf{D} = \epsilon \mathbf{E}$  is the electric displacement,  $\mathbf{B} = \mu_0 \mathbf{H}$  is the magnetic induction, and  $\mu_0$  is the magnetic permeability of vacuum. Using Eqs. (5.1) for a medium without dispersion, it is simple to find the wave equation for the electric field as

$$\nabla^2 \mathbf{E} - \frac{n^2}{c^2} \frac{\partial^2 \mathbf{E}}{\partial t^2} = 0, \quad (5.2)$$

where  $c = 1/\sqrt{\epsilon_0 \mu_0}$  is the speed of light in vacuum, and  $n = \sqrt{\epsilon/\epsilon_0}$  is the refractive index of the medium. The wave equation given in Eq. (5.2) has solutions in the form of plane waves given by

$$\mathbf{E}(r, t) = \mathbf{E}_0 \exp [i (\mathbf{k} \cdot \mathbf{r} - \omega t)], \quad (5.3)$$

where  $k = |\mathbf{k}|$  is the wave number and is related to the frequency by the dispersion relation

$$k = \frac{n}{c} \omega. \quad (5.4)$$

### 5.1.2 The laws of reflection and refraction

Let us assume we have a plane wave propagating in the x-y plane ( $k_z = 0$ ) that is incident upon a sharp boundary located at  $y = 0$ , which separates two media with different refractive indexes  $n_1$  and  $n_2$  as shown in Fig. 5.1. As this incident wave hits the boundary, a transmitted and reflected wave also appears. Therefore just before the boundary ( $y < 0$ ) we have a total electric field

$$\mathbf{E}(x, y < 0, t) = \mathbf{E}_i \exp [i (k_{ix}x + k_{iy}y - \omega t)] + \mathbf{E}_r \exp [i (k_{rx}x + k_{ry}y - \omega t)], \quad (5.5)$$

and just after the boundary ( $y > 0$ ) the electric field is

$$\mathbf{E}(x, y > 0, t) = \mathbf{E}_t \exp [i(k_{tx}x + k_{ty}y - \omega t)]. \quad (5.6)$$

Using the dispersion relation in Eq. (5.4) and imposing conservation of energy such that  $\omega$  is constant, we can relate the input ( $k_i$ ), reflected ( $k_r$ ), and transmitted ( $k_t$ ) wave numbers as

$$k_i = k_r = \frac{\omega}{c}n_1, \quad k_t = \frac{\omega}{c}n_2 = k_i \frac{n_2}{n_1}. \quad (5.7)$$

Because  $E_r$  is reflected at the boundary and must propagate in the negative  $y$  direction, it is clear that  $k_{ry} = -k_{iy}$ . In addition, we require that the phase of each wave match at the boundary ( $y = 0$ ). For this to occur for all values of  $x$ , we find that

$$k_{ix} = k_{rx} = k_{tx}. \quad (5.8)$$

For angles of incidence ( $\theta_i$ ), reflection ( $\theta_r$ ), and transmission ( $\theta_t$ ) measured relative to the surface normal as shown in Fig. 5.1, we can use  $k_x = k \sin \theta$  in Eq. (5.8) which leads to the relation

$$\sin \theta_i = \sin \theta_r = \frac{n_2}{n_1} \sin \theta_t. \quad (5.9)$$

This equation is a compact form of the law of reflection ( $\theta_i = \theta_r$ ) as well as Snell's law of refraction ( $n_1 \sin \theta_i = n_2 \sin \theta_t$ ).

One key feature of Snell's law occurs when  $n_1 > n_2$ . Under this condition, we can have certain incident angles where  $\frac{n_1}{n_2} \sin \theta_i > 1$ . In this case  $\theta_t$  is undefined, so there can be no transmitted wave. Therefore, the beam must be entirely reflected, a phenomenon known as total internal reflection (TIR). The critical angle,  $\theta_c$  is the incident angle above which TIR occurs. It is found by setting  $\theta_t = \pi/2$  and is given by the equation

$$\sin \theta_c = \frac{n_2}{n_1}. \quad (5.10)$$

TIR is the fundamental process behind optical waveguides, which has led to the development of the modern telecommunications industry [91]. Note that when the TIR condition is satisfied, the wave number becomes complex. If we use this value in Eq. (5.3), the field no longer propagates in space. Instead, it only exists very near the boundary, and decays exponentially for  $y > 0$ . This is the evanescent wave, which has been utilized for many applications such as beam splitters, fluorescence microscopes, and waveguide sensors or couplers [89, 91].

### 5.1.3 The Fresnel Equations

So far we have only looked at how the wave vectors bend when crossing the boundary. In order to find the reflected and transmitted fields, we have to apply the boundary conditions for an electromagnetic wave at a dielectric interface. In general these equations depend on whether the incident light is polarized perpendicular or parallel to the plane of incidence. For now we focus on the case where the electric field is polarized perpendicular to the plane of incidence, as it is more closely related to the space-time boundaries

that will be discussed later. However, there are corresponding equations for a parallel polarized electric field. For propagation in the x-y plane, the electric field polarized in the z-direction is perpendicular to the plane of incidence, and the boundary conditions that the electric and magnetic fields must be continuous at the boundary become

$$E_z(y = 0^-) = E_z(y = 0^+), \quad \mathbf{H}(y = 0^-) = \mathbf{H}(y = 0^+). \quad (5.11)$$

Because the frequency is constant across the boundary and the electric field is polarized in the z-direction, requiring the continuity of the x-component of the magnetic field,  $H_x$ , in Eq. (5.11) is the same as requiring that the derivative of the electric field ( $\partial E_z/\partial y$ ) be continuous at the boundary. Using Eqs. (5.5) and (5.6) in Eqs. (5.11), we find that the boundary conditions simplify to become

$$E_{iz} + E_{rz} = E_{tz}, \quad (5.12)$$

$$k_{iy}E_{iz} + k_{ry}E_{rz} = k_{ty}E_{tz}. \quad (5.13)$$

We can solve these equations to find the reflection and transmission coefficients given by

$$r = \frac{E_{rz}}{E_{iz}} = \frac{k_{iy} - k_{ty}}{k_{ty} + k_{ry}} = \frac{n_1 \cos \theta_i - n_2 \cos \theta_t}{n_2 \cos \theta_t + n_1 \cos \theta_i}, \quad (5.14)$$

$$t = \frac{E_t}{E_i} = \frac{k_{iy} - k_{ry}}{k_{ty} - k_{ry}} = \frac{2n_1 \cos \theta_i}{n_2 \cos \theta_t + n_1 \cos \theta_i}. \quad (5.15)$$

Equations (5.14) and (5.15) are together referred to as the Fresnel equations. Note that in the case of normal incidence ( $\theta = 0$ ) the coefficients in Eqs. (5.14) and (5.15) simplify to

$$r = \frac{n_1 - n_2}{n_1 + n_2}, \quad t = \frac{2n_1}{n_1 + n_2}. \quad (5.16)$$

This will be important when we later discuss the case of a moving refractive index boundary.

## 5.2 Time Boundary Reflection and Refraction

Temporal reflection and refraction, which occur when an electromagnetic pulse arrives at a temporal interface, have attracted less attention than their spatial counterparts [92–95]. The equations for this process were first derived by Morgenthaler in 1958 in regards to modulating the velocity of light [96]. Later works on the subject focused on photon acceleration and plasma waves [97–102]. More recently, changes in the refractive index have also been studied in the context of adiabatic wavelength conversion [103–109]. A temporal interface is the boundary across which the refractive index changes for the entire material. In other words, before the boundary the entire medium has a refractive index  $n_1$ , and after the boundary the entire medium has a refractive index  $n_2$ . Just as a traditional refractive index boundary breaks spatial translational symmetry, the time boundary breaks temporal translational symmetry. Therefore, when crossing the

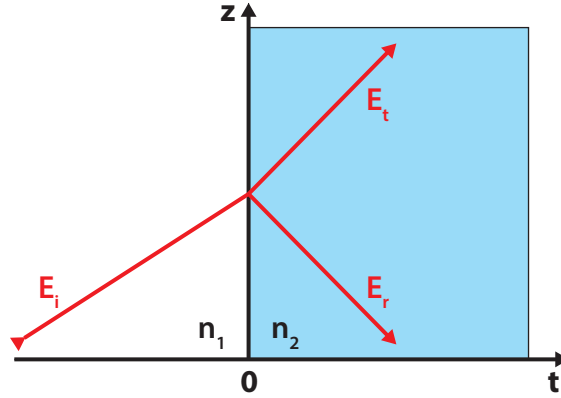


Figure 5.2: Diagram of the temporal reflection and refraction process. Note that the refractive index changes for the entire region at time  $t = 0$ .

temporal boundary the photon momentum is now conserved while the energy is free to change. Since the photon energy is proportional to the frequency, we see that crossing temporal boundaries leads to shifts in frequency.

### 5.2.1 Frequency Shifts at a Temporal Boundary

We can derive equations for the shifted frequencies in a similar manner to the spatial case. Beginning with the wave equation from Eq. (5.2), which still has solutions of the form given in Eq. (5.3). We now assume a sharp transition in the refractive index for the entire medium that occurs at time  $t = 0$ . As shown in Fig. 5.2, this creates two distinct time periods; one for  $t < 0$  where the medium has refractive index  $n_1$ , and one for  $t > 0$  where the medium has refractive index  $n_2$ . When the refractive index changes, a transmitted and reflected wave also appear. As expected, the transmitted pulse propagates forward through the new medium that has refractive index  $n_2$ . Unlike the spatial case where the reflected pulse propagates in the initial medium, the  $t < 0$  region is not accessible, as propagation into the past would violate causality. Therefore, the temporal reflection must propagate in the  $t > 0$  region with refractive index  $n_2$ , just like the transmitted wave. The total electric field before the temporal boundary ( $t < 0$ ) is then

$$\mathbf{E}(r, t < 0) = \mathbf{E}_i \exp [i (\mathbf{k} \cdot r - \omega_i t)], \quad (5.17)$$

and just after the boundary ( $t > 0$ ) the electric field is

$$\mathbf{E}(r, t > 0) = \mathbf{E}_t \exp [i (\mathbf{k} \cdot r - \omega_t t)] + \mathbf{E}_r \exp [i (\mathbf{k} \cdot r - \omega_r t)]. \quad (5.18)$$

We emphasize that the reflected wave does not propagate in the initial refractive index as it would in the spatial case, because the reflected wave can not travel into the past. Instead, the reflected wave propagates backward in space inside but in the new refractive index  $n_2$ .

As with the spatial boundary, we require the phases of the initial, reflected, and transmitted waves to be matched at the boundary ( $t = 0$ ) for all values of  $r$ . This occurs

when the wave vector  $\mathbf{k}$  is constant such that

$$k_i = k_r = k_t, \quad (5.19)$$

conserving momentum as expected for a boundary that breaks translational symmetry in time. We find the initial ( $\omega_i$ ), reflected ( $\omega_r$ ), and transmitted ( $\omega_t$ ) frequencies using the dispersion relation in Eq. (5.4) to substitute for  $k$  in Eq. (5.19) to get

$$|\omega_r| = \omega_t, \quad n_2\omega_t = n_1\omega_i. \quad (5.20)$$

Since the reflected and transmitted frequencies have the same magnitude, the only way  $E_r$  remains distinct from  $E_t$  is if  $\omega_r = -\omega_t$ . In this case, the negative frequency represents a wave with positive frequency traveling backward in space. Therefore, the temporal reflection propagates backward through space just like a spatial reflection.

The temporal Snell's law can be rewritten with the the substitution  $\tan \alpha = 1/n$  to more closely resemble the spatial law of reflection and Snell's law [93], but this provides no additional insight into the physics at play. One important feature of these equations is that there is no total internal reflection condition, since  $\omega_t$  exists for every possible  $\omega_i$ . This is a result of causality preventing the reflected waave from traveling into the past [93].

## 5.2.2 Temporal Fresnel Equations

We can find equivalents to the Fresnel formulae for a time boundary by imposing the temporal boundary conditions. There are two documented sets of boundary conditions in the published literature on temporal boundaries, with one requiring that  $D$  and  $B$  are continuous at the bounadary and the other that  $E$  and  $H$  be continuous. However, a previous study using a time transformation method found that the correct boundary conditions were on  $D$  and  $B$  because they correctly predict the compression of the transmitted wave [94]. Therefore our boundary conditions at the time boundary are

$$D(t = 0^-) = D(t = 0^+), \quad B(t = 0^-) = B(t = 0+). \quad (5.21)$$

Using the relations  $D = \epsilon E$  and  $B = \mu_0 H$  and applying these boundary conditions to Eqs. (5.17) and (5.18) gives

$$n_1^2 E_i = n_2^2 (E_r + E_t), \quad n_1 E_i = n_2 (E_t - E_r), \quad (5.22)$$

where the minus sign in the second equation is due to the reflected wave reversing its propagation direction ( $k_r = -k_i$ ). We can solve these equations to find the reflection and transmission coefficients given by

$$r = \frac{E_r}{E_i} = \frac{1}{2} \left( \frac{n_1^2}{n_2^2} - \frac{n_1}{n_2} \right), \quad (5.23)$$

$$t = \frac{E_t}{E_i} = \frac{1}{2} \left( \frac{n_1^2}{n_2^2} + \frac{n_1}{n_2} \right). \quad (5.24)$$

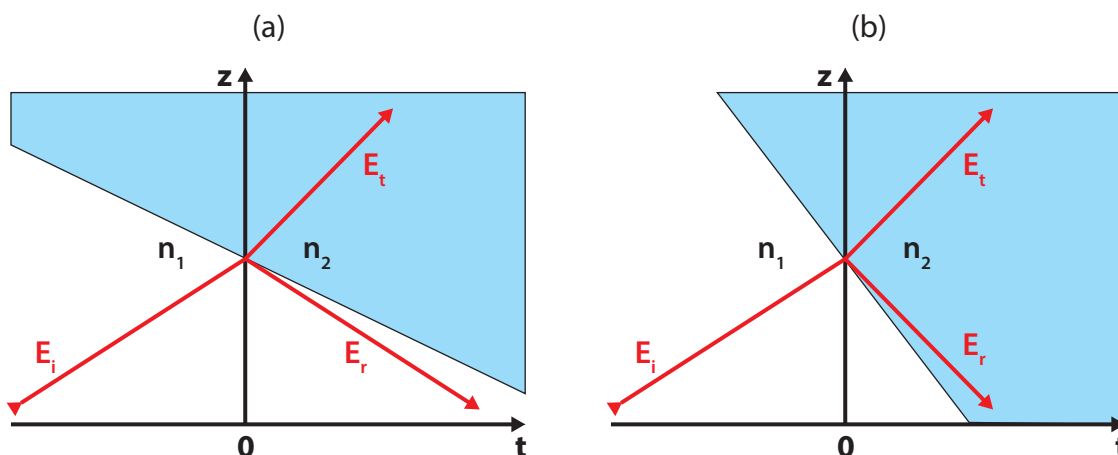


Figure 5.3: Diagram of the reflection and refraction from (a) a subluminal moving refractive index boundary and (b) a superluminal moving refractive index boundary. While the reflected wave travels backward in the negative  $z$ -direction for both (a) and (b), it is in a different refractive index in each case.

An important feature of the time reflection and transmission coefficients is that the sum of the intensities,  $|r|^2 + |t|^2$ , does not equal unity. This occurs because unlike other methods of wavelength conversion where the total pulse energy is conserved, such as four-wave mixing (FWM), the time reflection and refraction processes conserve the total number of photons. Total pulse energy is not conserved because this is an open system where energy is transferred between the pulse and the medium when the refractive index is changed [93,94].

### 5.3 Moving Boundary Reflection and Refraction

The moving refractive index boundary is a refractive index change that propagates through the material and shifts the refractive index from  $n_1$  to  $n_2$  as it propagates. Such boundaries have been studied extensively for years [102, 110–123]. The majority of work in this area has focused on exploring systems where the space-time boundary propagates in the direction opposite of the optical pulse. Just like the previous two forms of reflection and refraction, the transmitted pulse continues propagating forward and the reflected pulse still travels backward in space. Unlike the pure time boundary, however, the reflected pulse from a moving refractive index boundary can now exist in either the initial or final refractive index region. The region in which the reflected wave propagates is determined by the speed of the moving boundary,  $v_B$ , with subluminal boundaries ( $v_B < c/n_1$ ) causing reflections in the  $n_1$  region and superluminal boundaries ( $v_B > c/n_1$ ) causing reflections in the  $n_2$  region. Figure 5.3 shows diagrams for reflection and refraction from (a) a subluminal boundary, and (b) a superluminal boundary. We examine each of these cases in the next two sections.

### 5.3.1 Subluminal boundary

To find the behavior when crossing a subluminal boundary, we note that changing our reference frame to one where the moving boundary is stationary in space produces the same situation as the traditional spatial boundary [102, 110, 112, 113]. Therefore, we can solve for the spatial energy conservation and boundary conditions in the moving frame, then use the Lorentz transformations to convert back to the rest frame.

We once again assume an incident plane wave propagating in a non-dispersive medium. To simplify our discussion, we assume that the electric and magnetic fields are polarized in the x-y plane such that the light propagates with the electric field polarized in the y direction and the magnetic field polarized in the x direction. In this case, the electric and magnetic fields are given by

$$E_i(z, t) = E_i \exp[i(k_i z - \omega_i t)], \quad H_i(z, t) = \sqrt{\frac{\epsilon}{\mu_0}} E_i \exp[i(k_i z - \omega_i t)], \quad (5.25)$$

where we have the usual dispersion relation of  $k = n\omega/c$ . For a boundary in the x-y plane moving with speed  $v_B$  in the z-direction, we use the Lorentz transformation to relate the fields in the moving frame to the fields in the rest frame as

$$E' = \gamma \left( 1 - \frac{v_B}{c} \sqrt{\epsilon\mu} \right) E \quad (5.26)$$

$$H' = \gamma \left( 1 - \frac{v_B}{c} \sqrt{\epsilon\mu} \right) H. \quad (5.27)$$

where  $\gamma^{-2} = [1 - (v_B/c)^2]$ . We can similarly relate the moving and rest frame frequencies and wave vectors as

$$\omega' = \gamma \omega \left( 1 - \frac{n}{c} v_B \right), \quad (5.28)$$

$$k' = \gamma k \left( 1 - \frac{v_B}{n_1 c} \right), \quad (5.29)$$

where the frequency change is simply the relativistic Doppler shift. Note that for the reflected frequency we should replace  $v_B$  with  $-v_B$  in Eqs. (5.26)–(5.29). This is due to the reflected wave propagating in the negative  $z$  direction while the incident wave travels in the positive  $z$  direction.

Because Maxwell's equations are invariant under the Lorentz transformation, we can now treat our moving frame fields and frequencies just like we would a spatial boundary. If we apply conservation of energy in the moving frame,  $\omega'$  is the same on either side of the boundary such that

$$\omega_i \left( 1 - \frac{v_B}{c} n_1 \right) = \omega_r \left( 1 + \frac{v_B}{c} n_1 \right) = \omega_t \left( 1 - \frac{v_B}{c} n_2 \right). \quad (5.30)$$

We can now apply the boundary conditions from Eqs. (5.11) to the moving frame such that  $E'$  and  $H'$  are continuous at the boundary and substitute using Eqs. (5.26)

and (5.27). Assuming  $\mu = \mu_0$ , this leads to the system of equations given by

$$\left(1 - \frac{v_B}{c}n_1\right) E_i + \left(1 + \frac{v_B}{c}n_1\right) E_r = \left(1 - \frac{v_B}{c}n_2\right), \quad (5.31)$$

$$n_1 \left(1 - \frac{v_B}{c}n_1\right) E_i - n_1 \left(1 + \frac{v_B}{c}n_1\right) E_r = n_2 \left(1 - \frac{v_B}{c}n_2\right), \quad (5.32)$$

where the minus sign in front of the reflection term in Eq. (5.32) is once again because the reflected wave propagates backward. We can then solve for the reflection and transmission coefficients to find

$$r = \frac{E_r}{E_i} = \left(\frac{n_1 - n_2}{n_1 + n_2}\right) \left(\frac{1 - \frac{v_B}{c}n_1}{1 + \frac{v_B}{c}n_1}\right), \quad (5.33)$$

$$t = \frac{E_t}{E_r} = \left(\frac{2n_1}{n_1 + n_2}\right) \left(\frac{1 - \frac{v_B}{c}n_1}{1 - \frac{v_B}{c}n_2}\right). \quad (5.34)$$

As expected, these equations reduce to Eqs. (5.16) when  $v_B = 0$ , corresponding to a stationary boundary in space.

### 5.3.2 Superluminal boundary

The superluminal boundary has seen much less attention than the subluminal boundary [114,123]. For this type of boundary the reflected wave would be slower than the boundary if it propagated in the  $n_1$  region. Therefore the reflected wave must propagate in the second region with refractive index  $n_2$ . As with the subluminal case, we change to the moving frame using the Lorentz transformation. However, this time our transformation is not to a frame that is moving with the boundary, because this frame would have an imaginary  $\gamma$ . Instead, we shift into a frame in which the refractive index changes for the whole medium at the same time. This occurs for a reference velocity  $v_r = c^2/v_B$ . In this new reference frame the frequency and wave number are related to their moving frame counterparts as

$$\omega' = \gamma\omega \left(1 - \frac{nc}{v_B}\right), \quad (5.35)$$

$$k' = \gamma k \left(1 - \frac{c}{nv_B}\right), \quad (5.36)$$

Because we have a time boundary in the moving frame, we can now impose conservation of momentum in the moving frame such that  $k'_i = k'_r = k'_t$ . Using Eq. (5.36), we find the relation between the initial, reflected, and transmitted frequencies as

$$\omega_i \left(n_1 - \frac{c}{v_B}\right) = \omega_r \left(n_2 + \frac{c}{v_B}\right) = \omega_t \left(n_2 - \frac{c}{v_B}\right). \quad (5.37)$$

To apply the temporal boundary conditions, we relate the electric displacement and the magnetic induction in the moving frame to the rest frame variables as

$$D' = \gamma \left(1 - \frac{c}{v_B}\sqrt{\epsilon\mu}\right) D, \quad (5.38)$$

$$B' = \gamma \left( 1 - \frac{c}{v_B} \sqrt{\epsilon\mu} \right) B. \quad (5.39)$$

Applying these to Eq. (5.11) and solving for the reflection and transmission coefficients yields

$$r = \left( \frac{1 - \frac{c}{v_B} n_1}{1 + \frac{c}{v_B} n_2} \right) \left[ \frac{1}{2} \left( \frac{n_1^2}{n_2^2} - \frac{n_1}{n_2} \right) \right], \quad (5.40)$$

$$t = \left( \frac{1 - \frac{c}{v_B} n_1}{1 - \frac{c}{v_B} n_2} \right) \left[ \frac{1}{2} \left( \frac{n_1^2}{n_2^2} + \frac{n_1}{n_2} \right) \right]. \quad (5.41)$$

Equations. (5.40) and (5.41) reduce to the usual time reflection and transmission coefficients in Eqs. (5.14) and (5.15) the limit  $v_B \rightarrow \infty$ . Therefore, space and time boundaries are just special cases of the more general subluminal and superluminal boundaries.

### 5.3.3 Co-propagating moving boundary

Although the derivations above are applicable to co-propagating boundaries if the medium is non-dispersive, all of the previously referenced works have focused on a counter-propagating refractive index boundary in a non-dispersive medium. Our focus in this thesis will be on reflection and refraction of light at a co-propagating boundary in a dispersive medium. We treat these boundaries generally, allowing them to be produced through any linear or nonlinear process that dynamically shifts the refractive index (such as XPM, electro-optic phase modulation, plasma waves, etc.). Because the material is dispersive, this situation is the equivalent of spatial reflection and refraction according to the space-time analogy. We use this analogy to develop new applications for our so-called space-time refraction and reflection.

Many studies have observed the effects of space-time boundaries while exploring a specific process. For example, tremendous work has been done on the effects of the Kerr nonlinearity in dispersive waveguides [33]. Recently there has been growing interest in soliton scattering, where large frequency shifts are observed when a dispersive wave crosses an intense soliton pulse [124–127]. This same effect has also been observed using two solitons that produce temporal boundaries through XPM to trap pulses [128–133]. We emphasize that these studies are explorations of a specific implementation of the more general process of space-time refraction, using the properties of the Kerr nonlinearity in particular to explain the observed behavior.

Outside of the Kerr nonlinearity, a recent study by Rosanov *et al.* has explored forward propagating reflections in a dispersive plasma [134]. However, the study only explores the process in regard to plasma dispersion. There has also been a surge in interest for using optical analogs for gravity following the laboratory analog proposed by Leonhardt in 2002 [135]. These studies have used optical systems to explore the often difficult to observe physical phenomena associated with event horizons such as black holes, white holes, and Hawking radiation [125, 131, 136–143]. Such systems have already been used to experimentally demonstrate an analog of Hawking radiation, where photon pairs are generated from the quantum vacuum, from an optical event horizon by Rubino *et al.* [139]. In this study the event horizons are formed by the edges of a femtosecond

optical pulse focused inside of bulk fused silica such that the beam excites a single spatial filament, and the emitted photon pairs were detected at 90deg to the pump propagation axis. A similar method for generating analog Hawking radiation inside of optical fibers has also been proposed [136].

## Chapter 6

# Space-time Reflection and Refraction

As discussed in Chapter 5, a spatial boundary breaks translational symmetry. As a result, the momentum of a photon can change but its energy must remain unaffected. In the case of a stationary temporal boundary, translational symmetry is broken in time, so photon momentum remains unchanged while its energy must change. This chapter focuses on optical pulses propagating inside a dispersive medium to reveal novel temporal and spectral features occurring when the pulse experiences reflection and refraction at a co-propagating moving boundary. In this case, both the energy and momentum of a photon must change simultaneously while crossing the boundary. We will find, however, that a suitable choice of reference frame will allow us to treat the moving boundary like a temporal boundary, such that momentum is conserved in this reference frame. Section 6.1 begins with a numerical study to discern the behavior from such a boundary. We find that the frequency dependence of the dispersion of the medium in which the pulse is propagating plays a fundamental role in determining the frequency shifts experienced by the reflected and refracted pulses. In Sect. 6.2 we use the dispersion relation to find analytic expressions for these frequency shifts, and find the condition under which an analog of total internal reflection (TIR) occurs at the moving refractive index boundary. We then use this condition to show the existence of an analog to the Evanescent wave. Section 6.3 summarizes the main results of the chapter and briefly discusses experimental methods for observing the effect.

### 6.1 Numerical Study

To simplify the following discussion, we assume that the optical pulse is propagating inside a waveguide with the dispersion relation  $\beta(\omega)$  such that neither its polarization nor its transverse spatial shape changes during propagation. As discussed in Chapter 2, when the pulse contains multiple optical cycles,  $\beta(\omega)$  can be expanded in a Taylor series around its central frequency  $\omega_0$  as

$$\beta(\omega) = \beta_0 + \beta_1(\omega - \omega_0) + \frac{\beta_2}{2}(\omega - \omega_0)^2, \quad (6.1)$$

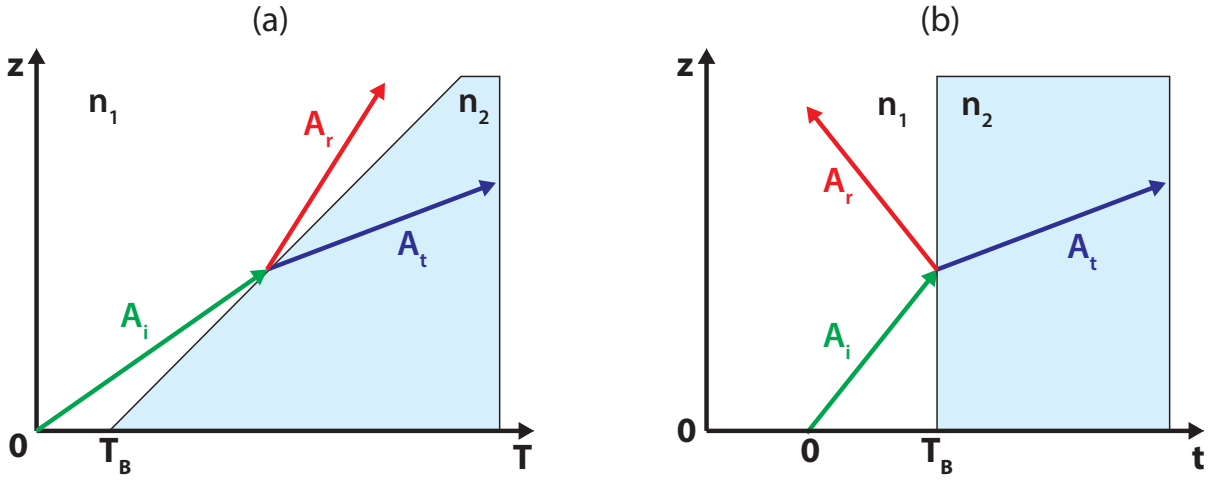


Figure 6.1: Diagram of the reflection and refraction process in a dispersive medium in (a) the laboratory frame and (b) the retarded time frame traveling with the moving boundary. The reflected and transmitted waves travel with different group velocities due to a change in frequency as indicated by the change in color of the arrow.

where we neglect all dispersion terms higher than the second order [33]. Recall that  $\beta_1 = \partial z / \partial T$  is the inverse of the group velocity and  $\beta_2$  is the GVD. As with the subluminal boundary from Sect. 5.3, we will work in a reference frame moving at the same speed as the boundary. This time, we will use the retarded time frame with the coordinate transformation  $t = T - z/v_B$ , where  $T$  is the time in the laboratory frame and  $t = 0$  is set to the peak of the optical pulse at  $z = 0$ . In this frame, the refractive index will appear to change for the entire medium ( $z > 0$ ) at the time  $t = T_B$  as shown in Fig. 6.1. Therefore, in the retarded time frame, the space-time boundary becomes a pure temporal boundary. Note that moving toward negative  $t$  is not moving into the past in the laboratory frame, as it would be for negative  $T$ . Instead, decreasing  $t$  corresponds to moving with a group velocity greater than  $v_B$ . Thus the reflected pulse can now exist in the  $t < T_B$  region while propagating in the forward  $z$  direction without violating causality.

The group velocity in the moving frame  $v'_g$  can be found as  $v'_g = \partial z / \partial t = v_g v_B / (v_B - v_g)$  where  $v_g$  is the group velocity in the laboratory frame. Using this moving frame group velocity, the dispersion relation in the moving frame changes to

$$\beta'(\omega) = \beta_0 + \Delta\beta_1(\omega - \omega_0) + \frac{\beta_2}{2}(\omega - \omega_0)^2, \quad (6.2)$$

where  $\Delta\beta_1 = 1/v'_g = \beta_1 - 1/v_B$  is the differential group delay (DGD) and is an indication of the group velocity mismatch between the optical pulse and the boundary. The dispersion relation in the moving frame is related to the laboratory frame dispersion relation through

$$\beta'(\omega) = \beta(\omega) - \frac{\omega - \omega_0}{v_B}. \quad (6.3)$$

Because our boundary is now a stationary temporal boundary in the moving frame, we can apply conservation of momentum in this moving frame just as we would for a temporal boundary. This means that the conserved quantity for the co-propagating boundary is  $\beta'$  rather than  $\beta$ . Interestingly, the conservation condition for both the superluminal and subluminal boundaries can be reduced to conserving the quantity  $\beta'$  if we use the definition  $\beta = n\omega/c$ . We stress that by including dispersion and allowing for a forward propagating reflected pulse from a co-propagating boundary, we have expanded on the concept of reflection and refraction from a moving boundary as discussed in Chapter 5.

In general, the refractive index can change as a function of time  $t$ . For a refractive index change of  $\Delta n(t)$ , the moving-frame dispersion relation will shift by a value  $\beta_B(t) = k_0 \Delta n(t)$ . The dispersion relation can therefore be expressed as

$$\beta'(\omega) = \beta_0 + \Delta\beta_1(\omega - \omega_0) + \frac{\beta_2}{2}(\omega - \omega_0)^2 + \beta_B(t). \quad (6.4)$$

The final term in this equation simply shows that the dispersion relation takes different values before and after the boundary. Outside of that time-scale, the dispersion relation is only a function of  $\omega$ .

We will model the pulse propagation by assuming the transverse shape of the optical field does not change during propagation, as in an optical fiber. The Fourier transform of the optical field,  $\tilde{E}(r, \omega - \omega_0)$  is found to satisfy the Helmholtz equation

$$\nabla^2 \tilde{E} + \epsilon(\omega)k_0^2 \tilde{E} = 0. \quad (6.5)$$

To further simplify our discussion, we assume a solution of the form

$$\tilde{E} = F(x, y) \tilde{A}(z, \omega - \omega_0) \exp(i\beta_0 z) \quad (6.6)$$

where  $F(x, y)$  is the transverse spatial profile, and  $\tilde{A}(z, \omega)$  is the Fourier transform of the slowly varying pulse envelope,  $A(z, t)$ . Substituting Eq. (6.6) into Eq. (6.5) and using  $\partial^2 \tilde{A} / \partial z^2 \approx 0$  for the slowly varying envelope leads to the following equation for  $\tilde{A}(z, \omega)$  [33]

$$\frac{\partial \tilde{A}}{\partial z} - i(\beta'(\omega) - \beta_0) \tilde{A} = 0. \quad (6.7)$$

If we now substitute  $\beta'$  from Eq. (6.4) into Eq. (6.7) and inverse Fourier transform, we find the time-domain equation given by

$$\frac{\partial A}{\partial z} + \Delta\beta_1 \frac{\partial A}{\partial t} + i \frac{\beta_2}{2} \frac{\partial^2 A}{\partial t^2} = i\beta_B(t)A \quad (6.8)$$

If we assume the refractive index changes as a step function in time at the boundary time  $T_B$ , we can express Eq. (6.8) as

$$\frac{\partial A}{\partial z} + \Delta\beta_1 \frac{\partial A}{\partial t} + i \frac{\beta_2}{2} \frac{\partial^2 A}{\partial t^2} = i\beta_B H(t - T_B)A \quad (6.9)$$

where  $H(t - T_B)$  is the Heaviside function, such that the final term is zero for  $t < T_B$

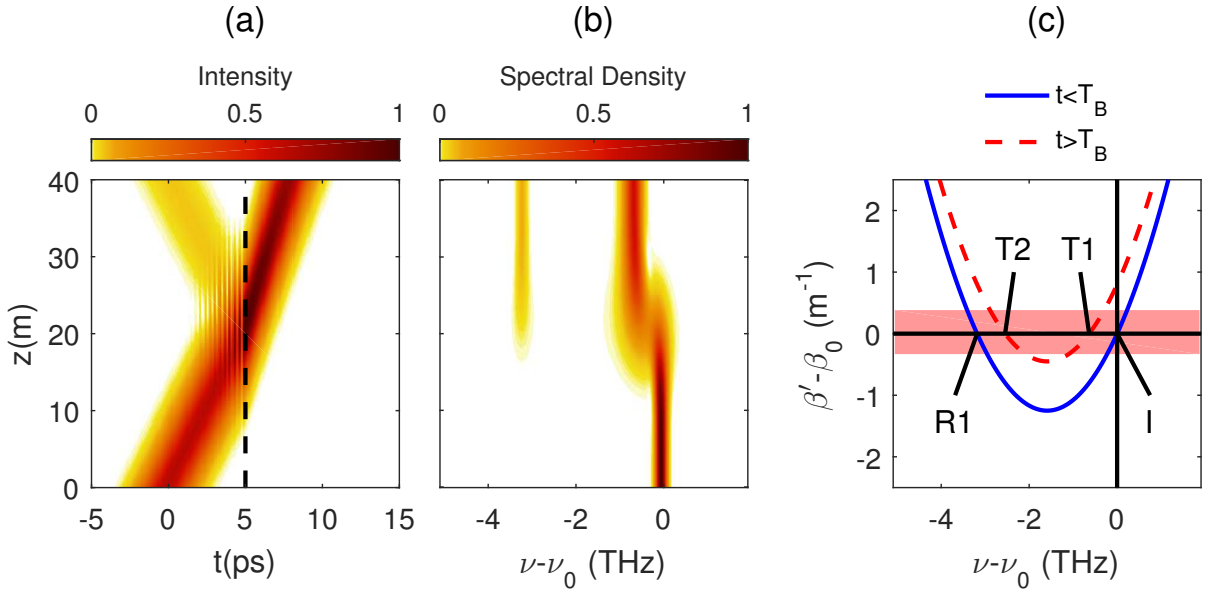


Figure 6.2: Evolution of (a) the pulse shape and (b) the spectrum for a Gaussian input pulse in the presence of a space-time boundary at  $T_B = 5$  ps (dashed white line) with  $\beta_B = 0.8$  m<sup>-1</sup>. The time axis is measured in a reference frame moving with the boundary such that  $t = T - z/v_B$ . (c) The dispersion curves for  $t < T_B$  (solid blue line) and  $t > T_B$  (dashed red line). The shaded region shows the corresponding range of propagation constants for the entire pulse bandwidth at the input ( $t < T_B$ ).

and  $\beta_B$  for  $t > T_B$ .

We solve Eq. (6.9) numerically with the standard split-step Fourier method [33], assuming a Gaussian-shaped input pulses of the form

$$A(0, t) = \exp \left[ -\frac{1}{2} \left( \frac{t}{T_0} \right)^2 \right], \quad (6.10)$$

where  $T_0$  is the  $1/e$  half-width of the pulse. For the numerical simulations that follow, the pulse width is set to  $T_0 = 1.5$  ps, the boundary is located at  $T_B = 5$  ps, and the magnitude of the dispersion is set to a realistic value for silica fibers ( $|\beta_2| = 0.025$  ps<sup>2</sup>/m). We choose  $\Delta\beta_1 = 0.25$  ps/m to ensure that the center of the optical pulse crosses the boundary halfway through the total propagation length of  $z = 40$  m. In general, the velocity of the temporal boundary should be chosen so that it is close to the group velocity of the optical pulse. For typical silica-based fibers with a group index  $n_g \approx 1.46$ , the temporal boundary should have a velocity close to  $v_B = 2 \times 10^8$  m/s.

As a first example of space-time reflection and refraction, Fig. 6.2 shows (a) temporal and (b) spectral evolutions of a Gaussian input pulse for  $\beta_B = 0.8$  m<sup>-1</sup>, a value corresponding to an index change of  $\Delta n \approx 1.27 \times 10^{-7}$  at a wavelength of  $1 \mu\text{m}$ . The temporal evolution in Fig. 6.2(a) is strikingly analogous to that of an optical beam hitting a spatial boundary. Most of the pulse energy is transmitted across the boundary, and this transmitted pulse "bends" toward the boundary by changing its speed. The transmitted pulse

is also narrower in time than the incident pulse, similar to how a refracted optical beam becomes narrower in space when it is bent toward the spatial interface. A small part of pulse energy is "reflected" and begins traveling away from the temporal boundary. This reflected pulse has the same temporal width as the initial pulse, but its speed increases considerably.

Figure 6.2(b) shows how the temporal changes are accompanied by a multitude of spectral changes. In particular, notice how the spectrum shifts and splits as the pulse crosses the refractive index boundary. Recall that the temporal analog of an angle is the frequency. The moving frame dispersion relation in Eq. (6.4) should be able to explain all spectral changes. Figure 6.2(c) shows the dispersion curves for  $t < T_B$  (solid blue) and  $t > T_B$  (dashed red). In the moving frame, the slope of these curves is related to the speed of the pulse relative to the temporal boundary, rather than the actual group velocity. As mentioned earlier, even though  $\beta$  (related to photon momentum) is not conserved, the corresponding moving-frame quantity  $\beta'$  is conserved. We use this conservation law to understand the spectral shifts of the refracted and reflected pulses.

To conserve  $\beta'$  when transitioning from the  $t < T_B$  region to the  $t > T_B$  region, each frequency component must shift from the solid curve in Fig. 6.2(c) to a point on the dashed curve with the same value of  $\beta'$ . Because the curve is locally parabolic, the two frequencies at points T1 and T2 on the solid curve match the initial  $\beta'$ . Only point T1 is a valid solution, however, since the slope, related to the speed of the pulse, should have the same sign for the transmitted pulse in order to carry the pulse across the boundary. If the slope had the opposite sign, like at point T2, the pulse would travel faster than the boundary and would not enter the  $t > T_B$  region. The entire pulse spectrum shifts toward the red side (for  $\beta_B > 0$ ) since each frequency component of the pulse must shift accordingly. Since the slope of the dispersion curve at the new central frequency is different, the transmitted pulse must travel at a different speed relative to the space-time boundary. This change in the group velocity is what leads to the apparent bending observed in Fig. 6.2(a), and is also the cause of the narrowing of the transmitted pulse in time. As the trailing edge of the initial pulse crosses the boundary, the transmitted light moves at a faster speed and catches up to the leading edge, which is still moving at the slower speed. Therefore, by the time the leading edge crosses the boundary, the trailing edge is closer in time than it would have been if there were no frequency shift.

The reflected pulse is caused by the second point on the solid curve that has the same value of  $\beta'$  as the input, marked as point R1 in Fig. 6.2(c). This point must have the opposite slope to ensure that the pulse travels back into the  $t < T_B$  region. We stress that the reflected pulse does not travel backward in time or space; rather its speed changes such that it remains in the  $t < T_B$  region. Both the "reflected" pulse and the refractive index boundary continue to propagate through the dispersive medium in the  $+z$  direction. Figure 6.2(b) shows that the spectrum of the reflected pulse is shifted toward the red side by about 3.18 THz. It also shows that such a large spectral shift occurs over a relatively small distance during which the pulse interacts with the boundary.

So far, we have considered only the central frequency of the optical pulse. However, the pulse has a finite spectral width and  $\beta'$  must be conserved for all frequencies in the spectrum. In Fig. 6.2(c), the shaded region shows the corresponding range of propagation constants for the entire pulse bandwidth when  $t < T_B$ . We can see that the transmitted

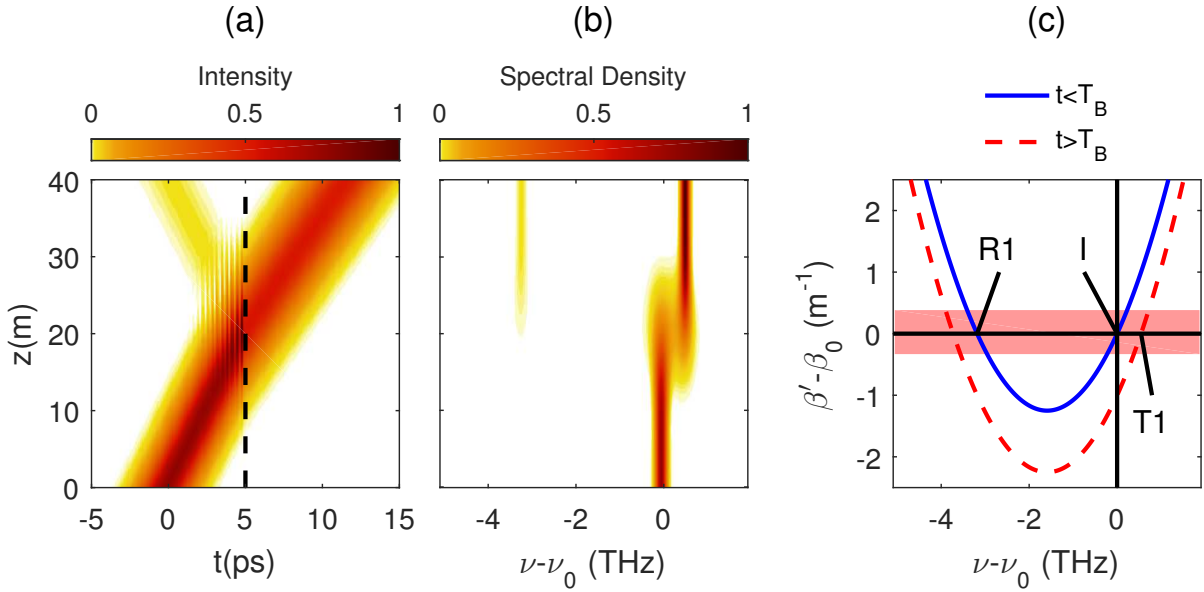


Figure 6.3: Evolution of (a) the pulse shape and (b) the spectrum in the presence of a space-time boundary at  $T_B = 5$  ps (dashed white line) with  $\beta_B = -1$  m<sup>-1</sup>. The time axis is measured in a reference frame moving with the boundary such that  $t = T - z/v_B$ . (c) The dispersion curves for  $t < T_B$  (solid blue line) and  $t > T_B$  (dashed red line). The shaded region shows the corresponding range of propagation constants for the entire pulse bandwidth at the input ( $t < T_B$ ).

curve overlaps the shaded region over a much wider spectral region than the incident curve. This leads to the spectral broadening that accompanies the temporal narrowing of the refracted pulse. The width of the overlap region is largely dependent on the slope of the dispersion curve at the initial and transmitted frequencies, with a lower dispersion slope leading to the spectral broadening observed here.

We can now ask what happens if the refractive index is decreased across the space-time boundary such that  $\beta_B$  is negative. Figure 6.3 shows the evolution of the (a) shape and (b) spectrum for the same pulse and material used in Fig. 6.2, but with  $\beta_B = -1$  m<sup>-1</sup>. From Fig. 6.3(a) we see that the initial pulse still splits into a reflected and a transmitted pulse as it crosses the boundary. Unlike Fig. 6.2(a), the transmitted pulse bends away from the boundary, traveling at an even slower group velocity than the initial pulse. At the same time, the transmitted pulse now becomes wider in time after crossing the boundary, in contrast to the narrowing we saw previously. Looking at the spectral evolution in Fig. 6.3(b), we see that the slower velocity is accompanied by a blue shift of the transmitted frequency while the reflected frequency stays the same. From Fig. 6.3, we find that the change in velocity is caused by an increase in the slope of the dispersion curve at point T1. Furthermore, the transmitted curve now overlaps the shaded region for a much narrower spectral range than before, so the spectrum of the transmitted pulse is compressed, leading to a temporal expansion.

One may ask how much the momentum changes in the laboratory frame. Since  $\beta'$  remains constant, Eq. (6.3) shows that  $\beta$  changes by an amount  $(\omega - \omega_0)/v_B$ . Clearly, a

moving boundary breaks both temporal and spatial symmetries, forcing momentum and energy to change simultaneously. This is similar to the behavior observed in interband photonic transitions [119]. However, by working in the moving reference frame we can apply the momentum conservation rules of a temporal boundary.

## 6.2 Space-time laws of reflection and refraction

To obtain analytic expressions for the spectral shifts caused during reflection and refraction, we apply conservation of momentum for a temporal boundary in our moving frame. This is equivalent to conserving  $\beta'$  given in Eq. (6.4) at the boundary. Unlike the previous subluminal and superluminal boundaries, the reflected pulse continues to propagate forward in the positive  $z$  direction, but in the initial refractive index region ( $t < T_B$ ). Therefore we find the reflected frequency by setting  $\beta'(\omega_i, t < T_B) = \beta'(\omega_r, t < T_B)$ . Since the input frequency is  $\omega_i = \omega_0$ , we find the reflected frequency using Eq. (6.4) as

$$\omega_r = \omega_0 - \frac{2\Delta\beta_1}{\beta_2}. \quad (6.11)$$

Note that there is a second solution  $\omega_r = \omega_0$ . However, the DGD at this frequency would not carry the pulse back into the  $t < T_B$  region, and is therefore not a valid solution.

We similarly find the transmitted frequency by setting  $\beta'(\omega_i, t < T_B) = \beta'(\omega_t, t > T_B)$ . Solving the resulting quadratic equation again, we obtain

$$\omega_t = \omega_i + \frac{\Delta\beta_1}{\beta_2} \left[ -1 \pm \sqrt{1 - \frac{2\beta_B\beta_2}{(\Delta\beta_1)^2}} \right]. \quad (6.12)$$

As discussed earlier, only positive sign corresponds to a physical solution shown as point T1 in Fig. 6.2(c). In the limit  $\Delta\beta_1 \gg \sqrt{\beta_B\beta_2}$ , this equation can be approximated as

$$\omega_t = \omega_i - \frac{\beta_B}{\Delta\beta_1} = \omega_i - \frac{k_0\Delta n}{\Delta\beta_1}. \quad (6.13)$$

The numerical results shown in Fig. 6.2 agree with these analytic expressions derived using the concept of momentum conservation.

These analytic results provide considerable insight into the phenomena of temporal reflection and refraction of optical pulses. Consider first the frequency shift of the reflected pulse. Eq. (6.11) indicates that this shift depends on both the sign and magnitude of the GVD governed by the parameter  $\beta_2$ . In particular, it disappears as  $\beta_2 \rightarrow 0$ . It follows from Eq. (6.4) that the parabolic dispersion curve seen in Fig. 6.2(c) reduces to a straight line in this limit, indicating that point R1 in Fig. 6.2(c) ceases to exist. We can see this behavior in Fig. 6.4, which shows the same simulation as Fig. 6.2 but with  $\beta_2 = 0$  ps<sup>2</sup>/m. We clearly see that there can be no momentum conservation on the solid curve for  $t < T_B$ . Instead, all of the energy must be transmitted to point T1. Furthermore, because the slope of the dispersion curve is not changed, the pulse duration and spectral width remain the same while crossing the boundary.

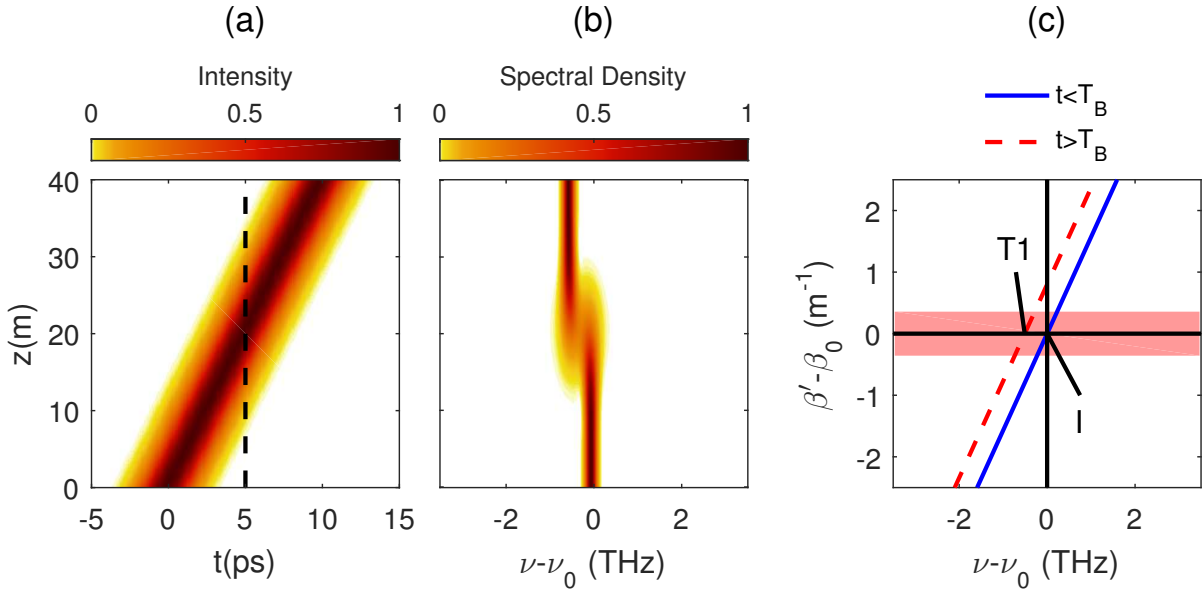


Figure 6.4: Evolution of (a) the pulse shape and (b) the spectrum in the presence of a space-time boundary at  $T_B = 5$  ps (dashed white line) with  $\beta_B = 0.8$  m<sup>-1</sup> and  $\beta_2 = 0$ . The time axis is measured in a reference frame moving with the boundary such that  $t = T - z/v_B$ . (c) The dispersion curves for  $t < T_B$  (solid blue line) and  $t > T_B$  (dashed red line). The shaded region shows the corresponding range of propagation constants for the entire pulse bandwidth at the input ( $t < T_B$ ).

Note also that the direction of frequency shifts in Eqs. (6.11) and (6.12) depends on the nature of GVD. A red shift occurring for normal dispersion becomes a blue shift in the case of anomalous dispersion. Figure 6.5 shows the propagation of the same pulse as before, but with the sign of  $\beta_2$  reversed. In order to have the same value of  $\Delta\beta_1$ , the input frequency is now located to the left of the maximum of the parabola. As predicted, this leads to a blue-shift of the pulse frequency. Interestingly, the behavior in time is the same as that observed in Fig. 6.3(a), while the spectral shifts are mirrored around  $\nu - \nu_0 = 0$ . Another noteworthy feature of Eq. (6.11) is that the reflected frequency shift does not depend on the refractive index change  $\Delta n$  across the boundary. Of course, the energy transferred to the reflected pulse depends strongly on the magnitude of  $\beta_B$ . These features are analogous to what occurs at a spatial interface, where the reflected angle is the same regardless of the refractive index change. Equation (6.11) indicates that even larger spectral shifts are possible by reducing the magnitude of the GVD parameter, i.e., by operating close to the zero-dispersion wavelength of the waveguide used to observe this phenomenon. However, for the same value of  $\beta_B$ , this will reduce the energy transferred to the reflected frequency.

The refracted pulse also undergoes a spectral shift that is analogous to a change in the direction of an optical beam refracted at a spatial boundary. As seen in Eq. (6.12), this shift depends on the magnitude of  $\beta_B$  in addition to the GVD parameter,  $\beta_2$ , and the DGD,  $\Delta\beta_1$ , of the pulse. In the limit  $\Delta\beta_1 \gg \sqrt{\beta_B\beta_2}$  the spectral shift becomes independent of  $\beta_2$ . Its magnitude in all cases is much smaller than that found for the

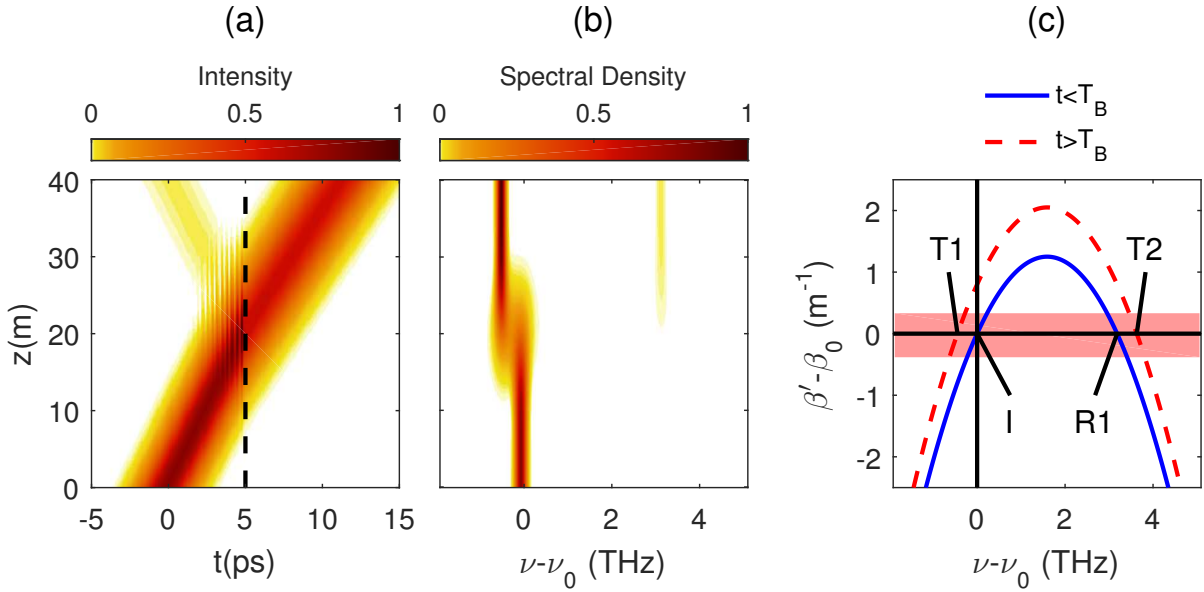


Figure 6.5: Evolution of (a) the pulse shape and (b) the spectrum in the presence of a space-time boundary at  $T_B = 5$  ps (dashed white line) with  $\beta_B = 0.8$  m<sup>-1</sup> and  $\beta_2 = 0.025$  ps<sup>2</sup>/m. The time axis is measured in a reference frame moving with the boundary such that  $t = T - z/v_B$ . (c) The dispersion curves for  $t < T_B$  (solid blue line) and  $t > T_B$  (dashed red line). The shaded region shows the corresponding range of propagation constants for the entire pulse bandwidth at the input ( $t < T_B$ ).

reflected pulse. As an example, for the case examined in Fig. 6.2, this shift is 0.64 THz, which is much lower than the 3.18 THz shift of the reflected pulse.

In Sect. 6.1, our simulations showed that the pulse spectrum can either narrow or broaden during refraction. In general, the output spectral width can be found using Eq. (6.12) to determine the output frequency for each frequency in the input pulse spectrum. We can then define a spectral broadening factor, which is simply the ratio of the transmitted spectral width ( $\Omega_t$ ) to the input spectral width ( $\Omega_i$ ). For narrow bandwidths, we can approximate the broadening factor as the ratio of the input dispersion slope to the output dispersion slope. Taking the derivative of Eq (6.2) with  $\omega$  for the dispersion slope and using Eq. (6.12), we find the broadening factor is approximately

$$\frac{\Omega_t}{\Omega_i} \approx \left( \sqrt{1 - \frac{2\beta_B\beta_2}{(\Delta\beta_1)^2}} \right)^{-1}. \quad (6.14)$$

When  $\beta_B\beta_2 < 0$ , the broadening factor is  $< 1$ , corresponding to spectral narrowing. As  $\beta_B$  increases, the broadening factor becomes even smaller, approaching zero for  $|\beta_B| \gg 0$ . In the limit where  $\beta_B$  approaches infinity, the transmitted pulse will be quasi-monochromatic with a corresponding temporal width approaching infinity. However, this large refractive index change results in very little energy being transferred to the transmitted pulse, with most of the pulse energy going to the reflected pulse. For  $\beta_B\beta_2 > 0$ , the broadening factor becomes  $> 1$ , resulting in a spectral broadening and a compression of the pulse

in time. As  $\beta_B$  increases, the broadening factor approaches infinity when  $2\beta_B\beta_2 = \Delta\beta_1^2$ . In practice, the broadening factor will not approach infinity because the approximation used to obtain Eq. (6.14) begins to break down for pulses with large bandwidths, because the dispersion slope changes considerably across the pulse spectrum.

One may ask what the space-time equivalents of the laws of reflection and refraction are. It is difficult to find analogous relations since the concept of an angle, familiar in the spatial context, is replaced with the DGD. Nevertheless, one may gain some insight if we use the location of the extremum of the dispersion curve in Fig. 6.2(c) as a reference frequency  $\omega_c$ , where the slope  $d\beta'/d\omega = 0$ . If we shift the origin in Fig. 6.2(c) so that all frequencies are measured from the reference frequency  $\omega_c = \omega_0 - \Delta\beta_1/\beta_2$  and use the notation  $\Delta\omega = \omega - \omega_c$ , the reflected and transmitted frequencies are related to the input frequency as

$$\Delta\omega_r = -\Delta\omega_i, \quad \Delta\omega_t = \Delta\omega_i \sqrt{1 - \frac{2\beta_B\beta_2}{(\Delta\beta_1)^2}}. \quad (6.15)$$

The first equation is analogous to the law of reflection. The second one can be written in the following suggestive form:

$$\Delta\omega_t = \Delta\omega_i \cos \alpha, \quad \sin \alpha = \sqrt{\frac{2\beta_B\beta_2}{(\Delta\beta_1)^2}}. \quad (6.16)$$

For small values of  $\beta_B$ ,  $\alpha$  remains relatively small, resulting in small frequency shifts during refraction, and small changes in the pulse speed. Frequency shifts increase with increasing  $\beta_B$ , but at some value of parameters,  $\alpha$  becomes  $\pi/2$ , and  $\Delta\omega_t = 0$ . At that point, the transmitted pulse's central frequency coincides with the frequency  $\omega_c$ .

We must ask what happens if  $\beta_B$  is large enough that  $\alpha$  loses its meaning. Since  $\Delta\omega_t$  becomes complex, no refracted pulse can propagate past the space-time boundary and the incident pulse must be totally reflected. This is the temporal analog of the well-known phenomenon of total internal reflection (TIR). The condition for the temporal TIR is found from Eq. (6.16) to be

$$\sqrt{2\beta_B\beta_2} > \Delta\beta_1. \quad (6.17)$$

Temporal TIR can also be understood from the two dispersion curves shown in Fig. 6.2(c). When  $\beta_B$  is large enough to shift the red curve in Fig. 6.2(c) completely out of the shaded region, momentum conservation or phase matching cannot be achieved for any spectral component of the incident pulse. As a result, no pulse energy can propagate in the  $t > T_B$  region beyond the boundary. However, the momentum can still be conserved for the reflected pulse, meaning the pulse should be completely reflected at the boundary. We performed numerical simulations to confirm that this is indeed the case. Figure 6.6 shows the numerical results for  $\beta_B = 1.7 \text{ m}^{-1}$ , a value that places the transmitted curve just above the shaded region. As predicted by our simple theory, there is no transmitted pulse and the entire pulse is reflected. The spectral evolution in Fig. 6.6(b) shows how the pulse energy is transferred to the reflected pulse over a small distance after the trailing end of the incident pulse hits the boundary.

So far we have said that the transmitted frequency becomes undefined in Eq. (6.16)

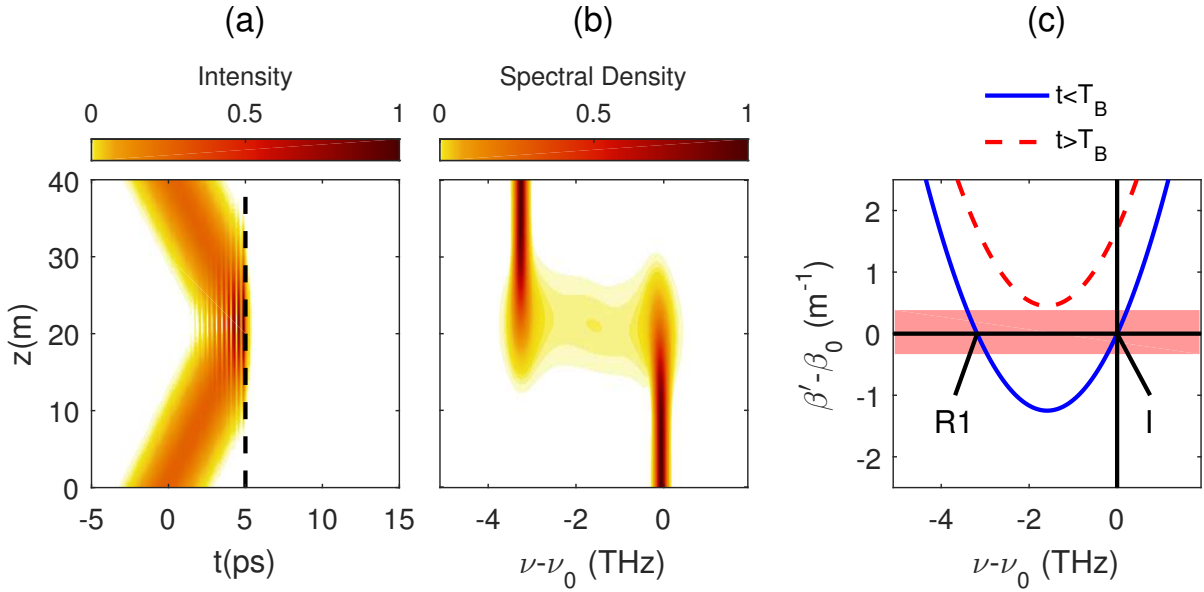


Figure 6.6: (a) Temporal and (b) spectral evolutions of an optical pulse undergoing TIR at a space-time boundary located at  $T_B = 5$  ps (dashed white line) with  $\beta_B = 1.7$  m $^{-1}$ . Time is measured in a reference frame that is moving with the boundary. The time axis is measured in a reference frame moving with the boundary such that  $t = T - z/v_B$ . (c) The dispersion curves for  $t < T_B$  (solid blue line) and  $t > T_B$  (dashed red line). The shaded region shows the corresponding range of propagation constants for the entire pulse bandwidth at the input ( $t < T_B$ ).

when the TIR condition is satisfied. If we impose the TIR condition onto Eq. (6.15), we see that the transmitted frequency becomes complex, following the relation

$$\Delta\omega_t = i\Delta\omega_i \sqrt{\frac{2\beta_B\beta_2}{(\Delta\beta_1)^2} - 1}. \quad (6.18)$$

This produces a field with an exponential decay term,  $\exp[-|\Delta\omega_t|(t - T_B)]$ , centered at the boundary time  $T_B$  and extending into the  $t > T_B$  region with a decay rate of  $|\Delta\omega_t| = |\Delta\omega_i| \sqrt{\frac{2\beta_B\beta_2}{(\Delta\beta_1)^2} - 1}$ . This is the same behavior as the spatial evanescent wave, and we can observe this effect by more closely inspecting how the pulse interacts with the space-time boundary. Figure 6.7(a) shows the same simulation as in Fig. 6.6 but with the time axis scaled to focus on the boundary. The oscillations in the intensity profile are caused by the interference between the incident and reflected pulse. We see that as the pulse hits the boundary, a portion of the pulse energy extends past the time  $t = T_B$  but no energy is carried beyond the boundary. Because the evanescent wave still matches the momentum of the reflected frequency, energy can still be transferred to the reflected frequency and carried away from the boundary, eventually depleting the evanescent wave.

With the spatial evanescent wave, the length of the tail that extends past the boundary depends on the magnitude of the change in refractive index, with a larger change in index leading to a shorter tail. Thanks to the space-time analogy, we expect to see this

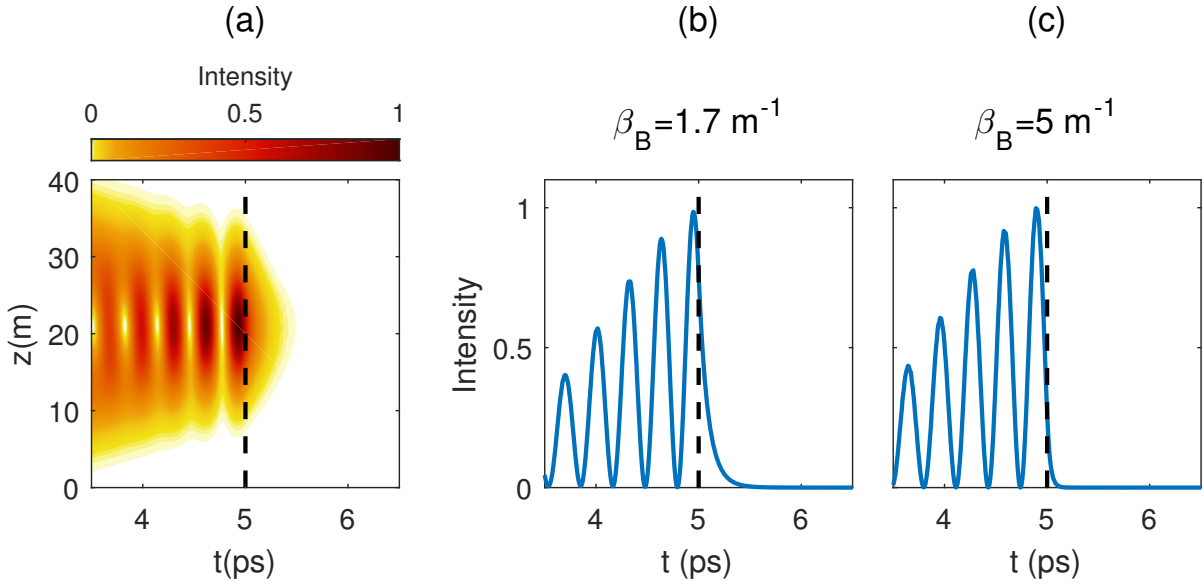


Figure 6.7: (a) A closer view of the same temporal evolution as Fig. 6.6. Intensity profile at  $z = 20\text{m}$  for (b)  $\beta_B = 1.7 \text{ m}^{-1}$  and (c)  $\beta_B = 5 \text{ m}^{-1}$ . The time axis is measured in a reference frame moving with the boundary such that  $t = T - z/v_B$ .

same behavior in our analog to the evanescent wave. We can easily see from Eq. (6.18) that for the temporal evanescent wave the  $1/e^2$  decay time ( $T_D = 1/|\Delta\omega_t|$ ) decreases as  $\beta_B$  becomes large because  $|\Delta\omega_t| \propto \sqrt{\beta_B}$ . Figure 6.7(b) and (c) show the intensity profile in time at  $z = 20 \text{ m}$  for (b)  $\beta_B = 1.7 \text{ m}^{-1}$  and (c)  $\beta_B = 5 \text{ m}^{-1}$ . As expected, the evanescent tail in Fig. 6.7(b) is longer than the one in Fig. 6.7(c). Using the simple theory above, we find  $1/e^2$  decay times of  $T_D = 0.167 \text{ ps}$  and  $T_D = 0.058 \text{ ps}$  for (b) and (c) respectively. Because the pulse contains a range of spectral components with slightly different decay times, the actual evanescent tails in Figs. 6.7(b) and (c) differ slightly from these calculated values. Indeed if we look at longer pulses with narrower bandwidths, we find that the decay times approach the values calculated above.

The existence of temporal TIR seems to contradict the findings in Ref. [93], where a temporal analog of Snell's law is derived that does not allow for TIR to occur. However, the study in Ref. [93] was only examining an non-moving temporal boundary, where the reflected pulse travels backward in space as discussed in Chapter 5. In this situation there is no condition under which the transmitted pulse would not satisfy momentum conservation while the reflected does because both exist in the post-boundary medium (dashed red curve).

### 6.3 Conclusions

In summary, we have shown that when an optical pulse approaches a moving refractive index boundary across which the refractive index changes, it undergoes a space-time analog of reflection and refraction of optical beams at a spatial boundary. The main difference is that the role of angle is played by changes in the frequency. The dispersion

curve of the material in which the pulse is propagating plays a fundamental role in determining the frequency shifts experienced by the reflected and refracted pulses. The analytic expressions that we were able to obtain for these two frequency shifts show that the spectral shift is relatively small for the refracted pulse but can be quite large for the reflected pulse. Moreover, the shifts can be either on the red side or on the blue side of the spectrum of the incident pulse, depending on the nature of both the group-velocity dispersion and the refractive index change. These spectral shifts are caused by a transfer of energy between the pulse and the moving boundary while the number of photons is conserved [93]. Because our refractive index boundary is induced by an external source, this is not a closed system and energy is not conserved in the pulse. We have also indicated the conditions under which an optical pulse experiences the temporal analog of TIR. Numerical results confirm all analytical predictions based on the physical concept of momentum conservation in the moving frame.

An experimental observation of reflection, refraction, and TIR at a space-time boundary will be of immense interest. Our estimates show that changes in the refractive index across this boundary can be as small as  $10^{-6}$  for verifying our theoretical and numerical predictions. The main issue is how to control the relative speed of the pulse with respect to the moving boundary. One possibility is to use a traveling-wave electro-optic modulator in which a microwave signal propagates at a different speed than that of the optical pulse. A pump-probe configuration in which cross-phase modulation would be used to produce a moving boundary may also be possible but will require pump pulses of high energies. We will explore the pump-probe configuration in greater detail in Chapter 10.

---

## Chapter 7

# Temporal Waveguides for Optical Pulses

The fundamental concept of total internal reflection (TIR) at a dielectric interface has been known since 1840 and is discussed thoroughly in optics textbooks [32, 90]. It has been used to make optical waveguides that confine an optical beam to the vicinity of a central core region whose refractive index is chosen to be higher than the surrounding cladding regions [144, 145]. A multitude of applications has been found for waveguides, notably in the optical fibers used extensively for designing modern telecommunication systems [91].

In this chapter, I show that two temporal boundaries that satisfy the temporal TIR condition can be used to make a temporal analog of an optical waveguide, which confines the pulse to a central time window inside which the refractive index is different from the outer regions. In Sect. 7.1 I use the conditions for TIR derived in Sect. 6.2 to form a temporal waveguide in which a short pulse bounces back and forth between two temporal boundaries. Analogous to conventional spatial waveguides, a temporal waveguide supports a finite number of modes. This topic is discussed in Sect. 7.2. As shown in Sect. 7.3, single-mode temporal waveguides can be designed such that a pulse trapped inside it maintains its width even in the presence of group-velocity dispersion (GVD). The main results are summarized in Sect. 7.4.

### 7.1 Example of a Temporal Waveguide

We ask what happens when an optical pulse is located between two space-time boundaries that both move at the same speed and satisfy the TIR condition given in Eq. (6.17). If the group velocity of the pulse differs from that of the space-time boundaries, we expect that the pulse will travel toward one of the boundaries and be reflected completely. Since the spectrum of the reflected pulse will be shifted as indicated in Eq (6.11), it will move away from that first boundary with a new group velocity. However, unlike the single boundary case, the pulse will now arrive at the second temporal boundary, where it will once again experience TIR, but this time its center frequency will shift back to the initial value. This process should repeat itself, trapping the pulse between the two boundaries. This

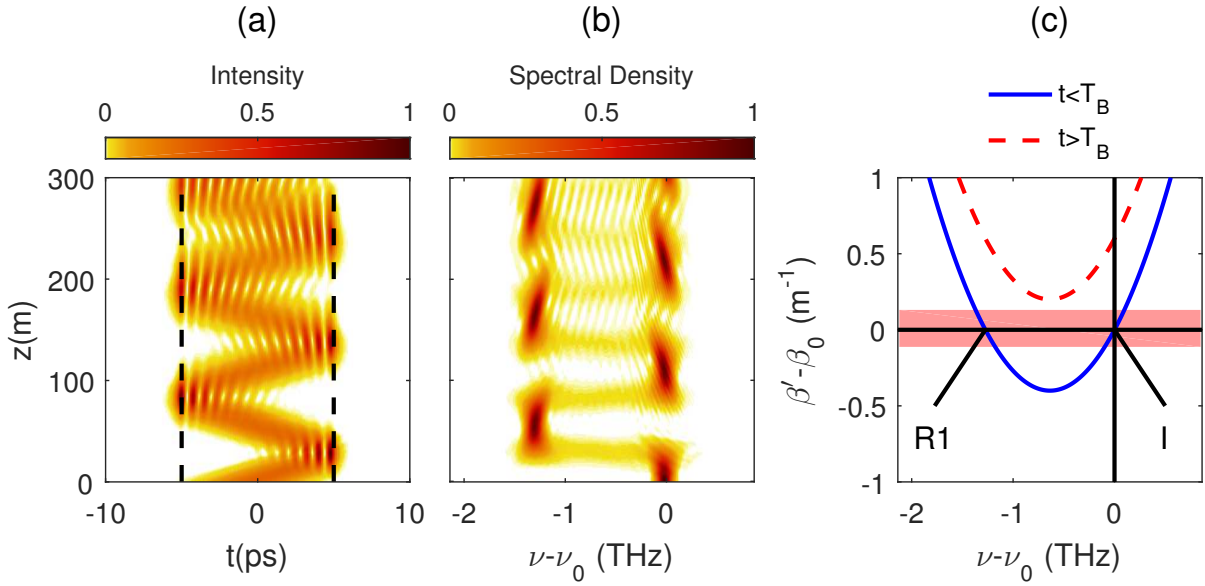


Figure 7.1: Evolution of the (a) shape and (b) spectrum of a Gaussian pulse ( $T_0 = 2.5$  ps) inside a 10-ps-wide temporal waveguide. Dashed vertical lines show the temporal boundaries that form the waveguide core. The time axis is measured in a reference frame moving with the boundary such that  $t = T - z/v_B$ . (c) Dispersion curves for inside the waveguide (solid blue) and outside the waveguide (dashed red). The pink-shaded region shows range of propagation constants over the bandwidth of the pulse spectrum. The time  $t$  is measured in the reference frame moving at the same speed as the two boundaries.

behavior is analogous to that of an optical beam inside two spatial boundaries that form the core of a conventional waveguide such that the beam undergoes TIR multiple times as it travels through the waveguide. Because of this analogy, we refer to the configuration with two space-time boundaries as a temporal waveguide. The trapping effect has been previously examined in the context of soliton fission [129, 146], but we stress that the temporal waveguide does not require optical nonlinearities.

To explore the behavior of an optical pulse inside such a temporal waveguide, we launch a Gaussian pulse ( $T_0 = 2.5$  ps) with its peak located in the middle of a 10-ps-wide temporal waveguide and study how the pulse shape and spectrum evolve along a 300-m-long optical fiber by solving Eq. (6.8) numerically. We emphasize that we are still working in the moving reference frame  $t = T - z/v_B$ , where  $T$  is the laboratory time frame, and  $v_B$  is the speed of the moving boundary. Figure 7.1 shows the temporal and spectral evolutions using the parameters  $\Delta\beta_1 = 0.2$  ps/m,  $\beta_2 = 0.05$  ps<sup>2</sup>/m,  $\beta_B = 0.6$  m<sup>-1</sup> for  $|t| > 5$  ps but 0 for  $|t| < 5$  ps. Notice that with this choice of  $\beta_B$ , the refractive index is smaller inside the core of our temporal waveguide, a situation that is impossible for traditional spatial waveguides.

Figure 7.1 shows how the optical pulse bounces back and forth between the two temporal boundaries, where it is completely reflected as predicted by the TIR condition in Eq. (6.17). The reflection at the right-most boundary is accompanied by the frequency shift of  $\Delta\nu_r = -1.27$  THz (see Fig. 1), which changes the relative group velocity of the

pulse so that it now moves toward the other boundary located at  $t = -5$  ps. When the pulse is totally reflected at this boundary, its center frequency is shifted back to its original value, and it begins to travel at its original group velocity toward the first boundary again. This process repeats multiple times with further propagation. Temporal fringes near the two boundaries are a consequence of the spectral shifts required for TIR to occur. Indeed, the 0.79-ps fringe spacing correlates perfectly with the 1.27-THz spectral shift.

One may ask whether the 2.5-ps pulse can remain confined within the 10-ps time window indefinitely, while maintaining its original shape and size. In Fig. 7.1(a) we see the pulse broadens noticeably after 150 m. Broadening occurs because the dispersion length is 125 m for the parameter values used here. We cannot make dispersion negligible because temporal TIR does not occur in its absence. The GVD also causes certain wavelengths to reflect sooner leading to the tapered appearance of the spectrum during propagation as seen in Fig. 7.1(b). The predicted behavior is analogous to that observed in spatial multimode waveguides designed with a core whose size is much larger than the beam width. Since the 10-ps core of our temporal waveguide is much wider than the 2-ps pulse, multiple modes are excited, which interfere with each other as the pulse propagates down the medium. This suggests that we should analyze the optical modes supported by a temporal waveguides.

## 7.2 Modes of a Temporal Waveguide

The spatial modes of planar waveguides have been extensively studied [144, 145]. By definition, the shape of an individual mode does not change during propagation. To develop an analogous theory for the modes of a temporal waveguide, we seek solutions to Eq. (6.8) that do not change with propagation except for a phase shift. Therefore, we assume a modal solution of the form

$$A(z, t) = M(t) \exp[i(Kz - \Omega t)], \quad (7.1)$$

where  $M(t)$  is the temporal shape of the mode,  $K$  is the rate at which the mode accumulates phase during propagation, and  $\Omega$  is a frequency shift such that  $\omega_0 + \Omega$  becomes the new central frequency of the mode. There is no spatial analog of this frequency shift. It is needed in the temporal case because of the first derivative in Eq. (6.8) related to the speed at which the pulse approaches a temporal boundary.

Substituting Eq. (7.1) into Eq. (6.8) and equating the real and imaginary parts, we obtain

$$(\Delta\beta_1 + \beta_2\Omega) \frac{dM}{dt} = 0, \quad (7.2)$$

$$\frac{d^2M}{dt^2} + \frac{2}{\beta_2} \left( K - \Omega\Delta\beta_1 - \frac{\beta_2\Omega^2}{2} - \beta_B \right) M = 0. \quad (7.3)$$

From Eq. (7.2), we find that the frequency shift  $\Omega$  must be chosen as  $\Omega = -\Delta\beta_1/\beta_2$ . This frequency corresponds to a pulse that will propagate at the same speed as the two temporal boundaries. A spectral shift is necessary if the mode were to remain confined

within the temporal waveguide, otherwise the mode would naturally drift outside of the waveguide region ( $|t| < T_B$ ).

Using this value for  $\Delta\beta_1$  to replace  $\Omega$  in Eq. (7.3), the mode shape is governed by the simple equation

$$\frac{d^2M}{dt^2} + \frac{2}{\beta_2} \left( K + \frac{(\Delta\beta_1)^2}{2\beta_2} - \beta_B \right) M = 0. \quad (7.4)$$

To be as general as possible, we assume that  $\beta_B$  takes different values for  $|t| < T_B$ ,  $t > T_B$ , and  $t < -T_B$ . We label these three values as  $\beta_{B0}$ ,  $\beta_{B1}$ , and  $\beta_{B2}$ , respectively. The temporal waveguide becomes symmetric when  $\beta_{B1} = \beta_{B2}$ .

To solve Eq. (7.4), we follow a procedure analogous to that used for spatial planar waveguides [144] and write its solution in the form

$$M(t) = \begin{cases} B_1 \exp[-\Omega_1(t - T_B)] & t > T_B, \\ A \cos(\Omega_0 t - \phi) & |t| < T_B, \\ B_2 \exp[\Omega_2(t + T_B)] & t < -T_B, \end{cases} \quad (7.5)$$

where the parameters  $\Omega_0$ ,  $\Omega_1$ , and  $\Omega_2$  are defined as

$$\Omega_0^2 = \frac{2K}{\beta_2} + \left( \frac{\Delta\beta_1}{\beta_2} \right)^2 - \frac{2\beta_{B0}}{\beta_2}, \quad (7.6)$$

$$\Omega_1^2 = \frac{2\beta_{B1}}{\beta_2} - \frac{2K}{\beta_2} - \left( \frac{\Delta\beta_1}{\beta_2} \right)^2, \quad (7.7)$$

$$\Omega_2^2 = \frac{2\beta_{B2}}{\beta_2} - \frac{2K}{\beta_2} - \left( \frac{\Delta\beta_1}{\beta_2} \right)^2. \quad (7.8)$$

The four constants  $B_1$ ,  $B_2$ ,  $A$ , and  $\phi$  can be related by imposing the boundary conditions that both  $M(t)$  and its derivative  $dM/dt$  be continuous across the two temporal interfaces. The boundary conditions lead to the following two relations:

$$\tan(\Omega_0 T_B - \phi) = \frac{\Omega_1}{\Omega_0}, \quad \tan(\Omega_0 T_B + \phi) = \frac{\Omega_2}{\Omega_0}. \quad (7.9)$$

These equations can be used to find the eigenvalue equation in the form

$$2\Omega_0 T_B = m\pi + \tan^{-1} \left( \frac{\Omega_1}{\Omega_0} \right) + \tan^{-1} \left( \frac{\Omega_2}{\Omega_0} \right), \quad (7.10)$$

where the integer  $m = (0, 1, 2, \dots)$  denotes the mode order. For each value of  $m$ , the eigenvalue equation can be solved to find the value of  $K$  for that specific mode at that value of  $\Delta\beta_1$ . We stress that the value of  $K$  changes with  $\Delta\beta_1$  such that  $K + (\Delta\beta_1/2\beta_2)^2$  is the same for a given mode of the waveguide. In analogy with spatial waveguides, we call the  $m = 0$  mode the fundamental temporal mode of the waveguide.

For simplicity we focus on symmetric waveguides for which the index jump is identical at both temporal boundaries so that  $\Omega_1 = \Omega_2$ . In this case, the eigenvalue equation takes

a much simpler form:

$$\Omega_1 = \Omega_0 \tan(\Omega_0 T_B + m\pi/2). \quad (7.11)$$

We also introduce a dimensionless parameter as [144]

$$V = T_B \sqrt{\Omega_0^2 + \Omega_1^2} = \sqrt{\frac{2(\beta_{B1} - \beta_{B0})T_B^2}{\beta_2}}. \quad (7.12)$$

It plays an important role in determining the number of modes supported by the temporal waveguide. In complete analogy with the spatial case, the waveguide supports mode  $m$  when  $V > m\pi/2$ . In particular, a temporal waveguide will support only the fundamental  $m = 0$  mode if it is designed such that  $V < \pi/2$ .

Consider the temporal waveguide used for Fig. 7.1. Using the known parameter values in Eq. (7.12), we find that this waveguide has  $V = 24.5$  and supports 16 modes. The temporal and spectral evolution of several modes ( $m = 0, 2, 10$ ) of this waveguide are shown in Fig. 7.2. As expected, the modes propagate without changing their shape or spectrum. In analogy with a spatial waveguide, the  $m$ th-order mode has  $m + 1$  distinct peaks inside the temporal window of the waveguide.

The new feature in the temporal case is different spectral shifts associated with different modes. The fundamental mode propagates with a central frequency shifted by  $\Omega/(2\pi) = 1.59$  THz, which matches the frequency shift predicted by  $\Omega = -\Delta\beta_1/\beta_2$ . The spectra of all of the higher-order modes ( $m > 0$ ) exhibit two intense peaks located at approximately  $(\Omega \pm \Omega_0)/(2\pi)$ . The two spectral peaks beat together to form the temporal oscillations of the cosine term in Eq. (7.5), resulting in the multiple-peaked structure of the higher-order modes ( $m > 0$ ). For the highest-order mode supported by the waveguide, the value of  $\Omega_0$  is the highest frequency offset that still satisfies the TIR condition at both of the temporal boundaries. In addition to the two main spectral peaks, all modes have several lower-intensity spectral peaks that are separated by  $\Delta\nu = 1/(2T_B)$ . These spectral peaks are caused by an interference between the evanescent tails of the mode, which are separated in time by  $2T_B$ . For less confined modes, these oscillations become more intense as more of the pulse energy is contained in the evanescent tails.

So far we have focused on the simple case of a waveguide formed by two step-index boundaries (zero rise time). Most practical temporal boundaries will experience dispersion during propagation, leading to changes in the boundary rise time. The precise evolution of a temporal boundary will be determined by the exact physical mechanism used to generate the boundary. For example, when an intense pulse propagating as an optical soliton is used to create a temporal boundary through the nonlinear phenomenon of cross-phase modulation, the temporal boundary created by it will have a finite rise time that is unaffected by dispersion. We have verified numerically that temporal boundaries with a finite rise time also exhibit temporal modes with shapes that depend on the magnitude of rise time. Figure 7.3 shows the evolution if the same modes from Fig. 7.2 are launched into a waveguide with a functional form given by

$$\beta_B(t) = \beta_B \left[ 1 + \frac{1}{2} \tanh \left( \ln(9) \frac{t - T_B}{T_R} \right) + \frac{1}{2} \tanh \left( -\ln(9) \frac{t + T_B}{T_R} \right) \right], \quad (7.13)$$

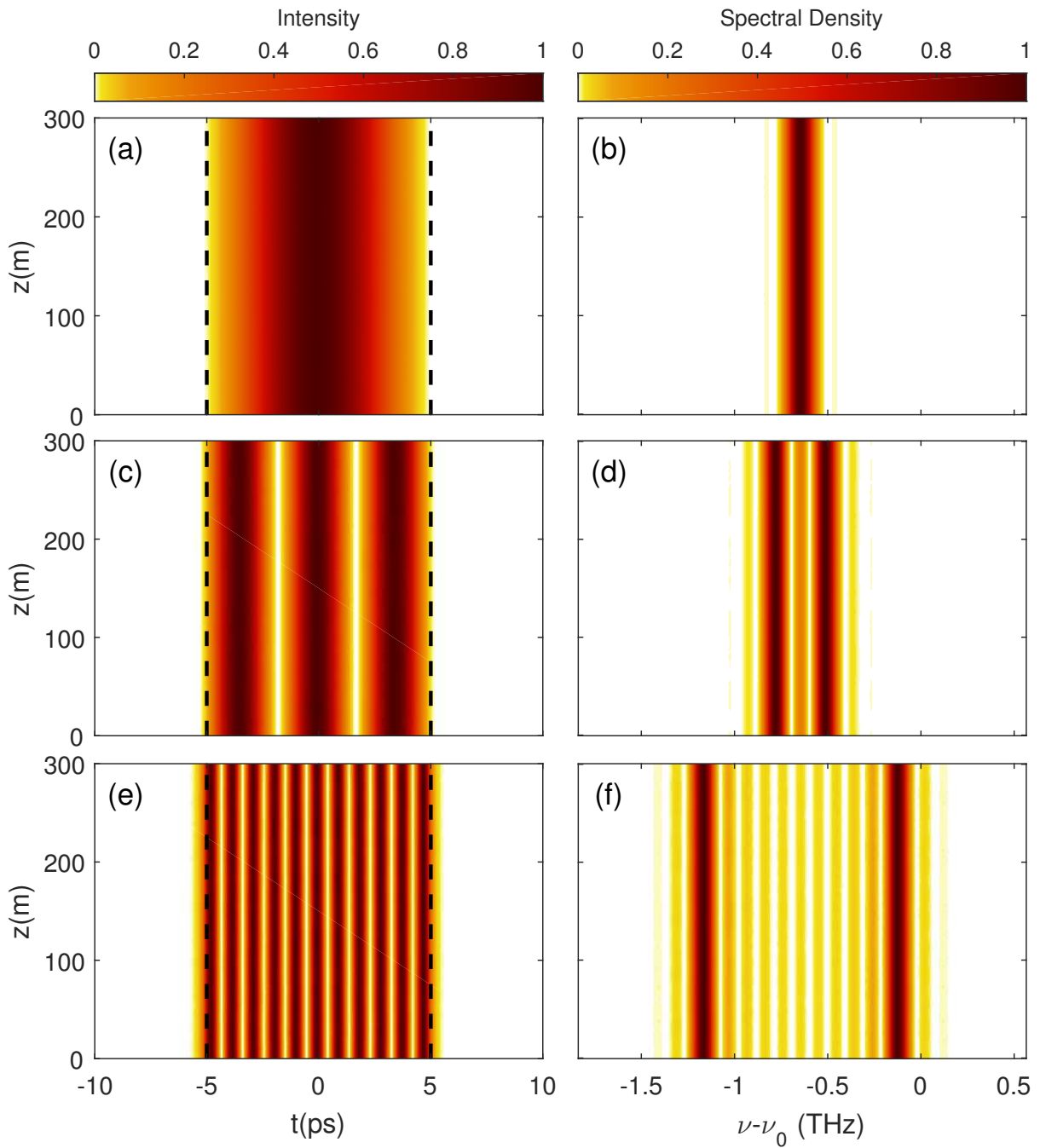


Figure 7.2: Evolution of shapes (left) and spectra (right) for modes with [(a),(b)]  $m = 0$ ; [(c),(d)]  $m = 2$ ; and [(e),(f)]  $m = 10$  for a 10-ps-wide temporal waveguide with  $V = 24.5$ . The time axis is measured in a reference frame moving with the boundary such that  $t = T - z/v_B$ .

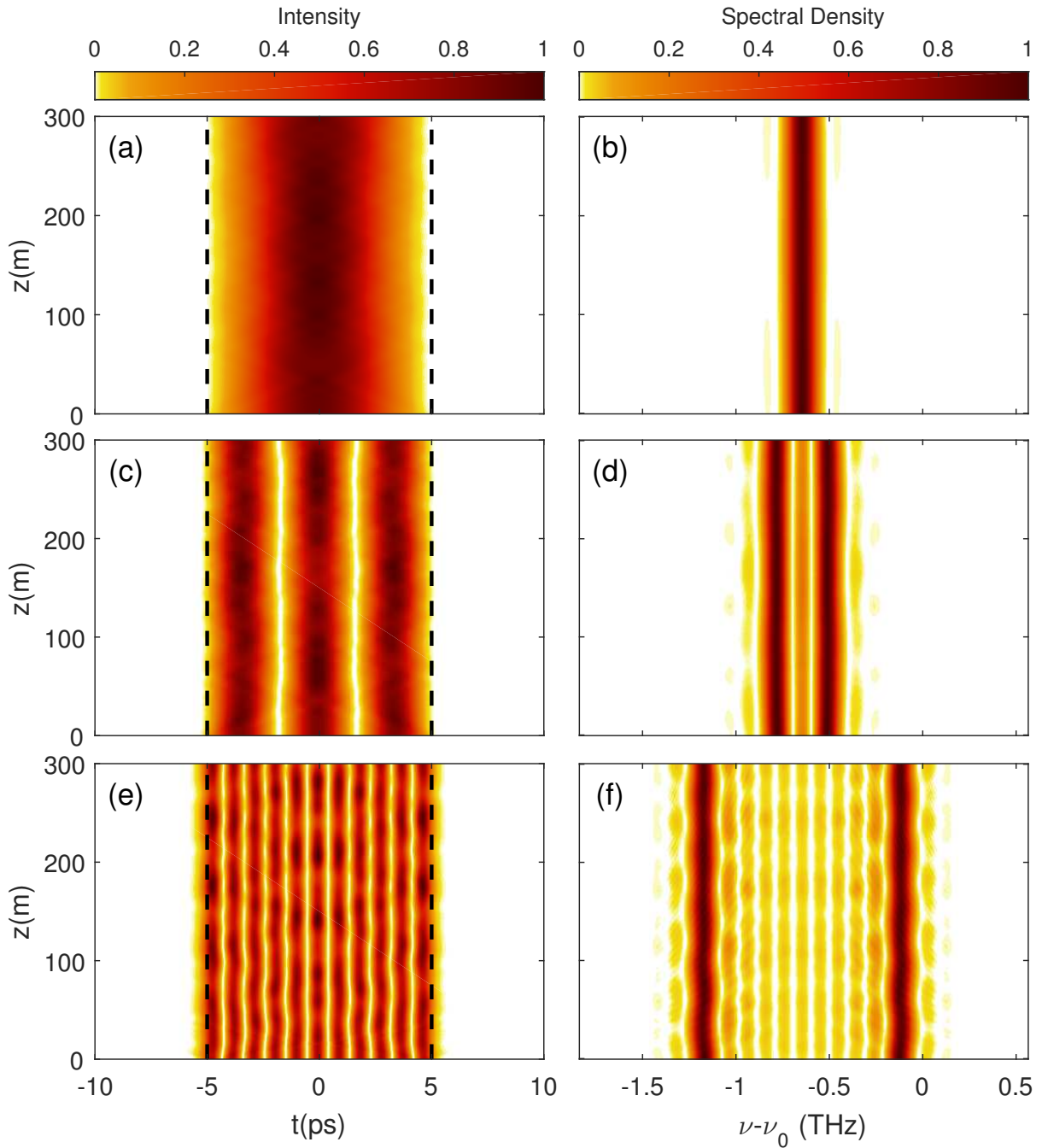


Figure 7.3: [(Evolution of shapes (left) and spectra (right) for modes with [(a),(b)]  $m = 0$ ; [(c),(d)]  $m = 2$ ; and [(e),(f)]  $m = 10$  for a 10-ps-wide temporal waveguide formed by two boundaries with the same refractive index change as in Fig. 7.2 but with a finite rise time of  $T_R = 0.5$  ps. The time axis is measured in a reference frame moving with the boundary such that  $t = T - z/v_B$ .

where  $T_R$  is the rise time of the boundary. The rise time was taken to be 5% of the waveguide width for each boundary ( $T_R = 0.5$  ps). We can clearly see that the modes are no longer unchanging during propagation. Instead, the pulses adjust their shape and

spectrum and evolve toward the mode of the new waveguide. The fundamental mode appears to change the least with the change in rise time, particularly when compared to the  $m = 10$  mode. This makes sense as the higher order modes have significant peaks near the boundary time  $T_B$ , so they are more susceptible to changes in the boundary rise times. If we adjust the value of  $\beta_B$  while keeping the same waveguide width, we find that the shape of the waveguide modes are more tolerant of finite rise times when the parameter  $V$  is small. This leads us to conclude that for few-mode temporal waveguides the results obtained in this section would apply qualitatively to temporal boundaries with a finite rise time as long as its magnitude is a small fraction (below 10%) of the waveguide's temporal window. If a single-mode waveguide with  $V < \pi/2$  is used, the mode shape is largely unchanged for rise times as large as 30% of the waveguide width. Conversely, for highly-multimode waveguides, the tolerable rise-times become significantly reduced, and the mode shapes become significantly distorted.

### 7.3 Single-Mode Temporal Waveguide

Spatial waveguides supporting a single mode have found a variety of applications. It is therefore useful to consider single-mode temporal waveguides. As discussed earlier, only a single mode will propagate if the temporal waveguide is designed with  $V < \pi/2$ . From Eq. (7.12) we see that this condition can be satisfied by either reducing the width of the waveguide (parameter  $T_B$ ) or by decreasing the magnitude of the index change at the temporal boundaries (parameter  $\beta_B$ ). Such a waveguide will support only the  $m = 0$  mode with a temporal shape similar to that shown in Fig. 7.2(a).

An important question is how an optical pulse with a shape different from that of the fundamental mode behaves when launched into such a single-mode waveguide. Figure 7.4 shows the simulated behavior for a Gaussian input pulse with  $T_0 = 3.5$  ps inside a 10-ps-wide symmetric temporal waveguide designed with  $V = 1.414$ . The pulse is launched with an initial differential group delay of  $\Delta\beta_1 = 10$  ps/km. From Fig. 7.4(a) we see that the pulse initially bounces off a few times at the two temporal boundaries through TIR, losing a considerable portion of its energy into the “cladding” region (outside of dashed boundaries) a behavior similar to dispersive waves [33]. However, it eventually stops oscillating and acquires the shape of the fundamental mode supported by the waveguide. This behavior is analogous to that which occurs when an optical beam traveling at an angle is launched into a spatial waveguide.

The spectral evolution seen in Fig. 7.4(b) appears strange and has a “chevron” shape that does not match the spectrum of the fundamental mode. This apparent discrepancy occurs because the total electric field at any location contains both the guided and unguided light at different frequencies. As a result of their interference, the simulated spectrum acquires a fringe-like structure. Numerically it is easy to filter out the unguided components. Figure 7.4(c) shows the resulting spectrum, which exhibits the expected behavior. More specifically, the spectrum oscillates initially in a manner discussed in Sect. 7.1 but eventually settles down to take the shape associated with the guided mode, with its center frequency shifted by just the right amount (about 32 GHz).

We stress that the shift of the central frequency is not caused by the entire pulse

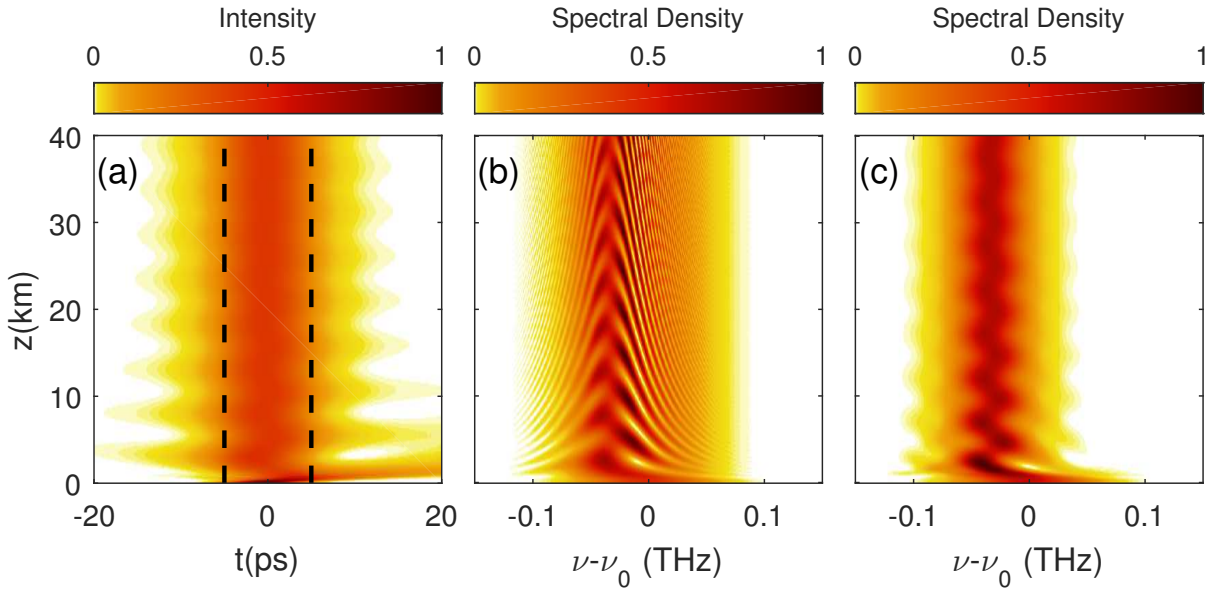


Figure 7.4: Evolution of the (a) shape and (b) spectrum of a Gaussian pulse with  $T_0 = 3.5$  ps inside a 10-ps-wide single-mode temporal waveguide designed with  $\beta_B = 2 \text{ km}^{-1}$ . The spectral evolution of only the guided pulse is shown in (c). Dashed horizontal lines show the temporal boundaries that form the waveguide core. The time axis is measured in a reference frame moving with the boundary such that  $t = T - z/v_B$ .

spectrum shifting to this value of  $\Omega$ . Figure 7.5 shows the early evolution of the spectrum in Fig. 7.4 in greater detail. As this figure shows, a portion of the input pulse spectrum overlaps with the spectrum of the single-mode waveguide and is guided. From this perspective, the efficiency with which the pulse couples into the fundamental mode of the temporal waveguide can be improved by launching a pulse at a frequency shifted by  $\Omega$ .

The reshaping of the optical pulse occurs for any pulse that is launched into a single-mode temporal waveguide, regardless of its temporal duration or shape. Figure 7.6 shows the evolution of three different Gaussian pulses with (a)  $T_0 = 2.5$  ps, (b)  $T_0 = 5$  ps, and (c)  $T_0 = 10$  ps. Each pulse was launched into the same single-mode temporal waveguide used for Fig. 7.4, but its spectrum was centered at the shifted frequency  $\Omega$  to improve coupling into the fundamental temporal mode. The 2.5-ps pulse quickly broadens because of GVD, filling the waveguide in less than 400 m. The pulse then loses considerable energy into the  $|t| > T_B$  regions as it reshapes itself into the fundamental mode of the waveguide. In contrast, the 10-ps pulse in Fig. 7.6(c) narrows down as it is initially much wider than the waveguide. Narrowing occurs because the portion of the pulse outside of the guiding region is mostly shed off through dispersion. The portion lying inside the central core region reshapes itself until it once again matches the shape of the fundamental mode. The 5-ps pulse in Fig. 7.6(b) is just wide enough that most of its energy lies inside the temporal waveguide. As a result, much less energy is shed into the dispersive waves as it acquires the shape of the fundamental mode. Clearly, this is the optimum situation if the objective is to couple most of the pulse energy inside a single-mode temporal waveguide.

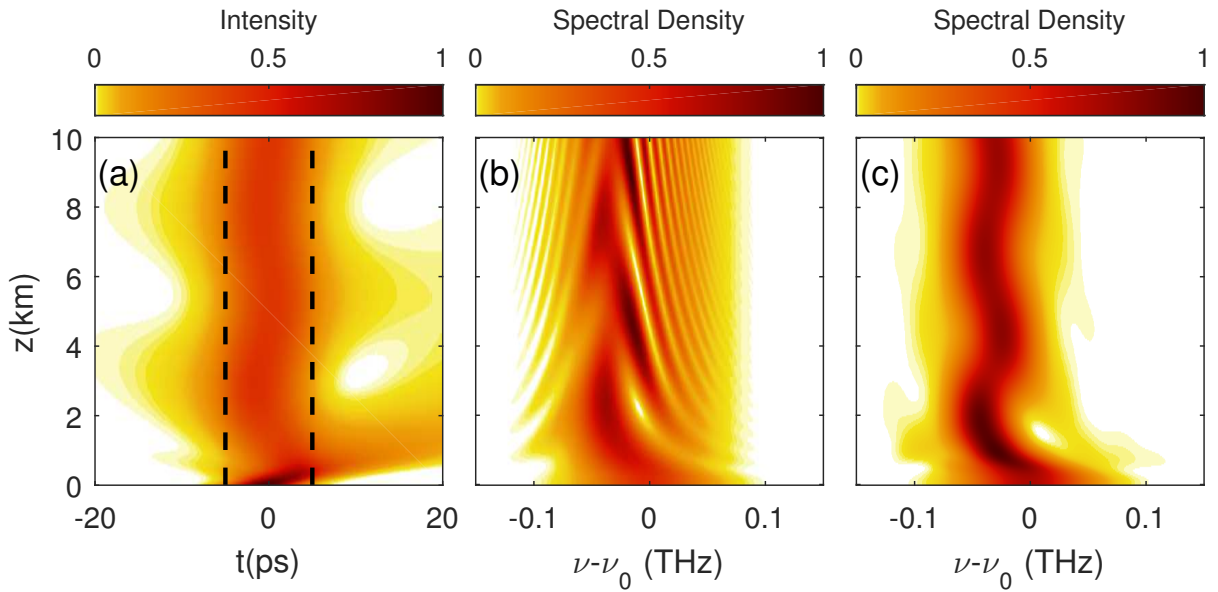


Figure 7.5: Early evolution of the (a) shape and (b) spectrum for the optical pulse from Fig. 7.4. The spectral evolution of only the guided pulse is shown in (c).

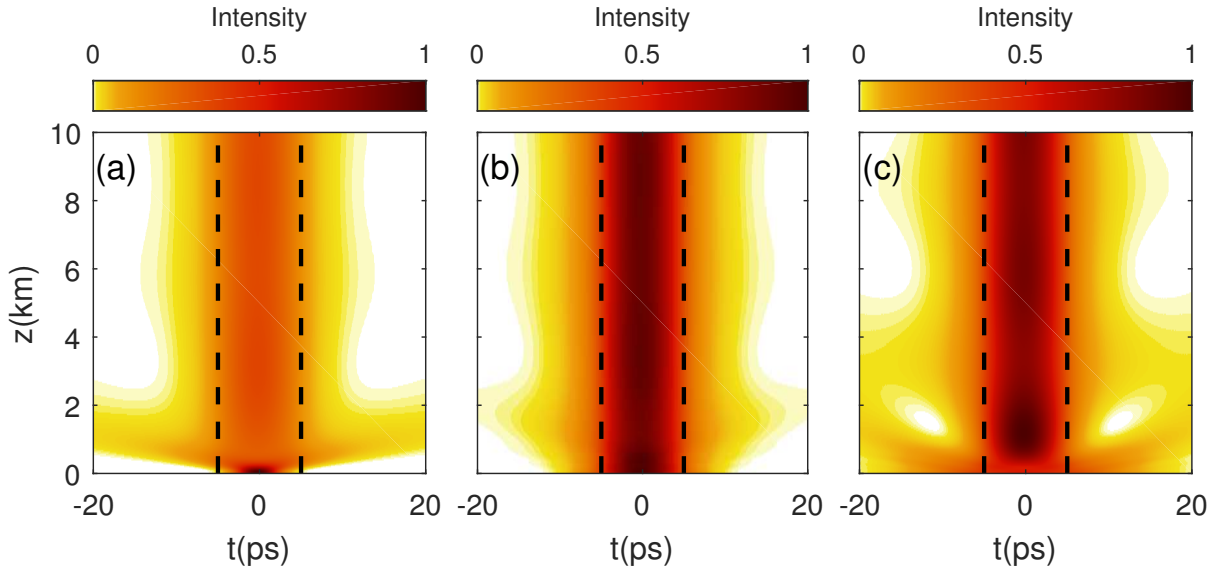


Figure 7.6: Evolution of the shape of Gaussian pulses with (a)  $T_0 = 2.5$  ps, (b)  $T_0 = 5$  ps, and (c)  $T_0 = 10$  ps into the same waveguide used in Fig. 7.4. Dashed horizontal lines show the temporal boundaries that form the waveguide core. The time axis is measured in a reference frame moving with the boundary such that  $t = T - z/v_B$ .

This is analogous to improving the coupling efficiency into optical fibers by matching the optical beam to the mode diameter and numerical aperture of an optical fiber.

The timing delay,  $T_D$ , between the pulse and the center of the waveguide also plays an important role in the coupling efficiency into the time waveguide. This is equivalent to matching the transverse position of an optical beam spot to a waveguide. Figure 7.7

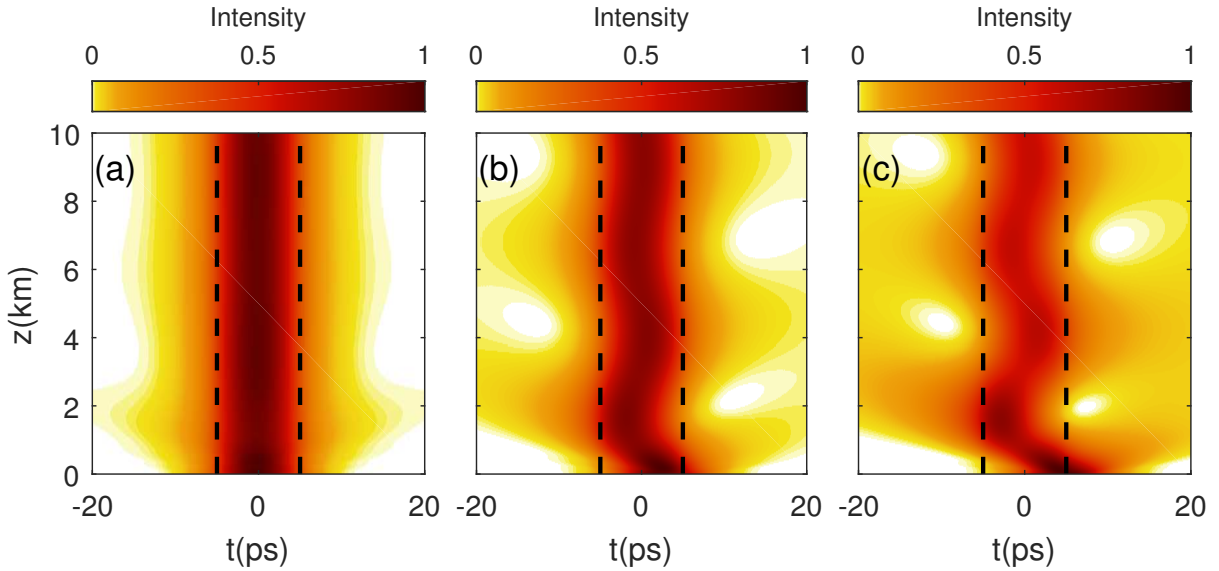


Figure 7.7: Evolution of the shape of Gaussian pulses with (a)  $T_D = 0$  ps, (b)  $T_D = 2.5$  ps, and (c)  $T_D = 5$  ps into the same waveguide used in Fig. 7.4. Dashed horizontal lines show the temporal boundaries that form the waveguide core.

shows the evolution of three different Gaussian input pulses with  $T_0 = 5$  ps and a timing delay between the pulse and the waveguide center of (a)  $T_D = 0$  ps, (b)  $T_D = 2.5$  ps, and (c)  $T_D = 5$  ps. In each case, the energy trapped inside the waveguide still reshapes to match the fundamental mode shape. However, as the pulse becomes more decentered in the waveguide, less of the pulse energy is guided, with more energy escaping to the wings. As  $T_D$  increases, a larger fraction of the pulse begins outside of the waveguide, and is therefore never guided in the first place.

The last factor that affects the coupling efficiency is the matching the input pulse frequency to the center frequency of the mode  $\omega_0 + \Omega$ . Figure 7.8 shows the temporal evolution and dispersion curve for three different pulses with frequency offsets of [(a),(b)]  $\Omega = 0$  GHz, [(c),(d)]  $\Omega = 100$  GHz, and [(e),(f)]  $\Omega = 300$  GHz. From the evolution of the pulse shapes, we see that the coupling efficiency decreases as the spectral offset increases. Looking at the corresponding dispersion curves, we can clearly see that this is caused by a larger portion of the pulse spectrum no longer satisfying the TIR condition. In Fig. 7.8(b), nearly the entire pulse spectrum satisfies the TIR condition and therefore most of the pulse energy is trapped by the waveguide. However, for larger values of  $\Omega$ , the same spectral range will cover a much larger range of dispersion values, and so more of the spectrum can undergo refraction and escape the waveguiding region. Matching the input pulse frequency such that  $\Omega = 0$  is analogous to matching the wave-vector to the propagation axis of a waveguide in the spatial case. As with the other cases, the light that is confined within the waveguide eventually reshapes to match the fundamental mode shape. However, larger deviations from the mode shape require longer propagation distances for the reshaping process to complete.

One may ask how the optical phase varies across the pulse. It follows from Eq. (7.4) that  $M(t)$  is a real quantity, indicating a constant phase. However, we should not forget

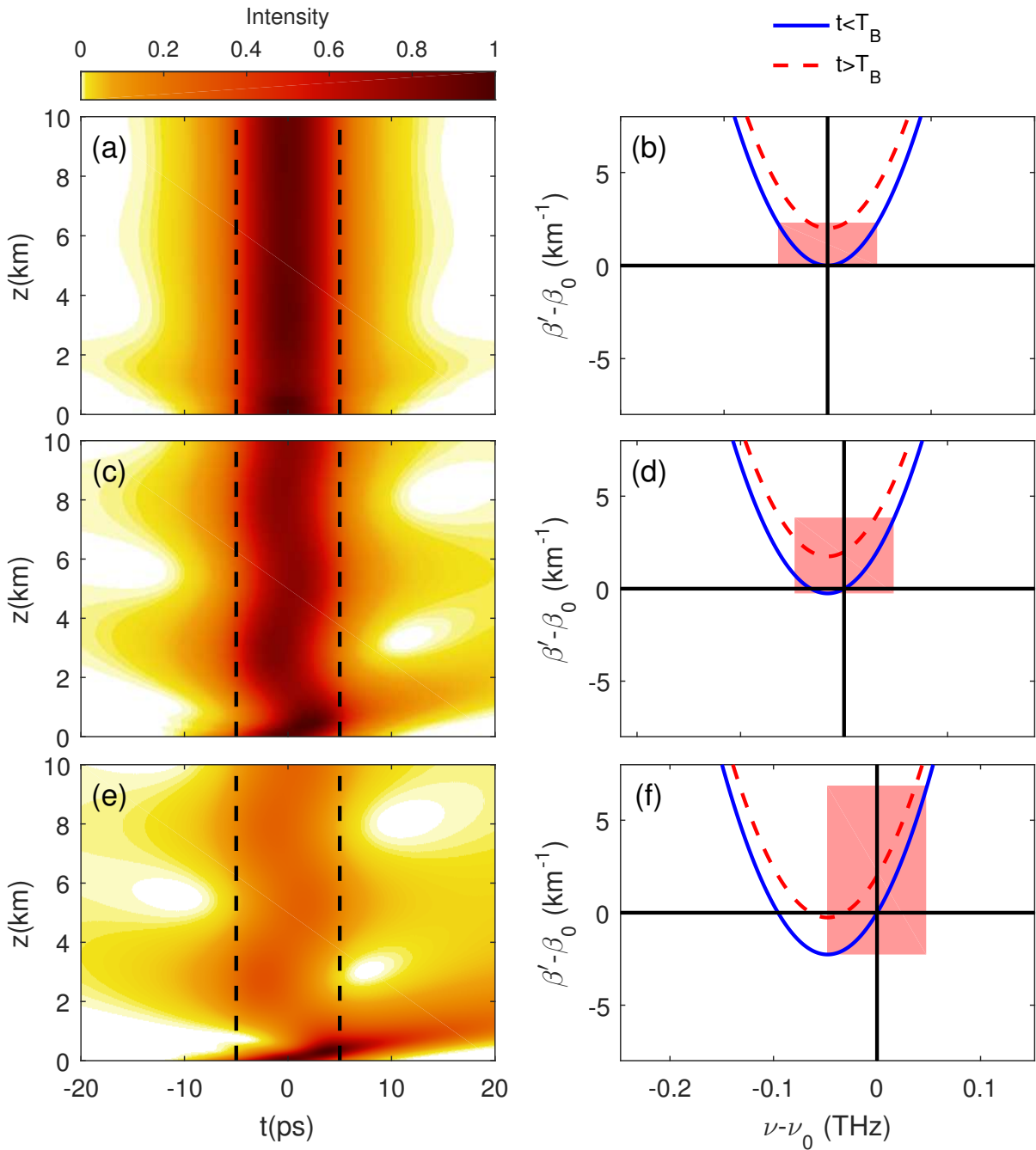


Figure 7.8: [(a),(c),(e)]Evolution of the shape of Gaussian pulses with (a)  $\Omega = 0$  GHz, (c)  $\Omega = 100$  GHz, and (e)  $\Omega = 300$  GHz into the same waveguide used in Fig. 7.4. Dashed horizontal lines show the temporal boundaries that form the waveguide core. The corresponding dispersion curves are shown in (b),(d), and (f) respectively. The shaded region shows the spectral region covered by the input pulse spectrum and the corresponding range of dispersion values.

the phase factor in Eq. (7.1). If the pulse is launched with its center frequency at  $\omega_0$ , the phase across the guided pulse would vary linearly in time. The slope of this temporal

phase corresponds to the frequency shift  $\Omega$ . However, if we shift the center frequency of the incident pulse by  $\Omega$ , the phase becomes flat in time. This is what occurred in the case of Fig. 7.6. Since the phase of the waveguide mode is uniform in time, we may say that the pulse is phase locked. We should stress that the phase is not constant since it increases with  $z$  at a rate  $K + \beta_2\Omega^2/2$ ; however, it increases uniformly for the entire pulse duration.

## 7.4 Conclusions

We have shown that the analog of TIR at a temporal boundary can be used to make temporal waveguides. Using numerical simulations, we have shown that a temporal waveguide can be produced by two co-propagating temporal boundaries that satisfy the condition for temporal total internal reflection. We were able to solve the underlying equations analytically to obtain the modes of a temporal waveguide. These modes are analogous to those of a planar waveguide except for a crucial frequency shift. In particular, we introduced a dimensionless parameter  $V$  whose value determines the number of modes supported by that waveguide. The single-mode condition  $V < \pi/2$  is then identical to that found for spatial waveguides.

We used numerical solutions to show that the modes propagate stably over long distances. Coupling into a single-mode waveguide was studied by launching Gaussian pulses of different widths. We discussed in detail the dynamics of how the launched pulse reshapes its shape and spectrum to evolve into the fundamental mode, shedding energy as dispersive waves in the process. We also showed that pulses that match more closely the shape and spectrum of the fundamental mode couple more efficiently into the temporal waveguide.

An experimental confirmation of temporal TIR and the temporal waveguide will be of great interest. Our estimates show that the change in refractive index across the temporal boundary can be lower than  $\Delta n = 10^{-6}$  for producing temporal TIR. The main issue is controlling the relative speed of the pulse with respect to the temporal boundary. A traveling-wave electro-optic phase modulator driven by co-propagating microwave pulses could be used to produce the two moving temporal boundaries. Alternatively, a pump-probe configuration using a rectangular pump pulse could be used to produce the temporal boundaries through cross-phase modulation, but will require pump pulses of high energies. In this case, the probe pulse would be launched in the middle of the pump with the two edges of the pump forming the waveguide boundaries. We will discuss this configuration more in Chapter 10.

---

## Chapter 8

# Single-pulse interference caused by temporal reflection at moving refractive-index boundaries

Double-slit interference, which occurs when light exiting from two closely spaced, narrow slits forms intensity fringes in a plane transverse to the direction of light propagation, has been a cornerstone of the wave nature of light for centuries [32]. Its temporal analog, where two short pulses propagate through a dispersive medium and form interference fringes in time, has also been explored through the well-known space–time analogy [10, 11, 14] as discussed in Chapter 2.

One useful tool that combines the double-slit interference with reflection is the Lloyd’s mirror configuration. In this case, diffracted light from a single slit is reflected from a mirror, creating an interference pattern that appears as if the initial slit was interfering with a virtual second slit that has a  $\pi$  phase-shift [89]. This configuration has seen use in photolithography [147], test-pattern generation [148], and radio astronomy [149]. However, a temporal analog of this arrangement has not yet been explored. In this chapter I show how space-time reflection from a moving refractive-index boundary leads to an analog of Lloyd’s mirror for optical pulses propagating inside a dispersive medium. I also discuss how this configuration relates to two-pulse interference in time.

In Sect. 8.1 I review two-pulse interference and its relation to the spatial counterpart, two-slit interference. In Sect. 8.2 I discuss how a temporal analog of Lloyd’s mirror is formed when an optical pulse reflects from a moving refractive-index boundary. Section 8.3 considers the temporal waveguide configuration from Chapter 7 [31] and discusses how it can be employed for either self-imaging or generation of a burst of pulses from a single pulse. The main results are summarized in Sect. 8.4.

### 8.1 Two-pulse interference

We first discuss how two large-bandwidth, temporally separated pulses propagating inside a dispersive medium can overlap in time as they broaden due to group-velocity dispersion and form interference fringes that mimic a double-slit diffraction pattern. We consider

optical pulses in the form of plane waves in the transverse spatial direction. Each frequency component of the pulses travels with a propagation constant  $\beta(\omega) = n(\omega)\omega/c$ , where  $n(\omega)$  is the refractive index at frequency  $\omega$ . For pulses containing multiple optical cycles,  $\beta(\omega)$  can be approximated by a Taylor expansion around the central frequency of the pulse such that

$$\beta(\omega) = \beta_0 + \beta_1(\omega - \omega_0) + \frac{\beta_2}{2}(\omega - \omega_0)^2, \quad (8.1)$$

where  $\beta_m = (d^m\beta/d\omega^m)_{\omega=\omega_0}$ . The parameter  $\beta_1$  is the inverse of pulses' group velocity. We simplify the following analysis by using the retarded time  $t = T - z\beta_1$ , giving us a moving-frame dispersion relation in the form

$$\beta'(\omega) = \beta_0 + \frac{\beta_2}{2}(\omega - \omega_0)^2. \quad (8.2)$$

Using the dispersion relation in Eq. (8.2) together with Maxwell's equations and the slowly varying envelope approximation, we obtain the time-domain equation

$$\frac{\partial A}{\partial z} + \frac{i\beta_2}{2} \frac{\partial^2 A}{\partial t^2} = 0, \quad (8.3)$$

where  $A(z, t)$  is the temporal envelope of the electric field at distance  $z$ . This equation is easily solved in the frequency domain using the Fourier transform method, and the solution is given by [33]

$$A(z, t) = \int_{-\infty}^{\infty} \tilde{A}(0, \omega) \exp \left[ i \frac{\beta_2 z}{2} (\omega - \omega_0)^2 - i\omega t \right] d\omega, \quad (8.4)$$

where  $\tilde{A}(0, \omega)$  is the Fourier transform of  $A(0, t)$ .

The integral in Eq. (8.4) can be performed in a closed form in only a few special cases. However, as we saw in Chapter 2, we can solve this equation analytically when  $L \gg L_D$ , or in other words when we satisfy the far-field condition  $(|\beta_2|z)^{-1} \ll \Omega_w^2$ , where  $\Omega_w$  is a measure of the width of the input-pulse spectrum. The output envelope in this limit mimics the shape of the input spectrum and has the form [9, 11]

$$A(z, t) = \tilde{A} \left( 0, \Omega = \frac{t}{\beta_2 z} \right) \exp \left( -i \frac{t^2}{2\beta_2 z} \right). \quad (8.5)$$

Note that the scaling factor between the frequency and time scales is simply the GDD,  $\beta_2 z$ .

We now assume that the temporal waveform at  $z = 0$  consists of two identical pulses separated in time by  $T_s$ :

$$A(0, t) = A_0(t - T_s/2) + A_0(t + T_s/2), \quad (8.6)$$

where  $A_0(t)$  governs the shape of each optical pulse. By performing the Fourier transform,

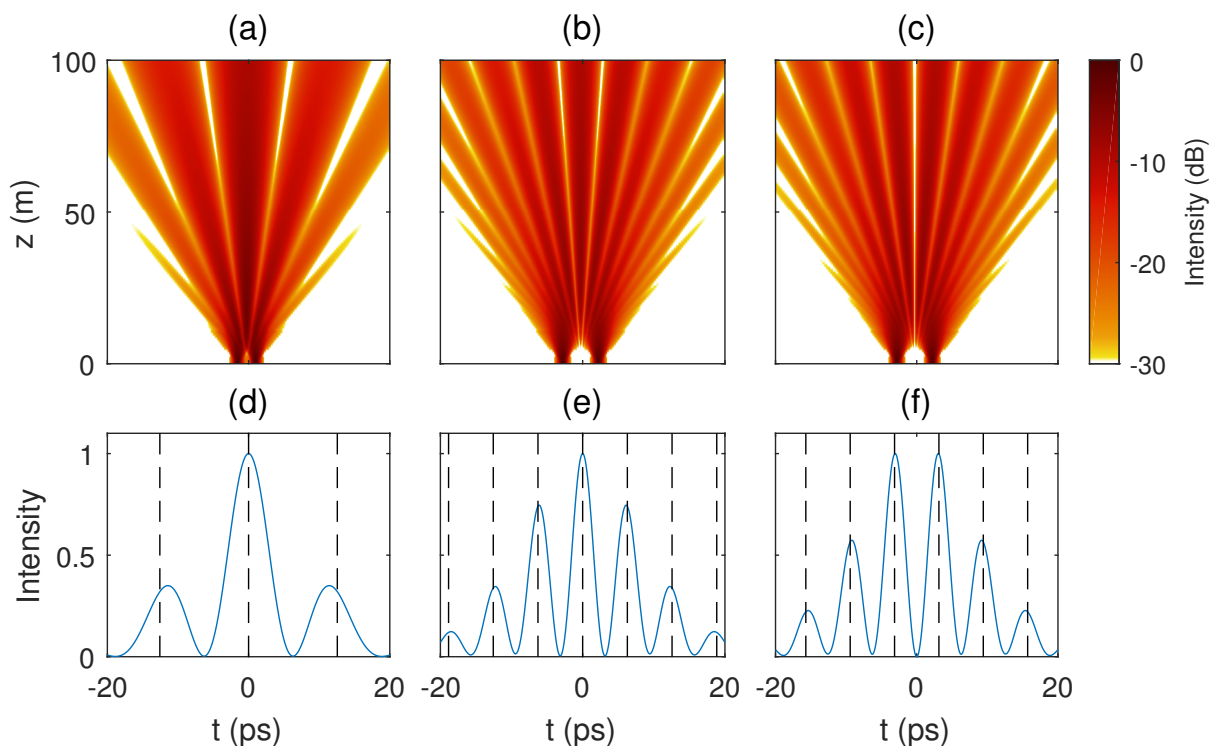


Figure 8.1: [(a)–(c)] Evolution of pulse shape for two hyperbolic secant pulses propagating in a dispersive medium with initial pulse separations of (a)  $T_s = 2.5$  ps, (b)  $T_s = 5$  ps, and (c)  $T_s = 5$  ps. The initial pulses in (c) have a  $\pi$ -phase offset. [(d)–(f)] The output pulse shapes for the same pulses, with the predicted fringe locations marked with dashed black lines.

it is easy to show that the input spectrum is given by

$$\tilde{A}(0, \omega) = 2\tilde{A}_0(\omega) \cos(\omega T_s/2), \quad (8.7)$$

where  $\tilde{A}_0$  is the Fourier transform of  $A(0, t)$ . It follows from the solution in Eq. (8.6) that when the two pulses are propagated through a long-enough dispersive medium to satisfy the far-field limit, the output intensity  $|A(z, t)|^2$  will have the form

$$|A(z, t)|^2 = 4|\tilde{A}_0|^2 \cos^2\left(\frac{T_s t}{2\beta_2 z}\right). \quad (8.8)$$

The cosine term in Eq. (8.8) leads to the formation of interference fringes in time with a fringe separation of  $T_f = 2\pi\beta_2 z/T_s$ . As the initial pulses (slits) are separated more in time, the fringes get closer together. Also, as the propagation distance  $z$  is increased, the fringe separation increases. This behavior is exactly analogous to the fringe separation seen in a double-slit diffraction pattern.

Figure 8.1 shows three simulations depicting the propagation of two hyperbolic-secant-shaped pulses propagating inside a dispersive medium with  $\beta_2 = 0.05$  ps<sup>2</sup>/m.

Specifically, we solved Eq. (8.3) with the input field of the form

$$A(0, t) = \operatorname{sech}\left(\frac{t - T_s/2}{T_0}\right) + \operatorname{sech}\left(\frac{t + T_s/2}{T_0}\right) \exp(i\phi), \quad (8.9)$$

where  $T_0$  is related to the pulse width and  $\phi$  is the phase offset between the two pulses. We choose  $T_0 = 0.3$  ps, giving a dispersion length ( $L_D = T_0^2/|\beta_2|$ ) of 1.8 m, and satisfying the far-field condition above. We varied  $T_s$  and  $\phi$  such that  $T_s = 2.5$  ps,  $\phi = 0$  for the first column;  $T_s = 5$  ps,  $\phi = 0$  for the second column; and  $T_s = 5$  ps,  $\phi = \pi$  for the third column. The top row shows the evolution of the pulse shape over 100 m on a decibel scale, and the bottom row shows the output pulse shape on a linear scale to more clearly mark the peak position. In all cases the two pulses broaden quickly due to group-velocity dispersion. As the dispersed pulses begin to overlap in time, they form interference fringes in a fan-like shape, appearing to form multiple pulses. As predicted by Eq. (8.8), a wider separation of input pulses in Fig. 8.1(b) leads to a smaller fringe spacing at the output compared to Fig. 8.1(a). The locations of fringe peaks in both Fig. 8.1(d) and 8.1(e) do not perfectly match the values predicted by Eq. (8.8) (dashed black lines), because the sinusoidal modulation is contained within the envelope of the initial pulse spectrum, resulting in a slight shift of the peaks of the interference fringes from the predicted times.

We next consider the case shown in the last column of Fig. 8.1 where the second pulse is identical to the first but has a phase offset of  $\phi = \pi$ . In this case, it is easily shown that the cosine term in Eq. (8.7) becomes a sine term and the output has the form

$$|A(z, t)|^2 = 4|\tilde{A}_0|^2 \sin^2\left(\frac{T_s t}{2\beta_2 z}\right). \quad (8.10)$$

As seen in Fig. 8.1(c), although the fringe spacing is the same as in Fig. 8.1(e), the locations of the "bright" and "dark" fringes have been reversed. This makes sense because bright and dark fringes differ by a phase shift of  $\pi$ . Figure 8.1(c) shows the propagation of the same two pulses as in Fig. 8.1(b) except for a relative phase shift of  $\phi = \pi$ . Again we see the pulses quickly broaden due to the GVD of the dispersive medium and form interference fringes. But as predicted, the bright and dark fringes have swapped locations compared to the  $\phi = 0$  case.

## 8.2 Self-interference caused by Time Reflection

In this section we consider the temporal reflection of an optical pulse inside a dispersive medium from a single moving refractive-index boundary. Unlike previous chapters, we will specifically look at the case where the incident pulse has a broadband spectrum, such that not all of the frequencies interact with the space-time boundary. As usual, we use a reference frame that is moving with the boundary such that  $t = T - z/v_B$ , where  $v_B$  is the speed of the boundary. We also Taylor expand the dispersion relation around a frequency whose group velocity matches the speed of the temporal boundary ( $\omega_0 = \omega_c$ ). Similar to the derivation of the nonlinear Schrodinger equation inside a dispersive nonlinear

medium, we introduce two time scales, a fast one at which the electric field oscillates and a slower one at which the amplitude envelope varies [33,62]. Assuming that the temporal transition region occurs on the slow time scale ( $> 10$  optical cycles), the evolution of the pulse envelope is governed by

$$\frac{\partial A}{\partial z} + \frac{i\beta_2}{2} \frac{\partial^2 A}{\partial t^2} = i\beta_B(t)A. \quad (8.11)$$

where  $\beta_B(t) = k_0\Delta n(t)$  is once again the shift in the dispersion curve caused by a time-dependent refractive-index change of  $\Delta n$ . Physically speaking, the dispersion relation of the medium beyond the temporal boundary takes the form [31,150]

$$\beta'(\omega) = \beta_0 + \frac{\beta_2}{2}(\omega - \omega_0)^2 + \beta_B(t). \quad (8.12)$$

We stress that the moving refractive index boundary is actually a temporal transition region where the refractive index change over a few optical cycles. But as long as the rise-time of this transition region is much shorter than the duration of the optical pulse, while still being longer than a few optical cycles, we can safely approximate the transition region as an step-like boundary.

Once again we impose conservation of momentum ( $\beta'(t = T_B^-) = \beta'(t = T_B^+)$ ), the reflected and transmitted pulse frequencies as

$$\Delta\omega_r = -\Delta\omega_i, \quad \Delta\omega_t = \Delta\omega_i \sqrt{1 - \frac{2\beta_B}{\beta_2(\Delta\omega_i)^2}}, \quad (8.13)$$

where  $\Delta\omega_j = \omega_j - \omega_0$ . For this section we will work in the regime where the TIR condition of Eq. (6.17) is satisfied with  $2\beta_B > \beta_2\Delta\Omega_i^2$ . In this case, the temporal boundary acts like a perfect mirror [150].

We solved Eq. (8.11) numerically using the standard split-step Fourier method. Figure 8.2 shows the evolution of the (b) shape and (c) spectrum over 100 m of a single sech-shaped pulse launched with  $T_0 = 0.3$  ps and  $\Delta\omega_i = 0$  with a temporal boundary located at  $T_B = 0$ . The pulse is offset from the boundary by  $T_s/2 = 2.5$  ps. The parameter  $\beta_B = 2.5 \text{ m}^{-1}$  was chosen to ensure TIR at the boundary over the pulse bandwidth.

We can visually see that the TIR condition is satisfied by examining Fig. 8.2(d), which shows the initial dispersion curve for  $t < 0$  in solid blue and the shifted dispersion curve for  $t > 0$  in dashed red. Because momentum must be conserved at the boundary, frequencies must maintain the same value of  $\beta'$  when interacting with the boundary. Because the pulse starts in the  $t < 0$  region, all frequencies must begin with a value of  $\beta'$  on the blue curve. To be transmitted across the boundary, a given frequency must have a  $\beta'$  that is greater than the minimum of the red curve (shown with a dotted black line). We can easily see that there are no frequencies on the blue curve for which  $\beta'$  exceeds this value for the entire pulse spectrum shown in Fig. 8.2(c). Therefore, no frequencies can be transmitted across the boundary, and TIR must occur. Note, however, that only frequencies  $(\nu - \nu_0) > 0$  will actually interact with the boundary and undergo TIR, while frequencies  $(\nu - \nu_0) < 0$  have group velocities that take them away from the boundary.

Comparing Fig. 8.2 to Fig. 8.1, the fringe pattern we obtain in Fig. 8.2(a) appears to most closely match the case shown in Fig. 8.1(c) where the second pulse has a  $\pi$ -phase shift from the first pulse. This is analogous to the Lloyd's mirror configuration, which produces interference fringes using a single slit and a mirror [89]. Because we employed a temporal analog of reflection [14, 150], it is not surprising that TIR from a temporal boundary produces a  $\pi$ -phase shift. Indeed, a  $\pi$ -phase shift also occurs during traditional TIR when the angle between the surface plane and the wave vector is small. As this angle becomes larger, however, the phase shift begins to drop from  $\pi$  to zero. Therefore, we should expect to see a frequency-dependent phase shift across the temporal fringes. We can infer this effect by more closely examining the fringes in Fig. 8.2. Figure 8.2(c) compares the temporal fringe pattern obtained through TIR (solid blue curve) with the one in Fig. 8.1(f) (dotted red curve) obtained through two-pulse interference (on a dB scale). For times close to  $t = 0$ , the fringe spacing agrees extremely well in the two cases, indicating that a  $\pi$ -phase shift occurs during the TIR. As we get farther from  $t = 0$ , the bright fringes for the reflected pulse (solid blue curve) begin to shift inward toward the dark fringes of the dotted red curve because of a reduced phase shift.

To quantify the preceding numerical behavior analytically, we need to find the phase shift,  $\phi_r$ , added to the pulse when it reflects off of the temporal boundary. To find this phase, we must first derive the temporal analogs of the Fresnel equations. To that end, we write the total electric field of a specific frequency component before and after the boundary as (assuming linear polarization)

$$E(t) = \begin{cases} A_i e^{i(\beta'z - \Delta\omega_i t)} + A_r e^{i(\beta'z - \Delta\omega_r t)} & t < 0, \\ A_t e^{i(\beta'z - \Delta\omega_t t)} & t > 0, \end{cases} \quad (8.14)$$

where  $A_i$ ,  $A_r$ , and  $A_t$  are the incident, reflected, and transmitted amplitudes, respectively. We now apply the boundary conditions that the electric field  $E(t)$  and its derivative  $\partial E/\partial t$  be continuous across the temporal boundary [31]. Recalling that  $\beta'$  is conserved in the moving frame across a temporal boundary, the boundary conditions are satisfied when

$$A_i + A_r^* = A_t, \quad \Delta\omega_i A_i + \Delta\omega_r A_r^* = \Delta\omega_t A_t. \quad (8.15)$$

The complex conjugate  $A_r^*$  is due to the reflection process causing a time reversal of the input signal. Solving these equations, the reflection coefficient  $r = A_r^*/A_i$  and transmission coefficient  $t = A_t/A_i$  are found to be

$$r = \frac{\Delta\omega_i - \Delta\omega_t}{\Delta\omega_t - \Delta\omega_r}, \quad t = \frac{\Delta\omega_i - \Delta\omega_r}{\Delta\omega_t - \Delta\omega_r}. \quad (8.16)$$

Substituting the reflected and transmitted frequencies from Eq. (8.13) into Eq. (8.16), we find the temporal analog for the Fresnel reflection coefficient in a dispersive medium given by

$$r = \frac{1 - i\sqrt{Q-1}}{1 + i\sqrt{Q-1}}, \quad t = \frac{2}{1 + i\sqrt{Q-1}}, \quad (8.17)$$

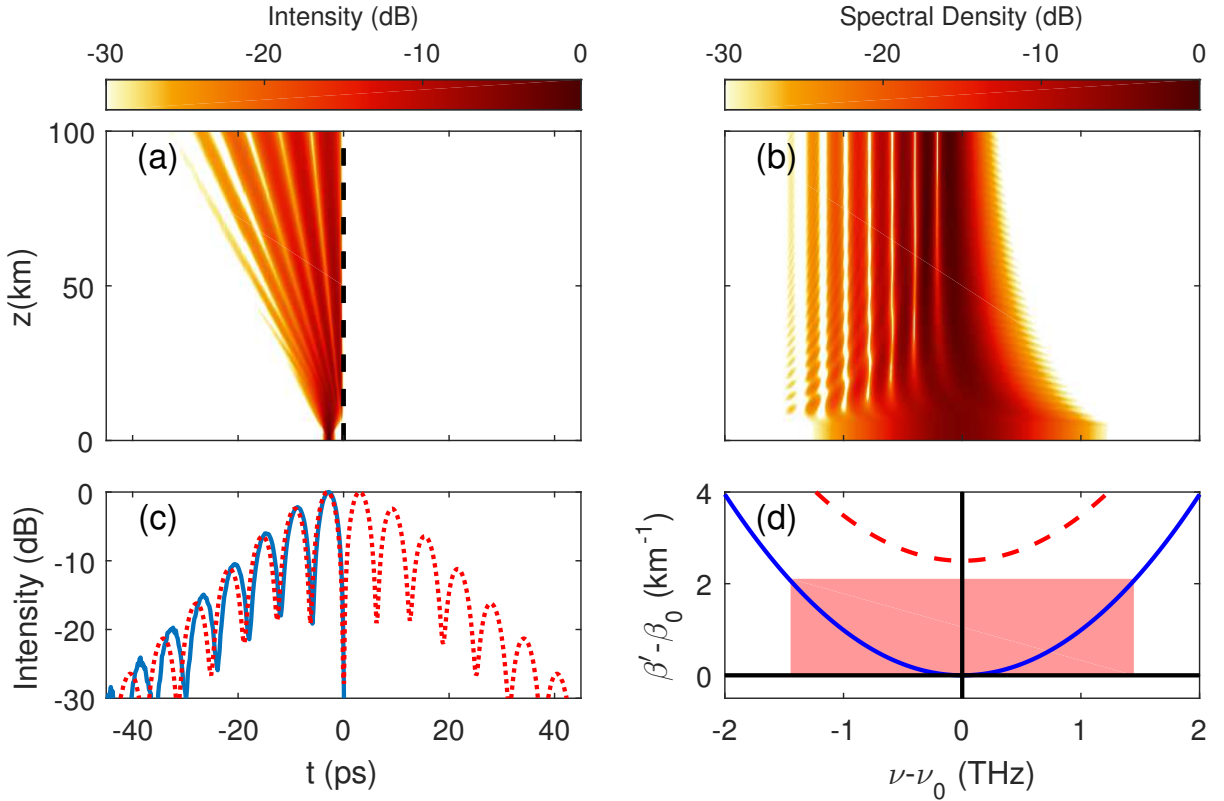


Figure 8.2: Evolution of the (a) shape and (b) spectrum of the single sech-shaped pulse propagating with the moving refractive-index boundary. (c) The fringe pattern after propagating 100 m for a single sech-shaped pulse with  $T_0 = 0.3$  ps (solid blue curve). The pulse is offset initially by 2.5 ps from a co-propagating refractive-index boundary. The two-pulse fringe pattern seen in Fig. 8.1(f) is represented by the dotted red curve. The time axis is measured in a reference frame moving with the boundary such that  $t = T - z/v_B$ . (d) The dispersion curves for  $t < 0$  (solid blue curve) and  $t > 0$  (dashed red curve). The shaded region shows the spectral extent of the input pulse and the corresponding range of  $\beta'$ . Note that only frequencies  $\nu - \nu_0 > 0$  will interact with the boundary and be reflected.

where we have assumed that the TIR condition is satisfied. The factor  $Q$  is given by

$$Q = \frac{2\beta_B}{\beta_2(\Delta\omega_i)^2}. \quad (8.18)$$

In the following discussion we focus only on the phase of the reflection coefficient since that is what determines the timing of the interference fringes. Note that when the TIR condition is satisfied, the magnitude of the reflection coefficient is unity ( $|r|^2 = 1$ ), as expected. Interestingly, the magnitude of the transmission coefficient is non-zero as  $|t| = 2/\sqrt{Q}$ . This is because the transmission coefficient does not account for the compression caused by the change group velocity. This compression factor is also frequency dependent as seen in Sect. 6.2, which makes it difficult to find an analytic solution to the transmitted

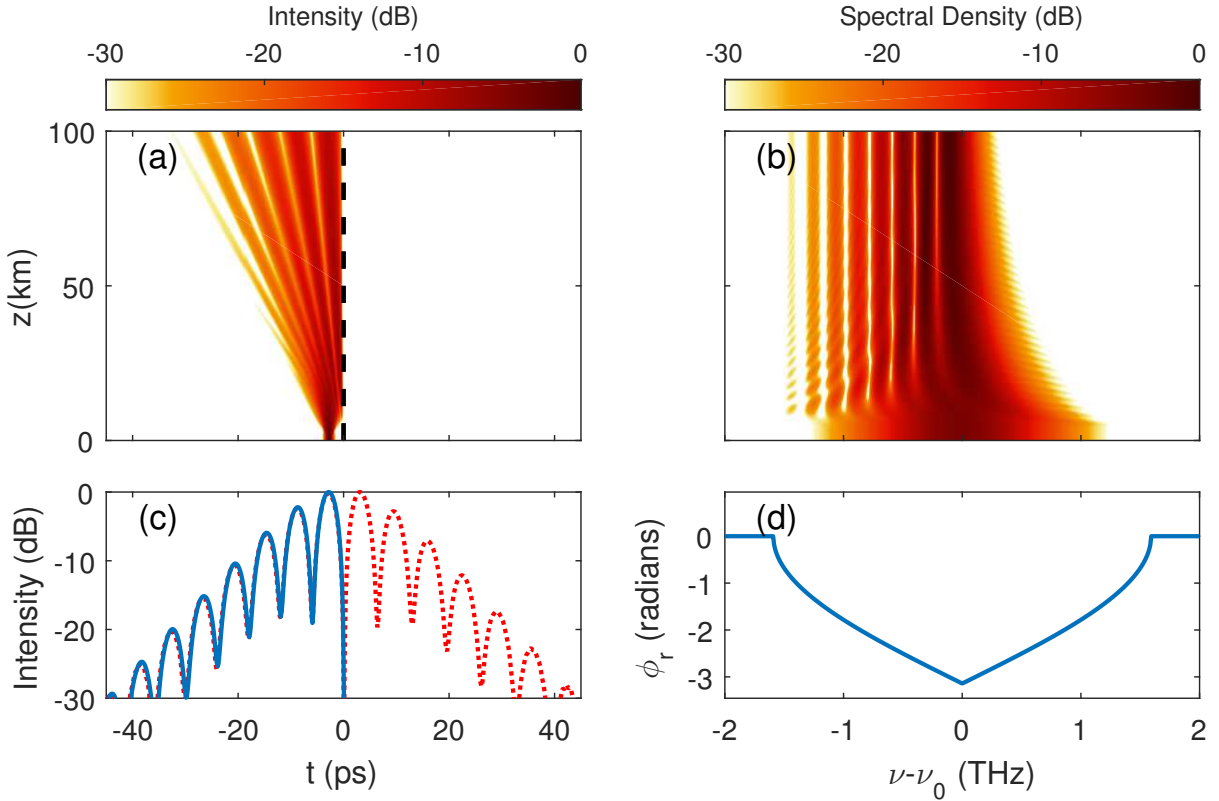


Figure 8.3: Evolution of the (a) shape and (b) spectrum of the single sech-shaped pulse propagating with the moving refractive-index boundary. (c) Output pulse shapes in the cases of a single pulse (solid blue curve) and two pulses (dotted red curve). The two fringe patterns match when the frequency-dependent phase shift  $\phi_r$  is applied to the second pulse. The time axis is measured in a reference frame moving with the boundary such that  $t = T - z/v_B$ . (d) Total internal reflection phase shift plotted as a function of frequency.

pulse shape. For now, we will ignore the transmission coefficient because we are working under the TIR condition where it is unimportant.

From Eq. (8.17) we obtain the following analytic expression for the phase shift,  $\phi_r$ , imparted to the reflected pulse during TIR:

$$\phi_r = -2 \tan^{-1}(\sqrt{Q-1}). \quad (8.19)$$

Figure 8.3(a) shows a plot of  $\phi_r$  versus  $\nu = \omega/2\pi$  for the same parameters used in Fig. 8.2. We see that the phase varies over the pulse spectrum as expected, starting at  $\phi_r = -\pi$  near  $\nu = \nu_0$  and going to zero when  $|\nu - \nu_0| = 1.42$  THz. This is analogous to the phase behavior for the traditional TIR. We can verify that the analytical prediction agrees with our numerical simulations using the double-slit analogy with a virtual reflected pulse. Figure 8.3(b) shows the output pulse shape for the reflected pulse (solid blue curve), and the dotted red curve shows the output for two interfering pulses when the reflection phase from Eq. (8.19) is applied to the second pulse. As the figure shows, the

two sets of fringes overlap perfectly for  $t < 0$ , indicating that the phase shift predicted by Eq. (8.19) is correct. The fringes for  $t > 0$  do not exist in the TIR case because both the reflected and initial pulses are trapped in the  $t < 0$  region.

Interference of a reflected pulse with the unreflected parts of the initial pulse has been previously seen in a numerical study devoted to propagation of solitons inside a dispersive nonlinear medium [133]. In this study, a dispersive wave reflected off of a temporal soliton. The effect was incorrectly attributed to scattering of the dispersive wave from the soliton, rather than an interference pattern formed by the initial pulse and the temporally reflected pulse.

### 8.3 Self-imaging in a Temporal Waveguide

In this section we add a second temporal boundary such that the input pulse is located between the two boundaries, forming a temporal waveguide [31, 129, 141]. In this configuration, multiple reflections occur through successive TIR at the two boundaries, and we expect that infinitely many virtual pulses will interfere with the original pulse, rather than just one. This situation is analogous to the Talbot effect, and the temporal Talbot effect has been known for many years [151]. When a train of pulses is launched into a dispersive medium, the pulses will self-image at multiples of the temporal Talbot distance  $z_T = T_s^2 / (2\pi\beta_2)$ , where  $T_s$  is the separation between adjacent pulses. Some changes are also expected, since unlike the traditional Talbot effect where all fields are in-phase, the waveguide produces a phase shift of approximately  $\pi$  between adjacent pulses.

As an example of the temporal Talbot effect, Fig. 8.4 shows the evolution of a train of 40 pulses separated by  $T_s = 5$  ps. Each pulse has a duration  $T_0 = 0.2$  ps, and adjacent pulses differ in phase by  $\pi$ . As the pulses overlap in time, they quickly interfere and briefly form fringes that eventually form distinct pulses at a higher repetition rate. At a distance  $z = z_T = 79.6$  m, the pulses return to their original shape and the process repeats itself. Note that unlike the traditional Talbot effect where the original pulse train re-forms twice in a given cycle, the pulse train in Fig. 8.4 re-forms only once before the process repeats. This is a result of the  $\pi$ -phase shift, which prevents self-imaging halfway from the full cycle.

Figure 8.5 shows the evolution of the (a) shape and (b) spectrum of a single sech-shaped pulse ( $T_0 = 0.2$  ps) propagating through a dispersive medium ( $\beta_2 = 0.05$  ps<sup>2</sup>/m) when it is confined to a 5-ps-wide temporal window formed by two refractive-index boundaries with  $\beta_B = 5$  m<sup>-1</sup>. In Fig. 8.5(a) we see that the pulse quickly broadens to fill the entire waveguide and begins to interfere with the reflecting pulses formed at the two edges through TIR. Multiple reflections lead to a more-complicated interference pattern that begins to form progressively fewer pulses at specific distances until two pulses are formed at a distance of about 42 m. This process reverses itself, and a single pulse is reformed at  $z = 85$  m (self-imaging). Figure 8.5(b) shows that the reflected frequencies overlap with the initial pulse spectrum, causing a spectral interference pattern that changes during propagation. Eventually the spectrum returns to its original shape at the same distance where the pulse is self-imaged. For longer propagation lengths, the whole process repeats itself periodically, just as required by the Talbot effect.

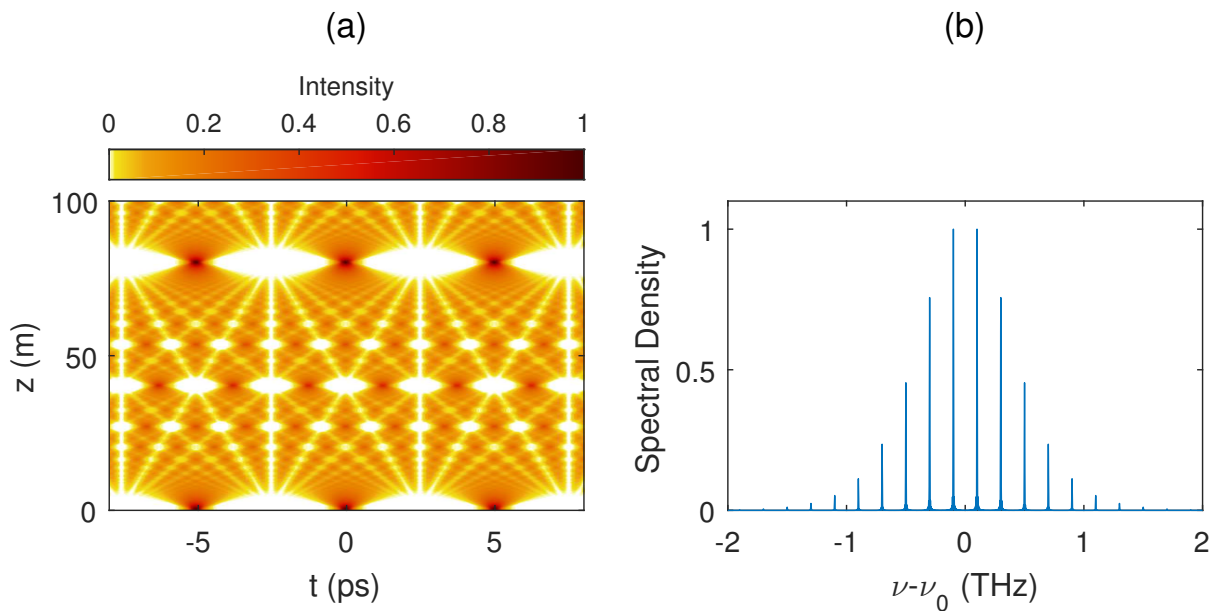


Figure 8.4: (a) Evolution of the pulse shape for a train of 40 sech-shaped pulses ( $T_0 = 0.2$  ps) with an initial separation of 5 ps. Adjacent pulses differ in phase by  $\pi$ . (b) The input pulse spectrum for the total pulse train

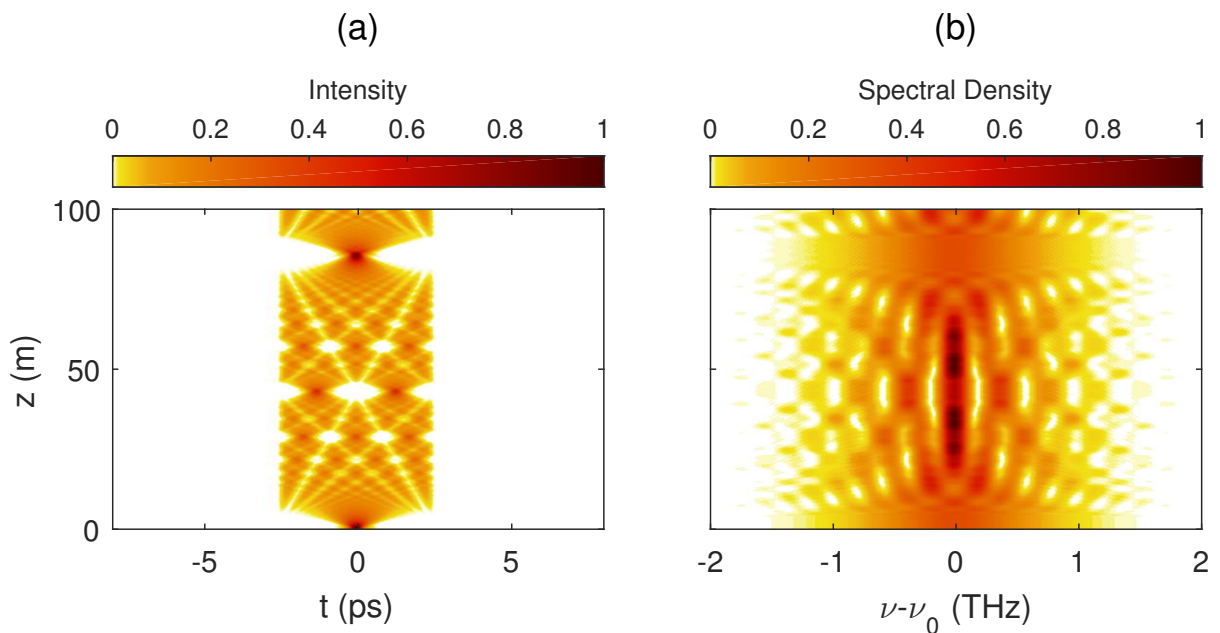


Figure 8.5: Evolution of the (a) shape and (b) spectrum of a sech-shaped pulse ( $T_0 = 0.2$  ps) confined to a 5-ps window through two temporal boundaries.

Although the pulse evolution in Fig. 8.5 is very similar to that in Fig. 8.4, the two are not identical. In particular, the distance over which the pulse is re-imaged is slightly longer in the single-pulse case. This is again related to the fact that TIR does not produce a precise phase shift of  $\pi$  across the entire pulse spectrum. As we saw in Eq. (8.19), the

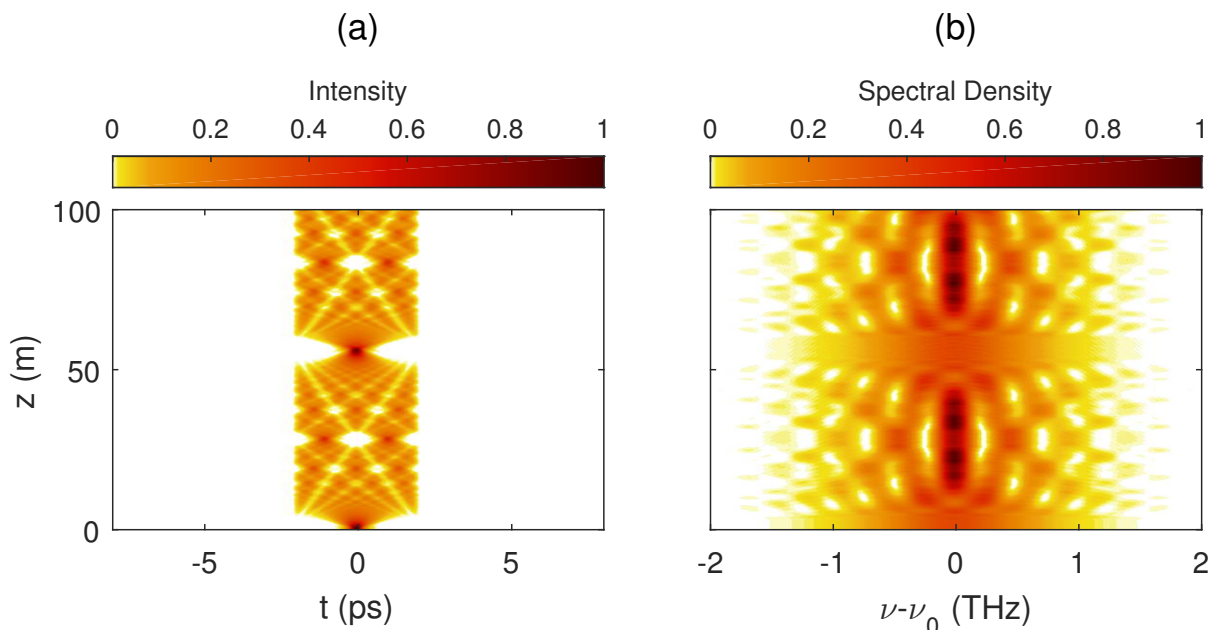


Figure 8.6: Evolution of the (a) shape and (b) spectrum of a sech-shaped pulse ( $T_0 = 0.2$  ps) confined to a 4-ps window through two temporal boundaries.

TIR-induced phase shift is frequency dependent. In Sec. 8.2, this frequency-dependent phase shift led to a slightly different interference pattern. If we perform the simulation in Fig. 8.4 again but apply the phase shift in Eq. (8.19), we find that the pattern matches perfectly the one shown in Fig. 8.5(a). Finally, we note that self-imaging in Fig. 8.5 is not perfect, with the re-formed pulse being slightly different from the original. By increasing value of  $\beta_B$ , however, the difference between the original and re-formed pulses can be reduced, resulting in nearly perfect self-imaging. This makes sense because the larger the value of  $\beta_B$ , the closer the reflection phase shift in Eq. (8.19) to  $\pi$  over the entire bandwidth of the optical pulse.

One may ask what affect the width of the waveguide has upon the self-imaging distance. Based on the temporal Talbot distance, we expect the self-imaging to occur much more quickly when the waveguide width is reduced. This is also the expected behavior based on self-imaging within traditional waveguides. Figure 8.6 shows the same simulation as Fig. 8.5 but with a 4-ps wide waveguide. As expected, the pulse is still re-imaged within the waveguide but at a much shorter distance of  $z = 56$  m. This differs even more from the predicted distance of  $z_T = 50.9$  m for a Talbot effect with  $\pi$  phase shifts. This discrepancy is caused by the temporal analog of the Goos-Hänchen shift [152], which causes an effective waveguide width of

$$T_{eff} = T_s + \frac{2\sqrt{2}}{\Omega_1}, \quad (8.20)$$

where  $\Omega_1$  is the waveguide parameter found in Chapter 7. For the fundamental mode of the waveguide in Fig. 8.6,  $\Omega_1=14.12$  THz, giving an effective waveguide width of

$T_{eff} = 4.2$  ps. We can now use this effective waveguide width to find the temporal Talbot distance to be  $z_T = 56.1$  m, which is much closer to the observed self imaging distance.

## 8.4 Conclusions

We have shown, both numerically and analytically, that temporal reflections from a moving refractive-index boundary act as an analog of Lloyd's mirror, allowing a single pulse to produce interference fringes in time as it propagates inside a dispersive medium with a temporal boundary across which the refractive index of medium changes. Our numerical simulations show that the pulse spectrum also develops a multi-peak structure in this situation. By comparing the temporal fringe pattern to that formed through two-pulse interference, we show that temporal reflection produces a frequency-dependent phase shift that varies between 0 and  $\pi$ . We used the boundary conditions across the temporal boundary to derive an explicit expression for the amplitude reflection coefficient when TIR occurs and found the frequency-dependent phase shift given in Eq. (8.19). Applying this phase shift to a virtual second pulse produces the same interference pattern as the pulse reflecting from the temporal boundary. This matches the behavior of traditional reflection, where the reflection can be interpreted as coming from a virtual source.

We also discussed the self-imaging occurring when a second temporal boundary is added, forming a temporal waveguide that confines an optical pulse inside it. In this case, a single pulse experiences multiple reflected pulses that interfere and form a complex fringe pattern before eventually forming an image of the original pulse. This self-imaging effect is also seen in spatial planar waveguides and is similar to the temporal Talbot effect [151], which requires interference from an infinite train of pulses. Although the re-imaging is not exact in general, increasing the refractive-index change across the boundary causes the re-imaged pulse to more closely match the shape of the initial pulse. This arrangement could be used to selectively convert a single pulse into two or more pulses, with the number of pulses set by the length of the dispersive medium.

An experimental realization of this effect would be of great interest. One approach would involve using a pump-probe configuration, where the pump produces the moving refractive index boundaries through cross-phase modulation. While our current discussion did not include the effects of third-order dispersion, our previous work has shown that higher-order dispersion can be largely ignored by working far from the zero-dispersion wavelength [153]. Working near the zero-dispersion wavelength could allow for even more interesting interference patterns, as multiple reflections can occur from a single boundary.

## Chapter 9

# Higher-Order Dispersion Effects

As discussed in Chapter 6, an essential gradient for temporal reflection to occur is the group-velocity dispersion of the medium in which an optical pulse approaches the temporal boundary [150]. However, the effects of higher-order dispersion have attracted little attention, apart from how it can shift the frequency of the reflected and refracted pulses. Since most practical media are likely to exhibit higher-order dispersive effects, in this chapter I describe how they can lead to the formation of multiple pulses with widely separated spectral bands at a single temporal boundary.

The chapter is organized as follows. In Sect. 9.1, I review the case where higher-order dispersion can be ignored in order to establish the general conventions that will be used when the higher-order terms are introduced. In Sect. 9.2 I focus on the effects of third-order dispersion to illustrate how the entire dispersion curve affects the reflected and transmitted frequencies. I then briefly discuss the impact of even higher-order dispersion terms in Sect. 9.3. The effect of higher-order dispersion on temporal waveguides is discussed in Sect. 9.4. The main results are summarized in Sect. 9.5.

### 9.1 Temporal Reflection and Refraction

As usual, we expand  $\beta(\omega)$  around a reference frequency  $\omega_0$  in a Taylor series. For now, we include only up to the GVD effects and neglect the higher-order dispersion terms. Working in the retarded time frame, the dispersion relation then becomes [150]

$$\beta'(\omega) = \beta_0 + \Delta\beta_1(\omega - \omega_0) + \frac{\beta_2}{2}(\omega - \omega_0)^2 + \beta_B(t). \quad (9.1)$$

where  $\beta_B(t) = k_0\Delta n(t)$  is the change in the propagation constant caused by the time-dependent index change  $\Delta n(t)$ , which we assume takes the form of a step function. Recall that  $\Delta\beta_1 = \beta_1 - 1/v_B$  is a measure of the relative speed of pulse's frequency component  $\omega$  relative to the boundary. We can further simplify our discussion by choosing our reference frequency such that the group velocity at that frequency matches the speed of the temporal boundary. In this case  $\Delta\beta_1 = 0$ , and the dispersion relation becomes

$$\beta'(\Delta\omega) = \beta_0 + \frac{\beta_2}{2}\Delta\omega^2 + \beta_B(t), \quad (9.2)$$

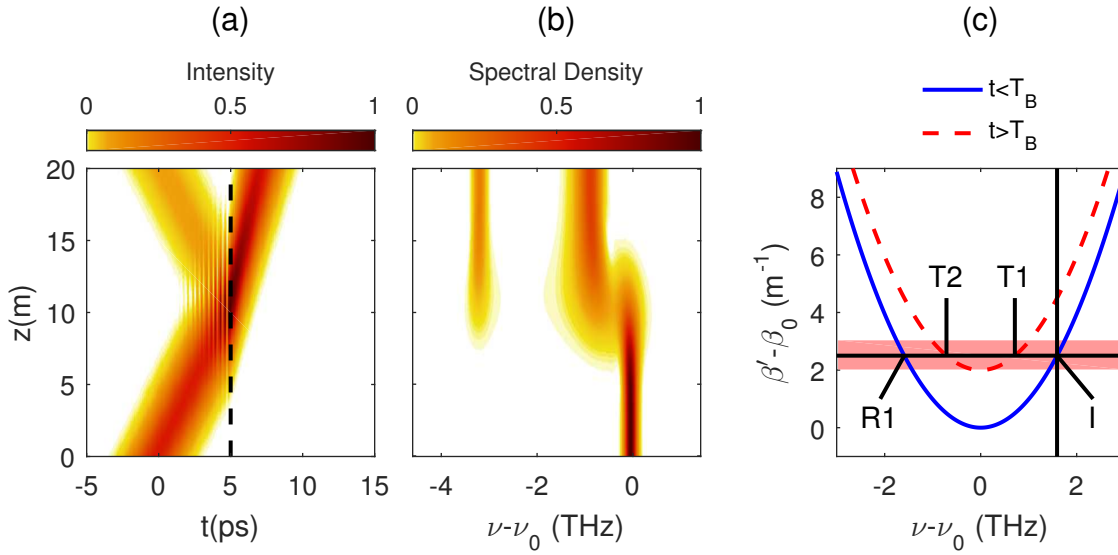


Figure 9.1: Evolution of (a) intensity and (b) spectrum as a Gaussian pulse crosses a temporal boundary (dashed black line) with  $\beta_B = 2 \text{ m}^{-1}$ . The time axis is measured in a reference frame moving with the boundary such that  $t = T - z/v_B$ . (c) Dispersion curves for  $t < T_B$  (solid blue) and  $t > T_B$  (dashed red).

where  $\Delta\omega$  is the frequency offset from the new reference frequency ( $\omega_c$ ). This method of using a reference frequency whose group velocity matches the boundary velocity will become important for higher-order dispersion, where the DGD term,  $\Delta\beta_1$ , no longer specifies a single on the dispersion curve. Furthermore, this convention allows us to shift along the same dispersion curve without having to change the values of  $\beta_m$ .

As in Chapter 6, we obtain the time-domain equation:

$$\frac{\partial A}{\partial z} + \frac{i\beta_2}{2} \frac{\partial^2 A}{\partial t^2} = i\beta_B(t)A, \quad (9.3)$$

and solve Eq. (9.3) numerically using the standard split-step Fourier method [33]. The temporal and spectral evolutions of a Gaussian pulse whose carrier frequency is shifted from  $\omega_c$  by  $\Delta\omega_i$  is shown in Fig. 9.1 using the input field in the form

$$A(0, t) = \exp[-t^2/(2T_0^2)] \exp(i\Delta\omega_i t), \quad (9.4)$$

with the parameter values  $T_0 = 1.5 \text{ ps}$ ,  $T_B = 5 \text{ ps}$ ,  $\Delta\omega_i = 10^{13} \text{ s}^{-1}$ ,  $\beta_2 = 0.05 \text{ ps}^2/\text{m}$ , and  $\beta_B = 2 \text{ m}^{-1}$ . The linear phase term in Eq. (9.4) shifts the frequency of the pulse by  $\Delta\omega_i$  without changing the shape of the pulse or spectrum.

The spectral evolution in Fig. 9.1(b) shows the same behavior seen in Chapter 6, with the spectrum shifting to lower frequencies and splitting into two distinct spectral bands that travel at different speeds. These shifts are caused by conservation of momentum in the moving frame. Mathematically, momentum is conserved by finding solutions to

$$\beta'(\Delta\omega, t) = \beta'(\Delta\omega_i, t = 0), \quad (9.5)$$

where the right side is the propagation constant of the initial pulse at  $(z = 0, t = 0)$  for  $\Delta\omega_i$ . Figure 9.1(c) shows a plot of the dispersion curve for  $t < T_B$  in solid blue and for  $t > T_B$  in dashed red. As marked in Fig. 9.1(c), I corresponds to the initial pulse frequency, R1 is the reflected pulse frequency, and T1 is the transmitted pulse frequency. The solution T2 to Eq. 9.5 on the transmitted curve is not a valid solution because the relative group velocity at that frequency would not carry the transmitted pulse across the boundary into the  $t > T_B$  region [150]. We can understand this by considering when the transmitted pulses forms at  $t = T_B$ . At this point, a negative relative group velocity, such as at point T2, would propagate into the  $t < T_B$  region, which corresponds to the solid blue curve in Fig. 9.1(c). However, the point T2 is only a solution in the  $t > T_B$  region, represented by the dashed red curve. Therefore, if T2 were to form it would immediately violate conservation of momentum by moving into the wrong medium. This requirement that the sign of the relative group velocity must take the pulse into the correct temporal region is referred to as the group-velocity restriction. Points that do not satisfy the group-velocity restriction will be unmarked in the rest of the figures in this chapter.

We solve Eq. (9.5) to find analytic expressions for the reflected and transmitted frequencies as

$$\Delta\omega_r = -\Delta\omega_i, \quad (9.6)$$

$$\Delta\omega_t = \Delta\omega_i \sqrt{1 - \frac{2\beta_B}{\beta_2 \Delta\omega_i}}, \quad (9.7)$$

As before, TIR occurs when there is no real-valued solution to Eq. (9.5).

We can now establish the important rules about space-time reflection and refraction. First, the possible frequencies for the reflected and transmitted pulses are determined by finding solutions to Eq. (9.5) for times before and after the boundary. Second, not all of these solutions will be valid, and so we must impose the group-velocity restriction, which requires that any valid frequency should have a group velocity that carries the pulse into the correct temporal region. That is, the reflected pulses propagate in the initial refractive index, and the transmitted pulses propagate in the new refractive index. Finally, if there are no valid solutions to Eq. (9.5) for either  $t > T_B$  or  $t < T_B$ , then no frequency can propagate in that region. When this happens on the transmitted frequency side, this leads to TIR.

## 9.2 Third-order Dispersion Effects

We now consider the case where the effects of third-order dispersion (TOD) are large enough that we can no longer ignore it in the Taylor expansion of  $\beta(\omega)$ . The dispersion relation then becomes

$$\beta'(\Delta\omega) = \beta_0 + \frac{\beta_2}{2}\Delta\omega^2 + \frac{\beta_3}{6}\Delta\omega^3 + \beta_B(t), \quad (9.8)$$

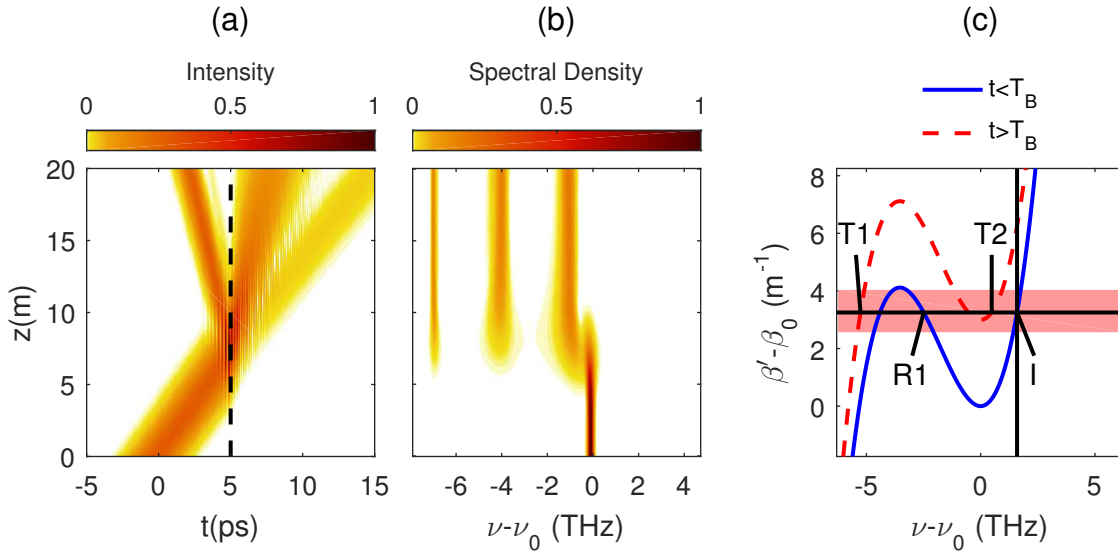


Figure 9.2: (a) and (b) Same as Fig. 9.1 except that TOD is included. The presence of TOD allows for two transmitted frequencies. The time axis is measured in a reference frame moving with the boundary such that  $t = T - z/v_B$ . (c) Dispersion curves for  $t < T_B$  (solid blue) and  $t > T_B$  (dashed red).

where  $\beta_3$  governs TOD, and we again use a reference frequency with a group velocity that matches the speed of the temporal boundary.

As before, when the pulse crosses the temporal boundary it shifts its frequency such that the momentum is conserved in the moving frame. To find these frequencies, we seek solutions to Eq. (9.5) and apply the group-velocity restriction. However, we now use Eq. (9.8) for the dispersion relation, which allows for up to three solutions for both the reflected ( $t < T_B$ ) and transmitted ( $t > T_B$ ) curves. Although the roots of a cubic polynomial are well known, in general they do not lead to simple relations such as those given in Eqs. (9.6) and (9.7). Moreover, there can be at most two reflected or two transmitted frequencies because of the group-velocity restriction (slope of the dispersion curve). This is because the cubic polynomial has two regions that have a slope of one sign, and one region between these two that has a slope of the opposite sign.

We first examine the case where two transmitted pulses can form, as shown in Fig. 9.2. For this simulation, we used the same parameters as in Fig. 9.1, but chose  $\beta_3 = 4.5$  ps<sup>3</sup>/km and  $\beta_B = 3$  m<sup>-1</sup> to clearly resolve all pulses that form while crossing the temporal boundary. We see the incident pulse split into three pulses, forming one reflected pulse and two transmitted pulses. The two transmitted pulses travel at different speeds, separating as they travel further through the material.

Figure 9.2(b) shows that reflection and refraction are once again accompanied by shifting and splitting of the spectrum, but the spectrum now splits into three distinct spectral bands. Examining the dispersion curves in Fig. 9.2(c) we see that the two transmitted pulses correspond to bands centered (T1) at  $-5.3$  THz and (T2) at  $0.48$  THz, and the reflected pulse corresponds to the middle frequency (R1) at  $-2.5$  THz. The new transmitted pulse (T1) forms because the TOD term bends the dispersion curve back

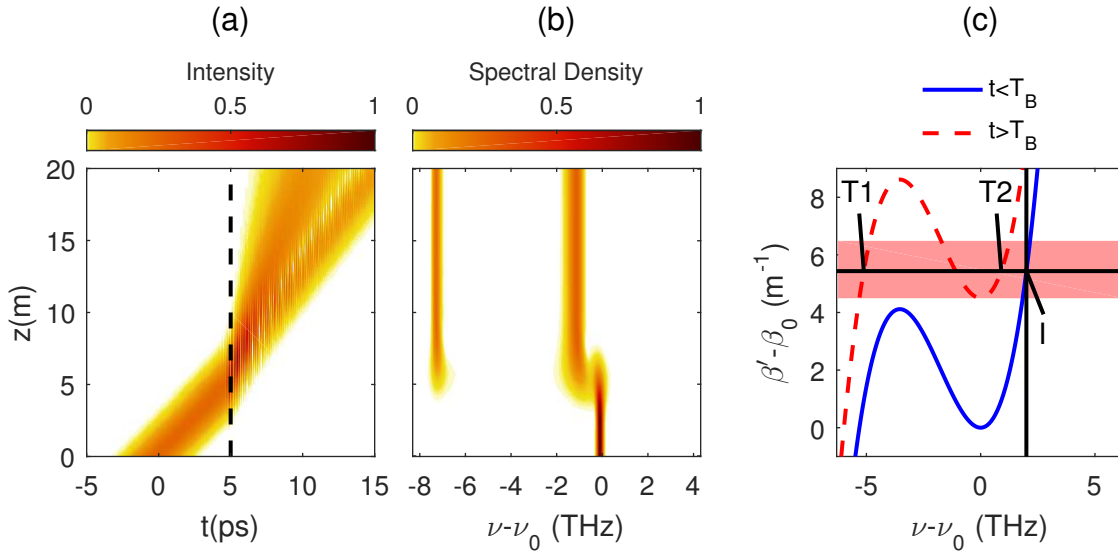


Figure 9.3: (a) and (b) Same as Fig. 2 but the initial frequency shift has been increased to  $\Delta\omega_i/(2\pi) = 2$  THz. The time axis is measured in a reference frame moving with the boundary such that  $t = T - z/v_B$ . (c) Dispersion curves for  $t < T_B$  (solid blue) and  $t > T_B$  (dashed red).

toward the initial value, creating two regions where the group-velocity restriction can be satisfied. We emphasize that both T1 or T2 are always present regardless of how large  $\beta_B$  becomes or what sign it takes. Therefore, in this case temporal TIR cannot occur. However, if the magnitude of  $\beta_B$  is large, the amount of energy transferred to the transmitted pulse is very small, and the pulse is almost entirely reflected.

Examining the dispersion curve in Fig. 9.2(c), we see that if the initial pulse frequency were shifted further to the right there would eventually be no solution for the reflected pulse on the incident curve (solid blue) that satisfies momentum conservation. This situation is similar to the Brewster angle in the case of a spatial boundary. Figure 9.3 shows a simulation where we have kept all of the parameters the same as in Fig. 9.2, but increased the initial frequency shift to  $\Delta\omega_i/(2\pi) = 2$  THz and the index shift at the boundary to  $\beta_B = 4$  m<sup>-1</sup>. As Fig. 9.3(a) and Fig.9.3(b) show, no reflected pulse is formed in this case since there is no valid solution in Fig. 9.3(c) on the blue curve where momentum conservation can be satisfied. Therefore, all of the pulse energy must be transferred to the transmitted frequencies, T1 and T2. If the magnitude of  $\beta_B$  were to be increased further, the root T2 would eventually no longer exist, and all of the pulse energy would be transferred to a single transmitted pulse at T1. If the sign of  $\beta_B$  were changed, the same situation would occur, but the initial pulse energy would be entirely transferred to point T2. The main point to note is that the presence of TOD modifies the dispersion curve so much that many novel and interesting scenarios can occur at a temporal boundary.

Another interesting case occurs when the initial pulse spectrum is located in the middle section of the dispersion curve, where the slope has the opposite sign from the two outer regions of the dispersion curve. In this configuration, we expect to see two

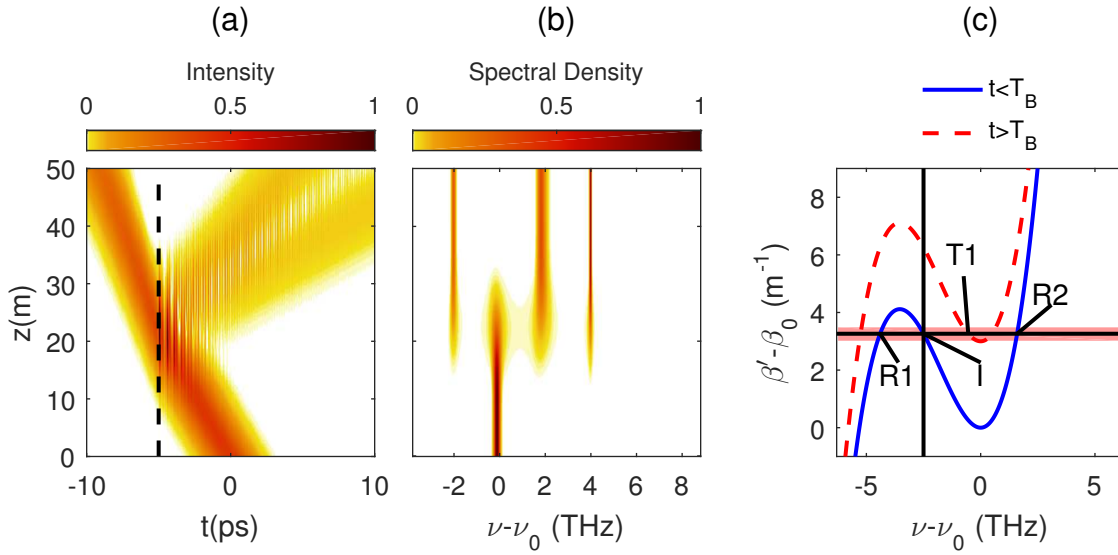


Figure 9.4: Evolution of (a) intensity and (b) spectrum for a Gaussian pulse in the presence of a temporal boundary (dashed black line) for  $\beta_B = 3 \text{ m}^{-1}$  and  $\Delta\omega_i/(2\pi) = -2.5 \text{ THz}$ . (c) Dispersion curves for  $t < T_B$  (solid blue) and  $t > T_B$  (dashed red).

reflected frequencies that satisfy both conservation of momentum and the group-velocity requirement. Figure 9.4 shows this situation using the same Gaussian pulse used in Fig. 9.2, but with an initial frequency shift of  $\Delta\omega_i/(2\pi) = -2.5 \text{ THz}$ . This frequency shift was chosen to match point (R1) in Fig. 9.2. Because the sign of the relative group velocity has changed (the dispersion slope is negative instead of positive), the pulse will move toward negative times. Recall that because we are in a reference frame moving with the boundary, this only means that the pulse is moving faster than the boundary. To account for this change in relative velocity, the temporal boundary must be moved to  $T_B = -5 \text{ ps}$  with the shift of  $\beta_B$  occurring for  $t < -5 \text{ ps}$  so that the optical pulse would still cross the same boundary. In Fig. 9.4(a), the optical pulse crosses the boundary and once again splits into three pulses. This time only one pulse is transmitted, while two pulses are reflected with different speeds. Figures 9.4(b) and 9.4(c) show that this corresponds to three spectral bands at points R1 and R2 for the reflected pulses, and the point T1 for the transmitted pulse.

Unlike Figs. 9.2 and 9.3, the process in Fig. 9.4 allows for temporal TIR. Indeed, if the magnitude of  $\beta_B$  is increased, there will no longer be any T1 point that satisfies momentum conservation. More interestingly, the TIR condition can be reached even if  $\beta_B$  has the opposite sign, which would shift the dispersion curve down. This is different from the case where TOD is not present, and the TIR condition can only be met using a particular sign for  $\beta_B$  because there is a single global minimum ( $\beta_2 > 0$ ) or maximum ( $\beta_2 < 0$ ), rather than the two extrema present with TOD. Figure 9.5 shows this behavior for the same dispersive parameters as Fig. 9.4, but with [(a)–(c)]  $\beta_B = 4 \text{ m}^{-1}$  and [(d)–(f)]  $\beta_B = -4 \text{ m}^{-1}$ . In both cases, the frequencies of R1 and R2 remain the same for both positive and negative  $\beta_B$ . However, the amount of energy transferred to R1 or R2 is highly affected by the sign of  $\beta_B$ . When  $\beta_B$  is negative, more energy is transferred to

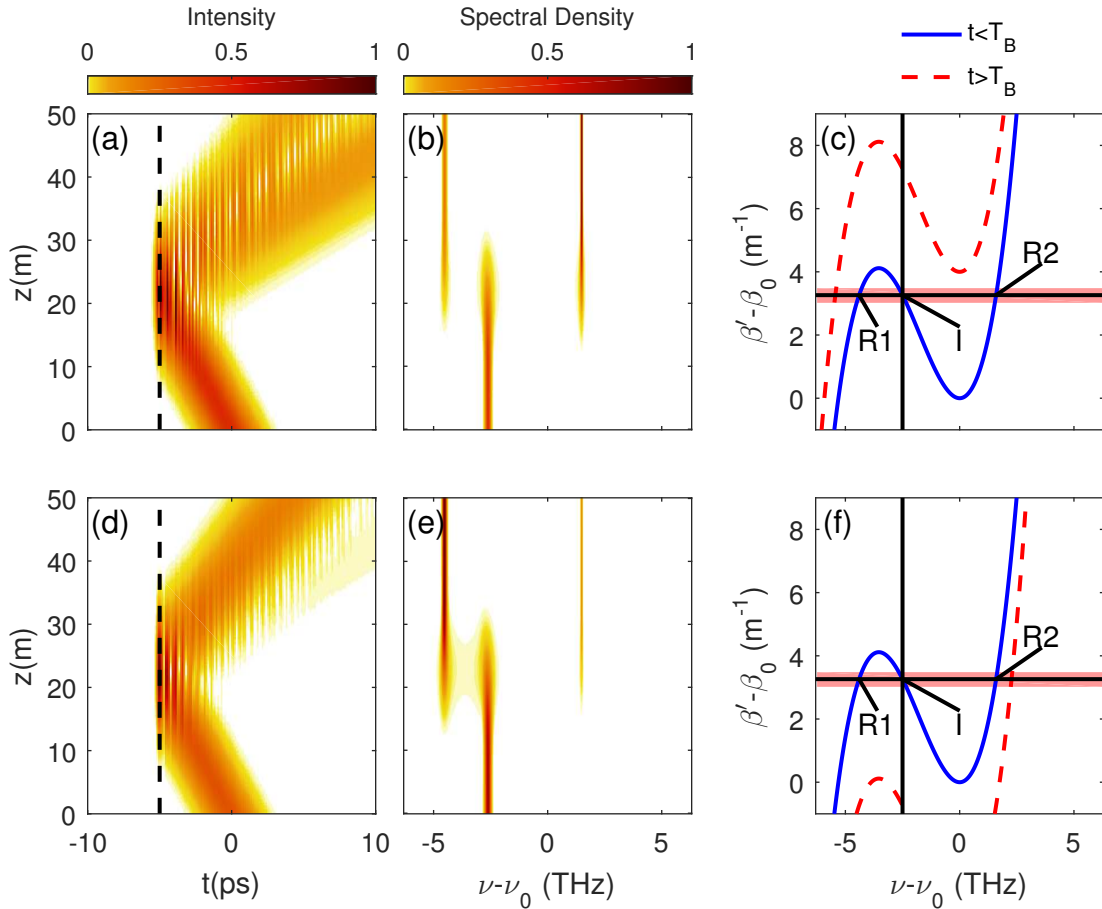


Figure 9.5: Evolution of [(a),(d)] intensity and [(b),(e)] spectrum for a Gaussian pulse in the presence of a temporal boundary (dashed black line) for  $\Delta\omega_i/(2\pi) = -2.5$  THz. [(c),(f)] Dispersion curves for  $t < T_B$  (solid blue) and  $t > T_B$  (dashed red). The shift of the dispersion curve is (top)  $\beta_B = 4.0 \text{ m}^{-1}$ , and (bottom)  $\beta_B = -4.0 \text{ m}^{-1}$ .

the frequency R1, which is closer to the incident frequency. However, simply by changing the sign of the refractive index change, more energy is transferred to R2. If we make the value of  $\beta_B$  very large and negative, the energies transferred to R1 and R2 begin to equalize. Unfortunately, we can not use the same method to solve for the reflection and transmission coefficients from Sect. 8.2 as there are still only two boundary conditions, but now three fields for which to solve. An analytic solution to this problem is of great interest, and will be explored in future works.

Finally, the spectrum of the reflected pulse narrows or broadens depending on where the input pulse lies on the dispersion curve. As we saw in Chapter 6, this occurs because a pulse contains a range of frequencies, and the dispersion relation must be conserved at each of these frequencies. For a given input frequency, the range of values the dispersion relation ( $\beta'$ ) can take depends on the slope of the dispersion curve. For a fixed input pulse spectrum, a higher dispersion slope will cover a wider range of  $\beta'$  values. Therefore, if the slope of the dispersion curve is larger at the input frequency than at the reflected frequency, the reflected pulse will have a wider spectrum, as in Fig. 9.2. However, if

the opposite is true, as in Fig. 9.4, the spectrum of the reflected pulse will be narrower. We can approximate the spectral broadening or compression in the same way we did in Sect. 6.1, by first finding the frequencies as detailed above, and then taking the ratio of the dispersion slopes. This approximation will still break down as either the initial or transmitted pulse bandwidths become large, but provides a useful way to predict the spectral behavior.

### 9.3 Higher-order Dispersion Effects

If we continue to increase the number of dispersion terms in the Taylor expansion in Eq. (1), the number of possible solutions to Eq. (9.5) will increase for both the reflected and transmitted curves. As with the TOD simulations, not every solution to Eq. (9.5) is permitted because of the group-velocity restriction. However, based on conservation of momentum and the group-velocity restriction, we can find the maximum number of reflected, transmitted, and total pulses that can form as the pulse crosses the boundary.

Figure 9.6 shows dispersion curves with  $\beta_B = 0.5$  ps/m,  $\beta_2 = -0.4$  ps<sup>2</sup>/m,  $\beta_4 = 4 \times 10^{-4}$  ps<sup>4</sup>/km, and [(a),(d)] no more higher-order terms, [(b),(e)]  $\beta_5 = 7 \times 10^{-6}$  ps<sup>5</sup>/km, and [(c),(f)]  $\beta_6 = 2.5 \times 10^{-7}$  ps<sup>6</sup>/km for two different initial frequencies. The  $\beta_2$  and  $\beta_4$  terms were chosen to match a commercially available photonic crystal fiber. The values for  $\beta_5$  and  $\beta_6$  do not correspond to this same fiber, but were chosen such that all roots exist over the spectral region to better illustrate the effect of higher order dispersion. We see that the maximum number of pulses that can form at the temporal boundary is equal to the order of the polynomial. Explicitly, this means that  $\beta_4$  generates up to four pulses,  $\beta_5$  up to five pulses, and  $\beta_6$  up to six pulses. This makes sense because transmitted pulses will form at solutions to Eq. (9.5) that have a slope matching the sign of the input frequency, while the reflected pulses will form at the solutions with a slope of the opposite sign.

The number of either reflected or transmitted pulses depends not only on the number of dispersion terms but also on where the input pulse spectrum is located. In the case of even-order dispersion, half of the solutions represent reflected pulses and the other half transmitted pulses. The situation becomes more complex when the last term is odd. For example, when terms up to  $\beta_5$  are included, five pulses are formed at the boundary. As seen in Fig. 9.6, three of them are transmitted when  $\Delta\omega_i > 0$  but three of them are reflected when  $\Delta\omega_i < 0$ . Similar to the TOD case, this occurs because the fifth-order dispersion curve has three regions with a slope of one sign, and only two regions with a slope of the opposite sign. Note that these are all upper limits to the number of reflected and transmitted pulses. If different dispersion parameters, initial frequencies, or  $\beta_B$  values are chosen, the number of pulses formed can decrease. We emphasize that even-order dispersion always allows for TIR to occur, regardless of the location of the initial pulse spectrum. This makes sense because even order polynomials have either a global maximum or a global minimum.

To verify that the process holds for higher order dispersion, Fig. 9.7 shows reflection and refraction of a pulse for the same dispersion parameters used in Fig. 9.6(a). The pulse duration was reduced to  $T_0 = 0.25$  ps so that the spectral lines would be wide enough to

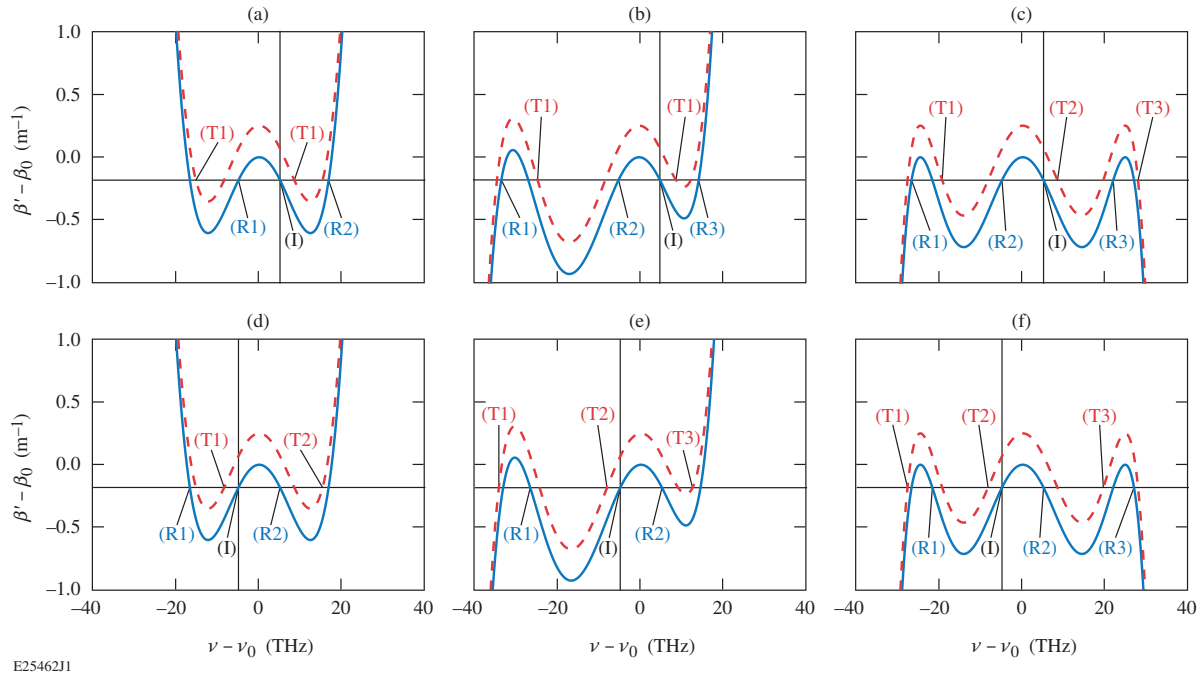


Figure 9.6: Example dispersion curves for  $t < T_B$  (solid blue) and  $t > T_B$  (dashed red) when the highest-order dispersion term is [(a),(d)]  $\beta_4$ , [(b),(e)]  $\beta_5$ , and [(c),(f)]  $\beta_6$ . The top row shows an initial frequency with a positive slope, and the bottom row shows an initial frequency with a negative slope. Note that the reflected and transmitted frequencies shift to points with the opposite relative group velocity between the top and bottom rows in order to satisfy the group velocity condition.

observe, and the boundary time was reduced to  $T_B = 0.75$  ps so that pulse would cross the boundary at a shorter distance. The total propagation distance was kept at 300 m so the individual pulses could separate in time. The intensity and spectral density are shown on a logarithmic scale to more clearly see the much weaker pulses formed at R1 and T2. Figure 9.7(a) shows that the pulse clearly breaks up into four distinct pulses that travel at different speeds, as predicted. The new frequencies generated in Fig. 9.7(b) match the points R1, R2, T1, and T2 as shown in Fig. 9.7(c).

## 9.4 Temporal Waveguides

As we saw in Chapter 7 if an optical pulse is placed between two temporal boundaries, the pulse can be trapped between the two boundaries, forming a temporal analog of an optical waveguide [31]. When higher-order dispersion is negligible, these waveguides behave like spatial planar waveguides, including having a finite number of supported modes. In this section we consider the effects of higher-order dispersion on temporal waveguides. Here we focus on the effects of TOD only since this is the most dominant term in practice. The new features that arise in this case are also expected to occur when fourth- or fifth-order dispersion terms are included.

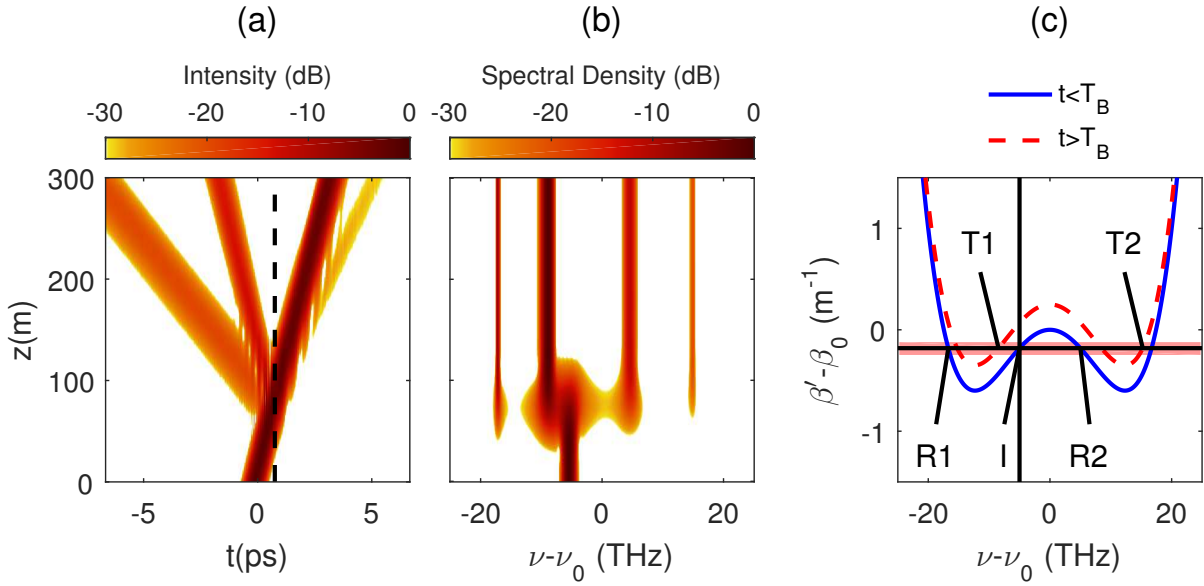


Figure 9.7: Evolution of (a) intensity and (b) spectrum for a Gaussian pulse in the presence of a temporal boundary (dashed black line) for the same dispersion parameters as Fig. 9.6(a). (c) Dispersion curves for  $t < T_B$  (solid blue) and  $t > T_B$  (dashed red).

Figure 9.8 shows the propagation of a Gaussian pulse with  $T_0 = 2$  ps under conditions of Fig. 9.4 except that we now have two temporal boundaries located at  $t = \pm 5$  ps. The value of  $\beta_B$  was increased to  $4.5 \text{ m}^{-1}$  to remove the transmitted frequency near  $\nu = \nu_0$  and allow for the TIR condition to be satisfied at the input wavelength. As Figs. 9.8(a) and 9.8(b) show, the TIR condition holds when the pulse hits the first boundary at  $t = -5$  ps, forming two reflected pulses (R1 and R2). These two pulses interfere with each other as they propagate, forming interference fringes. The reflected pulses travel with slightly different group velocities, and so they reach the second boundary at  $t = 5$  ps at different distances. When each of them hits the second boundary at  $t = 5$  ps, some energy is transmitted because the group-velocity restriction can now be satisfied since the slope of the dispersion curve at R1 and R2 is now positive allowing energy to transfer to T1. Because each of the reflected pulses hits the boundary at a different distance, two transmitted pulses form at the same frequency.

In addition to generating the transmitted pulses, both pulses also reflect off the boundary and travel back to the other boundary at  $t = -5$  ps. At this point, the process repeats itself, but because of the different distances at which the pulses reach the boundary there are two pulses at the initial frequency instead of one. After another round-trip through the waveguide, each of these two pulses will split into two more pulses. However, two of these new pulses will overlap in time, and so only three distinct pulses will be seen. This process can repeat as long as the pulses are trapped within the temporal waveguide, and the temporal waveguide will act as a pulse multiplier. For the simulations shown in Fig. 9.8, multiple pulses cannot be clearly distinguished because they overlap in time. By increasing the width of the waveguide, the reflected pulses will separate more in time before crossing the second boundary and forming two distinct pulses at the initial

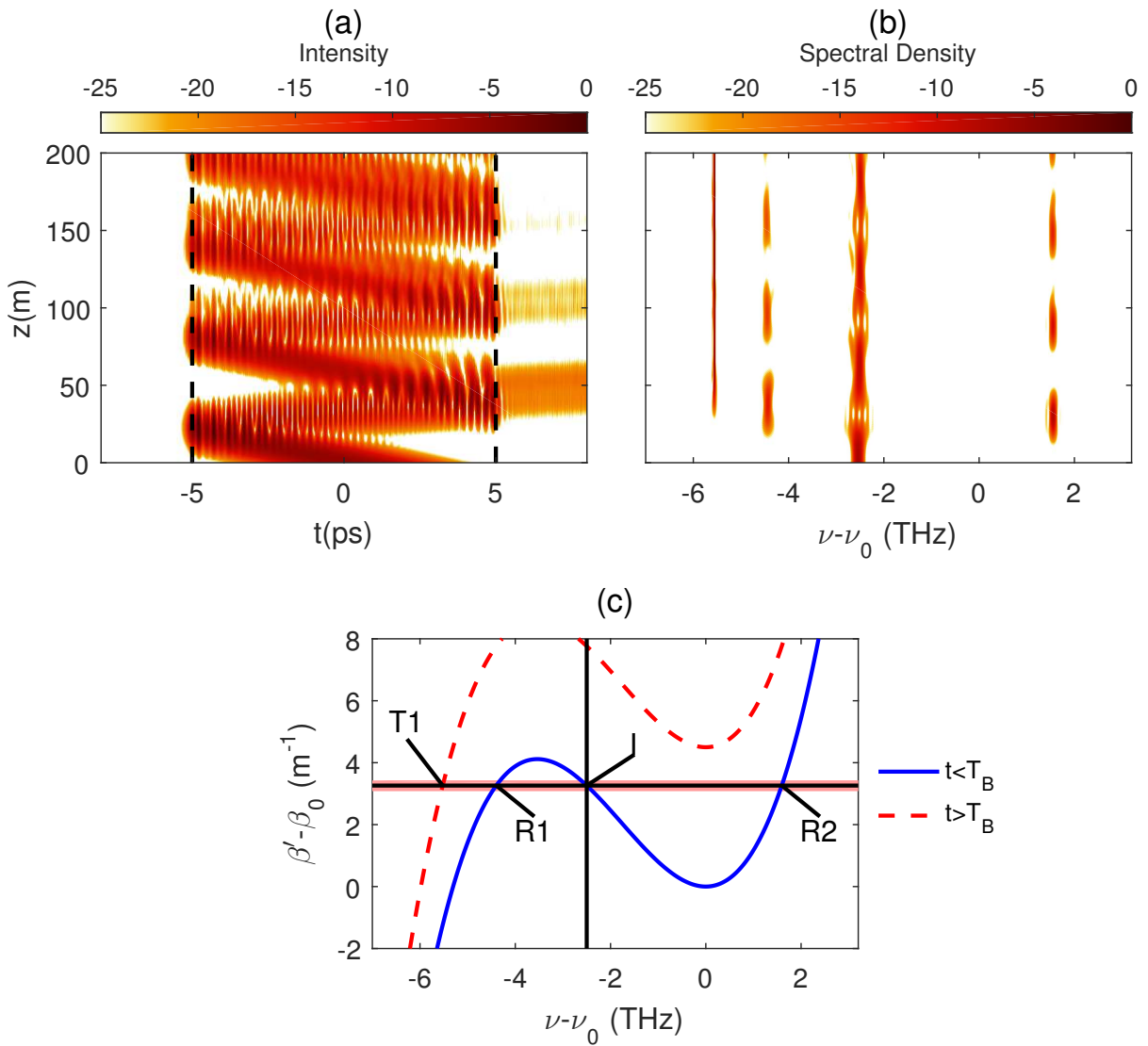


Figure 9.8: Evolution of (a) pulse shape and (b) spectrum in a temporal waveguide formed by two boundary (dashed black lines) in the same medium as Fig. 9.4 with  $\Delta\omega_i/(2\pi) = -2.5$  THz. Note that intensity and spectral density are now on a logarithmic scale to better show the transmitted pulses. (c) Dispersion curves inside (solid blue) and outside (dashed red) the waveguide.

frequency.

The behavior of the pulse within the waveguide can change dramatically if we change our initial frequency to one of the two reflected frequencies from Fig. 9.8, even though all of the central frequencies are the same. Figure 9.9 shows the same simulation as in Fig. 9.8 but with the initial frequency moved to point R1, with  $\Delta\omega_i = 10^{13}$  s<sup>-1</sup>. The evolution of the pulse (a) shape and (b) spectrum differ greatly from those from Fig. 9.8. First, the initial pulse reaches the boundary much more quickly due to the larger DGD at the new input frequency. Because of this larger initial DGD, the pulse spectrum covers a larger range of  $\beta'$  values, as we see by the larger shaded region in Fig. 9.9(c). This

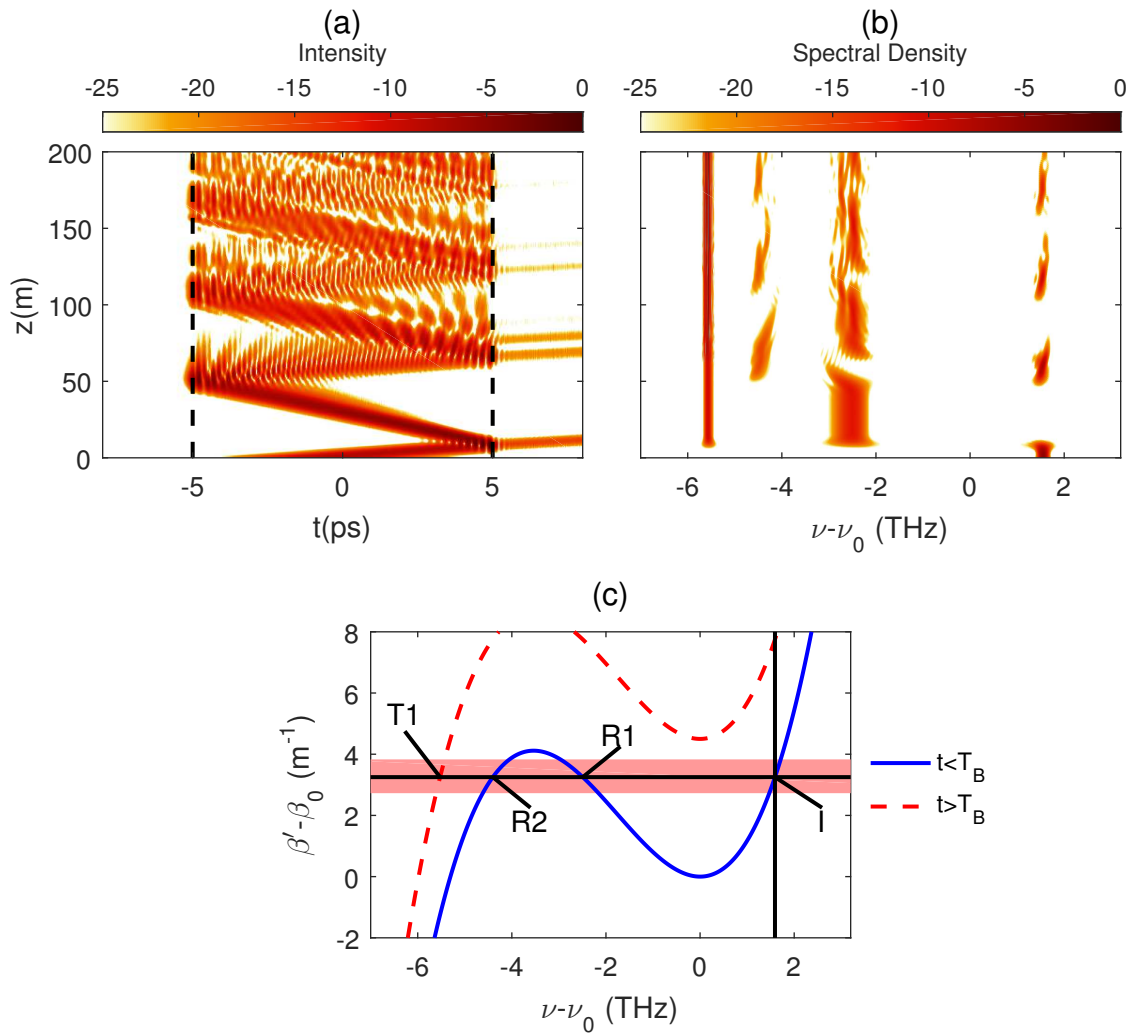


Figure 9.9: [(a),(b)] Same as Fig. 9.8 except that  $\Delta\omega_i = 10^{13} \text{ s}^{-1}$ . (c) Dispersion curves inside (solid blue) and outside (dashed red) the waveguide.

causes the spectral expansion that we see in Fig. 9.9(b) during the first reflection. This first reflection only produces one reflected band at R1, but the corresponding pulse will be compressed in time due to the decreased DGD. The transmitted pulse at T1 will also be narrower in time than the one in Fig. 9.8. This occurs because the DGD at T1 is now comparable to the DGD at point I instead of being much greater. This is also why the spectral bandwidth at T1 is now comparable to the spectral bandwidth of the initial pulse.

A transmitted frequency will always exist for either the incident or reflected pulses regardless of the magnitude of  $\beta_B$ , so this loss cannot be avoided for a waveguide with TOD. However, the loss can be significantly reduced by working at frequencies near either the local maximum or local minimum, whichever is further from the transmitted frequency. For example, Fig. 9.10 shows the spectral and temporal evolutions when the initial pulse frequency is changed to  $\Delta\omega_i/(2\pi) = -1 \text{ THz}$ . In this case, much less energy is transferred to frequencies R1 and T1, and the behavior more closely resembles that

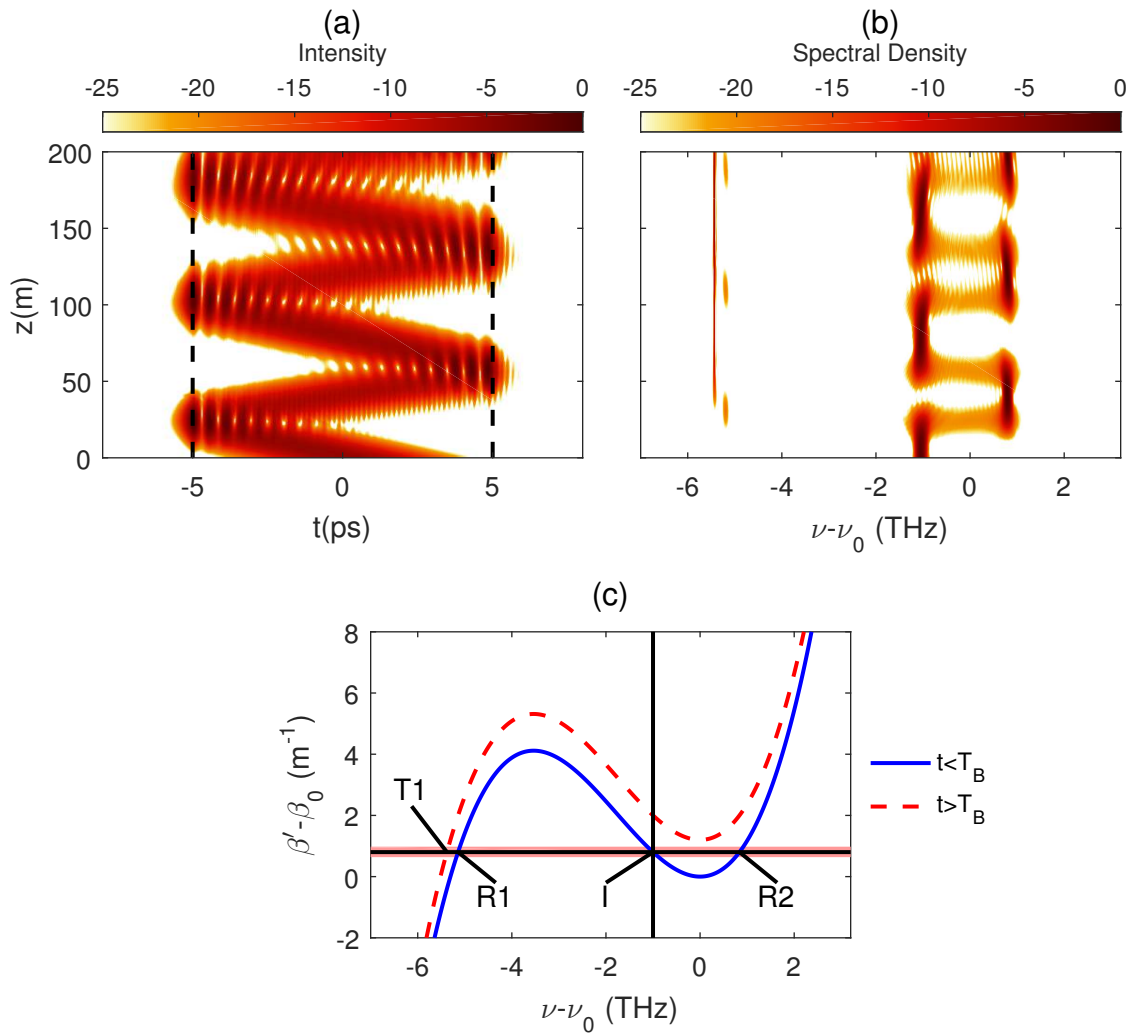


Figure 9.10: [(a),(b)] Same as Fig. 9.8 except that  $\Delta\omega_i/(2\pi) = -1$  THz and  $\beta_B = 1.2$  m<sup>-1</sup>. (c) Dispersion curves inside (solid blue) and outside (dashed red) the waveguide.

of a waveguide without TOD. Although there are still interference fringes in the time domain, these fringes arise from the beating of the input frequency with the reflected frequency R2, rather than from the two reflected frequencies beating with one another.

When the temporal waveguide supports several modes, the frequency of the fundamental mode will occur near the local minimum of the dispersion curve, similar to that in Fig. 9.10. The mode shape can then be well-approximated by ignoring the higher-order dispersion terms, and little energy will be lost at the temporal boundaries. However, the higher-order modes will have a larger  $\Delta\omega$ , and will be more strongly affected by TOD. As a result, higher-order modes will lose more energy as transmitted pulses, as in Fig. 9.8. A short optical pulse with a large spectral bandwidth is likely to excite several modes when launched into such a waveguide. However, given a long enough propagation distance, only the fundamental mode would remain confined within the waveguide, with the other modes losing energy to the transmitted frequency.

## 9.5 Conclusions

We have shown through numerical simulations that the spectrum of an optical pulse splits into multiple, widely separated, spectral bands when it arrives at a temporal boundary across which refractive index suddenly changes. At the same time, the pulse breaks into several temporally separated pulses traveling at different speeds. The number of such pulses depends on the dispersive properties of the medium, as well initial frequency of the optical pulse. In the case of a parabolic dispersion curve, the second-order dispersion governed by  $\beta_2$  splits the input pulse into up to two pulses with widely separated spectra that represent the temporal analogs of reflection and refraction at a spatial boundary [150]. The inclusion of higher-order dispersion makes it possible to form multiple reflected and transmitted pulses at a temporal boundary with widely separated spectral bands. More specifically, in the case of third-order dispersion, the pulse splits into three pulses, where the third one may correspond to either a reflected or a transmitted pulse depending on the wavelength of the input pulse. Furthermore, if the input wavelength is far enough from a wavelength where the dispersion curve exhibits an extremum, it is possible that only two transmitted pulses are formed without any temporal reflection. Conversely, if the input wavelength is close to a local maximum or minimum, the amount of energy transferred to the third pulse becomes negligible. The behavior of the pulse is then accurately modeled by neglecting the third-order dispersion term.

We also discussed the situation in which a temporal waveguide is formed by using two temporal boundaries. We found that the third-order dispersion introduces several new features. First, it is possible to produce two reflected pulses with widely separated spectra at one of the boundaries. These two pulses separate in time before arriving at the second boundary, leading to additional pulses. This process cascades each time the pulses bounce through the waveguide, allowing the temporal waveguide to act as a pulse multiplier. Unfortunately, undesirable transmitted pulses also form, representing loss of energy from a temporal waveguide. However, the energy loss can be minimized by suitably optimizing the input wavelength.

From a practical perspective, the importance of higher-order terms depends not only on the width of input pulses but also how far the input wavelength is from a maximum or minimum of the dispersion curve of the material. For example for silica fibers used in the telecom region near 1550 nm, the effects of  $\beta_2$  dominate and no more than two pulses will form at a temporal boundary because dispersion terms higher than second order will simply shift the frequencies of the reflected and transmitted pulses. However, if the pulse spectrum is located near the zero dispersion wavelength of the fiber, either by choosing the proper wavelength or by employing special dispersion-shifted fibers, the TOD term becomes significant and up to three pulses can form as in Figs. 9.2 and 9.4. Furthermore, microstructured and photonic crystal fibers make it possible to tailor the dispersion and can be designed with dispersion curves that exhibit more than one zero-dispersion wavelength. Such fibers could allow the formation of multiple pulses with widely separated spectral bands ( $> 50$  nm) if a suitable temporal boundary can be produced using a nonlinear effect such as cross-phase modulation. We will explore the XPM-based process in greater detail in the next chapter.

# Chapter 10

## XPM-Induced Time Reflection

The previous chapters have explored space-time boundaries in general, because any process that shifts the refractive index in time can be used to produce the effect. In this chapter, I explore the specific case of reflection and refraction from a XPM-induced space-time boundary, where an intense pump pulse produces the space-time boundary and a weaker probe pulse crosses it.

Section 10.1 explores what properties the dispersive medium must have to observe reflection and refraction by examining the cases of a Gaussian-shaped pump pulse and a soliton pump pulse. The same pulse shapes are used in Sect. 10.2 to determine how a waveguide can be implemented practically using XPM. Section 10.3 discusses how this XPM-induced waveguide can be used to remove inter-pulse jitter for two lasers with synchronized repetition rates. The main results of this chapter are summarized in Sect. 10.4

### 10.1 Time Reflection and Refraction

In order to observe both reflection and refraction, both the pump and probe pulses must have similar group velocities. If the group velocities are too different, the reflection coefficient will go to zero as seen in Eq. (8.17), and the transmitted frequency shift become smaller such that  $\Delta\omega_t \approx \Delta\omega_i$ . One way to have similar group velocities is to have the pump and probe wavelengths be close together. While this would allow reflection and refraction to occur, we must also consider that the spectrum of the pump pulse will also broaden due to self-phase modulation (SPM) and four-wave mixing, making it difficult to definitively say whether a generated wavelength arises from the pump or the probe pulse. This problem can be reduced somewhat by launching the pump and probe with orthogonal polarizations, but there will always be cross-talk between the two that obscures whether the frequency coming from reflection and refraction or nonlinear effects of the intense pump pulse.

A simple solution to this problem is to work at wavelengths that are more widely separated, but have similar group velocities. Accomplishing this requires a material with third-order dispersion or higher, and will create regions with varying GVD values,  $\beta_2$ . The behavior of the pump pulse in particular will be wildly affected by the value of the

GVD parameter at the pump wavelength.

We will explore the effects the evolving pump shape and spectrum by solving the coupled nonlinear Schrödinger equations given by [33]

$$\frac{\partial A_1}{\partial z} + \frac{i\beta_{21}}{2} \frac{\partial^2 A_1}{\partial t^2} = i\gamma (|A_1|^2 + 2|A_2|^2) A_1, \quad (10.1)$$

$$\frac{\partial A_2}{\partial z} + \Delta\beta_1 \frac{\partial A_2}{\partial t} + \frac{i\beta_{22}}{2} \frac{\partial^2 A_2}{\partial t^2} = i\gamma (|A_2|^2 + 2|A_1|^2) A_2, \quad (10.2)$$

where  $A_1$  is the pump pulse that produces the boundary and  $A_2$  is the probe pulse. The time  $t = T - z/v_{g1}$  is measured in a reference frame moving with the pump pulse at speed  $v_{g1}$ , and  $\Delta\beta_1 = \beta_{12} - \beta_{11}$  is a measure of the group velocity mismatch between the pump and probe pulses. The terms  $\beta_{21}$  and  $\beta_{22}$  are the GVD parameters at the pump and probe wavelengths respectively. We solve these equations numerically using the split-step Fourier method to observe reflection and refraction from super-Gaussian pulses and from solitons. In each case we use a Gaussian probe pulse of the form

$$A_2(t) = \sqrt{P_2} \exp \left[ -\frac{1}{2} \left( \frac{t}{T_{02}} \right)^2 \right]. \quad (10.3)$$

### 10.1.1 Super-Gaussian pump pulses

For the first set of simulations we use super-Gaussian pump pulses of the form

$$A_1(t) = \sqrt{P_1} \exp \left[ -\frac{1}{2} \left( \frac{t - T_D}{T_{01}} \right)^{2m} \right], \quad (10.4)$$

where  $P_1$  is the peak power of the pump pulse,  $T_D$  is the delay between the pump and probe pulses, and  $T_{01}$  is the 1/e width of the pump. The integer  $m$  is the order of the super-Gaussian and affects the decay rate of the pulse wings. A peak power of  $P_1$  produces maximum shift of the dispersion curve  $\beta_B = 2\gamma P_1$ .

We will first look at the simplest case where the pump pulse is located at the zero-dispersion wavelength such that  $\beta_{22} = 0$ . In this case, the pump pulse will not change shape during propagation, creating an unchanging boundary in time. We will also keep the probe pulse power low to keep it from influencing its own spectrum through SPM. Figure 10.1 shows the evolution of the pulse shape (left) and spectrum (right) for the probe pulse (top) and pump pulse (bottom). The parameter values used for the dispersive medium were  $\beta_{21} = 0$ ,  $\Delta\beta_1 = 31.4$  ps/km,  $\beta_{22} = 25$  ps<sup>2</sup>/km, and  $\gamma = 2$ . The pump and probe pulses had parameters  $T_{01} = 20$  ps,  $m = 4$ ,  $T_{02} = 10$  ps,  $T_D = 50$  ps,  $P_1 = 5$  W, and  $P_2 = 1$  mW.

Because  $\beta_{21} = 0$ , the pump pulse propagates without changing its shape in time even though its spectrum broadens significantly due to SPM. We can clearly see that as the probe pulse crosses the leading edge of the pump, it undergoes reflection and refraction as expected with the probe pulse and spectrum splitting in two. Therefore, the changing pump spectrum has no influence on the reflection and refraction of the probe. The only

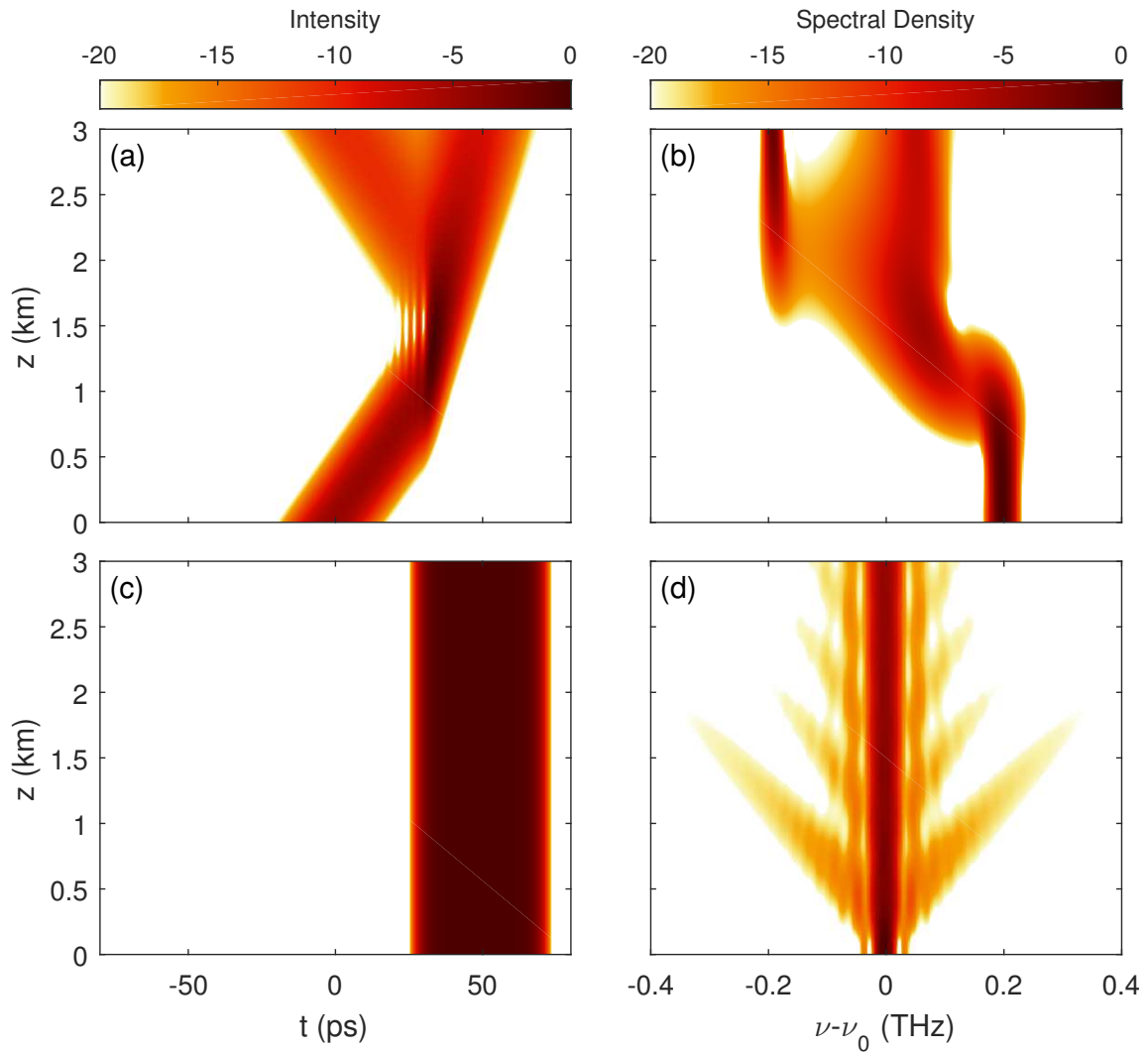


Figure 10.1: Evolution of the shape [(a),(c)] and spectrum [(b),(d)] for the [(a),(b)] probe pulse and [(c),(d)] pump pulse. The pump pulse is super-Gaussian and propagating at the zero-dispersion wavelength. The time axis is measured in a reference frame moving with the pump pulse such that  $t = T - z/v_{g1}$ .

important factor is the temporal profile of the pump pulse. An obvious difference between Fig. 10.1(b) and the ideal boundaries we have explored previously is that the shifting and splitting of the spectrum happens over a much longer distance. The shift for the transmitted frequency even gradually shifts before arriving at its final value. This effect is due to the finite rise time of the pump pulse, which causes probe pulse to gradually pass through an increasing refractive index change before arriving at the final shift when  $t = T_D$ . At the early part of this process, the refractive index change is small and so the pulse is mostly refracted. However, as the pump power quickly ramps up, more of the probe energy is reflected.

We can ask what happens if we increase the peak power of the probe pulse. In this case, the total energy transferred between the probe and the boundary must increase. In

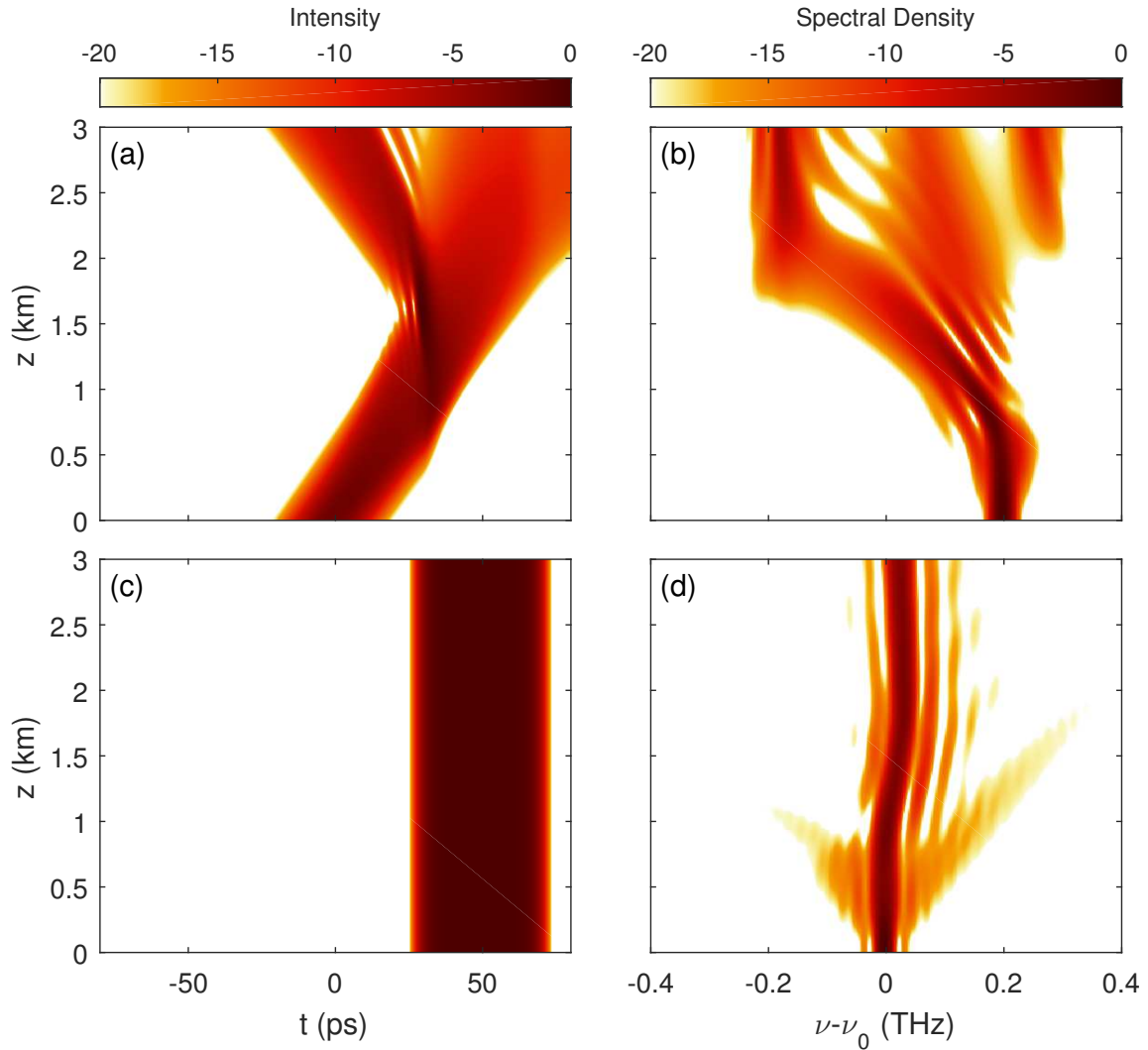


Figure 10.2: Same as Fig. 10.1 except the peak power of the probe pulse has been increased to  $P_2 = 2$  W. The time axis is measured in a reference frame moving with the pump pulse such that  $t = T - z/v_{g1}$ .

the past, our arbitrary boundary acted as a well for this energy. With the XPM induced boundary, however, our pump pulse is producing the boundary, meaning the energy should be transferred to or from it. Figure 10.2 shows the same simulation as Fig. 10.1, but with the peak power of the probe pulse increased to  $P_2 = 2$  W. The probe pulse still undergoes reflection at the edge of the pump, but this time we clearly see that the pump spectrum is blue-shifted to compensate the red-shift of the reflected and transmitted pulses. Increasing the probe pulse energy by increasing the pulse width  $T_{02}$  results in a larger shift of the pump frequency. We also see that an extra frequency is generated in the probe pulse spectrum. This extra frequency is likely caused by FWM of the reflected and transmitted frequencies at the point where the probe pulse is compressed against the edge of the pump pulse.

The above results assume that the pump wavelength is at the zero-dispersion

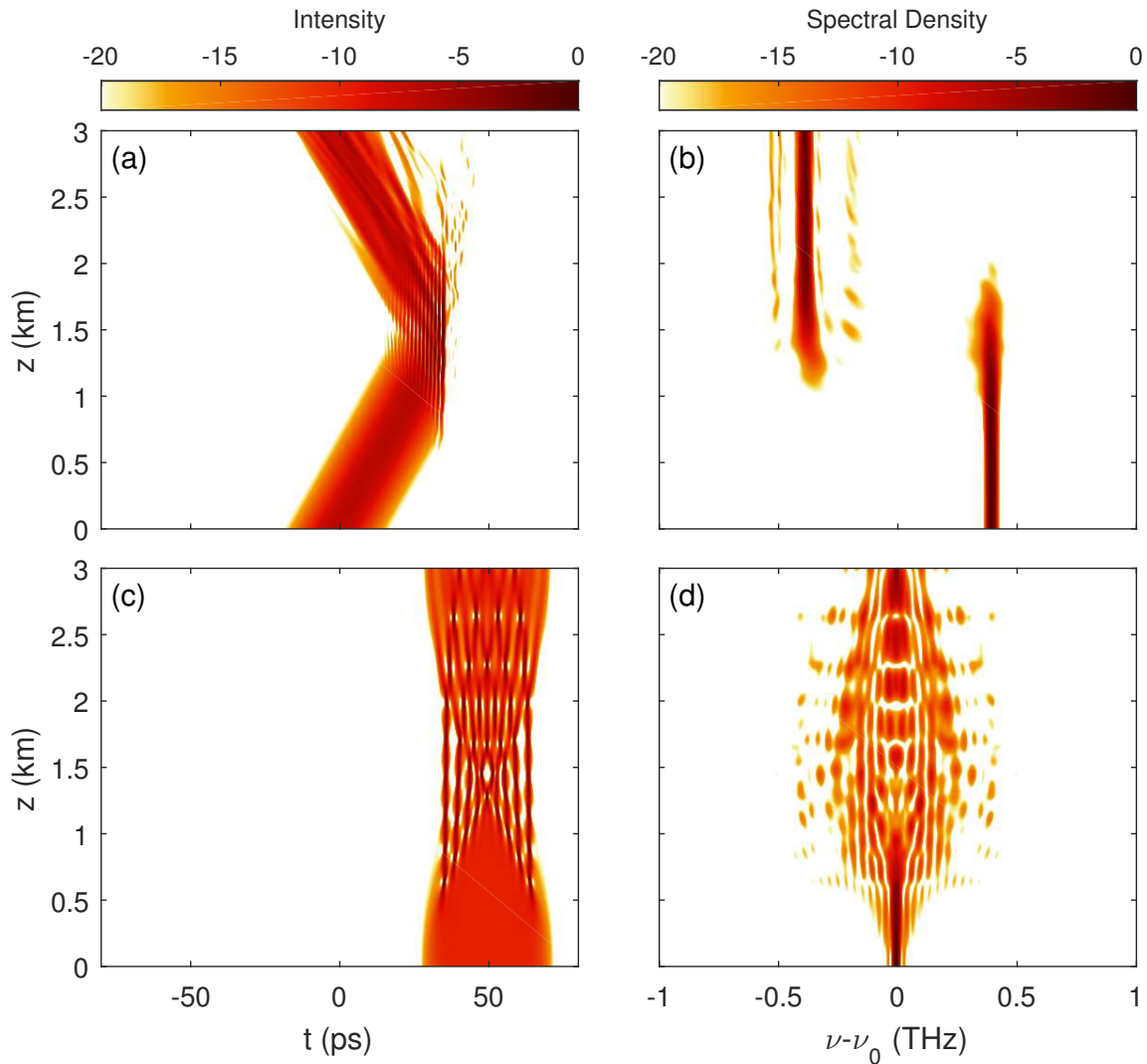


Figure 10.3: Same as Fig. 10.1 except the GVD of the pump was changed to  $\beta_{21} = -25 \text{ ps}^2/\text{km}$ . The time axis is measured in a reference frame moving with the pump pulse such that  $t = T - z/v_{g1}$ .

wavelength of the medium. In practice, this would require a material with a significant fourth-order dispersion parameter, such as a photonic crystal fiber, in order to match the group velocities. For more common single-mode fibers, the fourth-order dispersion term is not significant over most of the near infrared. Therefore, we should look at the behavior when the pump and probe have opposite signs of GVD. Figure 10.3 shows the same simulation as Fig. 10.1 but with the pump GVD set to  $\beta_{21} = -25 \text{ ps}^2/\text{km}$ . These parameters are similar to those one could expect from a single-mode fiber.

The behavior of both the pump and probe in Fig. 10.3 is markedly different from Fig. 10.1. The pump pulse now breaks down into multiple pulses with very high peak powers, which cause the probe to see a significantly higher refractive index change than in the non-dispersive case. We can see this effect in Fig. 10.3(a) and (b) as the pulse is now almost entirely reflected at the edge of the pump, and nearly all of the spectrum

is transferred to the reflected frequency. Moreover, there are additional frequencies generated around the main reflected frequency. These side bands arise because the pump pulse compresses in time as it propagates, causing the refractive index boundary to recede toward the center of the pump pulse as we can clearly see between  $z = 0.5$  km and  $z = 1$  km. This causes the boundary to move at a different velocity, which leads to different reflected and transmitted frequencies. Very little energy is transferred to these frequencies because the boundary is still moving at the group velocity of the pump pulse for most of the interaction with the probe.

If we reverse the sign of the pump GVD, the spectrum of the pump pulse broadens quickly due to SPM, and dispersion causes the pump pulse to spread out in time. Therefore, by the time the probe reaches the pump, the peak power of the pump is significantly reduced, and the shift of the refracted pulse is much smaller. Furthermore, the reflected pulse is almost entirely suppressed due to the slow rise time of the refractive index boundary. Experimentally, we could compensate for this by using a pump pulse that has been chirped with the opposite dispersion. This allows the pump to compress slightly before the probe arrives, leading to a sharp boundary and allowing reflection to occur.

### 10.1.2 Soliton pump

A simple solution to the breakdown of the pump pulse is to use a soliton as the boundary. While this limits the pump to the anomalous dispersion regime, the pump will no longer change shape during propagation, giving a consistent boundary. To study reflections from such a boundary, we will use first-order  $\text{sech}^2$  solitons of the form

$$A_1(t) = \sqrt{P_1} \operatorname{sech} \left( \frac{t - T_D}{T_{01}} \right). \quad (10.5)$$

Unlike the Gaussian pump, the peak power and width of the soliton are linked through the relation

$$P_1 = \frac{|\beta_{21}|}{\gamma T_{01}^2}. \quad (10.6)$$

Note that higher peak powers are only possible by reducing the width of the soliton.

We explore the effect of the soliton pump using the same simulation parameters as in Fig. 10.3. We keep the peak power the same,  $P_1 = 5$  W, which gives a soliton width of  $T_{01} = 1.58$  ps. The pulse separation was also reduced to  $T_D = 30$  ps so that the boundary would occur at approximately the same time. Figure 10.4 shows the evolution of the pump and probe pulses with this soliton pump. As expected, the soliton propagates without changing its shape or spectrum. The probe pulse still undergoes reflection and refraction at the boundary. However, we can see in the spectrum that transmitted frequency quickly returns back to the incident frequency. This occurs because the transmitted frequency encounters a second boundary on the trailing side of the soliton, and is refracted a second time. For this second refraction, the sign of the refractive index change is reversed, and so we return to the original frequency. Therefore, the transmitted pulse is also no longer compressed in time, as its group-velocity is unchanged.

The fast change back to the original frequency has one final effect. Because the soliton

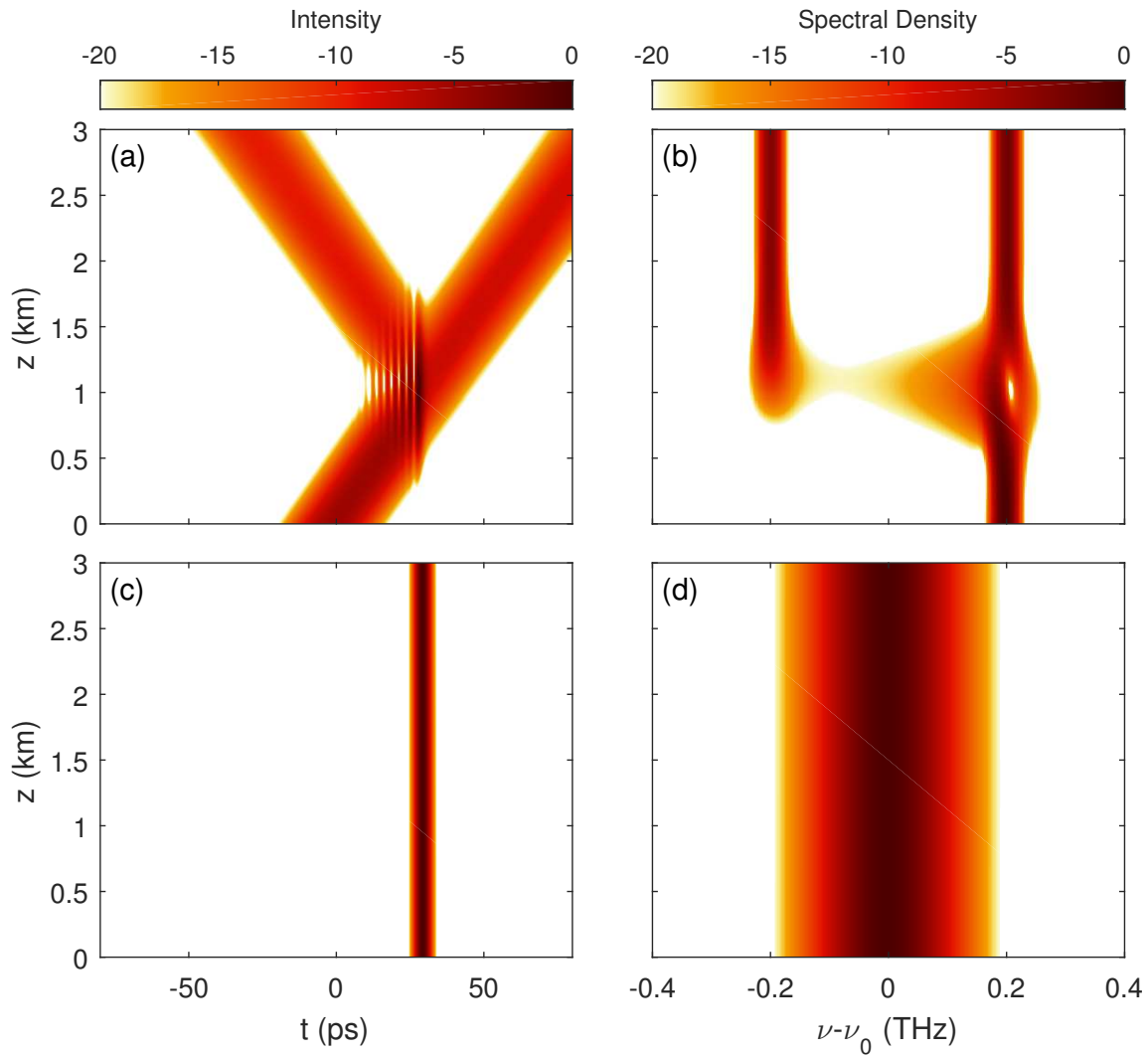


Figure 10.4: Same as Fig. 10.3 but with a soliton pump pulse. The time axis is measured in a reference frame moving with the pump pulse such that  $t = T - z/v_{g1}$ .

is so narrow in time that the evanescent wave can reach the other side, allowing for a temporal analog of frustrated TIR. In other words, the reflection energy transferred to the reflected pulse in Fig. 10.4 is lower than it should be. We can see this even more clearly if we increase the peak power of the pump pulse such that it should cause TIR for the entire bandwidth of the input pulse, as shown in Fig. 10.5 where the pump power was increased to  $P_1 = 8$  W. We see that while most of the probe pulse is reflected, a small portion of the pulse energy leaks through the boundary. Looking at Eq. (10.6), the frustrated TIR effect can be reduced using a pump wavelength with a higher GVD, which allows the soliton to be wider while still having the same peak power.

If we now increase the power of the probe pulse, we expect that the frequency of the soliton will change just as it did in Fig. 10.2. Figure 10.6 shows the same simulation as Fig. 10.5, but with the probe power increased to  $P_2 = 1$  W. As expected, the soliton frequency shifts by about 0.15 THz. Because there is GVD at the soliton wavelength, this

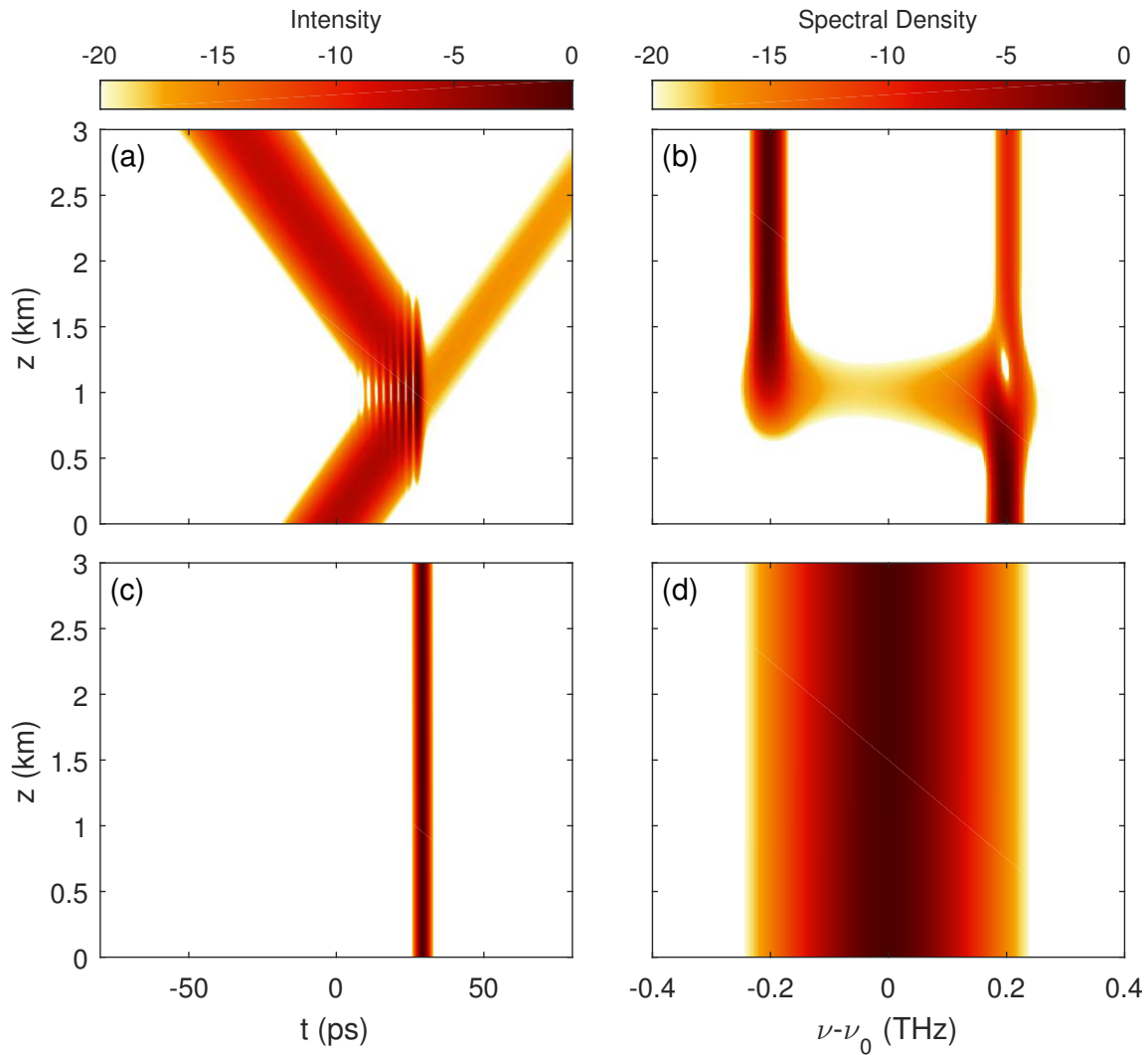


Figure 10.5: Same as Fig. 10.4 except the pump power has been increased to  $P_1 = 8$  W. The time axis is measured in a reference frame moving with the pump pulse such that  $t = T - z/v_{g1}$ .

frequency shift causes the soliton to change speed. As a result, the speed of the boundary is changing, and the momentum conservation condition at the boundary changes at later propagation distances. This leads to a shifting of the reflected frequency as seen in Fig. 10.6(b), and an increase in energy transmitted across the boundary.

## 10.2 Time Waveguide

Because the optical nonlinearity only causes a positive shift in the refractive index  $\beta_B > 0$ , we only have two possible methods for creating a temporal waveguide through XPM. The first is to have the probe in the anomalous dispersion region ( $\beta_2 < 0$ ), and the pump itself acts as the waveguide. In this case the waveguide width is simply the pump pulse

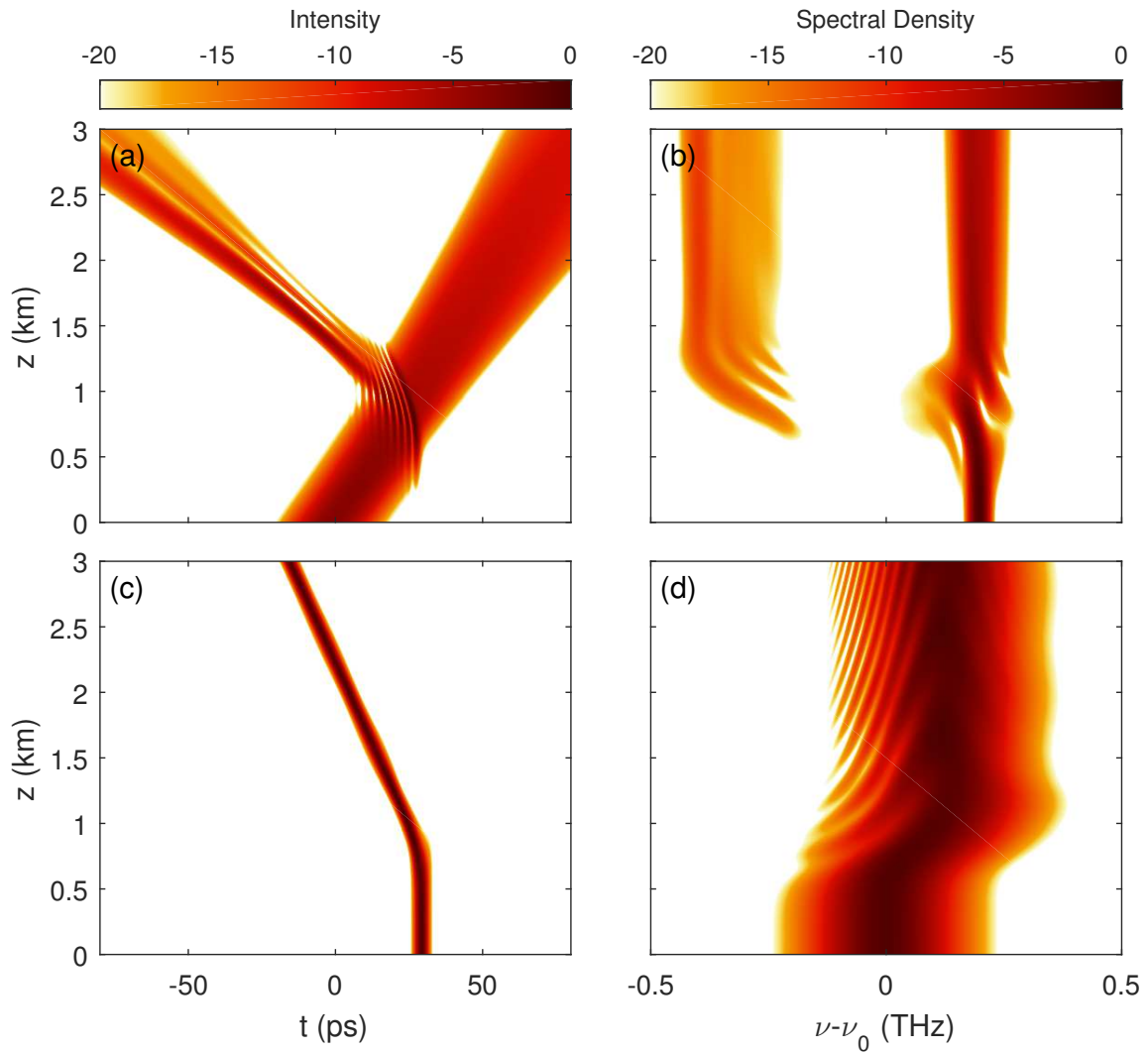


Figure 10.6: Same as Fig. 10.5 except the probe power has been increased to  $P_2 = 1$  W. The time axis is measured in a reference frame moving with the pump pulse such that  $t = T - z/v_{g1}$ .

width. The second method is for a probe in the normal dispersion region ( $\beta_2 > 0$ ) and uses two pump pulses as the waveguide boundaries. In any other arrangement, the pump will actually act as an anti-waveguide, creating a temporal window in which the probe can not propagate.

As before we can create the waveguide through Gaussian-type pump pulses, in which case the waveguide will vary during propagation. Alternatively, the waveguide can be formed with solitons, which present their own unique challenges. We will explore each of these in turn below.

### 10.2.1 Super-Gaussian boundaries

We will first use a super-Gaussian pump as described in Eq. (10.4) that is no longer delayed with respect to the probe such that  $T_D = 0$ . In this case the two edges of the pump pulse act as the boundaries of the waveguide. Because XPM always shifts the refractive index up inside of the pump, the probe pulse actually sees a drop in the refractive index across each boundary. Therefore, our probe must have a negative GVD in order to satisfy the TIR condition at each boundary. This situation is the same as a typical optical fiber, which has a core with a higher refractive index than its surroundings. As before the behavior of the pump pulse depends on the nature of the pump GVD,  $\beta_{21}$ .

Figure 10.7 shows the evolution of the pump and probe for a pump with GVD  $\beta_{21} = 0$ . The parameter values used for the dispersive medium were  $\beta_{21} = 0$ ,  $\Delta\beta_1 = 0$  ps/km,  $\beta_{22} = -25$  ps<sup>2</sup>/km, and  $\gamma = 2$  (Wm)<sup>-1</sup>. The pump and probe pulses had parameters  $T_{01} = 2.5$  ps,  $m = 1$ ,  $T_{02} = 1$  ps,  $T_D = 0$  ps,  $P_1 = 1$  W, and  $P_2 = 1$  mW. As before, the pump pulse does not change shape during propagation, while its spectrum changes due to SPM. The evolution of the probe pulse is nearly identical to the single-mode waveguide seen in Chapter 7. Indeed, if we use the values  $\beta_B = 2\gamma P_1$  and  $T_B = T_{01}$  in Eq. (7.12) for the waveguide  $V$  parameter, we find that the waveguide is in fact single-mode with a  $V = 1.41$ .

If the probe pulse is in a region with normal dispersion, the refractive index outside of the waveguide must be greater than the refractive index inside of the waveguide. Therefore, the waveguide must be formed by two pump pulses, with the waveguide occupying the region between them. Figure 10.8 shows the same simulation as Fig. 10.7, but with  $\beta_{22} = 25$  ps<sup>2</sup>/km and the two pump pulses separated by 12 ps. Note that the two pulses actually overlap, leading to a slightly smaller index change between the inside and outside of the waveguide. Although this reduces the  $V$  parameter of the waveguide, it also allows the number modes supported by the waveguide to be altered simply by changing the delay between the two pump pulses.

If the pump pulse is not at the zero dispersion wavelength, the GVD will cause the pump shape to change as seen in the previous section. This will cause the waveguide to broaden in the case of the single-pump configuration, and collapse entirely with the two-pump configuration. While some GVD can be tolerated at the pump wavelength, the corresponding probe GVD needs to be much higher to allow the probe pulse to fill the waveguide before the pump disperses. This ends up creating essentially the same behavior as the zero GVD condition. For the case of normal GVD at the pump wavelength ( $\beta_{21} > 0$ ), we can compensate for this by first chirping the pump with the opposite dispersion before propagating with the probe. Figure 10.9 shows the same simulation as Fig. 10.7, but with GVD of  $\beta_{21} = 25$  ps<sup>2</sup>/km. The pump pulse is chirped with a total DGD of  $D_p = -\beta_{21}L/2 = 37.5$  ps<sup>2</sup> to a width of 25 ps FWHM. Figure 10.9 shows that while the pump starts very broad, it compresses half-way through the propagation forming the waveguide. We see that although the probe pulse loses some of its initial energy before the pump finishes compressing, a significant portion of the probe is trapped in the waveguide between  $z = 1$  km and  $z = 2$  km. Likewise, the probe spectrum in Fig. 10.9(b) is largely unchanged until the pump pulse compresses enough to form the waveguide, but is eventually narrowed as expected. This method is less effective for

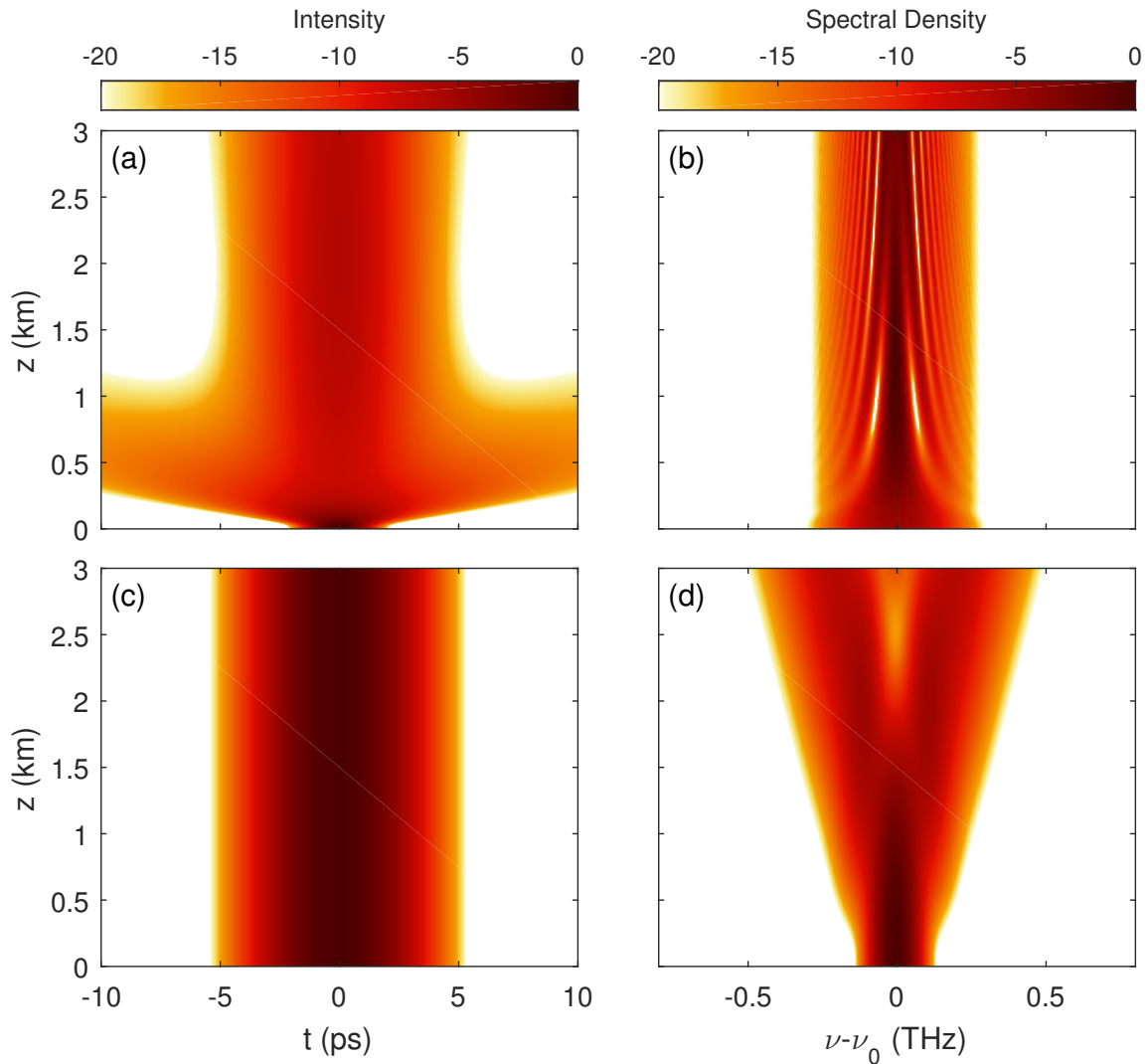


Figure 10.7: Evolution of pulse [(a),(c)] shape and [(b),(d)] spectrum for a Gaussian probe pulse (top) in a waveguide formed by a single super-Gaussian pump (bottom) with  $\beta_{21} = 0$ .

waveguides formed by two pump pulses, as the two dispersed pulses interfere with one another to form a more complex temporal profile when they are dispersed. However, this is still suitable for a sufficiently wide temporal waveguides where the two dispersed pulses won't overlap in time.

A simpler solution exists when we have anomalous pump dispersion, as the pump pulse chirps itself through SPM in such a way that the waveguide shape will be preserved for a longer distance. Figure 10.10 shows the evolution for the same parameters as Fig. 10.7, but with GVD  $\beta_{21} = -25 \text{ ps}^2/\text{km}$  and the pump power increased to  $P_1 = 2 \text{ W}$ . As Fig. 10.10(c) shows, the pump pulse broadens by a small amount, but the nonlinearities prevent further broadening. This allows the pump to persist over the entire propagation distance, and we can see that the probe pulse is trapped in a nearly the same way as the waveguide with zero GVD. Note that the pump pulse is simply evolving toward a soliton

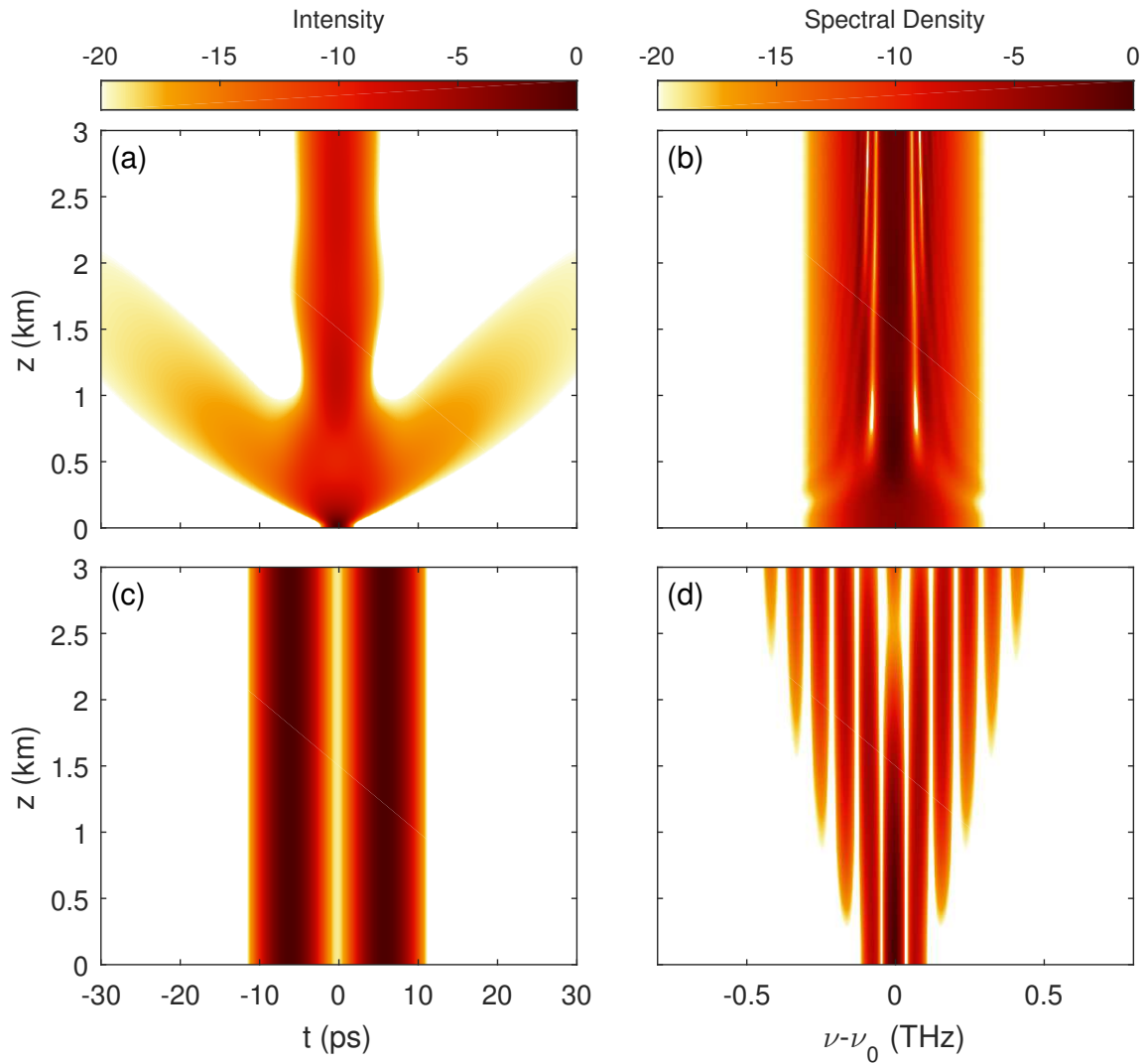


Figure 10.8: Evolution of pulse [(a),(c)] shape and [(b),(d)] spectrum for a Gaussian probe pulse (top) in a waveguide formed by two super-Gaussian pump pulses (bottom) with  $\beta_{21} = 0$ .

shape in Fig. 10.10(c). It would be prudent to examine the behavior when the pump is simply launched as a soliton.

### 10.2.2 Soliton boundaries

As we saw earlier, the width of a soliton and its peak power are linked. If we use the relation for the soliton peak power from Eq. (10.6) to calculate the  $V$  parameter of the waveguide in Eq. (7.12), we find that a soliton waveguide has a  $V$  parameter of

$$V = 2\sqrt{\frac{|\beta_{21}| T_B^2}{|\beta_{22}| T_{01}^2}}. \quad (10.7)$$

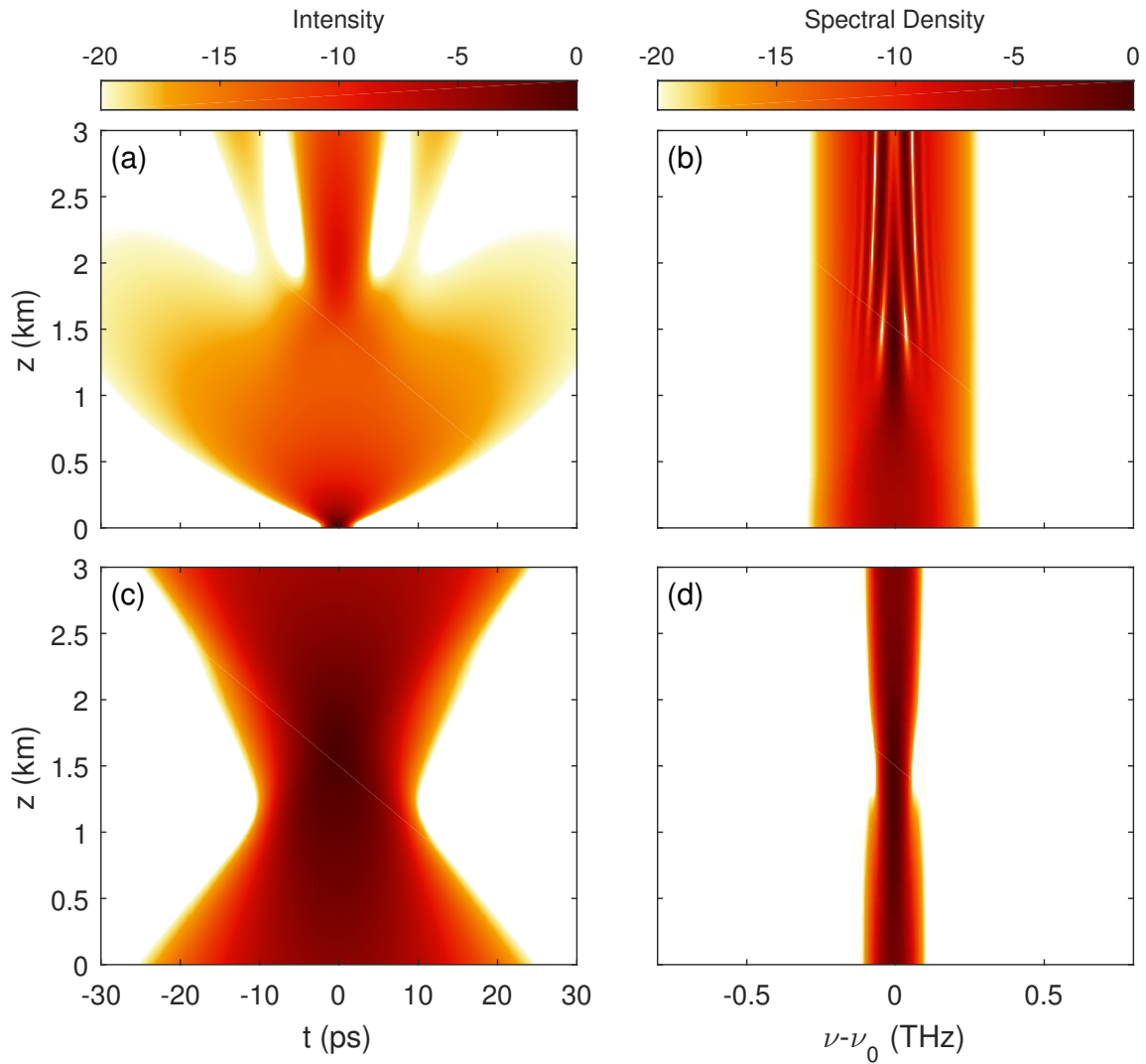


Figure 10.9: Evolution of pulse [(a),(c)] shape and [(b),(d)] spectrum for a Gaussian probe pulse (top) in a waveguide formed by a single super-Gaussian pump (bottom) with  $\beta_{21} = 25$ .

Note that this is no longer the exact  $V$  parameter of the waveguide, since the soliton has a finite rise time. However, it is a useful tool for approximating how many modes the waveguide should support.

Let us now examine the case where the waveguide is formed by a single soliton pulse. In this case, the half-width of the waveguide ( $T_B$ ) is approximately equal to  $T_{01}$ , and Eq. (10.7) reduces to

$$V \approx 2\sqrt{\frac{|\beta_{21}|}{\beta_{22}}}. \quad (10.8)$$

Thus the number of modes supported by the waveguide is almost entirely determined by the ratio of the GVD parameters at the pump and probe frequencies. Note that the width and peak power of the pump are not constrained, so the waveguide can be constructed

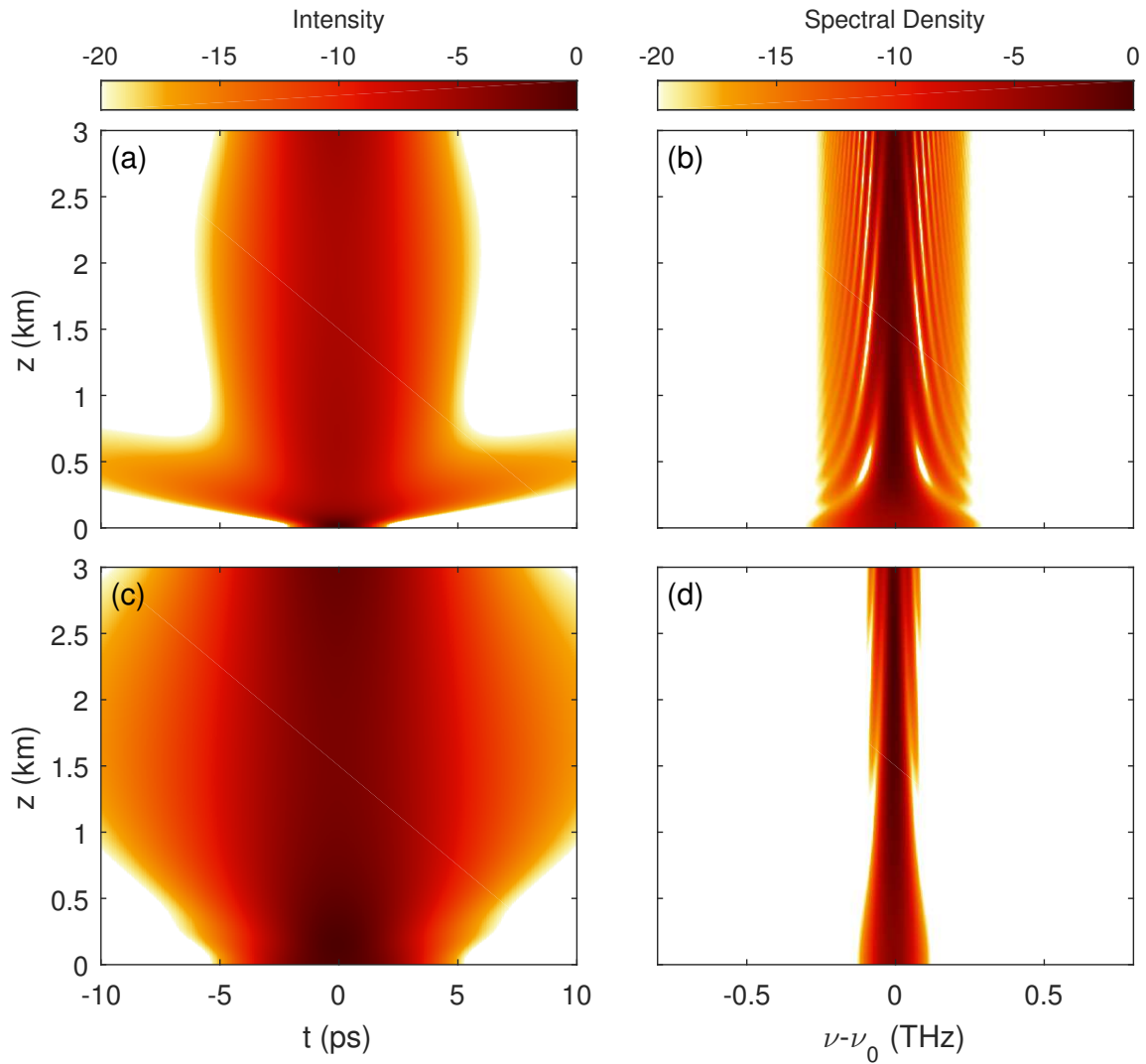


Figure 10.10: Evolution of pulse [(a),(c)] shape and [(b),(d)] spectrum for a Gaussian probe pulse (top) in a waveguide formed by a single super-Gaussian pump (bottom) with  $\beta_{21} = -25$ .

for any pulse width. The modes will simply scale their widths and spectra up or down to match the waveguide.

Figure 10.11 shows the evolution of probe pulses with  $T_{02} = 5$  ps and GVD of  $\beta_{21} = \beta_{22} = -25$  ps<sup>2</sup>/km and pump powers of (a)  $P_1 = 1$  W and (b)  $P_1 = 2$  W. These pump powers create waveguides that are about (a) 7 ps and (b) 15.8 ps wide. Because the GVD values are the same at the pump and probe, the  $V$  parameter is approximately 2. We see that in both cases the probe pulses evolve toward the waveguide shape, and seem to only excite one mode. This implies that the waveguide width is actually slightly less than  $2T_{01}$ . As expected, even though the waveguide width changes, the peak power changes in such a way that the mode is preserved. This also makes logical sense as the soliton profile must be able to produce a single-mode waveguide, as the soliton is essentially producing its own waveguide as well.

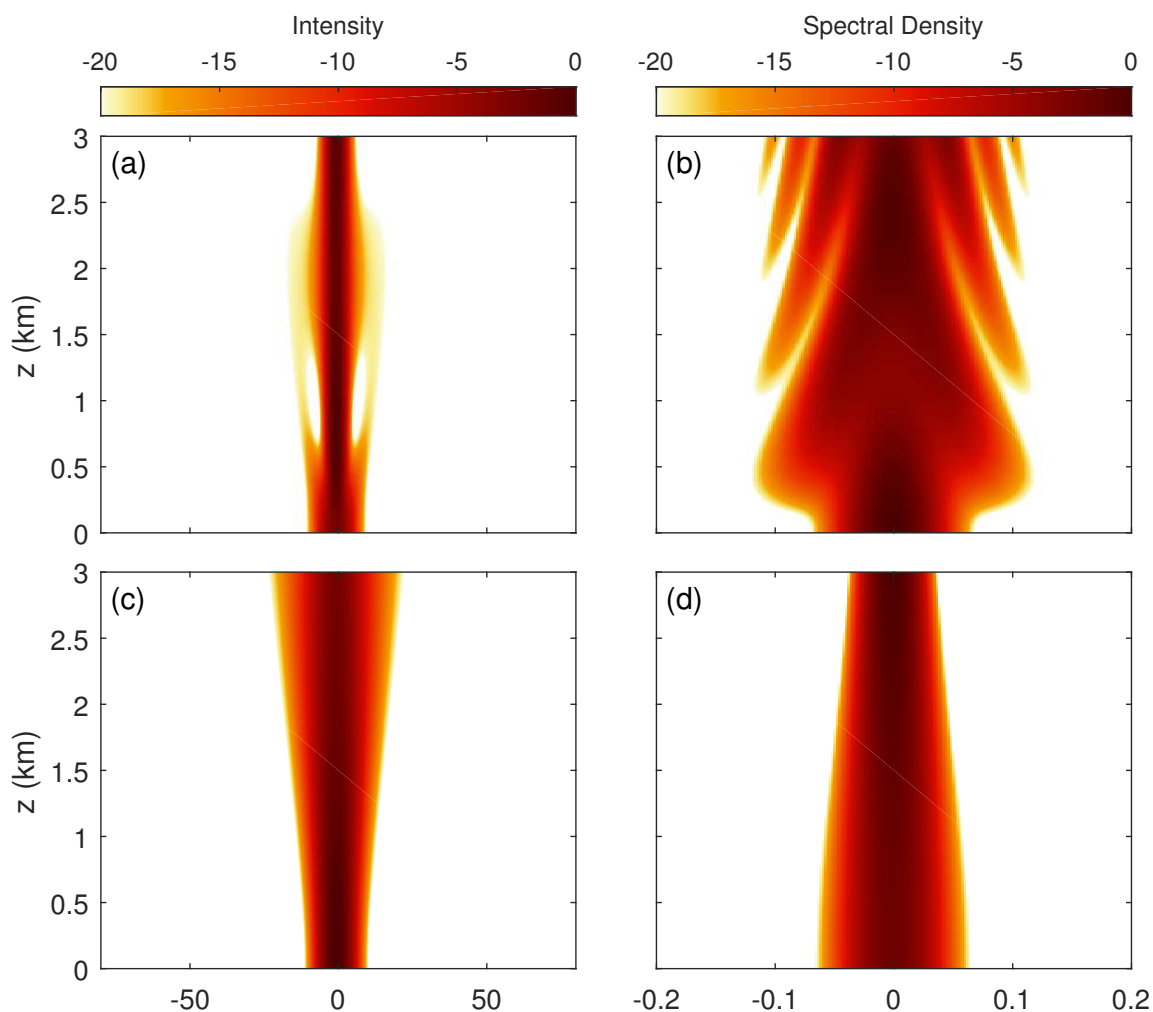


Figure 10.11: Evolution of pulse [(a),(c)] shape and [(b),(d)] spectrum for a Gaussian probe pulse in a waveguide formed by a single soliton with [(a),(b)]  $P_1 = 1$  W and [(c),(d)]  $P_1 = 0.2$  W.

If our waveguide is formed by two solitons, we can now arbitrarily set the waveguide width, and therefore the number of modes supported by the waveguide. If we wish to have a highly multimode waveguide, this is not a problem as we can either increase the power of the solitons or their separation. However, if we seek a single-mode waveguide, we begin to run into the problem of soliton attraction and repulsion. In this process, solitons that are close together in time will either pull together or push apart depending on the relative phase between the two pulses. In either case, the waveguide will eventually break down by either collapsing or widening until it becomes multi-mode again. As before, we can get around this by using a pump that has a low dispersion relative to the probe, which will force the  $V$  parameter to be small. Figure 10.12 shows the evolution of both the probe and pump pulses and their spectra for the same dispersion parameters as Fig. 10.11, but with the soliton power set to  $P_1 = 5$  W and the sign of the probe GVD inverted to allow waveguiding. At first, the probe pulse is confined between the two pump pulses.

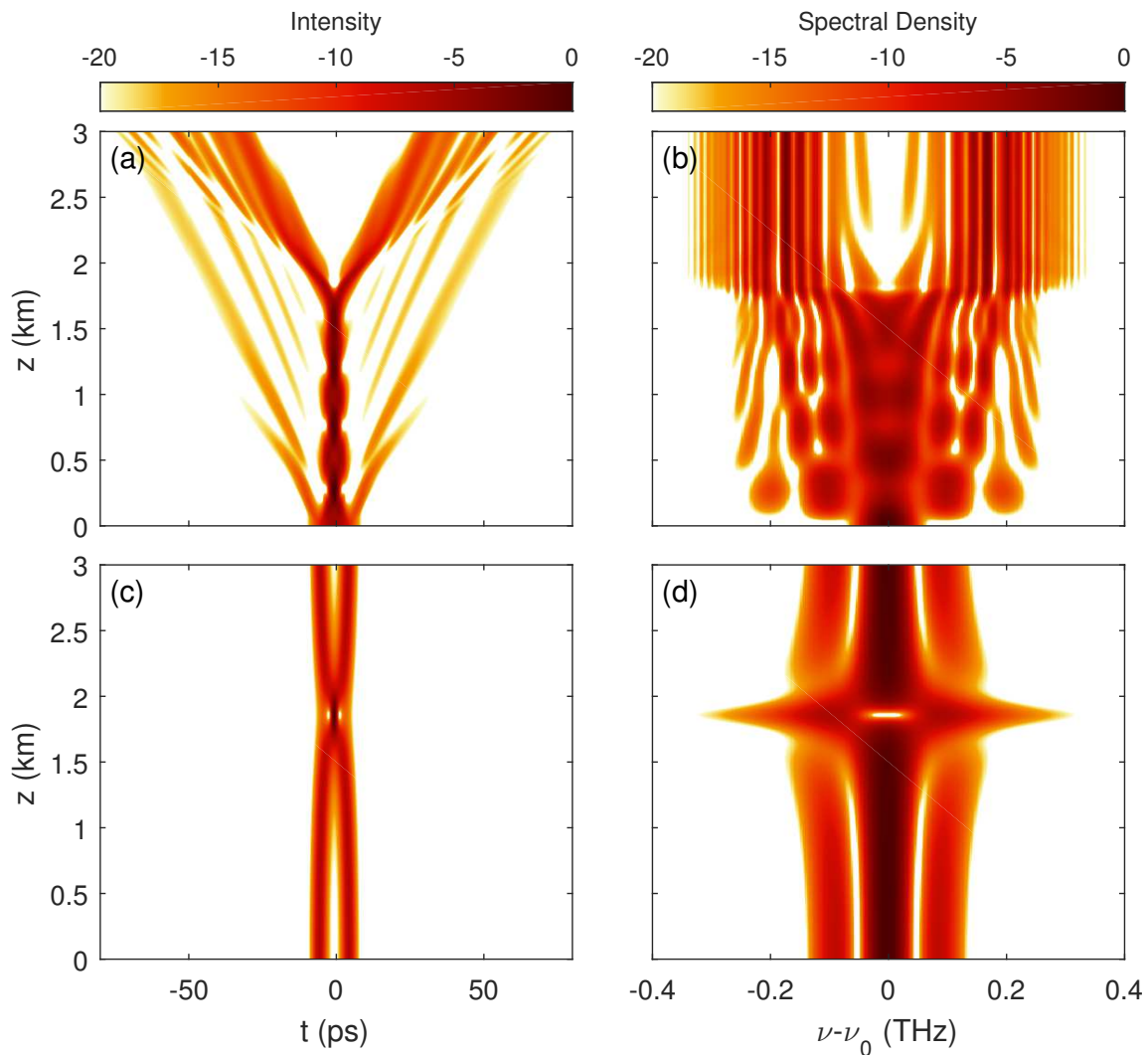


Figure 10.12: Evolution of pulse [(a),(c)] shape and [(b),(d)] spectrum for a Gaussian probe pulse (top) and the soliton pair (bottom).

However, soliton attraction eventually pulls the two pump solitons together, collapsing the waveguide. When this happens, the pump power spikes and forces the probe pulse out of the waveguide region.

### 10.3 Pulse jitter compensation

If two pulses laser sources have a synchronized repetition rate, there will still be some remaining jitter in the timing of these pulses. This inter-pulse jitter manifests as a varying delay between the center of the pulse. We can effectively remove this delay by splitting one pulse to produce a single-mode waveguide through XPM, while the other pulse propagates within it. As the probe pulse propagates, it will shed energy and reshape to match the shape of the fundamental mode, which is centered inside of the waveguide.

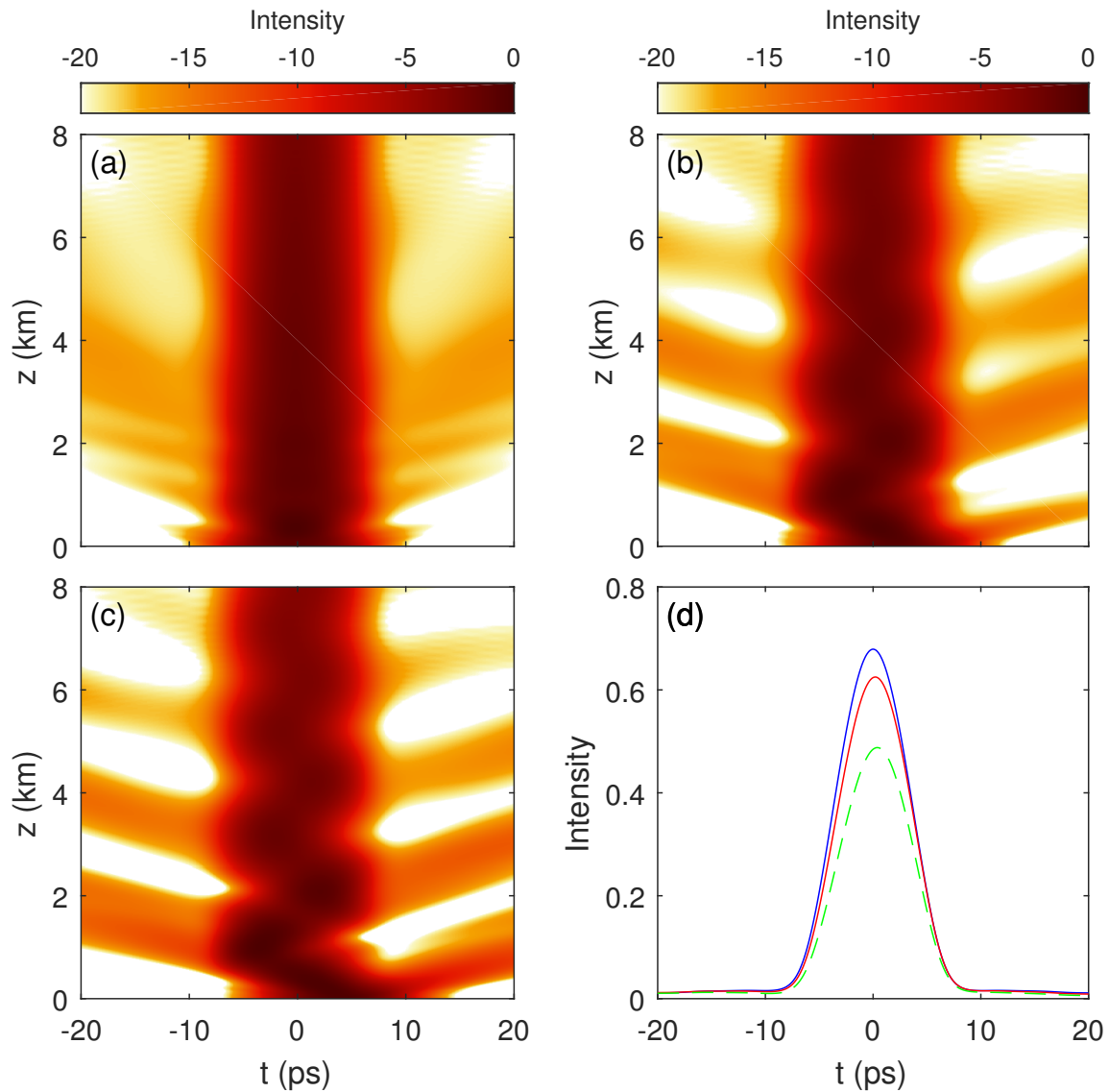


Figure 10.13: Evolution of the pulse shapes for probe pulses that are offset from the waveguide center by (a) 0 ps, (b) 2 ps, and (c) 4 ps. The output shapes of the probe pulses are shown in (d).

Figure 10.13 shows the evolution of three identical probe pulses with  $T_{02} = 5$  ps propagating inside of an 8 ps wide temporal waveguide formed by two super-Gaussian pump pulses with  $T_{01} = 4$  ps,  $m = 2$ , and  $P_1 = 1$  W. The pumps propagate in with anomalous dispersion with  $\beta_{21} = -10$  ps<sup>2</sup>/km, while the probes have a GVD of  $\beta_{22} = 60$  ps<sup>2</sup>/km to ensure that they fill the waveguide quickly. The probes are delayed with respect to the waveguide center by (a) 0 ps, (b) 2 ps, and (c) 4 ps. The output pulse shapes are shown in Fig. 10.13(d). We see that although the probe pulses all start with different offsets, they each lose energy outside of the waveguiding region and eventually settle to the center of the waveguide.

Examining the output pulse shapes in Fig. 10.13(d), we see that larger time offsets

lead to a reduction of the peak power of the probe pulse, as more energy has been lost to the region outside of the waveguide. However, for offsets less than 2 ps, the reduction in peak power is relatively small. This means that the waveguide can compensate jitter of nearly half the pulse width without significantly altering the probe pulse intensity. We note that the jitter compensation is not fully complete after the 8 km propagation distance, though the maximum offset from the waveguide center is reduced by nearly a factor of 4 to under half a picosecond. However, longer propagation distances allow for even better jitter compensation.

Note that if the two pulse trains were to produce shorter pulses, the waveguide could be much smaller than the one in Fig. 10.13. In this case, the probe pulses will also disperse faster and fill the waveguide more quickly. For this reason, the jitter compensation can be achieved in a much shorter length of fiber than needed for the longer pulses.

## 10.4 Conclusions

We have shown how XPM with a pump-probe configuration can be used to observe space-time reflection and refraction as well as to form a temporal waveguide. The temporal boundaries are produced by the edges of the pump pulses. For a general pump pulse shape, the boundaries will typically change during propagation due to GVD at the pump wavelength. If the pump GVD is negative, the pump pulse breaks into multiple smaller pulses, resulting in a higher refractive index change than the original pulse could provide. When the GVD is positive as with normal dispersion, the pump pulse will broaden much more quickly, and the reflected pulse will be significantly suppressed. These issues can be resolved by using solitons as the boundaries, but we find that the narrow solitons lead to frustrated reflection. Temporal waveguides face similar concerns, but are still feasible using parameters typical for optical fibers.

These simulations provide a basis for an experimental demonstration of time reflection and refraction using XPM. The soliton-induced boundaries are perhaps the simplest to implement in practice, as dispersion can be ignored for the pump pulse. For a standard single-mode fiber, this can be realized by using an intense pump pulse near 1550 nm and a probe pulse near 1100 nm. General use of temporal reflection and refraction through XPM requires careful consideration of the dispersive properties of the materials. For this reason, dispersion tailored waveguides such as photonic crystal fibers are a promising platform for observing these effects.

We emphasize that the simulations in this thesis did not account for longitudinal ( $z$ -dependent) fluctuations of the dispersion parameters that arise due to the waveguide fabrication process. In reality these terms can fluctuate considerably, particularly in the case of photonic crystal fibers where the dispersion parameters are highly dependent on the fiber core size. Future investigations of the effects these fluctuations in the dispersion parameters have on the time reflection and refraction process is of considerable interest.

# Appendix A

## Sample Code for Time Reflection

```

%% Initialize variables-----
clear;clc;close all; tic;
%Simulation Parameters
    tWindow=2^9; %Full extent of the time window
    Nz=2^13;     %Number of steps in z-direction
    Nt=2^13;     %Number of points in time array
%Plot Parameters
    Tlims=[-10 10]; %Max and min of plots in time
    nulims=[-5 5]; %Max and min of plots in frequency
    betalims=[-1 3]; %Range of beta in dispersion curve plot
    ILabelPos=[-1 -1]; %Position of I label
    RLabelPos=[1, -1;-1, 0.8;-1.0, 0.8];%Positions of R labels
    TLabelPos=[1, 0.8;-1, 0.8;-1.0, 0.8];%Positions of R labels
    NumTPlot=2^9; %Number of points in T to store
    NumZPlot=2^9; %Number of points in Z to store
    NumWPlot=2^9; %Number of points in W to store
%Material parameters
    L=60; %Propagation length in meters
    beta2=0.025;%GVD in ps^2/m
    beta3=0.000;%TOD in ps^3/m
%Pulse Parameters
    T0=1; %Input pulse width in ps
    dnu=-1.5;%Frequency offset in THz
%Boundary Parameters
    betaB1=0; %Boundary shift in 1/m for t>TB
    betaB0=0; %Boundary shift in 1/m for |t|>TB
    betaB2=0.7;%Boundary shift in 1/m for t<TB
    TB=5; %Position of temporal boundary in ps

%% Create time and frequency arrays-----
%Simulation arrays
    dt=tWindow/Nt; t=(-Nt/2:Nt/2-1)*dt;
    dW=2*pi/tWindow; W=(-Nt/2:Nt/2-1)*dW;
    dz=L/Nz; z=(0:Nz)*dz;

```

```

%Selection arrays for storage and plotting
    inds=1:Nt; %Index values for arrays
% Create array for selecting time values to store
    tselect=inds(and(t>=Tlims(1),t<=Tlims(2)));
    tselect=floor(linspace(tselect(1),tselect(end),NumTPlot));
% Create array for selecting frequency values to store
    Wselect=inds(and(W>=2*pi*nulims(1),W<=2*pi*nulims(2)));
    Wselect=floor(linspace(Wselect(1),Wselect(end),NumWPlot));
%Create Array for selecting distance values to store
    zselect=floor(linspace(1,Nz+1,NumZPlot));
    tPlot=t(tselect);    WPlot=W(Wselect);    zPlot=z(zselect);
% Find index values of input frequency, and input pulse bandwidth
    [~,idx0]=min(abs(W-2*pi*dnu));
    [~,idxneg]=min(abs(W-2*pi*dnu+2*pi*sqrt(log(10))/T0/2/pi));
    [~,idxpos]=min(abs(W-2*pi*dnu-2*pi*sqrt(log(10))/T0/2/pi));

%% Create boundary, phase terms, and probe pulse-----
%Boundary
    boundary=zeros(size(t));
    boundary(inds(t>TB))=betaB1;
    boundary(inds(t<-TB))=betaB2;
    boundary(inds(abs(t)<TB))=betaB0;
%Create Phase terms
    beta=beta2.*W.^2/2+beta3.*W.^3/6;
    disp=exp(1i*dz*ifftshift(beta));
    hhz=1i.*boundary*dz;
    slp=sign(beta(idx0+1)-beta(idx0-1));
%Probe and probe storage arrays
    Ain=exp(-0.5.*(t/T0).^2).*exp(-1i*2*pi*dnu.*t);
    specin=ifftshift(ifft(Ain).*Nt);
    AO=Ain;
    Ast=zeros(NumZPlot,NumTPlot); Ast(1,:)=AO(tselect);
    specst=zeros(NumZPlot,NumWPlot); specst(1,:)=specin(Wselect);

%% Calculate Reflected and Transmitted Frequencies-----
    if slp>0; betaB=betaB1-betaB0;
    else betaB=betaB2-betaB0; end
    p=[beta3/6 beta2/2 0 -beta(idx0);...
        beta3/6 beta2/2 0 -beta(idx0)+betaB];
    R=roots(p(1,:))/2/pi;
    T=roots(p(2,:))/2/pi;

%% Propagate Pulse-----
temp=AO.*exp(0.5*hhz);
jj=2;
for nn=2:Nz+1;

```

```

ftemp=ifft(temp).*disp;
A0=fft(ftemp);
temp=A0.*exp(hhz);
if zselect(jj)==nn
    Ap=temp.*exp(-0.5*hhz);
    Ast(jj,:)=Ap(tselect);
    Ap=ifftshift(ifft(Ap).*Nt);
    specst(jj,:)=Ap(Wselect);
    jj=jj+1;
end
end

%% Plots -----
set(0,'defaultlinelinewidth',1.5)
labelpos=[0.5 1.5];
hFig{1}=figure(1);
hAx{1}=subplot(1,3,1);%Create image of pulse evolution
imagesc(tPlot,zPlot,...
    10*log10((abs(Ast)./max(max(abs(Ast))))).^2)); hold all;
plot([TB TB], [0 L], '--k')
plot(-[TB TB], [0 L], '--k')
colormap(hot); hcb{1}=colorbar;caxis([-25 0]);
ylabel(hcb{1}, 'Intensity')
set(gca, 'Ydir', 'normal')
xlabel('t(ps)');ylabel('z(m)');
axis([Tlims 0 L])
text(labelpos(1),labelpos(2),'(a)',...
    'units','normalized',...
    'HorizontalAlignment','center',...
    'VerticalAlignment','top',...
    'color','k',...
    'fontsize',12);
hAx{2}=subplot(1,3,2);%Create image of spectral evolution
imagesc(WPlot/2/pi,zPlot,...
    10*log10((abs(specst)./max(max(abs(specst))))).^2));
colormap(hot); hcb{2}=colorbar;caxis([-25 0]);
ylabel(hcb{2}, 'Spectral Density')
set(gca, 'Ydir', 'normal', 'yticklabel', [])
axis([nulims 0 L])
xlabel('\nu-\nu_0 (THz)');
text(labelpos(1),labelpos(2),'(b)',...
    'units','normalized',...
    'HorizontalAlignment','center',...
    'VerticalAlignment','top',...
    'color','k',...
    'fontsize',12);
hAx{3}=subplot(1,3,3);% Plot dispersion curves

```

```

betashade=[beta(idxneg), beta(idxpos)];
betalow=min(betashade); betahigh=max(betashade);
fill([nulims(1) nulims(2) nulims(2) nulims(1)],...
     [betahigh betahigh betalow betalow],[1 0.6 0.6],...
     'edgecolor','none');hold all;
h2=plot(WPlot/2/pi,beta(Wselect),'-b',...
        WPlot/2/pi,beta(Wselect)+betaB,'--r');hold all;
plot(nulims,[beta(idx0) beta(idx0)],'-k');
plot([dnu dnu],[-300 300],'-k')
xlabel('\nu-\nu_0 (THz)');
ylabel('\beta^{\prime}-\beta_0 (m^{-1})');
axis([nulims betalims])
hleg=legend(h2,'t<T_B','t>T_B','location','eastoutside');
text(labelpos(1),1.2,'(c)','units','normalized',...
     'HorizontalAlignment','center','VerticalAlignment','top',...
     'color','k','fontsize',12);
plot([dnu,dnu+ILabelPos(1)],[beta(idx0), beta(idx0)+ILabelPos(2)],'-k')
text(dnu+ILabelPos(1),beta(idx0)+1.4*ILabelPos(2),'I','fontsize',11,...
     'HorizontalAlignment','center','VerticalAlignment','middle')

labels={'R1','R2','R3','R4'};
jk=1;
for ij=1:length(R)
    if and(isreal(R(ij)),and(R(ij)<nulims(2), R(ij)>nulims(1)))
        [~,idx]=min(abs(W/2/pi-R(ij)));
        if slp*(beta(idx+1)-beta(idx-1))<0
            plot([R(ij),R(ij)+RLabelPos(jk,1)],...
                 [beta(idx0), beta(idx0)+RLabelPos(jk,2)],'-k')
            text(R(ij)+RLabelPos(jk,1),beta(idx0)+RLabelPos(jk,2)*1.4,...
                 labels{jk},'HorizontalAlignment','center',...
                 'VerticalAlignment','middle','fontsize',11)
            jk=jk+1;
        end
    end
end

labels={'T1','T2','T3','T4'};
jk=1;
for ij=1:length(T)
    if and(isreal(T(ij)),and(T(ij)<nulims(2),T(ij)>nulims(1)))
        [~,idx]=min(abs(W/2/pi-T(ij)));
        if slp*(beta(idx+1)-beta(idx-1))>0
            plot([T(ij),T(ij)+TLabelPos(jk,1)],...
                 [beta(idx0) beta(idx0)+TLabelPos(jk,2)],'-k')
            text(T(ij)+TLabelPos(jk,1),beta(idx0)+TLabelPos(jk,2)*1.4,...
                 labels{jk},'HorizontalAlignment','center',...
                 'VerticalAlignment','middle','fontsize',11)
        end
    end
end

```

```
        jk=jk+1;
    end
end
end

%% Adjust plot sizes and positionspositions-----
xdim=2.5;    ydim=1.6;
x0=0.5;      y0=0.55;
xstep=2.8;   ystep=2.5;
cbydim=0.10; cbystep=0.1;
xleg=0.4;
set(gcf,'units','inches','Position',[10 0.5 6 5.5])

set(hAx{1},'units','inches','Position',[x0+0*xstep y0+ystep xdim ydim])
set(hAx{2},'units','inches','Position',[x0+1*xstep y0+ystep xdim ydim])
set(hAx{3},'units','inches','Position',[x0+xstep/2 y0 xdim ydim])

set(hcb{1},'location','northoutside','units','inches','position',...
    [x0 y0+ydim+cbystep+ystep xdim, cbydim])
set(hcb{2},'location','northoutside','units','inches','position',...
    [x0+xstep y0+ydim+cbystep+ystep xdim, cbydim])
set(hleg,'color','none','edgecolor','none','units','inches','position',...
    [x0+xstep/2+xdim+xleg y0+ydim/2 0 0])
toc
```

## Appendix B

### Spectral reflection and refraction

In the space-time analogy, it is often noted that the time lens provides the same function in the frequency domain that dispersion provides in the time domain. Put simply, dispersion causes the pulse to broaden in time while the spectrum is unchanged, while a time lens causes the spectrum to broaden in frequency while the pulse shape is unchanged. This occurs because the time and frequency domains are Fourier transforms of one another.

We now ask what happens if we have a quadratic phase profile in time, while the dispersion curve has a sharp boundary. In other words, there is a temporal phase of the form

$$\phi(t) = \frac{\Phi_2}{2} t^2, \quad (\text{B.1})$$

where  $\Phi_2$  is the second derivative of the temporal phase. For a dispersion discontinuity located at  $\omega = \omega_B$ , the dispersion curve has the form

$$\beta(\omega) = \beta_0 + \beta_B(\omega), \quad (\text{B.2})$$

where  $\beta_B$  is now the frequency dependent shift in the dispersion curve for  $\omega > \omega_B$ . This is the Fourier transform analog of the situation used to observe time reflection and refraction, and we therefore expect to observe a spectral analog of reflection and refraction.

Figure B.1 shows the evolution of the (a) shape and (b) spectrum of a Gaussian input pulse with  $T_0 = 0.25$  ps in a material satisfying the conditions for this spectral reflection and refraction. The simulation used dispersion parameters  $\beta_0 = 0$  and  $\beta_B = -0.5 \text{ m}^{-1}$ , and the temporal phase had  $\Phi_2 = -0.2 \text{ THz}^2/\text{m}$  with the input pulse offset by  $T_i = 3$  ps from the center of the phase profile. As expected, the spectral and temporal behavior is the reverse of the case of time reflection and refraction. The spectrum drifts during propagation due to the slope of the temporal phase at  $t = T_D$ , and eventually splits into multiple moving frequencies as the spectral boundary is crossed. At the same time, the pulse now splits and shifts in time, forming pulses at  $t = -3$  ps and  $t = 2$  ps. Figure B.1(c) shows how the jumps in time are caused by conservation of the temporal phase  $\phi(t)$  on each side of the spectral boundary. Note that the pulse does not spontaneously generate at the reflected or transmitted time. Instead, the pulse tails broaden significantly as the

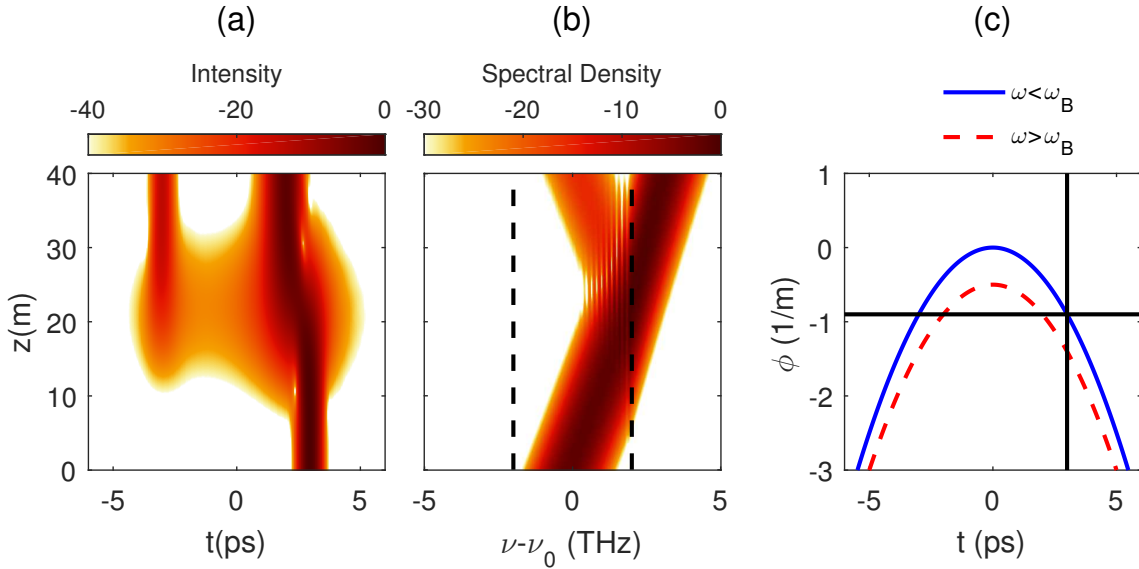


Figure B.1: Evolution of pulse (a) shape and (b) spectrum for a Gaussian input pulse in the presence of a parabolic temporal phase and a dispersion discontinuity. (c) The temporal phase profiles for  $\omega < \omega_B$  (solid blue) and  $\omega > \omega_B$  (dashed red).

spectral boundary is reached, and energy moves to the two new times.

We can find equations for the reflected and transmitted times in an analogous way to the frequencies in time reflection and refraction. In this case, we require that  $\phi(t) + \beta_B(\omega)$  be constant on either side of the spectral boundary. This leads to the spectral analogs of Snell's laws as

$$T_r = -T_i, \quad T_t = T_i \sqrt{1 - \frac{2\beta_B}{\Phi_2 T_i^2}}. \quad (\text{B.3})$$

Examining the transmitted time equation, we see that  $T_t$  becomes complex when  $2\beta_B > \Phi_2 T_i^2$ . In this case, we expect a spectral analog of TIR to occur, and all of the energy to be transferred to the reflected pulse at  $t = T_r$ . Figure B.2 shows the same simulation as Fig. B.1, but with  $\beta_B = -1.3$  so that the spectral TIR condition is satisfied for the whole pulse duration. We clearly see that the pulse entirely shifts to the time  $t = T_r = -3$  ps, as predicted. As with both the spatial and temporal cases, we can create a spectral waveguide can be formed using two dispersion boundaries that satisfy the TIR condition. This will confine the spectrum in frequency space in the same way a temporal waveguide confines a pulse in time.

Observing this effect would be of great interest. The biggest challenge is to create the sharp change in the dispersion profile, while still being able to generate the quadratic phase profile. One option for creating a sharp dispersion transition is to work near a resonant absorption in an atomic gas. In this case, there will be very little dispersion outside far away from the resonance, but the dispersion quickly spikes near resonance. However, this sharp change in dispersion is accompanied by a significant increase in absorption.

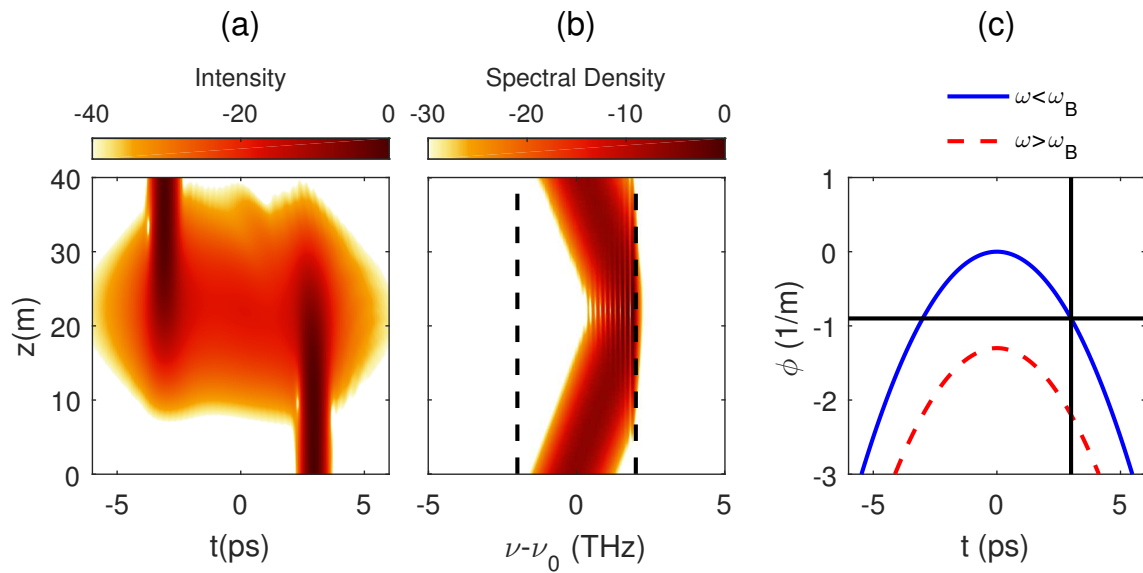


Figure B.2: Evolution of pulse (a) shape and (b) spectrum for a Gaussian input pulse in the presence of a parabolic temporal phase and a dispersion discontinuity. The dispersion changes by  $\beta_B = -1.3 \text{ m}^{-1}$  at the discontinuity. (c) The temporal phase profiles for  $\omega < \omega_B$  (solid blue) and  $\omega > \omega_B$  (dashed red).

---

## Bibliography

- [1] J. W. Goodman, *Introduction to Fourier Optics*, Roberts & Company Publishers, third ed., 2005.
- [2] P. Tournois, “Analogie optique de la compression d’impulsion,” *C. R. Acad. Sci.* **258**, pp. 3839–3842, 1964.
- [3] P. Tournois, J. L. Vernet, and G. Bienvenu, “Sur l’analogie optique de certains montages électroniques: Formation d’images temporelles de signaux électriques,” *C. R. Acad. Sci.* **267**, pp. 375–378, 1968.
- [4] S. A. Akhmanov, A. P. Sukhorukov, and A. S. Chirkin, “Nonstationary phenomena and space-time analogy in nonlinear optics,” *Sov. Phys. JETP* **28**, pp. 748–757, 1969.
- [5] R. Salem, M. A. Foster, and A. L. Gaeta, “Application of space–time duality to ultrahigh-speed optical signal processing,” *Adv. Opt. Photonics* **5**, pp. 274–317, Sept. 2013.
- [6] K. Goda and B. Jalali, “Dispersive Fourier transformation for fast continuous single-shot measurements,” *Nat Photon* **7**, pp. 102–112, Feb. 2013.
- [7] K. Goda, A. Mahjoubfar, C. Wang, A. Fard, J. Adam, D. R. Gossett, A. Ayazi, E. Sollier, O. Malik, E. Chen, Y. Liu, R. Brown, N. Sarkhosh, D. Di Carlo, and B. Jalali, “Hybrid Dispersion Laser Scanner,” *Sci. Rep.* **2**, pp. 445: 1–8, June 2012.
- [8] P. Kelkar, F. Coppinger, A. Bhushan, and B. Jalali, “Time-domain optical sensing,” *Electron. Lett.* **35**(19), pp. 1661 – 1662, 1999.
- [9] T. Jansson, “Real-time Fourier transformation in dispersive optical fibers,” *Opt. Lett.* **8**, pp. 232–234, Apr. 1983.
- [10] J. Azaña, L. R. Chen, M. A. Muriel, and P. W. E. Smith, “Experimental demonstration of real-time Fourier transformation using linearly chirped fibre Bragg gratings,” *Electron. Lett.* **35**(25), pp. 2223–2224, 1999.
- [11] M. A. Muriel, J. Azaña, and A. Carballar, “Real-time Fourier transformer based on fiber gratings,” *Opt. Lett.* **24**, pp. 1–3, Jan. 1999.

- 
- [12] B. H. Kolner, "Active pulse compression using an integrated electro-optic phase modulator," *Appl. Phys. Lett.* **52**, pp. 1122–1124, Apr. 1988.
- [13] A. A. Godil, B. A. Auld, and D. M. Bloom, "Time-lens producing 1.9 ps optical pulses," *Appl. Phys. Lett.* **62**, pp. 1047–1049, Mar. 1993.
- [14] B. Kolner, "Space-time duality and the theory of temporal imaging," *IEEE J. Quantum Electron.* **30**, pp. 1951–1963, Aug. 1994.
- [15] M. T. Kauffman, W. C. Banyai, A. A. Godil, and D. M. Bloom, "Time-to-frequency converter for measuring picosecond optical pulses," *Appl. Phys. Lett.* **64**, pp. 270–272, Jan. 1994.
- [16] J. Azana, N. Berger, B. Levit, and B. Fischer, "Spectro-temporal imaging of optical pulses with a single time lens," *IEEE Photonics Technol. Lett.* **16**, pp. 882–884, Mar. 2004.
- [17] Y. Dai and C. Xu, "Generation of high repetition rate femtosecond pulses from a CW laser by a time-lens loop," *Opt. Express* **17**, pp. 6584–6590, Apr. 2009.
- [18] J. van Howe, J. H. Lee, and C. Xu, "Generation of 3.5 nJ femtosecond pulses from a continuous-wave laser without mode locking," *Opt. Lett.* **32**(11), pp. 1408–1410, 2007.
- [19] C. Bennett and B. Kolner, "Principles of parametric temporal imaging - Part I: System configurations," *IEEE J. Quantum Electron.* **36**, pp. 430–437, Apr. 2000.
- [20] C. Bennett and B. Kolner, "Principles of parametric temporal imaging - Part II: System performance," *IEEE J. Quantum Electron.* **36**, pp. 649–655, June 2000.
- [21] R. Salem, M. A. Foster, A. C. Turner, D. F. Geraghty, M. Lipson, and A. L. Gaeta, "Optical time lens based on four-wave mixing on a silicon chip," *Opt. Lett.* **33**(10), pp. 1047–1049, 2008.
- [22] Y. Okawachi, R. Salem, M. A. Foster, A. C. Turner-Foster, M. Lipson, and A. L. Gaeta, "High-resolution spectroscopy using a frequency magnifier," *Opt Express* **17**(7), pp. 5691–5697, 2009.
- [23] R. Salem, M. A. Foster, A. C. Turner-Foster, D. F. Geraghty, M. Lipson, and A. L. Gaeta, "High-speed optical sampling using a silicon-chip temporal magnifier," *Opt. Express* **17**(6), pp. 4324–4329, 2009.
- [24] M. A. Foster, R. Salem, and A. L. Gaeta, "Ultra-high-Speed Optical Processing Using Space-Time Duality," *Opt. Photonics News* **22**, pp. 29–35, May 2011.
- [25] Y. Okawachi, R. Salem, A. R. Johnson, K. Saha, J. S. Levy, M. Lipson, and A. L. Gaeta, "Asynchronous single-shot characterization of high-repetition-rate ultrafast waveforms using a time-lens-based temporal magnifier," *Opt. Lett.* **37**, pp. 4892–4894, Dec. 2012.

- [26] M. T. Kauffman, A. A. Godil, B. A. Auld, W. C. Banyai, and D. M. Bloom, "Applications of time lens optical systems," *Electron. Lett.* **29**(3), pp. 268–269, 1993.
- [27] B. H. Kolner and M. Nazarathy, "Temporal imaging with a time lens," *Opt. Lett.* **14**, pp. 630–632, June 1989.
- [28] A. Pasquazi, Y. Y. Park, S. T. Chu, B. E. Little, F. Légaré, R. Morandotti, J. Azaña, and D. J. Moss, "Time-Lens Measurement of Subpicosecond Optical Pulses in CMOS Compatible High-Index Glass Waveguides," *IEEE J. Sel. Top. Quantum Electron.* **18**, pp. 629–636, Mar. 2012.
- [29] K. Wang, C. W. Freudiger, J. H. Lee, B. G. Saar, X. S. Xie, and C. Xu, "All fiber 1064-nm time-lens source for coherent anti-Stokes Raman scattering and stimulated Raman scattering microscopy," in *Proc. of SPIE*, **7903**, pp. 79030X: 1–6, 2011.
- [30] B. Jalali, D. R. Solli, and S. Gupta, "Silicon's time lens," *Nat Photon* **3**, pp. 8–10, Jan. 2009.
- [31] B. W. Plansinis, W. R. Donaldson, and G. P. Agrawal, "Temporal waveguides for optical pulses," *J. Opt. Soc. Am. B* **33**, pp. 1112–1119, June 2016.
- [32] M. Born and E. Wolf, *Principles of Optics: Electromagnetic Theory of Propagation, Interference, and Diffraction of Light*, Cambridge University, 7th expanded ed., Oct. 1999.
- [33] G. P. Agrawal, *Nonlinear Fiber Optics*, Elsevier, Amsterdam, 5 ed., 2013.
- [34] C. Bennett and B. Kolner, "Aberrations in temporal imaging," *IEEE J. Quantum Electron.* **37**, pp. 20–32, Jan. 2001.
- [35] S. Gupta and B. Jalali, "Time-warp correction and calibration in photonic time-stretch analog-to-digital converter," *Opt. Lett., OL* **33**, pp. 2674–2676, Nov. 2008.
- [36] W. J. Caputi, "Stretch: A Time-Transformation Technique," *IEEE Trans. Aerosp. Electron. Syst.* **AES-7**, pp. 269–278, Mar. 1971.
- [37] Y. C. Tong, L. Y. Chan, and H. K. Tsang, "Fibre dispersion or pulse spectrum measurement using a sampling oscilloscope," *Electron. Lett.* **33**, pp. 983–985, May 1997.
- [38] J. Azana and M. A. Muriel, "Real-time optical spectrum analysis based on the time-space duality in chirped fiber gratings," *IEEE J. Quantum Electron.* **36**, pp. 517–526, May 2000.
- [39] J. Chou, Y. Han, and B. Jalali, "Time-wavelength spectroscopy for chemical sensing," *IEEE Photonics Technol. Lett.* **16**, pp. 1140–1142, Apr. 2004.

- [40] J. Hult, R. S. Watt, and C. F. Kaminski, "High bandwidth absorption spectroscopy with a dispersed supercontinuum source," *Opt. Express, OE* **15**, pp. 11385–11395, Sept. 2007.
- [41] D. R. Solli, C. Ropers, P. Koonath, and B. Jalali, "Optical rogue waves," *Nature* **450**, pp. 1054–1057, Dec. 2007.
- [42] J. Chou, D. R. Solli, and B. Jalali, "Real-time spectroscopy with subgigahertz resolution using amplified dispersive Fourier transformation," *Appl. Phys. Lett.* **92**, pp. 111102: 1–3, Mar. 2008.
- [43] D. R. Solli, J. Chou, and B. Jalali, "Amplified wavelength–time transformation for real-time spectroscopy," *Nat Photon* **2**, pp. 48–51, Jan. 2008.
- [44] K. Goda and B. Jalali, "Noise figure of amplified dispersive Fourier transformation," *Phys. Rev. A* **82**, pp. 033827: 1–9, Sept. 2010.
- [45] Y. Sych, R. Engelbrecht, B. Schmauss, D. Kozlov, T. Seeger, and A. Leipertz, "Broadband time-domain absorption spectroscopy with a ns-pulse supercontinuum source," *Opt. Express, OE* **18**, pp. 22762–22771, Oct. 2010.
- [46] V. Torres-Company, J. Lancis, and P. Andrés, "Chapter 1 - Space-Time Analogies in Optics," in *Progress in Optics*, E. Wolf, ed., **56**, pp. 1–80, Elsevier, 2011.
- [47] D. R. Solli, G. Herink, B. Jalali, and C. Ropers, "Fluctuations and correlations in modulation instability," *Nat Photon* **6**, pp. 463–468, July 2012.
- [48] B. Wetzell, A. Stefani, L. Larger, P. A. Lacourt, J. M. Merolla, T. Sylvestre, A. Kudlinski, A. Mussot, G. Genty, F. Dias, and J. M. Dudley, "Real-time full bandwidth measurement of spectral noise in supercontinuum generation," *Sci. Rep.* **2**, pp. 882: 1–7, Nov. 2012.
- [49] Y. Park, T.-J. Ahn, J.-C. Kieffer, and J. Azaña, "Optical frequency domain reflectometry based on real-time Fourier transformation," *Opt. Express* **15**, pp. 4597–4616, Apr. 2007.
- [50] K. Goda, K. K. Tsia, and B. Jalali, "Serial time-encoded amplified imaging for real-time observation of fast dynamic phenomena," *Nature* **458**, pp. 1145–1149, Apr. 2009.
- [51] F. Qian, Q. Song, E.-k. Tien, S. K. Kalyoncu, and O. Boyraz, "Real-time optical imaging and tracking of micron-sized particles," *Optics Communications* **282**, pp. 4672–4675, Dec. 2009.
- [52] K. K. Tsia, K. Goda, D. Capewell, and B. Jalali, "Performance of serial time-encoded amplified microscope," *Opt. Express, OE* **18**, pp. 10016–10028, May 2010.
- [53] A. M. Fard, A. Mahjoubfar, K. Goda, D. R. Gossett, D. D. Carlo, and B. Jalali, "Nomarski serial time-encoded amplified microscopy for high-speed contrast-enhanced imaging of transparent media," *Biomed. Opt. Express* **2**, pp. 3387–3392, Dec. 2011.

- [54] S. H. Kim, K. Goda, A. Fard, and B. Jalali, "Optical time-domain analog pattern correlator for high-speed real-time image recognition," *Opt. Lett.* **36**, pp. 220–222, Jan. 2011.
- [55] A. Mahjoubfar, K. Goda, A. Ayazi, A. Fard, S. H. Kim, and B. Jalali, "High-speed nanometer-resolved imaging vibrometer and velocimeter," *Appl. Phys. Lett.* **98**, pp. 101107: 1–3, Mar. 2011.
- [56] K. Goda, A. Ayazi, D. R. Gossett, J. Sadasivam, C. K. Lonappan, E. Sollier, A. M. Fard, S. C. Hur, J. Adam, C. Murray, C. Wang, N. Brackbill, D. D. Carlo, and B. Jalali, "High-throughput single-microparticle imaging flow analyzer," *PNAS* **109**, pp. 11630–11635, July 2012.
- [57] T. T. W. Wong, A. K. S. Lau, K. K. Y. Wong, and K. K. Tsia, "Optical time-stretch confocal microscopy at 1 mm," *Opt. Lett., OL* **37**, pp. 3330–3332, Aug. 2012.
- [58] C. Lei, B. Guo, Z. Cheng, and K. Goda, "Optical time-stretch imaging: Principles and applications," *Appl. Phys. Rev.* **3**, pp. 011102:1–13, Mar. 2016.
- [59] L. K. Mouradian, F. Louradour, V. Messenger, A. Barthelemy, and C. Froehly, "Spectro-temporal imaging of femtosecond events," *IEEE J. Quantum Electron.* **36**, pp. 795–801, July 2000.
- [60] T. Hirooka and M. Nakazawa, "All-Optical 40-GHz Time-Domain Fourier Transformation Using XPM With a Dark Parabolic Pulse," *IEEE Photonics Technol. Lett.* **20**, pp. 1869–1871, Nov. 2008.
- [61] T. T. Ng, F. Parmigiani, M. Ibsen, Z. Zhang, P. Petropoulos, and D. J. Richardson, "Compensation of Linear Distortions by Using XPM With Parabolic Pulses as a Time Lens," *IEEE Photonics Technol. Lett.* **20**, pp. 1097–1099, July 2008.
- [62] R. W. Boyd, *Nonlinear Optics*, Academic Press, 2003.
- [63] M. A. Foster, R. Salem, D. F. Geraghty, A. C. Turner-Foster, M. Lipson, and A. L. Gaeta, "Silicon-chip-based ultrafast optical oscilloscope," *Nature* **456**(7218), pp. 81–84, 2008.
- [64] C. V. Bennett, R. P. Scott, and B. H. Kolner, "Temporal magnification and reversal of 100 Gb/s optical data with an up-conversion time microscope," *Appl. Phys. Lett.* **65**, pp. 2513–2515, Nov. 1994.
- [65] C. V. Bennett and B. H. Kolner, "Upconversion time microscope demonstrating 103x magnification of femtosecond waveforms," *Opt. Lett.* **24**, pp. 783–785, June 1999.
- [66] D. H. Broaddus, M. A. Foster, O. Kuzucu, A. C. Turner-Foster, K. W. Koch, M. Lipson, and A. L. Gaeta, "Temporal-imaging system with simple external-clock triggering," *Opt. Express* **18**(13), pp. 14262–14269, 2010.

- [67] J. D. Kafka, B. H. Kolner, T. Baer, and D. M. Bloom, "Compression of pulses from a continuous-wave mode-locked Nd:YAG laser," *Opt. Lett.* **9**, p. 505, Nov. 1984.
- [68] M. A. Foster, R. Salem, Y. Okawachi, A. C. Turner-Foster, M. Lipson, and A. L. Gaeta, "Ultrafast waveform compression using a time-domain telescope," *Nat Photon* **3**, pp. 581–585, Oct. 2009.
- [69] T. Kobayashi, H. Yao, K. Amano, Y. Fukushima, A. Morimoto, and T. Sueta, "Optical pulse compression using high-frequency electrooptic phase modulation," *IEEE J. Quantum Electron.* **24**, pp. 382–387, Feb. 1988.
- [70] J. van Howe, J. Hansryd, and C. Xu, "Multiwavelength pulse generator using time-lens compression," *Opt. Lett.* **29**, pp. 1470–1472, July 2004.
- [71] L. F. Mollenauer and C. Xu, "Time-lens timing-jitter compensator in ultra-long haul DWDM dispersion managed soliton transmissions," pp. CPBD1:1–3, (Long Beach, CA), May 2002.
- [72] L. A. Jiang, M. E. Grein, H. A. Haus, E. P. Ippen, and H. Yokoyama, "Timing jitter eater for optical pulse trains," *Opt. Lett.* **28**, pp. 78–80, Jan. 2003.
- [73] M. Nakazawa, T. Hirooka, F. Futami, and S. Watanabe, "Ideal distortion-free transmission using optical Fourier transformation and Fourier transform-limited optical pulses," *IEEE Photonics Technol. Lett.* **16**, pp. 1059–1061, Apr. 2004.
- [74] O. Kuzucu, Y. Okawachi, R. Salem, M. A. Foster, A. C. Turner-Foster, M. Lipson, and A. L. Gaeta, "Spectral phase conjugation via temporal imaging," *Opt. Express* **17**, pp. 20605–20614, Oct. 2009.
- [75] M. Fridman, A. Farsi, Y. Okawachi, and A. L. Gaeta, "Demonstration of temporal cloaking," *Nature* **481**, pp. 62–65, Jan. 2012.
- [76] W. R. Donaldson, R. Boni, L. Keck, and P. Jaanimagi, "A self-calibrating, multichannel streak camera for inertial confinement fusion applications," *Review of Scientific Instruments* **73**, pp. 2606–2615, June 2002.
- [77] R. Lerche, J. W. McDonald, R. L. Griffith, G. Vergel de Dios, D. S. Andrews, A. W. Huey, P. M. Bell, and O. L. Landen, "Preliminary performance measurements for a streak camera with a large-format direct-coupled charge-coupled device readout," *Review of Scientific Instruments* **75**, pp. 4042–4044, Oct. 2004.
- [78] J. Qiao, P. Jaanimagi, R. Boni, J. Bromage, and E. Hill, "Measuring 8–250 ps short pulses using a high-speed streak camera on kilojoule, petawatt-class laser systems," *Review of Scientific Instruments* **84**, pp. 073104: 1–5, July 2013.
- [79] B.-L. Qian and H. E. Elsayed-Ali, "Electron pulse broadening due to space charge effects in a photoelectron gun for electron diffraction and streak camera systems," *Journal of Applied Physics* **91**, pp. 462–468, Dec. 2001.

- [80] B. J. Siwick, J. R. Dwyer, R. E. Jordan, and R. J. D. Miller, “Ultrafast electron optics: Propagation dynamics of femtosecond electron packets,” *Journal of Applied Physics* **92**, pp. 1643–1648, July 2002.
- [81] A. Verna, G. Greco, V. Lollobrigida, F. Offi, and G. Stefani, “Space-charge effects in high-energy photoemission,” *J. Electron Spectrosc. Relat. Phenom.* **209**, pp. 14–25, May 2016.
- [82] R. Trebino, *Frequency-Resolved Optical Gating: The Measurement of Ultrashort Laser Pulses*, Springer Science & Business Media, 2012.
- [83] T. C. Wong and R. Trebino, “Single-frame measurement of complex laser pulses tens of picoseconds long using pulse-front tilt in cross-correlation frequency-resolved optical gating,” *J. Opt. Soc. Am. B, JOSAB* **30**, pp. 2781–2786, Nov. 2013.
- [84] I. Kang, C. Dorrer, and F. Quochi, “Implementation of electro-optic spectral shearing interferometry for ultrashort pulse characterization,” *Opt. Lett.* **28**(22), pp. 2264–2266, 2003.
- [85] B. Kolner and D. Bloom, “Electrooptic sampling in GaAs integrated circuits,” *IEEE J. Quantum Electron.* **22**, pp. 79–93, Jan. 1986.
- [86] M. A. Duguay, L. E. Hargrove, and K. B. Jefferts, “Optical frequency translation of mode-locked laser pulses,” *Appl. Phys. Lett.* **9**(8), pp. 287–290, 1966.
- [87] M. Duguay and J. Hansen, “Optical frequency shifting of a mode-locked laser beam,” *IEEE J. Quantum Electron.* **4**(8), pp. 477–481, 1968.
- [88] C. Dorrer and J. Bromage, “High-sensitivity optical pulse characterization using Sagnac electro-optic spectral shearing interferometry,” *Opt. Lett.* **35**(9), pp. 1353–1355, 2010.
- [89] E. Hecht, *Optics*, Addison-Wesley, 4th ed., 2002.
- [90] B. E. A. Saleh and M. C. Teich, *Fundamentals of Photonics*, Wiley, Hoboken, NJ, 2 ed., 2007.
- [91] G. P. Agrawal, *Fiber-Optic Communication Systems*, Wiley, 4 ed., 2010.
- [92] L. Felsen and G. Whitman, “Wave propagation in time-varying media,” *IEEE Trans. Antennas Propag.* **18**, pp. 242–253, Mar. 1970.
- [93] J. T. Mendonça and P. K. Shukla, “Time refraction and time reflection: Two basic concepts,” *Phys. Scr.* **65**, pp. 160–163, Aug. 2002.
- [94] Y. Xiao, D. N. Maywar, and G. P. Agrawal, “Reflection and transmission of electromagnetic waves at a temporal boundary,” *Opt. Lett.* **39**, pp. 574–577, Feb. 2014.
- [95] D. K. Kalluri, *Electromagnetics of Time Varying Complex Media: Frequency and Polarization Transformer, Second Edition*, CRC Press, Apr. 2016.

- [96] F. R. Morgenthaler, "Velocity Modulation of Electromagnetic Waves," *IRE Trans. Microw. Theory Tech.* **6**, pp. 167–172, Apr. 1958.
- [97] J. C. AuYeung, "Phase-conjugate reflection from a temporal dielectric boundary," *Opt. Lett.*, *OL* **8**, pp. 148–150, Mar. 1983.
- [98] D. K. Kalluri, "On reflection from a suddenly created plasma half-space: Transient solution," *IEEE Trans. Plasma Sci.* **16**, pp. 11–16, Feb. 1988.
- [99] S. C. Wilks, J. M. Dawson, W. B. Mori, T. Katsouleas, and M. E. Jones, "Photon accelerator," *Phys. Rev. Lett.* **62**, pp. 2600–2603, May 1989.
- [100] D. K. Kalluri, "Effect of switching a magnetoplasma medium on a traveling wave: Longitudinal propagation," *IEEE Trans. Antennas Propag.* **37**, pp. 1638–1642, Dec. 1989.
- [101] D. K. Kalluri, "Frequency shifting of electromagnetic radiation by sudden creation of a plasma slab," *Journal of Applied Physics* **72**, pp. 4575–4580, Nov. 1992.
- [102] J. T. Mendonça, *Theory of Photon Acceleration*, Series in Plasma Physics, Institute of Physics Publishing, 2001.
- [103] M. F. Yanik and S. Fan, "Time Reversal of Light with Linear Optics and Modulators," *Phys. Rev. Lett.* **93**, pp. 173903: 1–4, Oct. 2004.
- [104] M. Notomi and S. Mitsugi, "Wavelength conversion via dynamic refractive index tuning of a cavity," *Phys. Rev. A* **73**, pp. 051803: 1–4, May 2006.
- [105] S. F. Preble, Q. Xu, and M. Lipson, "Changing the colour of light in a silicon resonator," *Nat Photon* **1**, pp. 293–296, May 2007.
- [106] T. Tanabe, M. Notomi, H. Taniyama, and E. Kuramochi, "Dynamic Release of Trapped Light from an Ultrahigh-Q Nanocavity via Adiabatic Frequency Tuning," *Phys. Rev. Lett.* **102**, pp. 043907: 1–4, Jan. 2009.
- [107] T. Kampfrath, D. M. Beggs, T. F. Krauss, and L. K. Kuipers, "Complete response characterization of ultrafast linear photonic devices," *Opt. Lett.*, *OL* **34**, pp. 3418–3420, Nov. 2009.
- [108] T. Kampfrath, D. M. Beggs, T. P. White, A. Melloni, T. F. Krauss, and L. Kuipers, "Ultrafast adiabatic manipulation of slow light in a photonic crystal," *Phys. Rev. A* **81**, pp. 043837: 1–6, Apr. 2010.
- [109] A. Nishida, N. Yugami, T. Higashiguchi, T. Otsuka, F. Suzuki, M. Nakata, Y. Sentoku, and R. Kodama, "Experimental observation of frequency up-conversion by flash ionization," *Appl. Phys. Lett.* **101**(16), pp. 161118: 1–3, 2012.
- [110] C. Yeh and K. F. Casey, "Reflection and Transmission of Electromagnetic Waves by a Moving Dielectric Slab," *Phys. Rev.* **144**, pp. 665–669, Apr. 1966.

- [111] C. Yeh, “Reflection and Transmission of Electromagnetic Waves by a Moving Plasma Medium,” *Journal of Applied Physics* **37**, pp. 3079–3082, July 1966.
- [112] C. Tsai and B. A. Auld, “Wave Interactions with Moving Boundaries,” *Journal of Applied Physics* **38**, pp. 2106–2115, Apr. 1967.
- [113] K. Kunz, “Plane electromagnetic waves in moving media and reflections from moving interfaces,” *Journal of Applied Physics* **51**, pp. 873–884, Feb. 1980.
- [114] F. Biancalana, A. Amann, A. V. Uskov, and E. P. O’Reilly, “Dynamics of light propagation in spatiotemporal dielectric structures,” *Phys. Rev. E* **75**, pp. 046607: 1–12, Apr. 2007.
- [115] K. A. Lurie, “An introduction to the mathematical theory of dynamic materials,” in *Advances in Mechanics and Mathematics*, D. Y. Gao and R. W. Ogden, eds., **15**, Springer, New York, 2007.
- [116] N. N. Rosanov, “Transformation of electromagnetic radiation at moving inhomogeneities of a medium,” *JETP Lett.* **88**(8), pp. 501–504, 2008.
- [117] N. N. Rozanov, “Transformation of electromagnetic radiation by rapidly moving inhomogeneities of a transparent medium,” *J. Exp. Theor. Phys.* **108**(1), pp. 140–148, 2009.
- [118] Z. Yu and S. Fan, “Complete optical isolation created by indirect interband photonic transitions,” *Nat Photon* **3**, pp. 91–94, Feb. 2009.
- [119] M. Castellanos Muñoz, A. Y. Petrov, L. O’Faolain, J. Li, T. F. Krauss, and M. Eich, “Optically Induced Indirect Photonic Transitions in a Slow Light Photonic Crystal Waveguide,” *Phys. Rev. Lett.* **112**, pp. 053904: 1–5, Feb. 2014.
- [120] N. Chamanara and C. Caloz, “Electromagnetic spectrum transformation in space-time modulated and dispersion engineered graphene surface plasmons,” in *2016 10th European Conference on Antennas and Propagation (EuCAP)*, pp. 1–2, Apr. 2016.
- [121] Y. Hadad, D. L. Sounas, and A. Alu, “Space-time gradient metasurfaces,” *Phys. Rev. B* **92**, pp. 100304: 1–6, Sept. 2015.
- [122] H. Qu, Z.-L. Deck-Léger, C. Caloz, and M. Skorobogatiy, “Frequency generation in moving photonic crystals,” *J. Opt. Soc. Am. B, JOSAB* **33**, pp. 1616–1626, Aug. 2016.
- [123] Z.-L. Deck-Léger and C. Caloz, “Wave Scattering by Superluminal Spacetime Slab,” *arXiv:1611.01366*, Nov. 2016.
- [124] A. V. Gorbach and D. V. Skryabin, “Bouncing of a dispersive pulse on an accelerating soliton and stepwise frequency conversion in optical fibers,” *Opt. Express* **15**, pp. 14560–14565, Oct. 2007.

- [125] A. Demircan, S. Amiranashvili, and G. Steinmeyer, “Controlling light by light with an optical event horizon,” *Phys. Rev. Lett.* **106**, p. 163901, Apr. 2011.
- [126] E. Rubino, A. Lotti, F. Belgiorno, S. L. Cacciatori, A. Couairon, U. Leonhardt, and D. Faccio, “Soliton-induced relativistic-scattering and amplification,” *Sci. Rep.* **2**, p. 932, Dec. 2012.
- [127] L. Tartara, “Frequency shifting of femtosecond pulses by reflection at solitons,” *IEEE J. Quantum Electron.* **48**, pp. 1439–1442, Aug. 2012.
- [128] A. Shipulin, G. Onishchukov, and B. A. Malomed, “Suppression of soliton jitter by a copropagating support structure,” *J. Opt. Soc. Am. B* **14**, pp. 3393–3402, Dec. 1997.
- [129] R. Driben, A. V. Yulin, A. Efimov, and B. A. Malomed, “Trapping of light in solitonic cavities and its role in the supercontinuum generation,” *Opt. Express* **21**, p. 19091, Aug. 2013.
- [130] A. Demircan, S. Amiranashvili, C. Brée, U. Morgner, and G. Steinmeyer, “Supercontinuum generation by multiple scatterings at a group velocity horizon,” *Opt. Express* **22**, pp. 3866–3879, Feb. 2014.
- [131] J. Steinhauer, “Observation of self-amplifying Hawking radiation in an analogue black-hole laser,” *Nat Phys* **10**, pp. 864–869, Nov. 2014.
- [132] S. F. Wang, A. Mussot, M. Conforti, X. L. Zeng, and A. Kudlinski, “Bouncing of a dispersive wave in a solitonic cage,” *Opt. Lett.* **40**, pp. 3320–3323, July 2015.
- [133] Z. Deng, X. Fu, J. Liu, C. Zhao, and S. Wen, “Trapping and controlling the dispersive wave within a solitonic well,” *Opt. Express* **24**, pp. 10302–10312, May 2016.
- [134] N. N. Rosanov, N. V. Vysotina, and A. N. Shatsev, “Forward light reflection from a moving inhomogeneity,” *Jetp Lett.* **93**, pp. 308–312, May 2011.
- [135] U. Leonhardt, “A laboratory analogue of the event horizon using slow light in an atomic medium,” *Nature* **415**, pp. 406–409, Jan. 2002.
- [136] T. G. Philbin, C. Kuklewicz, S. J. Robertson, S. Hill, F. König, and U. Leonhardt, “Fiber-optical analog of the event horizon,” *Science* **319**, pp. 1367–1370, Mar. 2008.
- [137] F. Belgiorno, S. L. Cacciatori, M. Clerici, V. Gorini, G. Ortenzi, L. Rizzi, E. Rubino, V. G. Sala, and D. Faccio, “Hawking radiation from ultrashort laser pulse filaments,” *Phys. Rev. Lett.* **105**, p. 203901, Nov. 2010.
- [138] S. Robertson and U. Leonhardt, “Frequency shifting at fiber-optical event horizons: The effect of Raman deceleration,” *Phys. Rev. A* **81**, p. 063835, June 2010.

- [139] E. Rubino, F. Belgiorno, S. L. Cacciatori, M. Clerici, V. Gorini, G. Ortenzi, L. Rizzi, V. G. Sala, M. Kolesik, and D. Faccio, “Experimental evidence of analogue Hawking radiation from ultrashort laser pulse filaments,” *New J. Phys.* **13**(8), p. 085005, 2011.
- [140] D. Faccio, “Laser pulse analogues for gravity and analogue Hawking radiation,” *Contemp. Phys.* **53**, pp. 97–112, Dec. 2012.
- [141] D. Faccio, T. Arane, M. Lamperti, and U. Leonhardt, “Optical black hole lasers,” *Class. Quantum Grav.* **29**, p. 224009, Oct. 2012.
- [142] G. Genty, M. Erkintalo, and J. M. Dudley, “Do optical event horizons really exist? The physics of nonlinear reflection at a soliton boundary,” OSA, (Colorado Springs, CO), June 2012.
- [143] M. Petev, N. Westerberg, D. Moss, E. Rubino, C. Rimoldi, S. L. Cacciatori, F. Belgiorno, and D. Faccio, “Blackbody Emission from Light Interacting with an Effective Moving Dispersive Medium,” *Phys. Rev. Lett.* **111**, pp. 043902: 1–5, July 2013.
- [144] G. P. Agrawal, *Lightwave Technology: Components and Devices*, Wiley, 2004.
- [145] K. Okamoto, *Fundamentals of Optical Waveguides*, Academic Press, 2 ed., 2006.
- [146] A. V. Yulin, R. Driben, B. A. Malomed, and D. V. Skryabin, “Soliton interaction mediated by cascaded four wave mixing with dispersive waves,” *Opt. Express* **21**, pp. 14474–14479, June 2013.
- [147] X. Li, Y. Shimizu, S. Ito, W. Gao, and L. Zeng, “Fabrication of diffraction gratings for surface encoders by using a Lloyd’s mirror interferometer with a 405 nm laser diode,” *Proc SPIE* **8759**, p. 87594Q, 2013.
- [148] E. B. Hochberg and N. L. Chrien, “Lloyd’s mirror for MTF testing of MISR CCD,” *Proc SPIE* **2830**, pp. 274–285, 1996.
- [149] J. G. Bolton, G. J. Stanley, and O. B. Slee, “Positions of Three Discrete Sources of Galactic Radio-Frequency Radiation,” in *Classics in Radio Astronomy*, pp. 239–241, Springer Netherlands, 1982.
- [150] B. W. Plansinis, W. R. Donaldson, and G. P. Agrawal, “What is the temporal analog of reflection and refraction of optical beams?,” *Phys. Rev. Lett.* **115**, p. 183901, Oct. 2015.
- [151] J. Azaña and M. A. Muriel, “Technique for multiplying the repetition rates of periodic trains of pulses by means of a temporal self-imaging effect in chirped fiber gratings,” *Opt. Lett.* **24**(23), p. 1672, 1999.
- [152] J. Zhou, G. Zheng, and J. Wu, “Comprehensive study on the concept of temporal optical waveguides,” *Phys. Rev. A* **93**, pp. 063847: 1–5, June 2016.

- 
- [153] B. W. Plansinis, W. R. Donaldson, and G. P. Agrawal, "Spectral Splitting of Optical Pulses Inside a Dispersive Medium at a Temporal Boundary," *IEEE J. Quantum Electron.* **52**, p. 6100708, Nov. 2016.